Sources of Dust Extinction in Type Ia Supernovae

Measurements and constraints from X-rays to the Infrared

Joel Johansson

Doctoral Thesis in Physics

Department of Physics
Stockholm University
Stockholm 2015

Stockholm University

Doctoral Thesis in Physics

Sources of Dust Extinction in Type Ia Supernovae

Measurements and constraints from X-rays to the Infrared

Joel Johansson

Oskar Klein Centre for
Cosmoparticle Physics

and

Cosmology, Particle Astrophysics
and String Theory

Department of Physics
Stockholm University
SE-106 91 Stockholm

Stockholm, Sweden 2015

Cover image: Collage of observations at different wavelengths used in this thesis of SN 2011fe (top panels: 0.23, 3.6 and 70 μm), SN 2012cg (middle panels: 0.55, 1.2 and 3.6 μm) and SN 2014J (bottom panels: 0.44, 2.2 and 4.5 μm).

ISBN 978-91-7649-071-6 (pp. i–xviii, 1–60)

Printed by Universitetsservice US-AB, Stockholm, Sweden, 2015.

Typeset in pdfLaTeX

Abstract

The use of Type Ia supernovae (SNe Ia) as distance indicators is essential for studying the expansion history of the Universe and for exploring the nature of dark energy. However, a lack of understanding of the progenitor systems and the empirically derived colour-brightness corrections represent severe limitations for SNe Ia as cosmological probes. In this thesis, we study how dust along the line of sight towards SNe Ia affects the observed light over a wide range of wavelengths; from X-rays to infrared.

Unless properly corrected for, the existence of intergalactic dust will introduce a redshift dependent magnitude offset to standard candle sources and bias the cosmological parameter estimates as derived from observations of SNe Ia. We model the optical extinction and X-ray scattering properties of intergalactic dust grains to constrain the intergalactic opacity using a combined analysis of observed quasar colours and measurements of the soft X-ray background. We place upper limits on the extinction $A_B(z = 1) \lesssim 0.10 - 0.25$ mag, and the dust density parameter $\Omega_{\rm dust} \lesssim 10^{-5} - 10^{-4}(\rho_{\rm grain}/3\,{\rm g\,cm^{-3}})$, for models with $R_V \lesssim 12 - \infty$, respectively.

Dust in the host galaxies, and dust that may reside in the circumstellar (CS) environment, have important implications for the observed colours of SNe Ia. Using the *Hubble Space Telescope* and several ground based telescopes, we measure the extinction law, from UV to NIR, for a sample of six nearby SNe Ia. The SNe span a range of $E(B - V) \sim 0.1 - 1.4$ mag and $R_V \sim 1.5 - 2.7$, showing a diversity of dust extinction parameters. We present mid- and far-infrared (IR) observations for a number of SNe Ia, obtained with the *Herschel Space Observatory* and *Spitzer Space Telescope*, addressing CS dust as an explanation for "peculiar" extinction towards some SNe Ia. No excess IR emission is detected, limiting CS dust masses, $M_{\rm dust} \lesssim 10^{-5}$ $M_\odot$. In particular, the timely appearance of SN 2014J in M 82 - the closest SN Ia in several decades - allows for detailed studies, across an unprecedented wavelength range, of its lightcurve and spectral evolution along with the host galaxy and CS environment.

This thesis is dedicated to the brightest shining stars
in my universe – 1985M and 2014jp

Publications included in the thesis

The following papers, referred to in the text by their Roman numerals, are included in this thesis.

Paper I **J. Johansson** & E. Mörtsell. *Combined constraints on intergalactic dust from quasar colours and the soft X-ray background*, *MNRAS, Vol. 426, p. 3360-3368* (2012).

Paper II **J. Johansson**, R. Amanullah and A. Goobar. *Herschel limits on far-infrared emission from circumstellar dust around three nearby Type Ia supernovae*, *MNRAS, Vol. 431, L43-L47* (2013).

Paper III A. Goobar, **J. Johansson**, R. Amanullah, [31 additional authors]. *The Rise of SN 2014J in the Nearby Galaxy M 82*, *ApJL, Vol. 784, L12* (2014).

Paper IV R. Amanullah, A. Goobar, **J. Johansson**, [10 additional authors]. *The Peculiar Extinction Law of SN 2014J Measured with the Hubble Space Telescope*, *ApJL, Vol. 788, L21* (2014).

Paper V **J. Johansson**, A. Goobar, M. M. Kasliwal, [12 additional authors]. *Spitzer observations of SN 2014J and properties of mid-IR emission in Type Ia Supernovae*, *arXiv:1411.3332* (Submitted to MNRAS).

Paper VI R. Amanullah, **J. Johansson**, A. Goobar, [25 additional authors]. *Diversity in extinction laws of SNe Ia measured with The Hubble Space Telescope*, (Work in progress).

Publications not included in the thesis

The following papers are not included in this thesis.

Paper A1 E. Zackrisson, 10 additional authors including **J. Johansson**. *Hunting for dark halo substructure using submilliarcsecond-scale observations of macrolensed radio jets*, *MNRAS, Vol. 431, p. 2172-2183* (2012).

Paper A2 J. M. Silverman, 19 additional authors including **J. Johansson**. *SN 2000cx and SN 2013bh: Extremely Rare, Nearly Twin Type Ia Supernovae*, *MNRAS, Vol. 436, p. 1225-1237* (2013).

Paper A3 G. Leloudas, 11 additional authors including **J. Johansson**. *Supernova spectra below strong circum-stellar interaction*, arXiv:1306.1549 *(Accepted for publication in A&A)*.

Paper A4 G. H. Marion, 24 additional authors including **J. Johansson**. *Early Observations and Analysis of the Type Ia SN 2014J in M 82*, arXiv:1405.3970 *(Accepted for publication in ApJ)*.

Paper A5 E. Y. Hsiao, 53 additional authors including **J. Johansson**. *Strong near-infrared carbon in the Type Ia supernova iPTF13ebh*, (Submitted to A&A).

Paper A6 Y. Cao, 20 additional authors, including **J. Johansson**. *Ultraviolet Radiation from Supernova-Companion Collision in a Type Ia Supernova*, (Submitted to Nature).

Paper A7 L. P. Singer, 31 additional authors, including **J. Johansson**. *The Needle in the 100 deg2 Haystack: Uncovering Afterglows of FERMI GRBs with the Palomar Transient Factory*, (Submitted to ApJ)

Author's contribution

Behind observational data lies a great amount of work, which is not always fully visible in the publications. I have spent much time writing proposals for telescope time, "scanning" for the right objects to observe, collecting the data (preparing telescope triggers, downloading the data or actually staying up at night to observe) and processing the data (image reductions, calibrations).

For Paper I, I wrote most of the code, led and carried out the analysis, wrote the text and prepared the figures.

For Paper II and Paper V, I wrote the code to compute the expected IR fluxes and performed the image processing and measurements on the *Spitzer* mid-IR and *Herschel* far-IR data. I also prepared the text and figures.

In Paper III and Paper IV, focussing on the spectacular SN 2014J, I reduced all the optical data from the *NOT* (images and spectra), performed photometry measurements, light-curve fitting and extinction measurements. I wrote some of the text and prepared many of the figures.

For Paper VI, I reduced and analyzed the ground based optical and near-IR data, performed photometry on the *Swift* data and provided light-curve fits. I wrote minor sections of the text and prepared some of the figures.

Additionally, mainly as part of the *intermediate Palomar Transient Factory* (iPTF) collaboration, I have reduced spectra, performed photometry measurements and made contributions to the analysis for a number of publications (Papers A1–A7, not included in the thesis).

Joel Johansson
Stockholm, December 2014

Acknowledgments

First of all I wish to thank my supervisors; Ariel, Rahman and Edvard, for their guidance and encouragement during these years. It has been a privilege to work with you and the former (Linda, Jakob N, Jakob J and Giorgos) and present (Tanja, Raphael and Semeli) postdocs and students in the SNOVA group!

I am also grateful for the good atmosphere in the Oskar Klein Centre and the CoPS group - especially for the friendship of Kattis, Maja, Hugh, Jonas and Stefan and the “mentorship” of Jan!

I am thankful for all the support from my family; mom, dad and Emma-Li. Most importantly, this thesis and the work behind it would not have been possible without the love and support from Matilda and Jonna. Thank you!

Abbreviations

AGN	Active Galactic Nuclei
BAO	Baryon Acoustic Oscillations
CMB	Cosmic Microwave Background
CC	Core Collapse
CCD	Charged Coupled Device
CS	Circumstellar
CSM	Circumstellar medium
FIR	Far-infrared, $24 - 250$ μm
FOV	Field Of View
HST	Hubble Space Telescope
iPTF	intermediate Palomar Transient Factory
IR	Infrared, > 1 μm
IGM	Intergalactic medium
ISM	Interstellar medium
ΛCDM	model of the Universe, containing Λ and Cold Dark Matter (CDM)
MIR	Mid-infrared, $3.6 - 24$ μm
NIR	Near-infrared, $1 - 2.5$ μm
NOT	Nordic Optical Telescope
QSO	Quasi Stellar Objects, or "Quasars"
SDSS	Sloan Digital Sky Survey
SED	Spectral Energy Distribution
SN	Supernova
SNe	Supernovae
SXB	Soft X-ray Background (energy range 0.5 - 2 keV)
WD	White Dwarf
UV	Ultraviolet $10 - 4000$ Å
ZTF	Zwicky Transient Facility

Contents

Preface

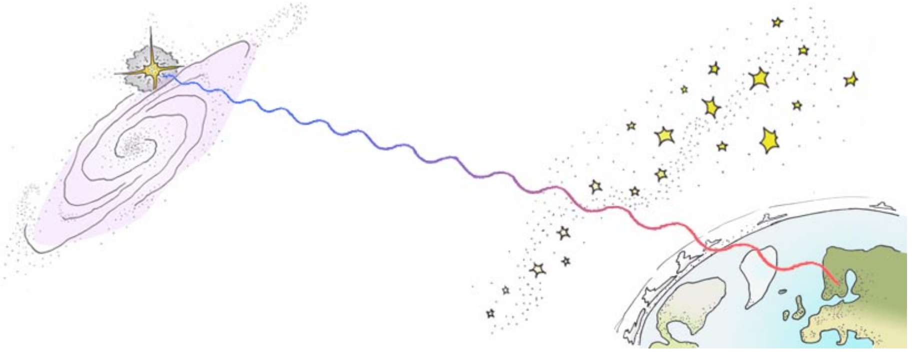

The currently favoured model for the Universe is the so called ΛCDM model. This model, backed up by a smörgåsbord of observations, estimates that the present energy content of the Universe is made up of approximately 4% baryonic matter, 23% cold dark matter (CDM) and 73% dark energy (possibly a cosmological constant, Λ).

Chapter 1 gives a brief history of how the expansion of the Universe was discovered, and introduces some of the basic concepts used in modern cosmology. Chapter 2 describes some of the transient events in the Universe, how one goes about to find them and what they are. Chapter 3 focusses on a particular class of optical transients – Type Ia Supernovae (SNe Ia) – and how they can be used as "standard candles" to probe the expansion history of the Universe. The light from these SNe Ia have to pass through dusty environments in their host galaxies, travel vast distances between galaxies and lastly through our own Galaxy before reaching our telescopes. Chapter 4 describes the dust in these different environments and how they affect our observations. In Chapter 5 we focus specifically on dust in the intergalactic medium, host galaxies and circumstellar surroundings of SNe, and how we can use a wide wavelength range of light – from X-rays, ultraviolet, visible to the infrared – to study its impact. Chapter 6 gives a summary and an outlook.

Chapter 1

An expanding Universe

In 1917, Vesto Slipher published spectroscopic observations of spiral galaxies. He found that the galaxies seemed to be moving away from the Solar System with velocities of ~ 600 km/s . The shifting of absorption lines to longer (redder) wavelengths is known as (Doppler) redshift, z, defined by

$$1 + z = \frac{\lambda_{\rm obs}}{\lambda_{\rm em}}\,, \tag{1.1}$$

where $\lambda_{\rm em}$ is the emitted wavelength and $\lambda_{\rm obs}$ is the observed wavelength. Vesto's colleague, Knut Lundmark plotted the recession velocities of the galaxies against their estimated distances (Lundmark, 1924). He assumed that the Andromeda galaxy is ~ 200 kpc away [1], then made rough determinations of the distances to other galaxies by comparing their sizes and brightnesses to that of Andromeda. Lundmark concluded that "there may be a relationship between the two quantities, although not a very definite one".

Using this data, Georges Lemaître proposed that the Universe is expanding and suggested an estimated value of the rate of expansion to be ~ 575 or $670\ \mathrm{km\,s^{-1}\,Mpc^{-1}}$ (Lemaître, 1927). Two years later, Hubble (1929) confirmed the existence of that law, by combining the redshifts with his own measurements of galaxy distances based on Henrietta Swan Leavitt's period-luminosity relationship for Cepheids (Leavitt & Pickering, 1912),

$$v = H_0 \cdot d\,, \tag{1.2}$$

today known as the Hubble law, where v is the velocity and d is the distance of the galaxy and H_0 is called the Hubble constant.

[1] the actual distance to Andromeda (M31) is more like 778 ± 17 kpc.

For nearby objects, ($z \lesssim 0.01$), most of the redshift is due to peculiar velocities ($z \approx v/c$). For distant objects, the dominant source of redshifting is the stretching of space-time. This cosmological redshift depends on how much the Universe has expanded since time t when light was emitted until it is observed today at time t_0,

$$1 + z = \frac{a(t_0)}{a(t)}\,, \tag{1.3}$$

where the scale factor $a(t)$ describes how distances are stretched as a function of time. To describe the expansion of the Universe, the Hubble parameter $H(t)$ can be defined from the scale factor $a(t)$, as

$$H(t) \equiv \frac{\dot{a}(t)}{a(t)}\,, \tag{1.4}$$

where $\dot{a}(t)$ is the time derivative of the scale factor. The value of the Hubble parameter today is denoted H_0 and is measured to be $73.8 \pm 2.4\,\mathrm{km\,s^{-1}\,Mpc^{-1}}$ (Riess et al., 2011).

1.1 Cosmological models

The Universe can be described by the Friedmann Lemaître Robertson Walker (FLRW) model. This requires that the universe can be approximated as homogenous and isotropic on large scales. Applying the FLRW model to the Einstein equations of general relativity gives the Friedmann equations, which describe the dynamics of the Universe,

$$H^2 = \left(\frac{\dot{a}}{a}\right)^2 = \frac{8\pi G\rho}{3} - \frac{k}{a^2} \tag{1.5}$$

and

$$\left(\frac{\ddot{a}}{a}\right) = -\frac{4\pi G}{3}\left(\rho + 3p\right)\,, \tag{1.6}$$

where G is the gravitational constant, ρ is the total energy density of the Universe, p is the total pressure and k is the curvature. From now on, we will assume that the universe is flat (i.e. $k = 0$, as indicated by measurements of the CMB).

It is often useful to resolve the different components contributing to the total energy density of the Universe, such that $\rho = \rho_r + \rho_m + \rho_\Lambda$

(radiation, matter and a cosmological constant). For each of these components, one can define an equation-of-state parameter, $w \equiv p/\rho$. For constant w, one can find a solution to equations 1.5 and 1.6 describing how the energy densities of the different components evolve,

$$\rho = \rho_0 a^{-3(1+w)} . \tag{1.7}$$

For non-relativistic matter (baryonic and dark matter) the pressure is zero ($w = 0$), for radiation $w = 1/3$, and for a cosmological constant ρ_Λ the equation of state parameter is $w = -1$. Normalizing these density components with the critical density of the Universe, $\rho_{\rm crit} \equiv 3H^2/8\pi G$ (defined as the total energy density needed to have a flat geometry without dark energy), one can express Eq. 1.5 in terms of dimensionless density parameters, $\Omega = \rho/\rho_{\rm crit}$,

$$H(z)^2 = H_0^2 \left[\Omega_r(1+z)^4 + \Omega_m(1+z)^3 + \Omega_\Lambda\right] . \tag{1.8}$$

In the case of the "simplest" dark energy model, the cosmological constant Λ, the energy density ρ_Λ is constant and $w \equiv -1$ (any fluid with $w < -1/3$ will cause the universe to accelerate as seen from Eq. 1.6). In more general or exotic dark energy models, the equation-of-state parameter changes with time, and this is usually parametrized by changing

$$\Omega_\Lambda \to \Omega_{DE} \exp\left[\int 3\,(1+w(z))\, d\ln(1+z)\right] , \tag{1.9}$$

where the dark energy equation-of-state can e.g. be parametrized by (Chevallier & Polarski, 2001; Linder, 2003),

$$w(z) = w_0 + w_a \frac{z}{1+z} . \tag{1.10}$$

1.2 Measuring distances in the Universe

Given a cosmological model, one can construct observables such as Ω_m and Ω_Λ. To measure these observables one usually uses dynamical probes (i.e. observing how structures grow) or geometrical probes (i.e. measuring distances).

There are two basic ways to measure physical distances in cosmology; one based on standard candles (sources of known intrinsic brightness, e.g. supernovae) and one based on standard rulers (sources of known physical size, e.g. baryon oscillations and fluctuations in the cosmic microwave background). Following Hogg (1999), one can derive to the total line-of-sight comoving distance (again assuming a flat universe, $k = 0$),

$$d_C = c \int_0^z \frac{dz'}{H(z')}\,, \tag{1.11}$$

where c is the speed of light and $H(z)$ is the Hubble constant as measured by a hypothetical astronomer working at redshift z, defined in Eq. 1.8.

The angular diameter distance, $d_A(z)$, is defined in terms of the ratio of the physical size x of an object at redshift z to its angular size, θ,

$$d_A(z) = \frac{x}{\theta} = \frac{1}{1+z} d_C\,. \tag{1.12}$$

The luminosity distance, d_L, is defined by the relationship between the flux F and the intrinsic luminosity L of an object,

$$d_L(z) = \sqrt{\frac{L}{4\pi F}} = (1+z) d_C\,. \tag{1.13}$$

In astronomy one usually measure *magnitudes* instead of fluxes. The apparent magnitude, m, of a source observed through a filter x, can be defined as,

$$m_x = -2.5 \log_{10} \left(\frac{F_x}{F_{x,\mathrm{ref}}} \right), \tag{1.14}$$

where F_x is the observed flux in filter x and $F_{x,\mathrm{ref}}$ is a reference flux (e.g. of the star Vega) in the same filter. The absolute magnitude, M, is defined as the apparent magnitude that a star would have if it was placed at a distance of 10 pc. One can define the *distance modulus*, μ, as

$$\mu \equiv m - M = 5 \log_{10} \frac{d_L(z)}{10\,\mathrm{pc}}\,. \tag{1.15}$$

By comparing the observed brightness of a standard candle with the known intrinsic brightness, the luminosity distance can be inferred. This distance depends on the redshift of the object and the cosmological parameters, $d_L(z; \Omega_m, \Omega_\Lambda, ...)$.

Chapter 2

A transient Universe

This chapter will give a general introduction to different kinds of optical transients in the Universe and how one goes about to find them. While "guest stars" – visible to the naked eye – and variable stars have been observed in the pre-telescopic era, it was not until the 1850's that astronomers could start to systematically study transient events in the Universe, with the aid of better telescopes and, maybe more importantly, photographic plates. Variable stars (e.g. cepheids, mentioned in Chapter 1) and novae (sudden or recurrent brightening of stars) were instrumental in understanding the inner workings of stars and played a key role as distance indicators.

2.1 Supernovae

Along with the understanding of the size of our Galaxy and the distances to other galaxies, came the insight that there were in fact two distinct classes of novae, with absolute magnitudes differing by ~ 10 mag. The more luminous ones where at first called *giant-* or *upper-class novae* (Lundmark, 1920, 1927), *exceptional novae* (Hubble, 1929) or *super-novae* Baade & Zwicky (1934). Baade and Zwicky, proposing *(1)* that supernovae (SNe) are explosions of massive stars that *(2)* produce cosmic rays and *(3)* would leave a remnant star consisting only of neutrons, started chasing supernovae to confirm their theories. Using the wide-field 18- and 48-inch Schmidt telescopes at Palomar, Zwicky discovered 123 supernovae during the course of 52 years.

Based on their spectral characteristics, the SNe were further divided into two classes: Type I (no hydrogen in their spectra) and Type II (have hydrogen) (Minkowski, 1941). By studying the infrared light-curves of

Type I SNe, Elias et al. (1985) found that these fall into two groups: Type Ia (the more common ones, with a secondary maximum hinted in the R-band lightcurve of the normal Type Ia SN in Fig. 2.1) and Type Ib (no secondary maximum). They also noted that the dispersion in absolute magnitudes of Type Ia SNe was small (± 0.2 mag) making them "potentially valuable for distance determination". We now have three subclasses of hydrogen-deficient Type I SNe: those whose early-time spectra show strong Si II (Type Ia), those with prominent He I (Type Ib, illustrated in Fig. 2.1) or those that do not show stong Si II or He I (Type Ic) in their spectra (Filippenko, 1997).

The physical understanding and classification of these events has evolved parallel to the characterization of their light-curve behavior and spectral properties, which makes the nomenclature a bit tedious. Stars of different mass follow different evolutionary tracks and face different end stages, which explains the large variety of luminosities and spectral features among the supernovae.

Stars born with masses $\gtrsim 8-10\ \mathrm{M}_{\odot}$ are heavy and hot enough ($T \sim 10^9$ K) to fuse increasingly higher mass elements, starting with hydrogen and then helium, until finally a core of iron and nickel is produced. When no further fusion can take place, the inert core will collapse while creating a shockwave propagating outwards. These core-collapse supernovae (CC SNe) show large variation in light-curve and spectral features, depending on the progenitor mass, circumstellar environment or whether the outer hydrogen or helium layers still exist, and are classified as Type II (showing hydrogen lines) and Ib/c (no hydrogen) SNe.

Stars with masses $\lesssim 8-10\ \mathrm{M}_{\odot}$ evolve in a different fashion. Hydrogen and helium are fused into carbon and oxygen, but no further burning takes place since the temperatures are too low. The outer hydrogen and helium envelopes are probably lost in the Red Giant evolution stage. This leaves a small carbon+oxygen (C+O) white dwarf (WD) which by some mechanism accretes mass until it reaches the Chandrasekhar limit of $\sim 1.4\ \mathrm{M}_{\odot}$. These WD stars are thought to be the origin of Type Ia Supernovae (see Chapter 3).

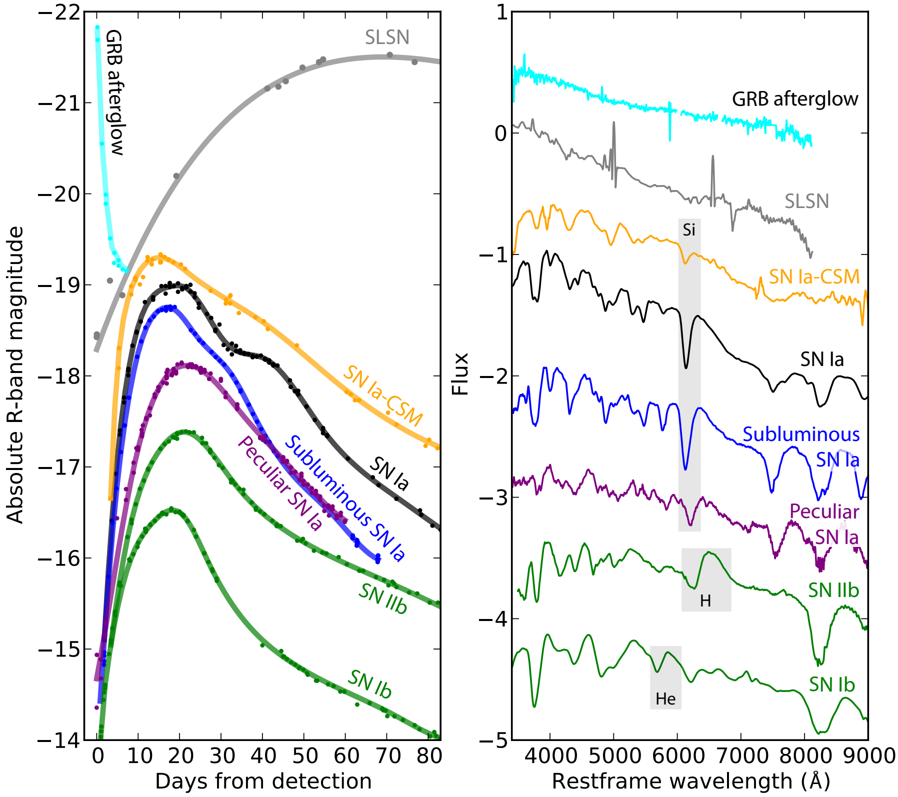

Figure 2.1. Left: Example light curves of transients discovered by PTF/iPTF, spanning a wide range of peak luminosities and decay time-scales. **Right:** Spectra around maximum brightness of the different types of transients. The regions of some characteristic spectral features (Silicon II for SNe Ia, helium in SNe Ib and hydrogen in SNe II) are marked with grey boxes.

2.2 Supernova searches

Searches for optical transients are conducted much differently today than only a few decades ago. The advent of charged coupled devices (CCD) cameras, allowing pixel based image-subtractions, has increased the number of discovered SNe dramatically. Until 1996 a total of ~1000 SNe had been discovered, while this year alone more than 1400 SN discoveries have been reported.

The two first "high redshift" supernovae were discovered by Hansen et al. (1989); Norgaard-Nielsen et al. (1989) through repeated deep optical imaging of a cluster at a redshift of $z \sim 0.3$. Although it took two years of extensive monitoring with a 1.5 m telescope with a small field of view (FOV), these discoveries were a "proof of concept" (also providing the first test of cosmological time dilation, broadening the lightcurve width by a $(1+z)$ factor), which inspired the *Supenova Cosmology Project* and the *High-Z Supernova Search* teams to use larger telescopes with wider FOV to find more high redshift SNe Ia. Modern wide-field imaging transient search projects (e.g. SDSS, SNLS, ESSENCE and Pan-STARRS) have also led to the discovery of new classes of rare stellar explosions (e.g. super-luminous SNe, shown in Fig. 2.1). One such survey is the *intermediate Palomar Transient Factory* (iPTF): an "untargeted" optical survey using the robotic Palomar 48" (1.2 m) telescope with a 7.2 deg^2 FOV with additional follow-up facilities all around the globe. iPTF (and its predecessor PTF) has discovered $>$ 2000 SNe since 2009. By 2017 iPTF is to be replaced by the *Zwicky Transient Facility* (ZTF) using the same telescope, but a CCD camera with a five times larger FOV, able to scan the sky with fast cadence to a depth of $\sim$ 21 mag. The aim is to discover nearby supernovae at the earliest possible stages and possibly detect optical counterparts to sources for gravitational waves or transients detected at other wavelengths, e.g. Fast Radio Bursts or Gamma Ray Burst afterglows (shown in Fig. 2.1). Future surveys (such as *LSST*) aim to discover vast numbers of SNe at high redshifts ($z \gtrsim 1$), where space-based infrared telescopes (e.g. *Euclid*, *WFIRST* and the *James Webb Space Telescope*) will be necessary in order to observe the most distant sources (since the UV/optical region, where SNe are brightest, will be redshifted to longer wavelengths).

Chapter 3

Type Ia supernovae and their use in cosmology

Type Ia supernovae have revolutionized our understanding of the Universe *twice*! In the beginning of November 1572, a bright new star appeared in the sky – so bright, it was visible even during daytime. This new star ("stella nova") was carefully studied by the danish astronomer Tycho Brahe, who claimed that this object was not an atmospheric phenomenon or a planet, because it did not change positions with respect to the other stars. Tycho's nova, belonging to the celestial sphere, thus provided the first evidence against the prevailing Aristotelian idea of the unchangeability of the realm of stars. Through observations of a scattered-light echo (more than 400 years after the first light from the explosion swept past Earth), we know today that SN 1572 was a Type Ia supernova that occurred in the Milky Way (Krause et al., 2008).

More recently, our picture of the Universe was once again altered. Not only is the Universe expanding, but its expansion accelerates (Riess et al., 1998; Perlmutter et al., 1999). This accelerated expansion was detected using observations of distant SNe Ia, and is attributed to an unknown "dark" energy component acting as a repulsive force. Today, many other cosmological probes consistently confirm the accelerated expansion.

3.1 The Type Ia Supernovae family

Type Ia Supernovae (SNe Ia) have very similar lightcurves. Around 20 days after the explosion they reach a maximum brightness $M_B \approx -19.3$

magnitudes in the B-band (Phillips, 1993; Hamuy et al., 1995) corresponding to a luminosity of $\sim 10^{10}\, L_{\odot}$, which is comparable to the luminosity of an entire galaxy. The dispersion of M_B at maximum brightness is of the order 0.3–0.4 mag (as illustrated in Figure 3.3). The SN then fades away quickly, after about two weeks it has diminished to half of its peak brightness (usually quantified by the decline rate during the first 15 days from B-band maximum, Δm_{15}^{B}, typically ranging from 0.9 to 1.6 mag for a normal SN Ia), and the subsequent exponential decline of the lightcurve is powered by the radioactive decay of ^{56}Ni created in the violent explosion. Based on spectral characteristics, there are further subclasses of "peculiar" SNe Ia, typically named after the prototypical SN:

- 1991T-like, have shallower absorption features in their pre-maximum spectra (Filippenko et al., 1992a) and slowly declining lightcurves ($\Delta m_B^{15} \lesssim 0.9$) and are over-luminous.

- 1991bg-like (Filippenko et al., 1992b; Leibundgut et al., 1993), exhibit strong Ti II features in their maximum-light optical spectra, These objects are found to be subluminous, have exceptionally fast-declining light curves ($\Delta m_B^{15} \gtrsim 1.6$) and lack the characteristic secondary maximum.

- 2002cx-like, (or SNe Iax) are spectroscopically similar to SNe Ia, but have lower maximum-light velocities. They typically have peak magnitudes > 1 mag below that of normal SNe Ia (Foley et al., 2013).

- Super-Chandrasekhar SN Ia (e.g. SN 2003fg Howell et al., 2006) are rare and even more luminous than 91T-like SNe ($M_V \sim -20$ mag). The ^{56}Ni mass necessary to produce the observed luminosity implies a total mass significantly in excess of the Chandrasekhar mass.

- Ia-CSM, (e.g. SNe 2002ic, Hamuy et al., 2003) are most likely thermonuclear events (Fox et al., 2014). Their spectra appear to be "diluted" versions of a bright (e.g. 91T-like) SN Ia along with narrow emission lines, indicating strong interaction with CSM.

While these peculiar SNe Ia could potentially contaminate and bias cosmological parameter estimations, the observed fraction of normal SNe Ia are $\sim 70\%$, and the remaining fractions are $\sim 9\%$ 91T, $\sim 15\%$ 91bg and $\sim 2\%$ 02cx-like SNe Ia, in a volume limited sample (Li et al., 2011).

Progenitor system

There are two commonly proposed mechanisms for triggering a Type Ia supernova explosion, both involving two stars in a close binary star system. In the **Single Degenerate** (SD) scenario a WD reaches the Chandrasekhar mass by accreting matter from a more massive binary companion star. The **Double Degenerate** (DD) scenario is where two binary WDs merge.

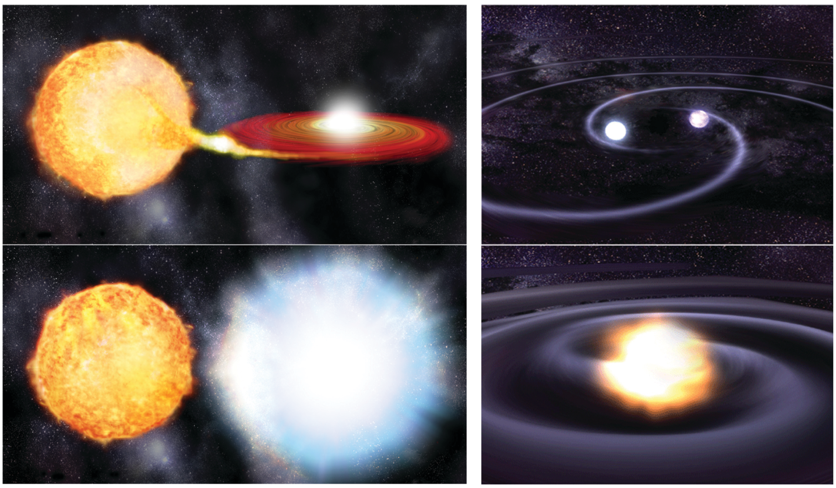

Figure 3.1. Artist's impression of two proposed mechanisms to make a SN Ia. **Left:** Single degenerate scenario, with a WD accreting mass from a companion star. **Right:** Double degenerate scenario, with two WDs merging. (Credit: NASA/CXC/M. Weiss)

As of today, no compact objects have been detected in pre- or post explosion images of known normal SNe Ia, indicating that the exploding star is disrupted and that any companion must be faint. Though debated, Ruiz-Lapuente et al. (2004) report the discovery of a star, similar to our Sun, moving at more than three times the mean velocity of the stars at that distance, which appears to be the surviving companion of the Tycho's Supenova.

However, the two scenarios have different signatures that could be observed. In the SD scenario, it is not unreasonable to expect hydrogen and/or helium rich gas from the companion star to be present in the circumstellar medium (CSM). Among the sub-class of peculiar SN Ia-CSM, PTF11kx provides the strongest evidence for being a thermonuclear event interacting with CSM expelled by a companion red giant star

(Dilday et al., 2012). No such hydrogen or helium emission has been seen in normal SNe Ia (Mattila et al., 2005; Lundqvist et al., 2013).

The interaction of the SN Ia ejecta with the CSM would probably also produce detectable radio and UV/X-ray emission, but as of yet, observational constraints at these wavelengths are limited to upper limits. Radio observations of a large number of nearby SNe Ia have been carried out (see e.g. Panagia et al., 2006; Hancock et al., 2011). No detections were made, and the resultant upper limits are generally consistent with pre-SN mass-loss rates $\dot{M} \lesssim 10^{-7}$ $M_{\odot}$ yr $^{-1}$. Shocks formed by the interaction of the SN with the surrounding CSM, may heat ambient material to very high temperatures ($\sim 10^6 - 10^7$ K) producing thermal X-rays emission. Immler et al. (2006) and Russell & Immler (2012) analyze a large number of SNe Ia observed with the *Swift* X-Ray Telescope. The non-detections yield a combined 3σ upper limit on the mass-loss rate is $\dot{M} \lesssim \cdot 10^{-6} (v_{\mathrm{wind}}/10\ \mathrm{km/s})$ $M_{\odot}$ yr^{-1}.

The collision of the SN ejecta with its companion star should produce detectable optical/UV emission in the hours and days following the explosion (Kasen, 2010). No such emission has been detected for normal SNe Ia. This has been used to put limits on the separation of the stars and the companion star radius. However, recent observations of a peculiar, sub-luminous (02cx/02es-like) SN Ia, showing a UV pulse within the first few days after explosion, is consistent with the collision signature between the SN ejecta and a companion star (Paper A6).

The SD scenario could provide an explanation to the observed homogeneity of SN Ia, but it seems necessary that the accretion rate is fine-tuned to $\dot{M} \sim 10^{-8}$ $M_{\odot}$/yr in order for the explosion to take place (Hachisu et al., 1996).

The DD scenario could explain why no signs of mass transfer have been detected, but it raises questions about the applicability of SNe Ia as standard candles. Since the total mass of the collapsing WDs would vary over a large range, a large variety of luminosities can be expected. This could provide a mechanism for "anomalous" sub-luminous and over-luminous Super-Chandrasekhar-mass SNe Ia. The inwards spiraling WDs should be strong sources of gravitational waves, which can potentially be probed by future experiments (e.g. LIGO/VIRGO).

All in all, it seems that neither the SD nor the DD hypothesis can currently be rejected or confirmed, and it is possible that SNe Ia are produced through both channels.

3.2 The Beauty and the Beast

SNe 2011fe and 2014J are two recent examples – perhaps the best to date – of nearby normal SNe Ia, that illustrate how we can address some of the unanswered questions regarding the progenitors, explosion physics, circumstellar environment and host galaxy properties of normal SNe Ia.

SN 2011fe was discovered on 2011 August 24.2 UT, merely 11 hours after the inferred time of explosion, by the Palomar Transient Factory. Due to its early detection, combined with its closeness (in the nearby "Pinwheel galaxy", M 101, at a distance of 6.4 ± 0.7 Mpc, which is $\sim$ 21 million light-years) it was the subject of a massive multi-wavelength observational campaign.

By analysing pre-explosion *HST* and *Spitzer* images Li et al. (2011) and Nugent et al. (2011) are able to put stringent limits on the luminosity of the companion star, ruling out red-giants and a majority of helium stars as the mass donor companion to the exploding white dwarf (WD). By studying the early rise of the light curves, Bloom et al. (2012) are able to show that the primary progenitor star must be compact $R_\mathrm{p} \lesssim 0.02$ $\mathrm{R}_\odot$, with WDs and neutron stars viable as the primary star of SN 2011fe. With few caveats, they also restrict the companion star radius to $R_\mathrm{c} \lesssim 0.1$ $\mathrm{R}_\odot$, excluding red giant and main-sequence companions to high significance. Early radio and X-ray observations (Horesh et al., 2012; Chomiuk et al., 2012) report non-detections, yielding very tight constraints on the pre-explosion mass-loss rate from the progenitor system $\dot{M} < 6 \cdot 10^{-10} - 10^{-8}(v_\mathrm{wind}/100 \text{ km/s})$ $\mathrm{M}_\odot$/yr. Although they are model dependent, these limits rule out a large portion of the parameter space of SD progenitor models for SN 2011fe. Patat et al. (2013) studied the properties of the circumstellar environment using multi-epoch, high-resolution spectroscopy. The absence of time-variant, blueshifted Na I D absorption features implies that the surroundings of SN 2011fe are "clean" and is consistent with the progenitor being a binary system with a main sequence star.

SN 2014J was serendipitously discovered by Fossey and students on 2014 January 21.81 UT, observing the "Cigar galaxy" (M 82, at a distance 3.5 ± 0.3 Mpc, which is $\sim$ 11 million light-years) during an astronomy course at the University of London Observatory. SN 2014J was by then one week after explosion, but the early light-curves could however be reconstructed. Pre-discovery iPTF narrow-band H_α, KELT, KAIT and amateur observations, indicate the time of explosion to be January 14.7 UT (Paper III, Zheng et al., 2014) and show signs of additional sources of luminosity in the first hours after the explosion (see right middle panel of Fig. 3.2, Goobar et al., 2014). Most notably, the proximity allowed for a first time detection of a SN Ia in gamma-rays (Diehl et al., 2014; Churazov et al., 2014), suggesting that about $0.6 \pm 0.1\,M_\odot$ of radioactive ^{56}Ni was synthesized during the explosion.

No activity (e.g. from nova outbursts) is detected in iPTF pre-explosion images, and analyses of archival *HST* images of M 82 exclude a progenitor system with a bright red giant mass-donor companion, but can not rule out a double degenerate progenitor system consisting of two WDs (Paper III, Kelly et al., 2014b). The non-detection in X-rays and radio yield constraints similar to those for SN 2011fe (Margutti et al., 2014; Pérez-Torres et al., 2014). In Paper III and Paper A4 we conclude that SN 2014J is a spectroscopically normal SN Ia, albeit with slightly higher than average expansion velocities (also studied by Foley et al., 2014; Brown et al., 2014; Ashall et al., 2014), being heavily obscured by dust. The dusty starburst galaxy M 82 has been the subject of numerous studies (e.g. Mattila et al., 2013; Hutton et al., 2014). High-resolution spectra indeed reveal that the line-of-sight towards SN 2014J is very rich in absorbing material. The nature of dust causing the extinction is examined in Paper IV and Paper V and summarized in Chapter 5.

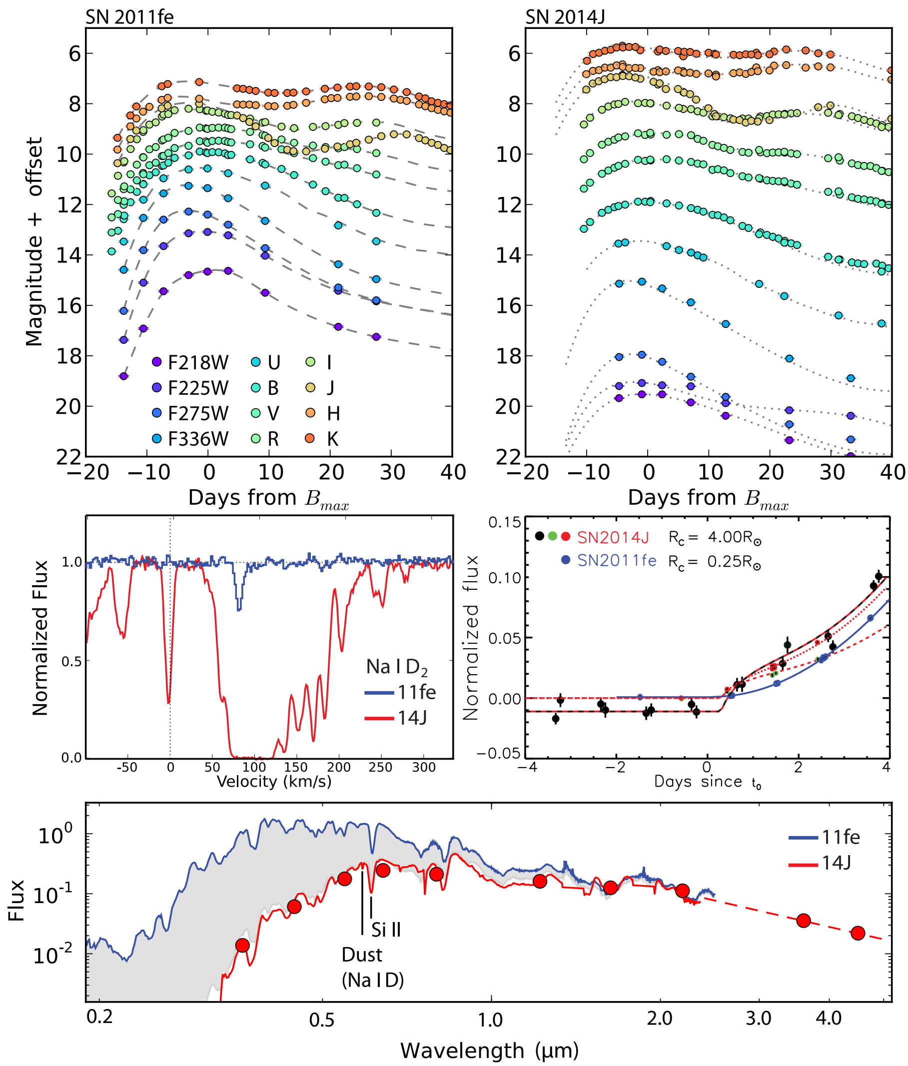

Figure 3.2. SNe 2011fe and 2014J (blue and red lines in middle and bottom panels, respectively) are the closest SNe Ia in the last decades. The light curves (top panels) show that SN 2014J is brighter than SN 2011fe at IR wavelengths but much fainter in the UV/optical, which is a combination of SN 2014J being closer while suffering from extinction by dust. By studying the wavelength dependence of the extinction, from UV to mid-IR wavelengths (bottom panel), and through high-resolution spectroscopy (left middle panel) we can probe the CSM and host galaxy ISM. By analyzing the early behavior of the light curves (right middle panel) the SN progenitor system can be studied (Goobar et al., 2014).

3.3 Cosmological parameters from Type Ia supernovae

To make SNe Ia into standard candles one has to apply empirical corrections. It has been shown by Phillips (1993) and Hamuy et al. (1995) that there is a correlation between the maximum intrinsic brightness and lightcurve shape, where bright supernovae decline slower (i.e. have wider lightcurves). Also, the maximum brightness is correlated with the SN colour, where bright supernovae are bluer (Tripp, 1998).

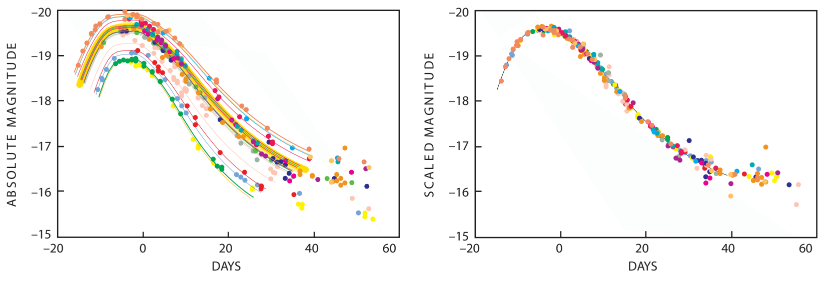

Figure 3.3. Left: V-band light curves of nearby, low-redshift SNe Ia measured by Hamuy et al. (1995). Absolute magnitude is plotted against time (in the SN rest frame) before and after peak brightness. **Right:** By stretching the time scales of individual light curves, and then scaling the brightness by an amount determined by the required time stretch, one can reduce the intrinsic scatter of the peak brightness. (Credit: Perlmutter et al., 1997)

The corrections of lightcurve shape and colour are done with *lightcurve fitters* (algorithms such as SALT2, MLCS2k2, SNooPy are commonly used). These lightcurve fitters differ slightly in parametrizing the corrections and use different training samples. For example, using the SALT parametrization of the lightcurve shape (i.e. "stretch", s) and colour c, the distance modulus can be expressed as,

$$\mu_B = m_B^\star + \alpha \cdot (s-1) - \beta \cdot c - M \,, \tag{3.1}$$

where the rest-frame B-band peak brightness $m_B^\star$, s and c are fitted from the light curves. α, β and the absolute magnitude M are global parameters which are fitted for the whole sample. After corrections to both lightcurve shape and colour are made, the dispersion of M reduces to ~ 0.13 magnitudes which corresponds to $\sim 7\%$ in distance (Astier et al., 2006). Figure 3.4 shows the state-of-the-art Hubble diagram (distance modulus μ vs. redshift z, similar to distance vs. velocity as in Eq. 1.2) from Betoule et al. (2014),

$$\mu_B(z) = 5 \log \frac{d_L(z; \Omega_M, \Omega_\Lambda)}{10\,\text{pc}}, \tag{3.2}$$

where $d_L(z; \Omega_M, \Omega_\Lambda)$ is the luminosity distance which depends on the cosmological parameters Ω_M and Ω_Λ. SNe Ia restrict a linear combination of Ω_M and Ω_Λ, and to break this degeneracy other probes such as Baryon Acoustic Oscillations (BAO) and the Cosmic Microwave Background (CMB) are needed. Together, they restrict the cosmological parameters $(\Omega_M, \Omega_\Lambda) = (0.27, 0.73)$ as seen in Figure 3.5.

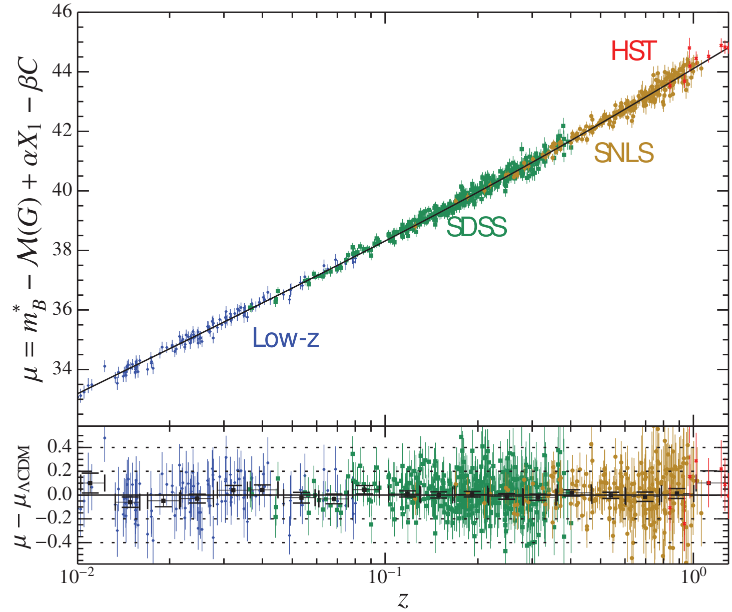

Figure 3.4. Top panel: Hubble diagram from the joint analysis of 740 SNe Ia from SDSS-II, SNLS and several other surveys, by Betoule et al. (2014). Bottom: Residuals from the best-fit ΛCDM cosmology as a function of redshift.

Sources of uncertainty

The SN Ia samples are growing rapidly and already today the systematic uncertainties are becoming dominant over statistical uncertainties. The ambitions of future SN Ia surveys (e.g. LSST) are to find thousands of

SNe up to $z \gtrsim 1$ and aim to constrain the equation-of-state parameter w to higher precision than today ($\sim 7\%$) or even a time-varying $w(z)$, as described in Chapter 1.1. A systematic shift in magnitude δm roughly correlates with the uncertainty in dark energy equation-of-state parameter as $\delta w \sim 2\delta m$ and with the matter density parameter as $\delta\Omega_m \sim \delta m$ (Zhang, 2008; Ménard et al., 2010a). Thus, an offset of $\sim 1\%$ due to dust extinction or photometric mis-calibration would bias the estimated cosmological parameters by a few percent, i.e. comparable to the error bars sought after.

For SNe Ia, systematic uncertainties typically include flux calibration, dust corrections, and population drift (see e.g. Nordin et al., 2008, for a more complete list).

- **Calibration:** Precise distance estimates with SNe Ia require very accurate photometric calibration, making it important to know the exact transmission curves of the filters used. Also, the K-corrections (used to convert the observed magnitudes into rest-frame magnitudes) introduce additional uncertainties.

- **Reddening and absorption:** Correcting for absorption of the SN light along the path from the source to the telescope is crucial for distance determinations. The mapping of dust in the Milky Way (Schlegel et al., 1998) is well known, allowing for accurate corrections. Dust in the intergalactic medium could introduce a magnitude offset which increases with redshift. Also, puzzling results are obtained when correcting SNe Ia colours for host galaxy reddening, indicating either that the dust or the intrinsic colours of SNe Ia are not fully understood. These are subjects that will be further discussed in following Chapters 4 and 5.

- **Redshift drift:** SN Ia cosmology requires that the intrinsic luminosities of nearby SNe are the same as those at high redshift. Anything that would alter intrinsic SN properties or introduce redshift-dependent offsets is therefore very undesirable. Factors that could cause high-redshift SNe to have different properties than local SNe are the composition, ages and masses of the *progenitor systems.* There is a correlation between *host galaxy types* and the SN brightness, where star forming, late-type galaxies host brighter SNe with wider lightcurves. Also, differences in metallicity and dust content between nearby and distant host galaxies could change the explosion properties and colours of the SNe.

- **Other uncertainties:** Selection effects, such as *Malmquist bias*, is an inherent difficulty when comparing the brightness of objects at different redshifts. If a supernova survey is brightness limited (and not limited by volume) the observer would be biased to find only the brightest objects at a certain distance. Through *gravitational lensing*, the light of a supernova can be magnified if there are galaxies or galaxy clusters in the line-of-sight. This magnification averages out, but most SNe would be slightly de-magnified while a few would be highly magnified (Jönsson et al., 2010).

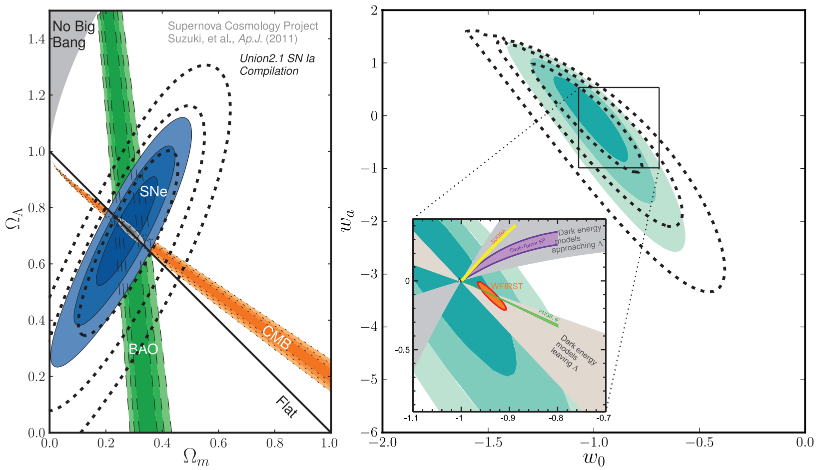

Figure 3.5. Left: 68.3%, 95.4%, and 99.7% confidence regions of the $(\Omega_m, \Omega_\Lambda)$-plane from SNe Ia combined with the constraints from BAO and CMB. The blue contours show the SN Ia confidence region including only statistical errors while the thick dotted lines show the SN Ia confidence regions with both statistical and systematic errors.
Right: 68.3%, 95.4%, and 99.7% confidence regions of a time-dependent dark energy equation-of-state parameter in the (w_0, w_a)-plane from SNe Ia combined with the constraints from BAO, CMB, and H_0, both with (black dotted lines) and without (solid contours) systematic errors. The zoomed in region illustrates that existing data cannot constrain a time-dependent w (the grey bands represent different dark energy models, decribed in Goobar & Leibundgut, 2011), and that future missions such as WFIRST aim to constrain this quantity. (Both figures adapted from Suzuki et al., 2012)

Chapter 4

Dust in the universe

Dust grains are present in almost every environment in the Universe: "non-cosmic" dust under your bed, interplanetary dust in the Solar system, circumstellar dust around stars, interstellar dust in the Milky Way and in other galaxies. Dust plays an increasingly important role in astrophysics - not only something that obscures objects and that has to be corrected for, but also as an important diagnostic tool. Cosmic dust grains are particles produced by stars, spanning a range of sizes from molecules with tens of atoms ($\lesssim$ few Å) to particles as large as a few microns.

4.1 Effects of cosmic dust

Most of the knowledge we have about cosmic dust arises from the interaction of dust with electromagnetic radiation: scattering, absorption and emission (see reviews by Draine, 2003a, 2004).

- **Extinction**: Dust grains scatter and absorb photons with a wavelength dependent cross-section. Typically, dust extinction is correlated with reddening of the incoming light.

- **Polarization**: The extinction is polarization-dependent, requiring that some of the grains are non-spherical and aligned, e.g., with respect to the magnetic fields in the galaxy.

- **Scattering of starlight**: A substantial fraction of the observed extinction in the optical is due to scattering, requiring that some of the grains must be large enough to efficiently scatter optical light.

- **Infrared emission**: Dust grains can absorb UV/optical photons which are re-emitted in the far-infrared.
- **X-Ray scattering**: Dust can scatter X-rays from point sources into extended, diffuse halos. The dust composition and size distribution must be such as to reproduce the observed strength and angular distribution of X-ray scattering by interstellar dust.
- **Microwave emission**: Dust-correlated microwave emission is attributed to rotational emission from very small dust grains.

Observations of cosmological sources (e.g. supernovae, quasars, gamma ray-bursts) are affected by dust in the immediate surroundings of the source and in the host galaxy, by dust in and around galaxies along the line-of-sight, dust in the intergalactic medium and finally by dust in the Milky Way. In the following sections we will review some of the observational constraints that will aid us when modeling the scattering, extinction and emission properties of dust that could affect observations of SNe Ia.

4.2 Dust in the Milky Way

In our Galaxy, the gas-to-dust ratio is about 100:1. Since the interstellar medium (ISM) is about 10% of the baryonic mass of the Galaxy, dust grains comprise roughly 0.1% of the baryonic mass.

The best studied feature of dust in the Milky Way is its ability to scatter and absorb light. The extinction, $A(\lambda)$, at a certain wavelength can be measured by comparing the spectra of pairs of identical types of stars. If $F_0(\lambda)$ is the flux of a star in absence of dust and $F(\lambda)$ is the flux of another dust extincted star, the extinction in magnitudes can be calculated as

$$A(\lambda) = -2.5 \log \frac{F(\lambda)}{F_0(\lambda)} \,. \tag{4.1}$$

The wavelength dependence of reddening is usually quantified by the total-to-selective extinction ratio, R_V, as

$$R_V \equiv \frac{A_V}{E(B-V)} = \frac{A_V}{A_B - A_V} \,, \tag{4.2}$$

where $E(B-V) = A_B - A_V$ is the colour excess and A_B and A_V are the extinction in the B and V-band (centered around $\lambda_B = 0.44\,\mu$m and $\lambda_V = 0.55\,\mu$m).

Extinction by interstellar dust in the Milky Way and nearby galaxies is usually parameterized using mean extinction laws, $A_\lambda = f(\lambda, R_V)$ (e.g. Cardelli et al., 1989; Fitzpatrick, 1999). Within the Milky Way, the reddening parameter ranges between $2.75 \lesssim R_V \lesssim 5.5$ for different sightlines, illustrated in Fig. 4.1. A typical value of the reddening in the diffuse ISM is $R_V \approx 3.1$ while the larger $R_V \approx 5$ is typical in denser molecular clouds.

There are a few "spectroscopic" features in the extinction curves. The strongest is a bump in the UV at 2175 Å (possibly due to small graphitic dust grains or ultra-small Polycyclic Aromatic Hydrocarbon molecules, PAHs) and some features in the IR at 9.7 μm and 18 μm (probably due to silicate dust grains).

Schlegel et al. (1998) (one of the most cited articles in astronomy) use COBE/DIRBE observations in the far-infrared to measure the dust temperature and thereby trace the dust column density to produce a full-sky dust extinction map. They do this assuming a constant, standard reddening law ($R_V = 3.1$), which is valid for most sight-lines (Mörtsell, 2013). However, several studies suggest that the maps could overestimate the extinction (or reddening) when the visual extinction is appreciable (Berry et al., 2012).

4.3 Dust in other galaxies

The "pair method" has also been used to probe the extinction law along different lines-of-sight in neighboring galaxies, such as the Small and Large Magellanic Clouds (SMC and LMC) and the Andromeda galaxy (M 31). The extinction laws are similar to the MW in the visible and IR, but show large variation in the UV, where the 2175 Å absorption bump is weaker (LMC) or absent (SMC).

As it becomes increasingly harder to measure spectra of individual stars with distance, other methods are used to probe the extinction of extragalactic dust. One method is to use quasars (QSOs) shining through foreground galaxies. In some cases the foreground galaxies act as strong gravitational lenses, producing multiple images of background quasars (Falco et al., 1999; Östman et al., 2008; Elíasdóttir et al., 2006). Studies of these QSO-galaxy systems probe the extinction properties of galaxies up to $z \sim 1$, and generally find extinction laws compatible with MW albeit with some scatter. But, e.g. Falco et al. (1999) find $R_V = 1.5$ for a $z = 0.96$ elliptical, to $R_V = 7.2$ for a $z = 0.68$ spiral galaxy. Of the 10 systems studied by Elíasdóttir et al. (2006), most are consistent with

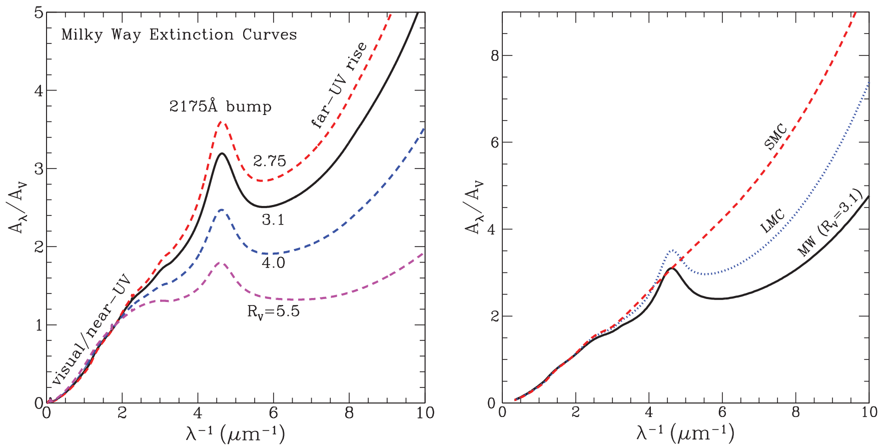

Figure 4.1. Left: Extinction at wavelength λ, relative to the extinction at $V = 0.55$ μm, as a function of inverse wavelength λ^{-1}, for Milky Way (MW) regions characterized by different values of $R_V = A_V/E(B-V)$, where A_B is the extinction at $B = 0.44$ μm, A_V is the extinction at $V = 0.55$ μm, and the reddening $E(B-V) = A_B - A_V$. **Right:** Extinction curves for the Small and Large Magellanic Clouds (SMC and LMC) compared to the canonical Milky Way reddening $R_V = 3.1$. (Credit: Li, 2007)

extinction with $R_V = 2.8 \pm 0.4$, whereas one system is consistent with an extinction law with $R_V = 2.1 \pm 0.1$.

Distant supernovae and gamma ray bursts (GRBs) can also be used as probes of the extinction properties of their host galaxies. If one identifies the colour excess of SNe as only due to dust extinction in the host galaxies, one can infer the reddening parameter (e.g. identifying the fitted $\beta = R_B = R_V + 1$ in Eq. 3.1). Studies of large SN Ia samples (see Chapter 5.2) find values of $R_V \sim 1.5-2$ indicating either that the dust is different from that of the MW or that there are intrinsic colour variations between the SNe.

The optical afterglow spectra of gamma-ray bursts (GRBs) probe dust extinction in host galaxies up to redshifts $z \approx 3$. The average host extinction curves have UV slopes comparable to that of the LMC, and some observations show signatures of the 2175 Å dust extinction feature as seen along MW and LMC sightlines (Elíasdóttir et al., 2009; Schady et al., 2012).

4.4 Dust around stars

The most likely producers of dust in the Universe are thought to be Asymptotic Giant Branch (AGB) stars and core-collapse (CC) supernovae (see e.g. the review by Gall et al., 2011). In present-day galaxies, the major dust producers are thought to be stars of initial masses $\lesssim 8M_\odot$ in their AGB evolutionary phase. During this phase, strong outflowing winds are developed, with mass-loss rates up to 10^{-4} $\mathrm{M_\odot yr^{-1}}$ towards their late stages (Schöier & Olofsson, 2001). The stars lose up to $\sim 80\%$ of their masses during the AGB phase and form circumstellar envelopes of gas and dust. Since these stars take a long time to evolve to their dust producing stages ($\sim 10^8 - 10^9$ yr), it is commonly believed that they cannot be responsible for all of the dust seen at high redshifts.

There is strong observational evidence for dust formation and pre-existing dust in CC SNe. The observed IR emission for a limited number of SNe implies dust masses which are generally smaller than 10^{-3} $\mathrm{M_\odot}$, corresponding to low condensation efficiencies compared to model predictions. Observations of relatively hot dust ($\sim 10^{-4}$ $\mathrm{M_\odot}$ at $\sim 500 - 1000$ K) have been reported from CC SNe at early epochs (Kotak et al., 2009; Fox et al., 2011) and large amounts of cold dust (~ 1 $\mathrm{M_\odot}$ at < 50 K) have been claimed in SN 1987A (Matsuura et al., 2014) and in older SN remnants.

Type Ia SNe are not believed to contribute to dust production in the universe. The latest models indicate that only little or no dust forms in the ejecta (Nozawa et al., 2011). Gomez et al. (2012) report a detection of warm dust ($\sim 3 - 9 \times 10^{-3}$ $\mathrm{M_\odot}$ at $\sim$90K) in the Kepler and Tycho supernova remnants (believed to be the results of normal Type Ia SNe). Their findings are consistent with the warm dust originating in the circumstellar and interstellar material swept up by the SNe.

4.5 Dust in the Intergalactic medium

The possibility of dust in the intergalactic medium (IGM) has been the subject of numerous studies. Based on estimates of the stellar density and metallicity as a function of redshift, several authors have inferred the existence of significant amounts of cosmic intergalactic dust with density $\Omega_{\mathrm{dust}} \sim 10^{-6} - 10^{-5}$ (Loeb & Haiman, 1997; Inoue & Kamaya, 2004; Fukugita, 2011).

There is observational evidence for the existence of dust beyond galactic disks. From the study of a low-redshift foreground/background galaxy superposition Holwerda et al. (2009) detected dust extinction up to about five times the optical extent of spiral galaxies. Using deep *Spitzer* and *Herschel* observations of M 82, Engelbracht et al. (2006) and Roussel et al. (2010) show that emission from hot and cold dust can be traced out to large distances ($\sim$ 20 kpc) from the centre of the galaxy. Furthermore, statistical analyses of galaxy (Peek et al., 2014) and quasar colours (QSOs, Ménard et al., 2010b) detect an excess reddening induced by foreground galaxies, on scales ranging from the circumgalactic ($\gtrsim$20 kpc) to the intergalactic medium ($\sim$ 1 Mpc). The observed reddening of QSOs by galaxies at $z \sim 0.3$ in Ménard et al. (2010b) implies a slope of the extinction curve, $R_V = 3.9 \pm 2.6$, which is consistent with that of Milky Way dust ($R_V = 3.1$), albeit with large uncertainties.

There are many different mechanisms that could be responsible for ejecting dust into the IGM. Both galaxy mergers or ram-pressure exerted on galaxies moving through the IGM, could expel interstellar gas and dust into the IGM. Radiation pressure from stars and supernova driven galactic winds could also eject dust grains into the IGM. Aguirre (1999a) and Bianchi & Ferrara (2005) find that these astrophysical processes which transfer dust into the intergalactic medium would preferentially destroy small grains, leaving only grains larger than $a \sim 0.1\mu$m, indicating that the intergalactic dust population could be different than in the interstellar medium. Large dust grains typically imply less reddening and higher values for R_V (often labeled "grey" dust).

4.6 Dust models

Many of the physical details are empirical as we do not yet know the precise composition of dust grains, nor do we know their precise physical properties. Nobody has yet convincingly been able to produce grains in the laboratory, much less reproduce the conditions they would experience in interstellar space.

In general, we are interested in calculating the following quantities for electromagnetic waves incident on a dust grain; the total scattering and absorption cross-sections, $\sigma_{\rm sca}$ and $\sigma_{\rm abs}$ (for extinction $\sigma_{\rm ext} = \sigma_{\rm sca} + \sigma_{\rm abs}$), and also the differential scattering cross-section, $d\sigma_{\rm sca}/d\Omega$.

Optical properties

From the observations of dust extinction in the Milky Way and other galaxies, outlined in Chapter 4.2 and 4.3, we know that the amount of extinction and reddening span a range of $1.5 \lesssim R_V \lesssim 7$. The larger values of the R_V in the MW are thought to be a consequence of different grain size distributions in environments with different dust densities, but it could also reflect differences in the physical grain properties.

To model the extinction curves from a population of dust grains one needs to specify the composition, size distribution, scattering and absorption properties of the dust grains. Mathis et al. (1977), hereafter MRN, found that extinction in the Milky Way is well fitted using a power-law distribution of sizes where $dn/da \propto a^{-3.5}$. Within the Milky Way, graphite grains typically range in size from 0.005 to 1 μm while silicate grain sizes range from 0.025 to 0.25 μm. In general, small grains preferentially scatter light with short wavelengths, producing a steep extinction law with small values for R_V. Very large grains would produce wavelength-independent "grey" extinction with $R_V \to \infty$.

The optical depth gives a measure of how opaque a medium is to radiation passing through it. If $I_0(\lambda)$ is the intensity at the source and $I_{\mathrm{obs}}(\lambda)$ is the observed intensity at a wavelength λ after a given path, the optical depth $\tau(\lambda)$ is defined by

$$I_{\mathrm{obs}}(\lambda) = I_0 e^{-\tau(\lambda)}\,, \tag{4.3}$$

with $\tau(\lambda) = \int n\sigma ds = N_{gr}\sigma(a, \lambda)$, where n is the number density of dust grains, N_{gr} is the column density of grains along the line-of-sight and σ is the cross section.

If the dust grains are spread out over cosmological distances, the total optical depth to scattering and/or absorption by dust grains between redshift 0 and z_{em} can be calculated as

$$\tau\left(\lambda_{\mathrm{obs}}, z_{\mathrm{em}}\right) = c \int_0^{z_{\mathrm{em}}} dz' \frac{n(z')\sigma(\lambda')(1+z')^2}{H(z')}\,, \tag{4.4}$$

where $n(z')$ is the comoving number density of dust grains and $H(z')$ is the Hubble parameter (see Eq. 1.8) at redshift z'. Each dust grain is assumed to be spherical, with radius a and cross section $\sigma(\lambda') = \pi a^2 Q(\lambda')$ where the efficiencies for scattering and absorption are Q_{scat} and Q_{abs}, the efficiency for extinction is $Q_{\mathrm{ext}} = Q_{\mathrm{scat}} + Q_{\mathrm{abs}}$, and $\lambda' = \lambda_{\mathrm{obs}}/(1+z)$.

In Paper I, Paper II and Paper V we focus on dust composed of silicate ($\rho_{\mathrm{grain}} \approx 3.2$ g/cm^3) and graphite grains ($\rho_{\mathrm{grain}} \approx 2.3$ g/cm^3) (described in Draine & Lee, 1984; Laor & Draine, 1993; Weingartner & Draine, 2001), which successfully reproduce both the extinction and IR emission from dust in the MW, LMC and SMC. The scattering and absorption efficiencies $Q_{\rm sca}$ and $Q_{\rm abs}$ are tabulated for wavelengths $\lambda = 10^{-3}$ to 10^{3} μm for grains with radii $a = 10^{-3}$ to 10 μm. The total-to-selective extinction ratio $R_V = A_V/(A_B - A_V)$ for the graphite (black lines) and silicate dust (red lines) dust models employed in Paper I are illustrated in Figure 4.2.

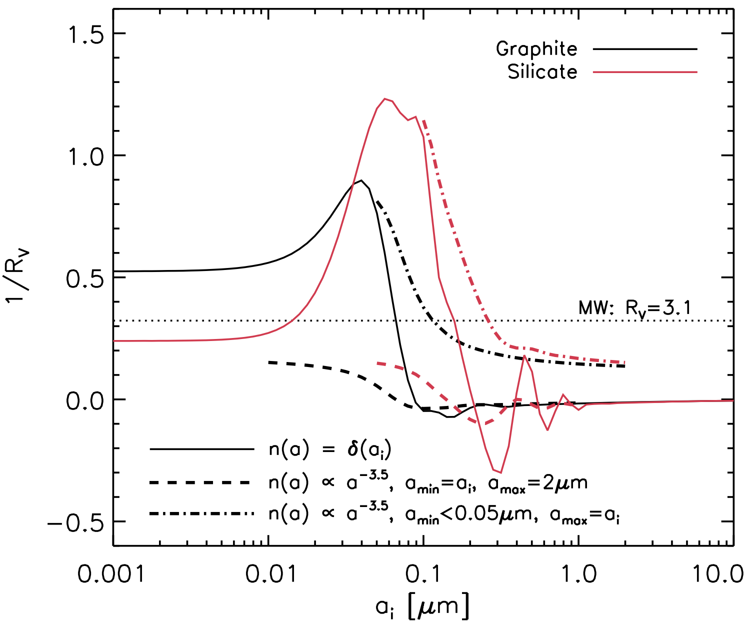

Figure 4.2. $R_V^{-1} = (A_B - A_V)/A_V$ reddening for dust models with graphite (black lines) and silicate (red lines) grains with a single grain size (solid lines) or models with truncated MRN grain size distributions with 0.05μm $< a_{\rm min} < 1.0\mu$m and $a_{\rm max} = 2.0\,\mu$m (dashed lines) or $a_{\rm min} = 0.02\,\mu$m (graphite) or $a_{\rm min} = 0.05\,\mu$m (silicate) and $0.1 < a_{\rm max} < 2.0\,\mu$m (dotted-dashed lines). The inclusion of grains with radii larger than $a \gtrsim 0.1 - 0.2\mu$m gives grey extinction with $R_V^{-1} \to 0$. The horizontal dotted line shows the average reddening for interstellar dust in the Milky Way, $R_V = 3.1$. (Figure from Paper I)

X-ray scattering

Small angle scattering of X-rays by dust grains along the line-of-sight can produce diffuse halos around X-ray point sources. This has been observed for galactic X-ray sources and measurements of the intensity and angular extent of such halos provide a quantitative test of interstellar grain models (Mathis & Lee, 1991; Smith & Dwek, 1998; Draine, 2003b).

As noted by Evans et al. (1985), intergalactic dust grains would in a similar way produce diffuse halos around X-ray sources on cosmological distances. Using approximations for the scattering properties (e.g. in Miralda-Escudé, 1999) and differential cross sections (the Rayleigh-Gans approximation is usually employed, Vaughan et al., 2006; Corrales & Paerels, 2012), one can model the flux as a function of scattering angle of an intergalactic X-ray halo (as seen in Fig. 4.3). The root-mean-square (rms) of the scattering angle θ indicates the typical size of the scattered halo,

$$\theta_{\rm rms} \approx 62.4 \left(\frac{1.0\,\mu\text{m}}{a}\right)\left(\frac{1\,\text{keV}}{E}\right) \text{arcsec.} \tag{4.5}$$

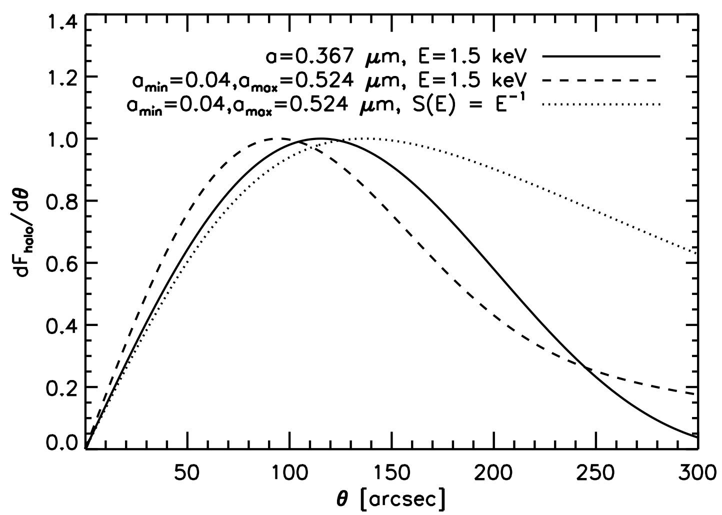

Figure 4.3. Modeled halo flux as a function of scattering angle for X-ray energies, $E \approx 1.5$ keV assuming a single grain size ($a = 0.37\mu$m, solid line) or a MRN distribution of grain sizes (with $a_{\rm min} = 0.04\,\mu$m and $a_{\rm max} = 0.52\,\mu$m, dashed line) or for a SED $S(E) \propto E^{-1}$.

Infrared emission

Dust grains can be heated, either by absorption of UV/visible photons or by collisions with atoms, cosmic rays or other dust grains. Once heated, grains can cool by emitting thermal radiation or by collisions with cold atoms or molecules.

The IR emission in the MW and in nearby galaxies can be reproduced by assuming a interstellar radiation field heating a mixture of silicate and carbonaceous (small PAHs and larger graphite) grains. Figure 4.4 illustrates how well the modeled spectral energy distribution (SED) reproduce the observations of the MW dust emission in the diffuse ISM. At far-infrared ($\gtrsim$100 μm) wavelengths, the SED is well fit by a black body spectrum with a temperature of $\sim$17.5 K.

Often, one is interested in deriving an estimate of the total mass of dust in a region (e.g. in a dust cloud, a supernova remnant or in an entire high-z galaxy). To model the IR/sub-mm emission from a dust cloud, the idealized case (described in Hildebrand, 1983) of an optically thin dust cloud of mass M_d with dust particles of radius a, thermally emitting at a single equilibrium temperature T_d is usually considered. The observed flux at a distance D can then be written as,

$$F_\nu = M_d \frac{\kappa_\nu(a) B_\nu(T_d)}{D^2}, \tag{4.6}$$

where $B_\nu(T_d)$ is the Planck blackbody function and the dust mass emissivity coefficient, $\kappa_\nu(a)$, is

$$\kappa_\nu(a) = \left(\frac{3}{4\pi\rho a^3}\right)\pi a^2 Q_\nu(a) = \frac{3Q_\nu(a)}{4a\rho}. \tag{4.7}$$

$Q_\nu(a)$ is the absorption efficiency and the dust bulk (volume) density $\rho \sim 2 - 3$ g/cm^3 depending on grain composition.

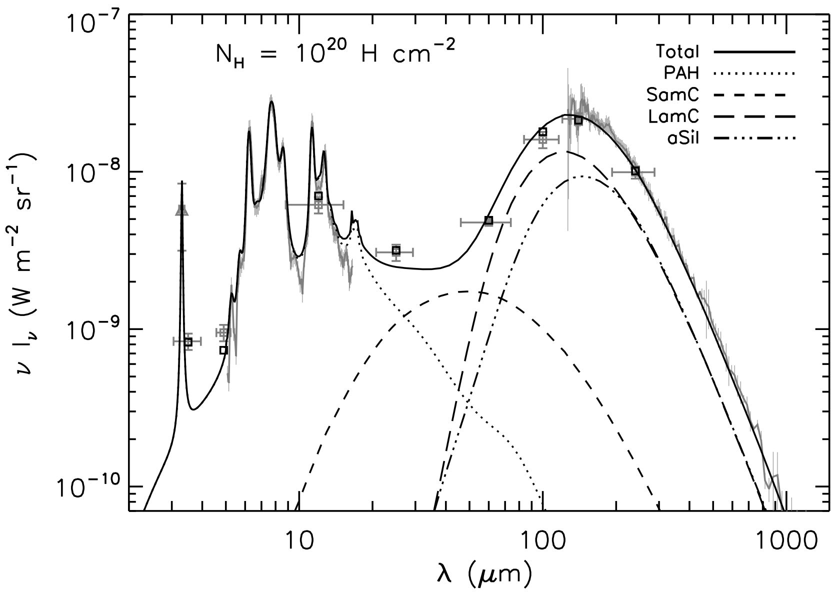

Figure 4.4. SED of the galactic ISM dust emission. Grey symbols and curves are measurements in the mid-IR ($\sim 5 - 15\mu$m) and far-IR ($\sim 100 - 1000\mu$m). Black lines and squares are the modeled emission from a mixture of polycyclic aromatic hydrocarbons (PAHs), amorphous carbon (SamC and LamC) and amorphous silicates (aSil) for a column density of $N_H = 10^{20} Hcm^{-2}$. (Credit: Compiègne et al., 2011)

Chapter 5

Dust and Type Ia Supernovae

In the following sections, we will look at the possibilities to constrain the amounts of dust in the intergalactic medium (studied in Paper I), investigate the diversity of host galaxy extinction for a sample of nearby SNe Ia through UV-to-NIR observations (studied in Paper IV and Paper VI) and how the influence of circumstellar dust around SNe Ia can be studied using near-, mid- and far-infrared observations (which is the subject of Paper II and Paper V).

5.1 Intergalactic dust

As mentioned in Chapter 4.5 there is a possibility that there is dust in the intergalactic medium (IGM). After the discovery of the cosmic acceleration in 1998, it was proposed that the faintness of SNe Ia at high redshifts could instead be caused by dust in the IGM (Aguirre, 1999b). The absence of detectable systematic reddening of SNe Ia with increasing redshift implies that any intergalactic dust extinction must be quite "grey" at optical wavelengths, suggesting that if dust does exist in large quantities at these redshifts, the grains must be large. Limits on the amounts of dust in the IGM have been obtained through observations of the cosmic far-infrared background Aguirre & Haiman (2000) and the lack of dust scattered X-ray halos around distant quasars (Petric et al., 2006; Corrales & Paerels, 2012). Furthermore, limits on the opacity of the IGM to optical photons have been obtained (red and yellow arrows in Fig. 5.1, Avgoustidis et al., 2009; More et al., 2009) by comparing different distance measurements (where the luminosity distance, $d_L(z)$, should be larger than the angular diameter distance, $d_A(z)$, by a factor $(1+z)^2$, as can be seen in equations 1.13 and 1.12).

Constraints on intergalactic dust from quasar colours and the soft X-ray background

In Paper I we put limits to the amount of extinction intergalactic dust can cause on distant objects using observed quasar colours together with measurements of the soft X-ray background.

Quasars (Quasi-Stellar Objects, QSOs) are very energetic Active Galactic Nuclei (AGN) that have been found to be relatively homogeneous in terms of colours and spectral features over a large redshift range. Mörtsell & Goobar (2003) and Östman & Mörtsell (2005) simulated the reddening by intergalactic dust using different parametrizations of Milky Way-type extinction laws, with $0 < R_V < 12$. They used observations of QSO colours and template spectra to put an upper limit on the dimming in the restframe B-band by intergalactic dust of a source at redshift $z = 1$ of $A_B(z = 1) \lesssim 0.02$ mag for $R_V \sim 3$ and $A_B(z = 1) \lesssim 0.1$ mag for $R_V \sim 10$.

The Soft X-ray Background (SXB, in the 0.5 - 2 keV range) comprises the integrated emission of X-ray sources; primarily AGN, extended emission from galaxy clusters, faint starburst and "normal" galaxies. While most of the SXB can be ascribed to emission from discrete sources (detected at other wavelengths), $\sim 6 \pm 6\%$ of the SXB remains unresolved (Moretti et al., 2003; Hickox & Markevitch, 2007). Dijkstra & Loeb (2009) argue that dust scattered X-ray halos around AGN can maximally account for a fraction $f_{\rm halo} \sim 5 - 15\%$ of the total measured SXB. This allows them to place an upper limit on the near-infrared extinction $\Delta m(z = 1, \lambda = 8269\text{Å}) \lesssim 0.15(f_{\rm halo}/10\%)$ mag.

Our analysis combines the methods in Mörtsell & Goobar (2003), Östman & Mörtsell (2005) and Dijkstra & Loeb (2009) in a consistent way. We use the SDSS DR7 Quasar Catalogue (Schneider et al., 2010) containing more than 100 000 spectroscopically confirmed QSOs with optical magnitudes measured in the $ugriz$ filters. We also use a QSO template spectrum (as derived by Vanden Berk et al., 2001; Telfer et al., 2002), believed to represent typical QSOs unaffected by dust.

Physical dust models are generated according to Eq. 4.4 for silicate and graphite dust grains. We study dust models that have either a single grain size or truncated MRN size distributions, varying the size of the smallest and largest grains. The intergalactic dust is assumed to be distributed homogeneously with a comoving number density of dust grains that is constant or proportional to the integrated star formation rate density. For each dust model we simulate the attenuation of the QSO template spectrum and perform synthetic photometry using the SDSS $ugriz$-filter functions. Simultaneously, for each dust model, we calculate the flux of X-ray photons observed in the Soft X-ray energy range $E = 0.5 - 2.0$ keV which is expected to be scattered into halos. We then compare the simulated QSO colours and X-ray halo flux with the observed colours and SXB measurements.

The impact of the smallest and largest grains in the MRN size distributions are studied separately, yielding a range of R_V-values from ~ 1.3 to ∞. Allowing dust grains $a \lesssim 0.1\ \mu$m, produces enough reddening at optical wavelengths that the QSO colours can limit the extinction in the B-band, $A_B(z = 1) \lesssim 0.10$ mag ($R_V \sim 12$, dark red arrow in Fig. 5.1) and correspondingly limit the dust density parameter, $\Omega_{\rm dust} \lesssim 10^{-5}(\rho_{\rm grain}/3\,{\rm g\,cm^{-3}})$. For models with $a_{\rm min} \gtrsim 0.1 - 0.3\ \mu$m ($R_V \sim \infty$, i.e. "completely grey" dust) we can limit the extinction in the B-band to $A_B(z = 1) \lesssim 0.25$ mag (black arrow in Fig. 5.1). Removing the very small grains can affect the opacity dramatically, without radically changing the total mass in dust. Therefore, the combined upper limits on the dust density are less constraining, $\Omega_{\rm dust} \lesssim 10^{-4}(\rho_{\rm grain}/3\,{\rm g\,cm^{-3}})$.

Our models with $R_V \lesssim 12$ relate well to the detected reddening of QSOs out to large distances around $z \sim 0.3$ galaxies by Ménard et al. (2010b) (with a reddening parameter, $R_V = 3.9 \pm 2.6$). Assuming a constant comoving dust density and extrapolating their result to $z = 1$ yields a *lower* limit on the extinction in the restframe B-band of $A_B(z = 1) \gtrsim 0.03$ mag, shown as blue lines in Figure 5.1.

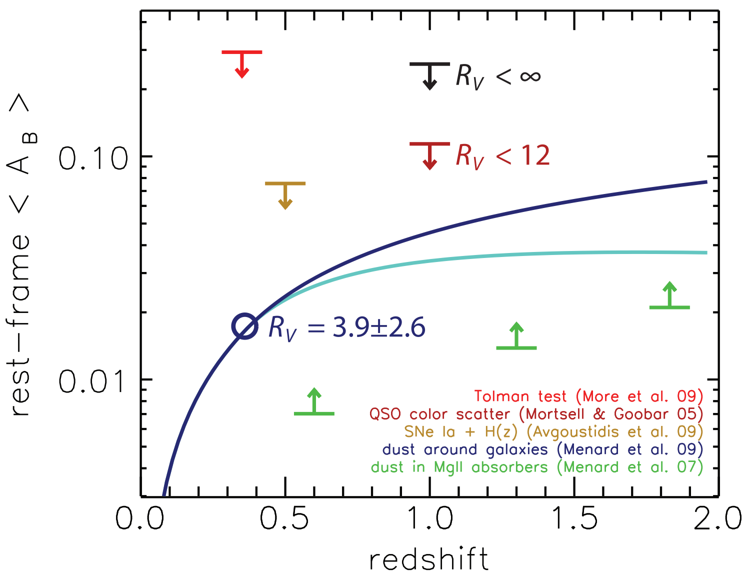

Figure 5.1. Opacity of the Universe as a function of redshift, in the rest-frame B-band. The blue curves show extrapolations of the measurement of dust around $z \sim 0.3$ galaxies by Ménard et al. (2010b) using different assumptions of the dust density evolution as a function of redshift. The upper limits on $A_B(z = 1)$ from Paper I (for models with $R_V \lesssim \infty$ and $R_V \lesssim 12$) are shown as black and dark red arrows together with the limits from More et al. (2009) (red arrow) and Avgoustidis et al. (2009) (yellow arrow). The green arrows are *lower* limits based on Mg II absorbers studied in Ménard et al. (2008). (Figure adapted from Ménard et al., 2010a)

5.2 Measuring extinction laws using SNe Ia

Having a source of known intrinsic colour (a “standard crayon”), one can compare reddened and unreddened objects to each other and infer the wavelength dependence of the dust extinction (much like the pair-method used to measure the extinction described in Chapter 4.2 for stars in the MW). Since SNe Ia have “predictable” light-curves in many filters, they can be used as standard crayons, allowing us to measure dust properties of distant galaxies where individual stars otherwise cannot be resolved.

Reddening from large samples and individual SNe Ia

Studies of large samples of nearby SNe ($z \lesssim 0.1$), correcting both for a stretch-luminosity and colour-brightness correlation, have typically found surprisingly low values of R_V. Analyses of optical or optical+NIR data yield values of R_V; e.g. 2.30 (Wang et al., 2006), ~ 1 (Conley et al., 2007), 1.75 (Nobili & Goobar, 2008), 1.7 (CfA, Hicken et al., 2009). Similarly, including SNe at higher redshifts (up to $z \sim 1$), fitting the colour-brightness relation jointly with cosmological parameters (minimizing the residuals in the SN Ia Hubble diagram) and interpreting the fitted $\beta \approx R_V + 1$ as solely due to dust extinction, also yields low values of R_V; e.g. 2.2 (SDSS, Kessler et al., 2009), 1.5 (Union2.1, Suzuki et al., 2012), 2.1 (PS1, Scolnic et al., 2014a).

In contrast to the analyses above, Chotard et al. (2011) arrive at a “normal” value of R_V when analysing the spectra of SNe Ia rather than photometry. Another interesting note, is that when Nobili & Goobar (2008) lower their colour cut from $E(B-V) < 0.7$ to < 0.25 mag their best fit R_V goes from 1.75 to ~ 1. However, when Folatelli et al. (2010) exclude two of their most reddened objects from the CSP sample (shown as grey circles in Fig. 5.2), the best fit R_V shifts from ~ 2 to 3.1. This indicates that the observed colours of SNe Ia may have a more complex origin, involving other processes than dust extinction in the host galaxies.

The extinction has also been studied in great detail for a number of individual highly-reddened SNe; e.g. 1999cl (R_V=2.0, Krisciunas et al., 2006), 2002cv (R_V=1.6, Elias-Rosa et al., 2008), 2003cg (R_V=1.8, Elias-Rosa et al., 2006), 2006X ($R_V = 1.5$, Wang et al., 2008). These SNe are shown as grey triangles in Figure 5.2.

The origin of these low R_V values is not clear. In the statistical treatment of large samples of SNe Ia, R_V could be biased to artificially low values if intrinsic colour variations are not taken into account (Scolnic et al., 2014b). The intrinsic colours can depend on the progenitor metallicity (Lentz et al., 2000) or variables such as explosion asymmetry or observational viewing angle (Kasen et al., 2009; Maeda et al., 2011) which might not be captured in the colour-brightness or light-curve shape corrections.

The most straight-forward explanation of the low values of R_V is that dust grain size distributions in the ISM of the host galaxies are different from that of the Milky Way. A low R_V would indicate the presence of smaller grains.

Alternatively, one could have standard dust grains, but in the circumstellar (CS) medium surrounding the SN. Through this geometrical distribution and multiple scattering of photons on "normal" dust grains, photons with shorter (bluer) wavelengths are affected more, causing the *effective* extinction law to steepen (Wang, 2005; Goobar, 2008). This effective extinction law can be parametrized as a power law, $A_\lambda = A_V(\lambda/\lambda_V)^p$. This CS dust scenario would also have other observable features; for example: *(1)* The multiply scattered photons will arrive later and will contribute to a plateu shape of the late-time tail of the lightcurve. Indications of such tails has also been seen (Förster et al., 2013). *(2)* The CS dust grains will be radiatively heated by absorption of UV/optical photons from the SN or collisionally heated by the SN shock, and would re-emit this energy at IR wavelengths. This second case is studied in Paper II and Paper V (covered in Chapter 5.3). *(3)* The largest difference between the galactic CCM/F99 and circumstellar G08 extinction-laws are in the U-band and bluewards (Folatelli et al., 2010). By extending the wavelength range from the NIR (where the extinction is smaller than in the optical, giving an "anchor point" when fitting the extinction parameters) to the UV (where the differences between the extinction-laws are larger) there is a possibility to differentiate between the scenarios.

Extinction laws from UV to NIR observations of SNe Ia

In Paper IV we study the extinction of the highly-reddened SN 2014J and in Paper VI a small sample of nearby SNe Ia with $E(B-V)$ ranging between 0.1–1.0 mag, using UV-data from *HST* and *Swift* and optical to near-IR data from ground based telescopes.

The SNooPy light-curve fitting package (Burns et al., 2011) is used to find $t^B_{\rm max}$ and the stretch (or Δm^B_{15}) of each supernova. We use SN 2011fe as a template of a pristine, unreddened SN Ia. As mentioned in Chapter 3.2, SN 2011fe was a normal Type Ia, with an optical and NIR colour evolution well described by the Hsiao et al. (2007) and Nobili & Goobar (2008) templates. However, based on the analysis of UV colours of SNe Ia by Milne et al. (2013), SN 2011fe is "NUV-blue". We take this into account by adapting a conservative NUV colour dispersion.

In Paper IV and Paper VI, we consider the reddening laws of Cardelli et al. (1989) and O'Donnell (1994) (here-after CCM+O), Fitzpatrick (1999) (F99), the empirically derived SALT2 colour law (Guy et al., 2007) and the CSM-motivated reddening law of Goobar (2008) (G08).

For SN 2014J (Paper IV) we find that the best fit for a MW type extinction law yield $R_V = 1.4 \pm 0.1$ and $E(B-V) = 1.37 \pm 0.03$ mag. We also find that the reddening is compatible with the G08 power-law extinction, $A_\lambda/A_V = (\lambda/\lambda_V)^p$ as expected from multiple scattering of light, with $p = -2.1 \pm 0.1$, although with similar goodness-of-fit as the CCM/F99 laws. By comparing spectra of SN 2014J and SN 2011fe , Foley et al. (2014) find that R_V evolves with time, which is interpreted as a sign of CS dust. Fitting a two-component CS+ISM dust model to the data, they find that roughly half of the extinction is caused by ISM dust and the other half from CS dust scattering. This interpretation is however challenged by Brown et al. (2014) and Paper V.

For the sample of SNe (2012bm, 2012cg, 2012cp, 2012cu and 2012et) in Paper VI with UV-to-NIR observation, we find a diversity among the fitted extinction parameters R_V and $E(B-V)$, shown as coloured symbols in figure 5.2. We find that the additional UV-data can break some of the degeneracy between R_V and $E(B-V)$. Due to the multiplicative nature of R_V and $E(B-V)$ (or β and c in Eq. 3.1) when determining the corrected magnitudes, these parameters are highly correlated (Burns et al., 2014). As $E(B-V)$ becomes small, the extinction models become less sensitive to R_V. The inset panel in Fig. 5.2 shows that the UV-data reduces the uncertainty in the fitted parameters R_V and $E(B-V)$ by up to ∼50%. For the low R_V (~ 1.5) SNe we find that a the G08 power-law generally provides a better fit to the extinction than the F99 and CCM+O laws. However, the MW-type extinction laws are empirical relations derived from lines of sight with $R_V > 2$. For the $R_V < 2$ we are thus extrapolating these relations and note that they consistently tend to underestimate the extinction in the region covered by the R and i-bands. Furthermore, we see no clear linear relationship between $E(B-V)$ and R_V as discussed in Mandel et al. (2011) and Burns et al. (2014).

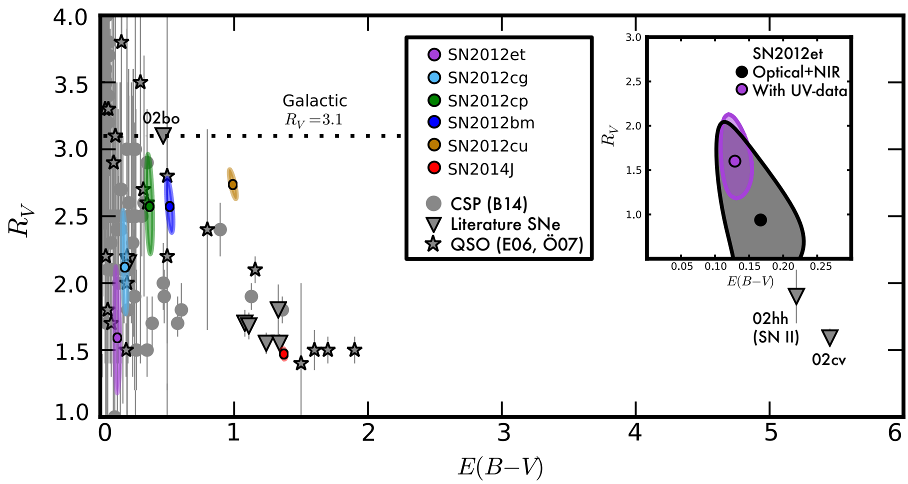

Figure 5.2. Coloured symbols show the best-fit extinction parameters R_V vs. $E(B-V)$ using UV to NIR data in Paper IVand Paper VI. The inset panel shows that adding UV-data further reduces the error. We also show the individual best fit parameters for the CSP sample (from u to H-band photometry, grey circles, Burns et al., 2014), various literature SNe Ia (grey triangles) and quasars shining through galaxies (Elíasdóttir et al., 2006; Östman et al., 2006). It is interesting to note that SNe 2002bo and 2002cv, that exploded in the same host galaxy, have very different R_V and $E(B-V)$ (Elias-Rosa et al., 2008).

5.3 Circumstellar dust

We saw in Chapter 3.1 that the two proposed SN Ia progenitor scenarios have different observational signatures. In the single degenerate channel one can expect to find CS material arising from the transfer of matter to the WD by its binary companion star. Dust may also reside in the CS environment, which could have important implications for observed colours of SNe Ia.

While previous searches for emission in H_α, radio, and X-ray observations have generally yielded only upper limits (mentioned in Chapter 3.1), there are a some indications of CS material in connection to "normal" SNe Ia. Variable Na I D lines have been seen in high-resolution spectra of some SNe Ia (e.g., SNe 2006X and 2007le, Patat et al., 2007; Simon et al., 2009), assumed to be from ionization of CS clouds within $\sim 10^{17}$ cm from the SN. Interestingly, e.g. SN 2006X is very reddened and has a low $R_V \sim 1.5$, raising the possibility that time variable Na I D absorption is connected to a dusty CSM. If pre-existing CS dust is the source of non-standard reddening, it will be radiatively heated by absorption of UV/optical photons from the SN or collisionally heated by the SN shock. Thermal emission at IR wavelengths could therefore be the "smoking gun" for detecting or ruling out the presence of CS dust.

Limits on CS dust from infrared observations

In Paper II we observed three SNe Ia (2011by, 2011fe and 2012cg) using the *Herschel Space Observatory* (Poglitsch et al., 2010; Pilbratt et al., 2010). *Herschel* was an ESA space observatory, active from 2009 to 2013, sensitive to the far-infrared and submillimetre wavebands ($60 - 670\,\mu$m). It is the largest infrared space telescope ever launched, carrying a single mirror of 3.5 meters in diameter. The observations of SNe 2011by, 2011fe and 2012cg were obtained using the *Photodetector Array Camera and Spectrometer* (PACS), each target was observed for 4 hours, with simultaneous imaging in the far-IR 70 μm and 160 μm bands.

In Paper V we analyze mid-IR observations of the reddened SNe 2014J, 2006X and 2007le, together with a sample of six SNe, using the *Spitzer Space Telescope* Channel 1 (CH1, centered around 3.6 μm) and Channel 2 (CH2, centered around 4.5 μm). *Spitzer* is a NASA space observatory operating in cryogenic mode between 2003 and 2009. Since then, the IRAC camera CH1 and CH2 are still operable with the same sensitivity as before in the Spitzer Warm Mission.

The thermal emission from a CS dust cloud, $F_\nu(\lambda)$ depends on the dust mass, M_d, and temperature, T_d (and on the dust grain properties, see Eq. 4.6). While the dust cloud could be in any geometrical configuration, we assume the simplistic "thin shell approximation" to provide estimates to be compared with the models for CS reddening proposed in (Goobar, 2008; Amanullah & Goobar, 2011). We estimate the minimal dust shell radius, $r_\mathrm{d} = ct/2$, that could give rise to a detectable IR signal at each observed epoch, t. For these radii (shown as the right-hand side vertical axis of Fig. 5.3) we can also estimate the expected temperatures and dust masses needed to cause $A_V \sim 1$ mag of extinction (black solid line in Fig. 5.3).

From the non-detections of the SNe in the far-IR 70 μm and 160 μm passbands we can calculate upper limits on the CS dust mass surrounding SNe 2011by, 2011fe and 2012cg (shown as blue lines and symbols in Fig. 5.3). In the near-IR and mid-IR, the SNe are detected (up to typically $\sim$ 300 days after maximum brightness), so here we search for *excess* emission with respect to an unreddened SN (assuming these are not affected by CS dust). After correcting the reddened SNe 2014J, 2006X for the extinction (using optical to H-band photometry) and taking distance uncertainties into account, we do not detect any significant excess in $K-$band (2.2μm) or in the *Spitzer* CH1 and CH2 (3.6 and 4.5 μm) data for these SNe, with respect to the unreddened SNe (e.g. SN 2011fe). The mid-IR non-detections of the SNe at late times are also analysed, since they constrain dust at larger radii. (Through this exercise, we compile the first composite mid-IR light curve templates of a SN Ia).

Using K-band data for SNe 2014J and 2006X, to explore possible emission from hot CS dust close to the exploding star ($T_\mathrm{d} \gtrsim$1200 K for $r_\mathrm{d} < 5 \cdot 10^{16}$ cm), we are able to rule out $M_d \gtrsim 10^{-5}$ $\mathrm{M}_\odot$ (green lines and symbols in Fig. 5.3). Maeda et al. (2014) recently performed a similar analysis, using near-IR (JHK) data to put limits on CS dust around SN 2006X and four other SNe Ia (besides assuming thin shells, they also study torus/ring-like distributions of dust). The *Spitzer* data significantly reduces the allowed parameter space, excluding $M_\mathrm{d} \gtrsim 10^{-6}$ $\mathrm{M}_\odot$ ($T_\mathrm{d} > 700$ K, for $r_\mathrm{d} < 2 \cdot 10^{17}$ cm), shown as red triangles and circles in Fig. 5.3.

Our limits (summarized in Fig. 5.3) exclude that the bulk of the observed extinction towards the highly-reddened SNe 2014J and 2006X is due to CS dust. Foley et al. (2014) claim that half of the extinction ($A_V \sim 1$ mag) towards SN 2014J can be attributed to CS dust, while the other half is due to interstellar dust in M 82. However, our limits on dust emission imply that at most $A_V \lesssim 0.1$ mag of extinction can be accounted for by CS dust. Thus, our findings reaffirm the conclusions from polarization studies of SNe 2014J and 2006X, which indicate that the dust in the line of sight towards these objects is most likely of interstellar nature (Patat et al., 2014; Kawabata et al., 2014). Furthermore, the lack of heated dust in the CS environment of SN 2014J is complementary to the limits derived from the X-ray and radio non-detections, that probe material within $\sim 10^{16}$ cm (Margutti et al., 2014; Pérez-Torres et al., 2014). While the non-detection of variable Na I D in SN 2014J (Paper III, Foley et al., 2014; Ritchey et al., 2014) is consistent with a clean CS environment within $\sim 10^{17}$ cm, a recent analysis by Graham et al. (2014) finds time variable K I which might be due to ionization of material at even larger distances ($\sim 10^{19}$ cm).

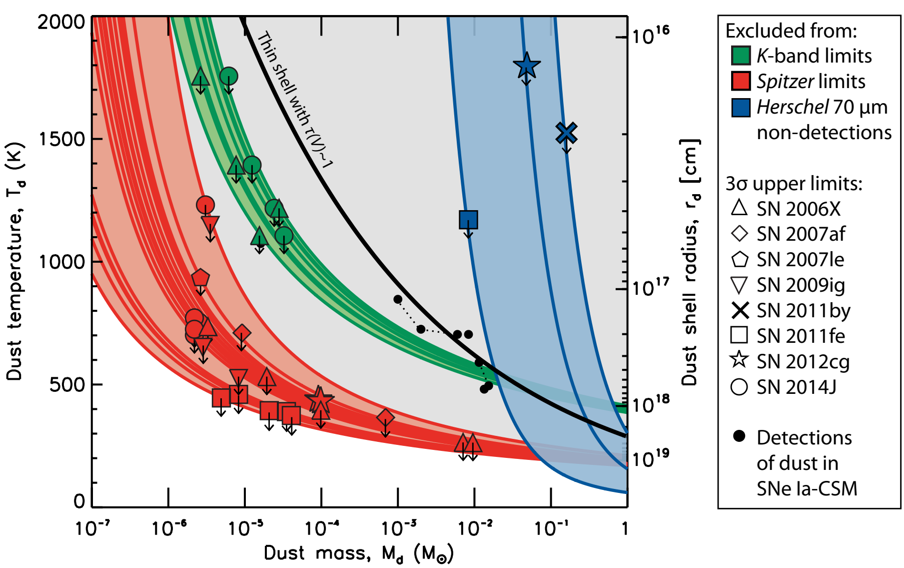

Figure 5.3. Upper limits on the circumstellar dust mass and temperature, assuming graphite dust grains of size $a = 0.1\,\mu$m for the SNe studied in Paper II and Paper V. The lines and symbols represent 3σ upper limits on excess emission in near-IR K-band (green lines) and *Spitzer* 4.5 μm (red lines) and from the *Herschel* 70 μm non-detections (blue lines). The black solid line indicates the expected dust mass needed to explain an observed optical extinction of $\tau_V \sim A_V \sim 1$ mag. Black dots are detections of warm dust around peculiar SNe Ia-CSM (Fox & Filippenko, 2013).

Chapter 6

Summary and outlook

In this thesis, I have outlined some of the potential hazards of cosmic dust when using Type Ia Supernovae as distance indicators to estimate cosmological parameters. We investigate how dust along the line-of-sight can dim the light and alter the colours to SNe Ia by making use of multi-wavelength X-ray, UV, optical and infrared data.

- In Paper I, we model the optical extinction and X-ray scattering properties of intergalactic dust grains to constrain the intergalactic opacity using a combined analysis of observed quasar colours and the soft X-ray background. Our current upper limit corresponds to ~ 0.10–0.25 magnitude dimming (for $R_V \sim 12$ to ∞, respectively) at optical wavelengths for a source at redshift $z = 1$, which is too small to alleviate the need for dark energy but large in terms of relative error. Depending on the exact details of the dust models, our limits on the density parameter $\Omega_{\rm dust} \sim 10^{-5}$ are close to the astrophysically interesting levels implied by studies of stellar evolution and metallicity as a function of redshift. Deep, high-resolution X-ray observations of individual QSOs (Corrales & Paerels, 2012) could provide further constraints on intergalactic "grey" dust that until now eludes optical methods.

- In Paper III and Paper IV we characterize the nearby SN 2014J using UV, optical and near-IR photometry together with low- and high-resolution spectra. We measure the extinction to high precision, over the full wavelength range 0.2–2μm. After correcting for differences in reddening, SN 2014J appears to be very similar to SN 2011fe over the 14 broadband filter light curves used in Paper IV.

- In Paper VI we present UV to near-IR observations of a sample of six SNe Ia, using *HST*, *Swift* and a number of ground based telescopes. We find a diversity of extinction parameters among the SNe.

- In Paper II and Paper V we present the first attempts to detect or rule out the presence of CS dust in normal SNe Ia using mid- and far-IR data. In particular, our *Spitzer* mid-IR observations of the heavily reddened SNe 2014J and 2006X severely constrains the amounts of CS dust in these supernovae; a surprising result, as a vast literature has used CS dust models to explain the peculiar extinction.

- In Paper V we compile the first mid-IR lightcurve templates, capturing the full range from before peak brightness to the nebular phase. We do not find evidence for variations in the mid-IR lightcurve shapes corresponding to the different optical decline rates in our sample, $\Delta m_{15}^{B} = 0.9$ to 1.3, suggesting that SNe Ia are a very homogeneous class of objects at mid-IR wavelengths. A larger sample of SNe Ia with multi-epoch mid-IR coverage is needed to make a more quantitative study.

Coping with the effects of dust continues to be the most difficult and (astrophysically) interesting systematic problem in supernova cosmology. Several methods have been suggested to actively reduce the influence of dust as a systematic error in SN Ia cosmology:

- **Observe in the near-IR**: We saw in Chapter 3.3 that first after correcting for light-curve shape and dust extinction, SNe Ia become *standardized* candles. However, SNe Ia seem to be standard candles in the NIR. Also, the amount of dust absorption roughly scales as $A(\lambda) \propto \lambda^{-1}$, so the effects of extinction in the K-band should be more than ~ 4 times smaller than for the B-band. Recently Barone-Nugent et al. (2012) presented NIR (J, H and K-band) light curves of SNe Ia in the Hubble flow (red symbols in Fig. 6.1). They find that the intrinsic scatter in peak luminosities of SNe Ia in the NIR J- and H-bands are smaller than previously thought, with an H-band dispersion $\sigma_H \approx 0.09$ mag. These results provide distance errors of $\sim 4\%$, making them the most precise standard candles for cosmology. However, SNe Ia are much fainter in the NIR (the fractional flux is about 2%, 1% and 0.5% in the J, H, K-band) and ground based observations in the near-IR are very challenging due to atmospheric emission.

- **SNe Ia sub-sets:** It has been shown that the scatter in the Hubble diagram can be decreased when SNe Ia are separated according to the host galaxy type (Sullivan et al., 2003). Further attempts to improve calibration accuracy by separating SN Ia samples based on spectral features (Wang et al., 2009; Foley & Kasen, 2011) or local host galaxy observables (e.g. H_α emission or UV surface brightness Rigault et al., 2013; Kelly et al., 2014a) seems promising.

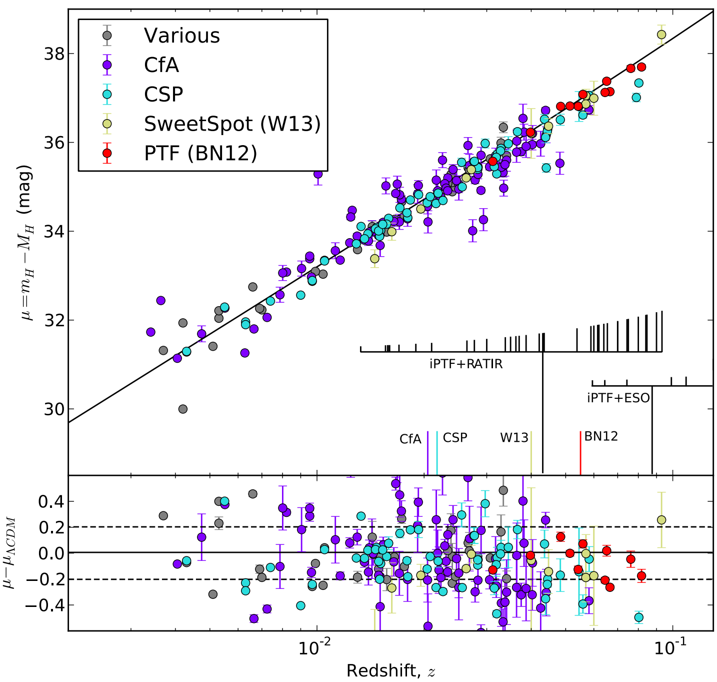

Figure 6.1. Top panel: Hubble diagram from H-band data of SNe Ia (from CfA (Friedman et al., 2014), CSP (Folatelli et al., 2010; Stritzinger et al., 2011), PTF (Barone-Nugent et al., 2012, ,BN12) and the SweetSpot survey (Weyant et al., 2014, W13)). The vertical lines indicate the median redshift of each survey, and the black lines indicate the redshifts of iPTF SNe with NIR follow-up from RATIR and VLT (Johansson et al., work in progress). Bottom: Residuals from the best-fit ΛCDM cosmology as a function of redshift.

Svensk sammanfattning

Relationen mellan avstånd och rödskift hos Typ Ia supernovor är en av de mest effektiva metoderna vi har för att mäta Universums expansion och egenskaperna hos den "mörka energi" som vi tror dominerar universums innehåll. Begränsningen i hur väl vi kan mäta avstånd utgörs idag inte av antalet observerade supernovor utan snarare av systematiska effekter i avståndsbedömningen. Den kanske viktigaste systematiska effekten är den från utsläckning av ljus, från stoft som ligger mellan oss och supernovorna.

Den här avhandlingen handlar om att mäta stoftegenskaper för att begränsa dess inverkan på avståndsmätningar med Typ Ia supernovor och därigenom göra det möjligt att lära sig mer om den mörka energin.

Ett sätt att studera stoft är att titta på hur det gör ljuskällor rödare. Kvasarer är idealiska källor för detta, eftersom de har liten spridning i sina intrinsiska färger. Genom att studera färgerna hos ett stort antal kvasarer på kosmologiska avstånd sätter vi gränser på mängden och egenskaperna av intergalaktiskt stoft. Ett annat sätt att begränsa stoftegenskaper är att titta på spridningen av röntgenstrålning från aktiva galaxkärnor. Om stofttätheten är hög kommer en stor del av ljuset spridas och vi kommer att observera en halo runt de aktiva galaxkärnorna. Avsaknaden av sådana halos begränsar stofttätheten ytterligare.

Med hjälp av observationer med *Hubble* och *Swift*-teleskopen samt en mängd markbaserade teleskop (t.ex. det *Nordiska Optiska Teleskopet*), studerar vi våglängdsberoendet (från ultraviolett, optiskt till infrarött ljus) av extinktionen från stoft i värdgalaxen för ett antal supernovor. Av dessa supernovor har vi särskilt noggrant studerat SN 2014J, den mest närbelägna Typ Ia supernovan på flera decennier.

Vi studerar även modeller där lokala stoftmoln kring supernovor påverkar våra observationer. Det upphettade stoftet förväntas återemittera ljus i infraröda våglängder vilket vi har observerat med *Spitzer*- och

Herschel-teleskopen. Vi har modellerat den förväntade emissionen från stoftmolnen, jämfört med vad vi faktiskt observerar och därigenom satt gränser för mängden stoft som kan omge våra observerade supernovor.

Oskar Klein Centret ingår sedan januari 2013 i kollaborationen *intermediate Palomar Transient Factory* (iPTF), vilket är ett projekt som avser att upptäcka supernovor och andra transienta astronomiska objekt så tidigt som möjligt. Vi förväntar oss även att antalet välobserverade supernovor kommer att öka snabbt inom den närmaste framtiden vilket kommer att öppna upp för nya analyser, inte nödvändigtvis begränsade till effekterna från stoft.

References

Aguirre, A. 1999a, ApJ, 525, 583

Aguirre, A., & Haiman, Z. 2000, ApJ, 532, 28

Aguirre, A. N. 1999b, ApJ, 512, L19

Amanullah, R., & Goobar, A. 2011, ApJ, 735, 20

Ashall, C., Mazzali, P., Bersier, D., et al. 2014, MNRAS, 445, 4424

Astier, P., Guy, J., Regnault, N., et al. 2006, A&A, 447, 31

Avgoustidis, A., Verde, L., & Jimenez, R. 2009, JCAP, 6, 12

Baade, W., & Zwicky, F. 1934, Proceedings of the National Academy of Science, 20, 254

Barone-Nugent, R. L., Lidman, C., Wyithe, J. S. B., et al. 2012, MNRAS, 425, 1007

Berry, M., Ivezić, Ž., Sesar, B., et al. 2012, ApJ, 757, 166

Betoule, M., Kessler, R., Guy, J., et al. 2014, A&A, 568, A22

Bianchi, S., & Ferrara, A. 2005, MNRAS, 358, 379

Bloom, J. S., Kasen, D., Shen, K. J., et al. 2012, ApJ, 744, L17

Brown, P. J., Smitka, M. T., Wang, L., et al. 2014, ArXiv e-prints, arXiv:1408.2381

Burns, C. R., Stritzinger, M., Phillips, M. M., et al. 2011, AJ, 141, 19

—. 2014, ApJ, 789, 32

Cardelli, J. A., Clayton, G. C., & Mathis, J. S. 1989, ApJ, 345, 245

Chevallier, M., & Polarski, D. 2001, International Journal of Modern Physics D, 10, 213

Chomiuk, L., Soderberg, A. M., Moe, M., et al. 2012, ApJ, 750, 164

Chotard, N., Gangler, E., Aldering, G., et al. 2011, A&A, 529, L4

Churazov, E., Sunyaev, R., Isern, J., et al. 2014, Nature, 512, 406

Compiègne, M., Verstraete, L., Jones, A., et al. 2011, A&A, 525, A103

Conley, A., Carlberg, R. G., Guy, J., et al. 2007, ApJ, 664, L13

Corrales, L., & Paerels, F. 2012, ApJ, 751, 93

Diehl, R., Siegert, T., Hillebrandt, W., et al. 2014, Science, 345, 1162

Dijkstra, M., & Loeb, A. 2009, MNRAS, 397, 1976

Dilday, B., Howell, D. A., Cenko, S. B., et al. 2012, Science, 337, 942

Draine, B. T. 2003a, ARA&A, 41, 241

—. 2003b, ApJ, 598, 1026

Draine, B. T. 2004, in The Cold Universe, Saas-Fee Advanced Course 32, Springer-Verlag, 308 pages, 129 figures, Lecture Notes 2002 of the Swiss Society for Astronomy and Astrophysics (SSAA), Springer, 2004. Edited by A.W. Blain, F. Combes, B.T. Draine, D. Pfenniger and Y. Revaz, ISBN 354040838x, p. 213, ed. A. W. Blain, F. Combes, B. T. Draine, D. Pfenniger, & Y. Revaz, 213

Draine, B. T., & Lee, H. M. 1984, ApJ, 285, 89

Elias, J. H., Matthews, K., Neugebauer, G., & Persson, S. E. 1985, ApJ, 296, 379

Elias-Rosa, N., Benetti, S., Cappellaro, E., et al. 2006, MNRAS, 369, 1880

Elias-Rosa, N., Benetti, S., Turatto, M., et al. 2008, MNRAS, 384, 107

Elíasdóttir, Á., Hjorth, J., Toft, S., Burud, I., & Paraficz, D. 2006, ApJS, 166, 443

Elíasdóttir, Á., Fynbo, J. P. U., Hjorth, J., et al. 2009, ApJ, 697, 1725

Engelbracht, C. W., Kundurthy, P., Gordon, K. D., et al. 2006, ApJ, 642, L127

Evans, A., Norwell, G. A., & Bode, M. F. 1985, MNRAS, 213, 1P

Falco, E. E., Impey, C. D., Kochanek, C. S., et al. 1999, ApJ, 523, 617

Filippenko, A. V. 1997, ARA&A, 35, 309

Filippenko, A. V., Richmond, M. W., Matheson, T., et al. 1992a, ApJ, 384, L15

Filippenko, A. V., Richmond, M. W., Branch, D., et al. 1992b, AJ, 104, 1543

Fitzpatrick, E. L. 1999, PASP, 111, 63

Folatelli, G., Phillips, M. M., Burns, C. R., et al. 2010, AJ, 139, 120

Foley, R. J., & Kasen, D. 2011, ApJ, 729, 55

Foley, R. J., Challis, P. J., Chornock, R., et al. 2013, ApJ, 767, 57

Foley, R. J., Fox, O. D., McCully, C., et al. 2014, MNRAS, 443, 2887

Förster, F., González-Gaitán, S., Folatelli, G., & Morrell, N. 2013, ApJ, 772, 19

Fox, O. D., & Filippenko, A. V. 2013, ApJ, 772, L6

Fox, O. D., Chevalier, R. A., Skrutskie, M. F., et al. 2011, ApJ, 741, 7

Fox, O. D., Silverman, J. M., Filippenko, A. V., et al. 2014, ArXiv e-prints, arXiv:1408.6239

Friedman, A. S., Wood-Vasey, W. M., Marion, G. H., et al. 2014, ArXiv e-prints, arXiv:1408.0465

Fukugita, M. 2011, arXiv:1103.4191, arXiv:1103.4191

Gall, C., Hjorth, J., & Andersen, A. C. 2011, A&A Rev., 19, 43

Gomez, H. L., Clark, C. J. R., Nozawa, T., et al. 2012, MNRAS, 420, 3557

Goobar, A. 2008, ApJ, 686, L103

Goobar, A., & Leibundgut, B. 2011, Annual Review of Nuclear and Particle Science, 61, 251

Goobar, A., Kromer, M., Siverd, R., et al. 2014, ArXiv e-prints, arXiv:1410.1363

Graham, M. L., Valenti, S., Fulton, B. J., et al. 2014, ArXiv e-prints, arXiv:1412.0653

Guy, J., Astier, P., Baumont, S., et al. 2007, A&A, 466, 11

Hachisu, I., Kato, M., & Nomoto, K. 1996, ApJ, 470, L97

Hamuy, M., Phillips, M. M., Maza, J., et al. 1995, AJ, 109, 1

Hamuy, M., Phillips, M. M., Suntzeff, N. B., et al. 2003, Nature, 424, 651

Hancock, P. P., Gaensler, B. M., & Murphy, T. 2011, ApJ, 735, L35

Hansen, L., Jorgensen, H. E., Norgaard-Nielsen, H. U., Ellis, R. S., & Couch, W. J. 1989, A&A, 211, L9

Hicken, M., Challis, P., Jha, S., et al. 2009, ApJ, 700, 331

Hickox, R. C., & Markevitch, M. 2007, ApJ, 661, L117

Hildebrand, R. H. 1983, qjras, 24, 267

Hogg, D. W. 1999, ArXiv Astrophysics e-prints, arXiv:astro-ph/9905116

Holwerda, B. W., Keel, W. C., Williams, B., Dalcanton, J. J., & de Jong, R. S. 2009, AJ, 137, 3000

Horesh, A., Kulkarni, S. R., Fox, D. B., et al. 2012, ApJ, 746, 21

Howell, D. A., Sullivan, M., Nugent, P. E., et al. 2006, Nature, 443, 308

Hsiao, E. Y., Conley, A., Howell, D. A., et al. 2007, ApJ, 663, 1187

Hubble, E. 1929, Proceedings of the National Academy of Science, 15, 168

Hutton, S., Ferreras, I., Wu, K., et al. 2014, MNRAS, 440, 150

Immler, S., Brown, P. J., Milne, P., et al. 2006, ApJ, 648, L119

Inoue, A. K., & Kamaya, H. 2004, MNRAS, 350, 729

Johnson, H. M., & Hanna, M. M. 1972, ApJ, 174, L71

Jönsson, J., Sullivan, M., Hook, I., et al. 2010, MNRAS, 405, 535

Kasen, D. 2010, ApJ, 708, 1025

Kasen, D., Röpke, F. K., & Woosley, S. E. 2009, Nature, 460, 869

Kawabata, K. S., Akitaya, H., Yamanaka, M., et al. 2014, ApJ, 795, L4

Kelly, P. L., Filippenko, A. V., Burke, D. L., et al. 2014a, ArXiv, arXiv:1410.0961

Kelly, P. L., Fox, O. D., Filippenko, A. V., et al. 2014b, ApJ, 790, 3

Kessler, R., Becker, A. C., Cinabro, D., et al. 2009, ApJS, 185, 32

Kotak, R., Meikle, W. P. S., Farrah, D., et al. 2009, ApJ, 704, 306

Krause, O., Tanaka, M., Usuda, T., et al. 2008, Nature, 456, 617

Krisciunas, K., Prieto, J. L., Garnavich, P. M., et al. 2006, AJ, 131, 1639

Laor, A., & Draine, B. T. 1993, ApJ, 402, 441

Leavitt, H. S., & Pickering, E. C. 1912, Harvard College Observatory Circular, 173, 1

Leibundgut, B., Kirshner, R. P., Phillips, M. M., et al. 1993, AJ, 105, 301

Lemaître, G. 1927, Annales de la Societe Scietifique de Bruxelles, 47, 49

Lentz, E. J., Baron, E., Branch, D., Hauschildt, P. H., & Nugent, P. E. 2000, ApJ, 530, 966

Li, A. 2007, in Astronomical Society of the Pacific Conference Series, Vol. 373, The Central Engine of Active Galactic Nuclei, ed. L. C. Ho & J.-W. Wang, 561

Li, W., Bloom, J. S., Podsiadlowski, P., et al. 2011, Nature, 480, 348

Linder, E. V. 2003, Physical Review Letters, 90, 091301

Loeb, A., & Haiman, Z. 1997, ApJ, 490, 571

Lundmark, K. 1920, Kungl. Svenska Vetenskapsakademiens Handlingar, 60, 1

—. 1924, MNRAS, 84, 747

—. 1927, Nova Acta Regiae Soc. Sci. Upsaliensis Ser. V, 1

Lundqvist, P., Mattila, S., Sollerman, J., et al. 2013, MNRAS, 435, 329

Maeda, K., Nozawa, T., & Motohara, K. 2014, ArXiv e-prints, arXiv:1411.3778

Maeda, K., Leloudas, G., Taubenberger, S., et al. 2011, MNRAS, 413, 3075

Mandel, K. S., Narayan, G., & Kirshner, R. P. 2011, ApJ, 731, 120

Margutti, R., Parrent, J., Kamble, A., et al. 2014, ApJ, 790, 52

Mathis, J. S., & Lee, C.-W. 1991, ApJ, 376, 490

Mathis, J. S., Rumpl, W., & Nordsieck, K. H. 1977, ApJ, 217, 425

Matsuura, M., Dwek, E., Barlow, M. J., et al. 2014, ArXiv e-prints, arXiv:1411.7381

Mattila, S., Fraser, M., Smartt, S. J., et al. 2013, MNRAS, 431, 2050

Mattila, S., Lundqvist, P., Sollerman, J., et al. 2005, A&A, 443, 649

Ménard, B., Kilbinger, M., & Scranton, R. 2010a, MNRAS, 406, 1815

Ménard, B., Nestor, D., Turnshek, D., et al. 2008, MNRAS, 385, 1053

Ménard, B., Scranton, R., Fukugita, M., & Richards, G. 2010b, MNRAS, 405, 1025

Milne, P. A., Brown, P. J., Roming, P. W. A., Bufano, F., & Gehrels, N. 2013, ApJ, 779, 23

Minkowski, R. 1941, PASP, 53, 224

Miralda-Escudé, J. 1999, ApJ, 512, 21

More, S., Bovy, J., & Hogg, D. W. 2009, ApJ, 696, 1727

Moretti, A., Campana, S., Lazzati, D., & Tagliaferri, G. 2003, ApJ, 588, 696

Mörtsell, E. 2013, A&A, 550, A80

Mörtsell, E., & Goobar, A. 2003, JCAP, 9, 9

Nobili, S., & Goobar, A. 2008, A&A, 487, 19

Nordin, J., Goobar, A., & Jönsson, J. 2008, JCAP, 2, 8

Norgaard-Nielsen, H. U., Hansen, L., Jorgensen, H. E., Aragon Salamanca, A., & Ellis, R. S. 1989, Nature, 339, 523

Nozawa, T., Maeda, K., Kozasa, T., et al. 2011, ApJ, 736, 45

Nugent, P. E., Sullivan, M., Cenko, S. B., et al. 2011, Nature, 480, 344

O'Donnell, J. E. 1994, ApJ, 422, 158

Östman, L., Goobar, A., & Mörtsell, E. 2006, A&A, 450, 971

—. 2008, A&A, 485, 403

Östman, L., & Mörtsell, E. 2005, JCAP, 2, 5

Panagia, N., Van Dyk, S. D., Weiler, K. W., et al. 2006, ApJ, 646, 369

Patat, F., Chandra, P., Chevalier, R., et al. 2007, Science, 317, 924

Patat, F., Cordiner, M. A., Cox, N. L. J., et al. 2013, A&A, 549, A62

Patat, F., Taubenberger, S., Cox, N. L. J., et al. 2014, ArXiv e-prints, arXiv:1407.0136

Peek, J. E. G., Ménard, B., & Corrales, L. 2014, ArXiv e-prints, arXiv:1411.3333

Pérez-Torres, M. A., Lundqvist, P., Beswick, R. J., et al. 2014, ApJ, 792, 38

Perlmutter, S., Aldering, G., Deustua, S., et al. 1997, in Bulletin of the American Astronomical Society, Vol. 29, American Astronomical Society Meeting Abstracts, 1351

Perlmutter, S., Aldering, G., Goldhaber, G., et al. 1999, ApJ, 517, 565

Petric, A., Telis, G. A., Paerels, F., & Helfand, D. J. 2006, ApJ, 651, 41

Phillips, M. M. 1993, ApJ, 413, L105

Pilbratt, G. L., Riedinger, J. R., Passvogel, T., et al. 2010, A&A, 518, L1

Poglitsch, A., Waelkens, C., Geis, N., et al. 2010, A&A, 518, L2

Riess, A. G., Filippenko, A. V., Challis, P., et al. 1998, AJ, 116, 1009

Riess, A. G., Macri, L., Casertano, S., et al. 2011, ApJ, 730, 119

Rigault, M., Copin, Y., Aldering, G., & Antilogus, e. a. 2013, A&A, 560, A66

Ritchey, A. M., Welty, D. E., Dahlstrom, J. A., & York, D. G. 2014, ArXiv e-prints, arXiv:1407.5723

Roussel, H., Wilson, C. D., Vigroux, L., et al. 2010, A&A, 518, L66

Ruiz-Lapuente, P., Comeron, F., Mendez, J., et al. 2004, Nature, 431, 1069

Russell, B. R., & Immler, S. 2012, ApJ, 748, L29

Schady, P., Dwelly, T., Page, M. J., et al. 2012, A&A, 537, A15

Schlegel, D. J., Finkbeiner, D. P., & Davis, M. 1998, ApJ, 500, 525

Schneider, D. P., Richards, G. T., Hall, P. B., et al. 2010, AJ, 139, 2360

Schöier, F. L., & Olofsson, H. 2001, A&A, 368, 969

Scolnic, D., Rest, A., Riess, A., et al. 2014a, ApJ, 795, 45

Scolnic, D. M., Riess, A. G., Foley, R. J., et al. 2014b, ApJ, 780, 37

Simon, J. D., Gal-Yam, A., Gnat, O., et al. 2009, ApJ, 702, 1157

Smith, R. K., & Dwek, E. 1998, ApJ, 503, 831

Stritzinger, M. D., Phillips, M. M., Boldt, L. N., et al. 2011, AJ, 142, 156

Sullivan, M., Ellis, R. S., Aldering, G., et al. 2003, MNRAS, 340, 1057

Suzuki, N., Rubin, D., Lidman, C., et al. 2012, ApJ, 746, 85

Telfer, R. C., Zheng, W., Kriss, G. A., & Davidsen, A. F. 2002, ApJ, 565, 773

Tripp, R. 1998, A&A, 331, 815

Vanden Berk, D. E., Richards, G. T., Bauer, A., et al. 2001, AJ, 122, 549

Vaughan, S., Willingale, R., Romano, P., et al. 2006, ApJ, 639, 323

Wang, L. 2005, ApJ, 635, L33

Wang, X., Wang, L., Pain, R., Zhou, X., & Li, Z. 2006, ApJ, 645, 488

Wang, X., Li, W., Filippenko, A. V., et al. 2008, ApJ, 675, 626

Wang, X., Filippenko, A. V., Ganeshalingam, M., et al. 2009, ApJ, 699, L139

Weingartner, J. C., & Draine, B. T. 2001, ApJ, 548, 296

Weyant, A., Wood-Vasey, W. M., Allen, L., et al. 2014, ApJ, 784, 105

Zhang, P. 2008, ApJ, 682, 721

Zheng, W., Shivvers, I., Filippenko, A. V., et al. 2014, ApJ, 783, L24

Paper I

J. Johansson & E. Mörtsell
Combined constraints on intergalactic dust from quasar colours and the soft X-ray background
MNRAS, Vol. 426, p. 3360-3368 (2012).

Monthly Notices of the ROYAL ASTRONOMICAL SOCIETY
Mon. Not. R. Astron. Soc. **426,** 3360–3368 (2012) doi:10.1111/j.1365-2966.2012.21940.x

Combined constraints on intergalactic dust from quasar colours and the soft X-ray background

Joel Johansson[1,2]⋆ and Edvard Mörtsell[1,2]
[1]*Physics Department, AlbaNova University Center, Stockholm University, SE-106 91 Stockholm, Sweden*
[2]*The Oskar Klein Center, Stockholm University, SE-106 91 Stockholm, Sweden*

Accepted 2012 August 15. Received 2012 June 13; in original form 2012 February 20

ABSTRACT

Unless properly corrected for, the existence of intergalactic dust will introduce a redshift-dependent magnitude offset to standard candle sources. This would lead to overestimated luminosity distances compared to a dust-free universe and bias the cosmological parameter estimation as derived from, e.g., Type Ia supernova observations. In this paper, we model the optical extinction and X-ray scattering properties of intergalactic dust grains to constrain the intergalactic opacity using a combined analysis of observed quasar colours and the soft X-ray background. Quasar colours effectively constrain the amount of intergalactic dust grains smaller than ∼0.2 μm, to the point where we expect the corresponding systematic error in the Type Ia supernova magnitude–redshift relation to be sub-dominant. Soft X-ray background observations are helpful in improving the constraints on very large dust grains for which the amount of optical reddening is very small and therefore is more difficult to correct for. Our current upper limit corresponds to ∼0.25 mag dimming at optical wavelengths for a source at redshift $z = 1$, which is too small to alleviate the need for dark energy but large in terms of relative error. However, we expect it to be possible to lower this bound considerably with an improved understanding of the possible sources of the X-ray background, in combination with observations of compact X-ray sources such as active galactic nuclei.

Key words: scattering – dust, extinction – intergalactic medium – cosmology: theory.

1 INTRODUCTION

The use of Type Ia supernovae (SNe Ia) as standardized candles to probe the redshift–distance relation remains essential for establishing and exploring the dark energy universe. The fact that complementary cosmological probes agree on the concordance cosmological model with current accelerated cosmological expansion makes it unlikely that the observed dimming of SNe Ia are solely due to dust extinction. Nonetheless, it is still possible that dust extinction could bias cosmological parameter estimation. Also, when trying to explore specific dark energy properties, it becomes crucial to be able to constrain the effect of dust on SN Ia observations (Corasaniti 2007; Ménard, Kilbinger & Scranton 2010).

The presence of dust in the intergalactic medium (IGM) has been the subject of numerous studies. Based on the estimates of the stellar density and metallicity as a function of redshift, several authors have inferred the existence of significant amounts of dust in the IGM with density $\Omega_{\rm dust} \sim 10^{-6}$–$10^{-5}$ (Loeb & Haiman 1997; Inoue & Kamaya 2004; Fukugita 2011).

Dust grains scatter and absorb photons with an energy-dependent cross-section and typical dust extinction is correlated with reddening of the incoming light. The amount of reddening is usually quantified by the total-to-selective extinction ratio $R_V \equiv A_V/E(B-V) = A_V/(A_B - A_V)$, where $E(B-V)$ is the colour excess and A_B and A_V are the extinction in the B and V band, respectively. Ménard et al. (2010) report a statistical detection of dust reddening of quasars (QSOs) out to large distances (a few Mpc) aroundgalaxies at $z = 0.3$. The observed reddening implies a slope of the extinction curve, $R_V = 3.9 \pm 2.6$, which is consistent with that of Milky Way dust ($R_V = 3.1$), albeit with large uncertainties. Extrapolating this result to higher redshifts yields a lower limit estimate of the extinction in the rest-frame B band of $A_B(z = 1) \gtrsim 0.03$ magnitudes.

Aguirre (1999) and Bianchi & Ferrara (2005) find that astrophysical processes which transfer dust into the IGM would preferentially destroy small grains, leaving only grains larger than $a \sim 0.1$ μm, implying less reddening and higher values for R_V (often labelled 'grey' dust). The absence of detectable systematic reddening of SNe Ia with increasing redshift implies that any intergalactic dust extinction must be quite grey at optical wavelengths, suggesting that the grains must be large. Since the dust correction for SNe Ia depends on the reddening, large grains will be more difficult to

⋆E-mail: joeljo@fysik.su.se

correct for. Mörtsell & Goobar (2003) and Östman & Mörtsell (2005) simulated the reddening by intergalactic dust based on the different parametrizations of mean extinction laws of Milky Way-like dust, with $0 < R_V < 12$. They used observations of QSO colours and template spectra to put an upper limit on the dimming in the rest-frame B band by intergalactic dust of a source at redshift $z = 1$ of $A_B(z = 1) \lesssim 0.02$ for $R_V \sim 3$ and $A_B(z = 1) \lesssim 0.1$ for $R_V \sim 10$.

Apart from the reddening of cosmological sources, the presence of dust grains can also be inferred from the absorption of UV/optical photons which are re-emitted in the far infrared. Aguirre & Haiman (2000) calculated the contribution from intergalactic dust to the cosmic far-infrared background, assuming it was heated by intergalactic radiation. They found that dust densities of $\Omega_{\rm dust} \sim$ a few $\times\, 10^{-5}$, necessary to account for the dimming of SNe Ia, would produce most of the far-infrared background. However, observational data leave little room for any such diffuse emission component, since discrete sources detected by the Submillimetre Common-User Bolometer Array (SCUBA) survey account for almost all of the background at 850 μm (Hauser & Dwek 2001).

Intergalactic dust would also scatter X-rays from point sources into extended, diffuse X-ray haloes. If the size of the halo is large enough, the scattered radiation will effectively be part of the unresolved soft X-ray background (SXB). Dijkstra & Loeb (2009) argue that dust scattered X-ray haloes around active galactic nuclei (AGN) can maximally account for a fraction $f_{\rm halo} \sim$ 5–15 per cent of the total measured SXB. This allows them to place an upper limit on the optical/near-infrared extinction $\Delta m(z = 1, \lambda = 8269\,\text{Å}) \lesssim 0.15(f_{\rm halo}/10\,\text{per cent})$. The absence of an X-ray halo around a single $z = 4.3$ QSO observed with *Chandra* allows Petric et al. (2006) and Corrales & Paerels (2012) to place upper limits on the dust density parameter $\Omega_{\rm dust} \lesssim 10^{-6}$–$10^{-5}$ assuming a constant comoving number density of dust grains of size $a = 1$ μm or with a power law distribution of grain sizes $0.1 \le a \le 1$ μm.

In this paper we will combine a QSO colour analysis with an SXB analysis to constrain the amount of both small and large dust grains. The outline of the paper is as follows: in Section 2 we continue discussing existing constraints on intergalactic dust and argue for a physical model of the intergalactic dust. In Section 3 we evaluate the effects of intergalactic dust on QSO colours and in Section 4 we examine how the unresolved SXB can put further constraints on these dust models. We present our results in Section 5 and summarize and discuss these results and some future prospects in Section 6.

2 INTERGALACTIC DUST

Dust grains are present in our Galaxy, in the host galaxies of cosmological sources, in galaxies along the line of sight and possibly in the immediate surroundings of the source (e.g. Schlegel, Finkbeiner & Davis 1998; Östman, Goobar & Mörtsell 2006, 2008; Goobar 2008). In this paper, we will study the effect of intergalactic dust along the line of sight to cosmological sources. Extinction by interstellar dust in the Milky Way and nearby galaxies, such as the Small and Large Magellanic Clouds, is usually parametrized using mean extinction laws, $A_\lambda = f(\lambda, R_V)$ where A_λ is the extinction for wavelength λ and the reddening parameter, $R_V = A_V/(A_B - A_V)$, is the slope of the extinction curve in the optical region (e.g. Cardelli, Clayton & Mathis 1989; Fitzpatrick 1999). Within the Milky Way, the reddening parameter is in the range $2 \lesssim R_V \lesssim 6$ for different sightlines and is usually approximated as $R_V = 3.1$. It is not known if these parametrizations are valid for an intergalactic dust population where the dust properties might be different from those in the interstellar medium. Small grains preferentially scatter light with short wavelengths, producing a steep extinction law with small values for R_V. Very large grains would produce wavelength-independent grey extinction with $R_V \to \infty$.

To build up extinction curves from a generic population of dust grains one needs to know the composition, size distribution, scattering and absorption properties of the dust grains. Mathis, Rumpl & Nordsieck (1977), hereafter MRN, found that interstellar extinction in the Milky Way is well fitted using separate populations of bare silicate and graphite grains with a power-law distribution of sizes where $\mathrm{d}n/\mathrm{d}a \propto a^{-3.5}$. Within the Milky Way, graphite grains typically range in size from 0.005 to 1 μm while silicate grain sizes range from 0.025 to 0.25 μm.

We will study dust models that have either a single grain size or truncated MRN size distributions, varying the size of the smallest and largest grains $a_{\rm min}$ and $a_{\rm max}$. The intergalactic dust is assumed to be distributed homogeneously with a constant comoving number density of dust grains, $n(z)$. It is reasonable to assume that the dust density traces the stellar mass density in the universe, and we also investigate cases where the comoving dust density is proportional to the integrated star formation rate density, $n(z) \propto \int_z^\infty \mathrm{d}z' \frac{\dot\rho_\star}{(1+z')\mathcal{E}(z')}$, where we use the analytical expression for the star formation rate, $\dot\rho_\star$, derived by Hernquist & Springel (2003).

2.1 Optical depth to scattering and absorption

The total optical depth to scattering and/or absorption by dust grains between redshift 0 and $z_{\rm em}$ can be calculated as

$$\tau\,(\lambda_{\rm obs}, z_{\rm em}) = \frac{c}{H_0}\int_0^{z_{\rm em}} \mathrm{d}z' \frac{n(z')\sigma(\lambda')(1+z')^2}{\mathcal{E}(z')}\,, \tag{1}$$

where $n(z')$ is the comoving number density of dust grains at redshift z'. Each dust grain is assumed to be spherical, with radius a and geometrical cross-section $\sigma(\lambda') = \pi a^2 Q(\lambda')$ where the efficiencies for scattering and absorption are $Q_{\rm scat}$ and $Q_{\rm abs}$, the efficiency for extinction is $Q_{\rm ext} = Q_{\rm scat} + Q_{\rm abs}$ and $\lambda' = \lambda_{\rm obs}/(1+z)$. The dimensionless expansion factor $\mathcal{E}(z') = \sqrt{\Omega_M(1+z)^3 + \Omega_\Lambda}$. For a distribution of grain sizes, equation (1) becomes

$$\tau\,(\lambda_{\rm obs}, z_{\rm em}) = \frac{c}{H_0}\int_0^{z_{\rm em}} \mathrm{d}z' \int_{a_{\rm min}}^{a_{\rm max}} \mathrm{d}a\, \frac{\mathrm{d}n}{\mathrm{d}a}\frac{\sigma(\lambda')(1+z')^2}{\mathcal{E}(z')}\,, \tag{2}$$

where $\frac{\mathrm{d}n}{\mathrm{d}a}\mathrm{d}a$ denotes the comoving number density of dust grains with radii in the range $a \pm \mathrm{d}a/2$.

In this paper we focus on dust composed of silicate ($\rho_{\rm grain} \approx 3.2\ \mathrm{g\,cm^{-3}}$) and graphite grains ($\rho_{\rm grain} \approx 2.3\ \mathrm{g\,cm^{-3}}$) (described in Draine & Lee 1984; Laor & Draine 1993; Weingartner & Draine 2001). The original astronomical silicate model constructed by Draine & Lee (1984) used laboratory measurements of crystalline olivine in the vacuum ultraviolet, resulting in an absorption feature at $\lambda \sim 0.15$ μm not seen in astronomical objects. In this paper, we use the smoothed astronomical silicate model dielectric function obtained by removing this absorption feature (Weingartner & Draine 2001). The publicly available scattering and absorption efficiencies $Q_{\rm sca}$ and $Q_{\rm abs}$ are given for wavelengths $\lambda = 10^{-3}$ to 10^3 μm for grains with radii $a = 10^{-3}$ to 10 μm, see Fig. 1. For wavelengths shorter than $\lambda \lesssim 10^{-3}$ μm (corresponding to X-ray energies $E \gtrsim 0.5$ keV) we use the scattering approximations (Alcock & Hatchett 1978; Miralda-Escudé 1999; Dijkstra & Loeb 2009)

$$Q_{\rm scat} \approx \begin{cases} 0.7(a/\mu\mathrm{m})^2(6\,\mathrm{keV}/E)^2 & Q_{\rm scat} < 1 \\ 1.5 & \text{otherwise.}\end{cases} \tag{3}$$

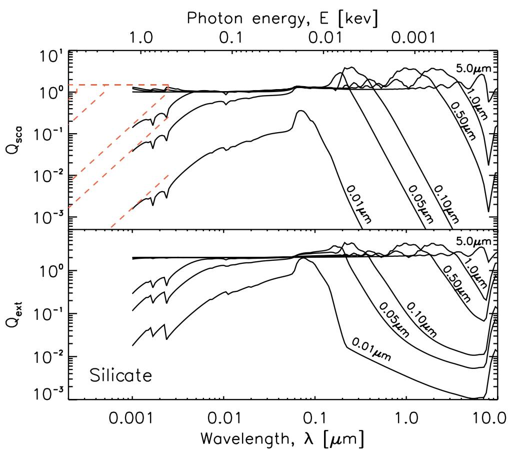

Figure 1. Upper panel: scattering efficiency as a function of wavelength, $Q_{\rm sca}(\lambda)$, for spherical silicate dust grains of radii, $a = 0.01 - 5.0$ µm. The solid black lines show $Q_{\rm sca} = \sigma_{\rm sca}/\pi a^2$, where $\sigma_{\rm scat}$ is the scattering cross-section, from Laor & Draine (1993) and the dashed red lines show the approximation made in equation (3). Lower panel: extinction efficiency as a function of wavelength, $Q_{\rm ext}(\lambda) = Q_{\rm sca} + Q_{\rm abs}$, for spherical silicate dust grains of radii, $a = 0.01{-}5.0$ µm.

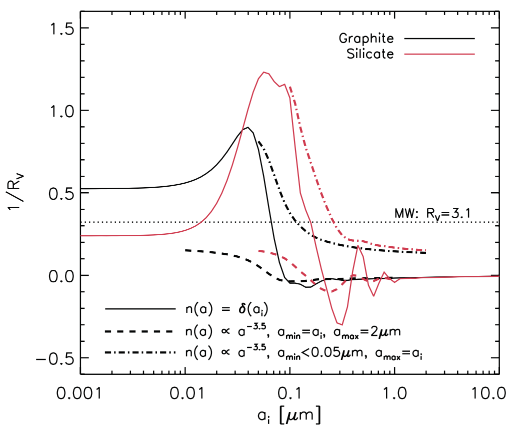

Figure 2. $R_V^{-1} = (A_B - A_V)/A_V$ reddening for dust models with graphite (black lines) and silicate (red lines) grains with a single grain size (solid lines) or models with truncated MRN grain size distributions with $0.05 < a_{\rm min} < 1.0$ µm and $a_{\rm max} = 2.0$ µm (dashed lines) or $a_{\rm min} = 0.02$ µm (graphite) or $a_{\rm min} = 0.05$ µm (silicate) and $0.1 < a_{\rm max} < 2.0$ µm (dot–dashed lines). The inclusion of grains with radii larger than $a \gtrsim 0.1$–0.2 µm gives grey extinction with $R_V^{-1} \to 0$. The horizontal dotted line shows the average reddening for interstellar dust in the Milky Way, $R_V = 3.1$.

In Fig. 2, we show the corresponding total-to-selective extinction ratio $R_V = A_V/(A_B - A_V)$ for the graphite (black lines) and silicate dust (red lines) models employed in this paper. The solid lines correspond to single size models, dashed and dash–dotted lines to truncated MRN grain size distributions where $a_{\rm min}$ and $a_{\rm max}$ are varied, respectively. The inclusion of large grains gives $A_B \approx A_V$, which drives $R_V^{-1} \to 0$. Note that the R_V-value only refers to the modelled optical extinction in the B and V band and does not necessarily describe the entire extinction curve as observed for Milky Way dust. In fact, the variations in the Q-values for silicate dust grains $a \sim 0.25$ µm can also introduce a small blueing effect with $R_V \lesssim 0$.

2.2 X-ray scattering by dust

Small angle scattering of X-rays by dust grains along the line of sight can produce diffuse haloes around X-ray point sources, as observed for many galactic X-ray sources. Measurements of the intensity and angular extent of such haloes provide a quantitative test of interstellar grain models (Mauche & Gorenstein 1986; Mathis & Lee 1991; Smith & Dwek 1998; Draine 2003). In a similar way, intergalactic dust grains would produce diffuse haloes around X-ray sources on cosmological distances. In common with X-ray haloes seen around galactic point sources, the angular extent of an intergalactic halo is determined by the scattering properties of the grains (Evans, Norwell & Bode 1985; Petric et al. 2006; Vaughan et al. 2006).

The differential cross-section in the Rayleigh–Gans approximation for a spherical dust grain of radius a is given by (Hayakawa 1970; Mauche & Gorenstein 1986)

$$\frac{{\rm d}\sigma_{\rm sca}}{{\rm d}\Omega} = A_E \left(\frac{a}{1.0\,\mu{\rm m}}\right)^6 \left[\frac{j_1(x)}{x}\right]^2 (1+\cos^2\theta)\,, \qquad (4)$$

where $x = (4\pi a/\lambda)\sin(\theta/2)$ and $j_1(x) = (\sin x)/x^2 - (\cos x/x)$ is the spherical Bessel function of the first order. A_E is a normalization depending on the grain composition and energy E of the X-rays being scattered,

$$A_E = 1.1 \left(\frac{2Z}{M}\right)^2 \left(\frac{\rho_{\rm grain}}{3\,{\rm g\,cm^{-3}}}\right)^2 \left(\frac{F(E)}{Z}\right)^2, \qquad (5)$$

where $F(E)$ is the atomic scattering factor (Henke et al. 1982; Henke, Gullikson & Davis 1993), Z is the atomic charge, M is the atomic mass number and $\rho_{\rm grain}$ is the mass density of the dust grain. The central core of equation (4) is approximately Gaussian, and the root mean square (rms) of the scattering angle θ indicates the typical size of the scattered halo (Mauche & Gorenstein 1986), $\theta_{\rm rms} \approx 62.4\,(1.0\,\mu{\rm m}/a)\,(1\,{\rm keV}/E)$ arcsec.

For low optical depths ($\tau_{\rm sca} \ll 1$), the halo influence per unit scattering angle is (Vaughan et al. 2006)

$$\frac{{\rm d}F_{\rm halo}}{{\rm d}\theta} \propto 2\pi\theta A_E \left(\frac{a}{1.0\,\mu{\rm m}}\right)^6 \left[\frac{j_1(x)}{x}\right]^2 (1+\cos^2\theta) N_{\rm g} F_{\rm X}\,, \qquad (6)$$

where $N_{\rm g}$ is the dust grain column density along the line-of-sight and $F_{\rm X}$ is the unscattered flux of the X-ray point source.

Smith & Dwek (1998) showed that the Rayleigh–Gans approximation and the more exact Mie theory are in close agreement, given that the photon energy E (in keV) of the X-ray being scattered is larger than the grain radius a (in µm). For our purposes, where we want to study the contribution of dust-scattered X-ray haloes around AGN to the 0.5–2.0 keV SXB, we note that the average photon energy at the site of the scattering dust grain is higher than the observed energy by a factor $(1 + z_{\rm grain})$, which tends to alleviate the error introduced by the use of the Rayleigh–Gans approximation for the larger grains.

3 CONSTRAINTS FROM QUASAR COLOURS

QSOs have been found to be relatively homogeneous in terms of colours and spectral features over a large redshift range. The Sloan

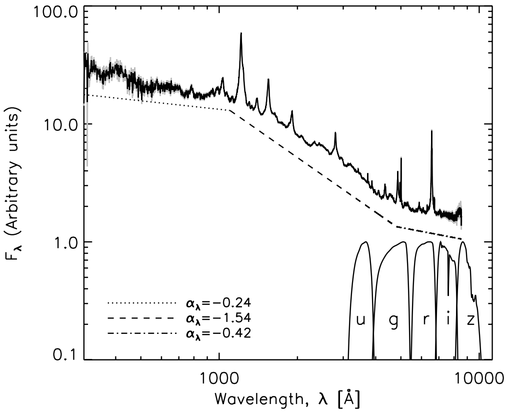

Figure 3. The composite QSO spectral template together with a broken power law, $F_\lambda \propto \lambda^{\alpha_\lambda}$, with spectral indices $\alpha_\lambda = -0.24$ (dotted line, for $\lambda < 1200$ Å), $\alpha_\lambda = -1.54$ (dashed line, for $1200 < \lambda < 4850$ Å) and $\alpha_\lambda = -0.42$ (dot–dashed lines for $\lambda > 4850$ Å). Shown are also the SDSS *ugriz* transmission curves.

Digital Sky Survey (SDSS) Data Release 7 (DR7) QSO catalogue (Schneider et al. 2010) contains 105 783 spectroscopically confirmed QSOs with optical magnitudes measured through five broad-band filters (u, g, r, i, z). We only include point sources (removing QSOs flagged as extended) brighter than the limiting magnitudes [u, g, r, i, z] = [22.3, 22.6, 22.7, 22.4, 20.5], corresponding to S/N greater than 5:1. Objects deviating by more than 2σ from the mean colour are rejected (Mörtsell & Goobar 2003; Östman & Mörtsell 2005).

3.1 Composite quasar spectral template

For our purposes it is preferable to use an unabsorbed QSO spectrum. We use the SDSS median composite spectrum (as derived by Vanden Berk et al. 2001) spliced with the *Hubble Space Telescope* (*HST*) radio-quiet composite spectrum (Telfer et al. 2002) to achieve a wavelength range $302 < \lambda < 8552$ Å. The continuum is well fitted by a broken power law ($F \propto \lambda^{\alpha_\lambda}$) with spectral indices $\alpha_\lambda = -0.24$ blueward of Lyα ($\lambda \lesssim 1200$ Å), $\alpha_\lambda = -1.56$ for $1200 < \lambda < 4850$ Å and $\alpha_\lambda = -0.42$ for $\lambda > 4850$ Å, see Fig. 3. Although the statistical uncertainties in the continuum fits are small, the quoted systematic uncertainties in the spectral indices are $\sigma_{\alpha_\lambda} \sim 0.10-0.15$.

3.2 Simulated quasar colours

The observed dust attenuated flux $F_{\rm obs}$ of an object at redshift $z_{\rm em}$ observed at wavelength $\lambda_{\rm obs}$ is given by

$$F_{\rm obs}(\lambda_{\rm obs}, z_{\rm em}) = F_{\rm em} \cdot {\rm e}^{-\tau_{\rm ext}(\lambda_{\rm obs}, z_{\rm em})}, \quad (7)$$

where $F_{\rm em}$ is the intrinsic flux and the optical depth to extinction $\tau_{\rm ext}$ can be calculated using equations (1) and (2) for graphite and silicate dust grains. The dimming (i.e. increase in apparent magnitude) of light emitted at redshift $z_{\rm em}$ observed at a wavelength $\lambda_{\rm obs}$ is then $\Delta m\,(\lambda_{\rm obs}, z_{\rm em}) = \frac{2.5}{\ln 10}\tau_{\rm ext}\,(\lambda_{\rm obs}, z_{\rm em})$. For each dust model we simulate the attenuation of the median QSO template spectrum and perform synthetic photometry using the SDSS *ugriz*-filter functions. For each pair of filters X and Y, we compare the simulated colours with observed colours,

$$\Delta(X-Y)_z \equiv (X-Y)_z^{\rm obs} - (X-Y)_z^{\rm sim}. \quad (8)$$

For each set of filters X and Y, we calculate the mean colour $(X-Y)_z^{\rm obs}$ in redshift bins of $\Delta z = 0.05$ in the redshift range $0.5 < z < 3$. At higher redshifts the flux decrement due to the Lyα break makes the bluer bands inefficient, so for the u and g band we only include QSOs with $z < 1.5$ and $z < 2.3$ respectively in the analysis.

The probabilities of different dust scenarios for each colour $X-Y$ are then calculated using

$$\chi^2(X-Y) = \sum_{i,j=1}^{N} \Delta(X-Y)_{z_i} V(X-Y)^{-1}_{j,i} \Delta(X-Y)_{z_j}, \quad (9)$$

where i and j index the N redshift bins. The covariance matrix $V(X-Y)_{i,j}$ is

$$V(X-Y)_{i,j} = \sigma(X-Y)^2_{\rm cal} + \sigma(X-Y)^2_{\rm temp} + \delta_{ij}\sigma(X-Y)^2_{\rm obs}. \quad (10)$$

The uncertainties in the photometric calibration $\sigma(X-Y)_{\rm cal} \lesssim 0.02$ and the typical observed colour variance in the QSO sample $\sigma(X-Y)^2_{\rm obs} \lesssim 0.003$ for redshifts $0.5 < z < 2.5$. The major source of uncertainty in this analysis is $\sigma(X-Y)_{\rm temp}$, due to the tilting of the spectral template according to the systematic uncertainties of the measured continuum spectral indices, $\sigma_{\alpha_\lambda} \approx 0.10$. In practice, we combine the results from all possible colour combinations taking into account the correlations between different colours and redshifts. This is accomplished using Monte Carlo simulations to create a total covariance matrix.

4 CONSTRAINTS FROM THE SOFT X-RAY BACKGROUND

4.1 The cosmic x-ray background

The cosmic X-ray background comprises the integrated emission of X-ray sources, primarily AGN, extended emission from galaxy clusters, faint starburst and 'normal' galaxies. Moretti et al. (2003) measure the total SXB in the 0.5–2 keV band to be $(7.53 \pm 0.35) \times 10^{-12}$ ergs s^{-1} cm^{-2} deg^{-2} and find that $94^{+7.0}_{-6.7}$ per cent of the SXB can be ascribed to discrete source emission, i.e. $\sim 6 \pm 6$ per cent of the SXB is unresolved. Similarly, Hickox & Markevitch (2007) find that the total SXB in the 1–2 keV band is $(4.6 \pm 0.3) \times 10^{-12}$ ergs s^{-1} cm^{-2} deg^{-2}. After excluding regions of radius $\lesssim$2–20 arcsec around detected X-ray, *HST* and *Spitzer* sources, they find a remaining unresolved SXB of $(3.4 \pm 1.4) \times 10^{-13}$ ergs s^{-1} cm^{-2} deg^{-2}, which is 7.3 ± 3.0 per cent of the total SXB.

4.2 AGN X-rays scattered by dust

AGN produce a dominant fraction ($\sim$80 per cent) of the SXB at energies $0.5 < E < 2.0$ keV. If dust pervades throughout the IGM, its scattering opacity would produce diffuse X-ray haloes around AGN. If the angular extent of these haloes are large enough, they will effectively contribute to the unresolved SXB. This fact, along with the observational upper limits on the unresolved SXB, allows us to constrain the amount and properties of intergalactic dust.

Dijkstra & Loeb (2009) argue that dust scattered X-ray haloes around AGN can maximally account for a fraction $f_{\rm halo} \sim$ 5–15 per cent of the SXB, allowing them to put upper limits on the opacity of intergalactic dust grains $\tau_{\rm dust}(z=1, \lambda = 8269\,\text{Å}) \lesssim 0.1 - 0.2(f_{\rm halo}/10\,\text{per cent})$, depending on grain size or size distribution.

In the spirit of this approach, we calculate the flux of X-ray photons observed in the soft X-ray energy range $E = 0.5$–$2.0\,\mathrm{keV}$, which is expected to be scattered into haloes,

$$F_{\rm halo} = \int_{0.5\,\rm kev}^{2.0\,\rm kev} S(E)\,\mathrm{d}E \int_0^\infty \mathcal{F}(z') \times \left[\mathrm{e}^{\tau_{\rm sca}(E,z')} - 1\right] \mathrm{d}z', \qquad (11)$$

where the optical depth to scattering $\tau_{\rm sca}$ is calculated using equations (1) and (2). We take the observed spectral energy density of the AGN to be given by $S(E) \propto E^{-1.4}$ normalized to unity over the energy range (the final results of the analysis depend only weakly on the choice of the spectral index, Moretti et al. 2003; Dijkstra & Loeb 2009) and

$$\mathcal{F}(z) = \frac{\mathcal{L}(z)}{(1+z)^2 \mathcal{E}(z)}. \qquad (12)$$

The comoving X-ray emissivity $\mathcal{L}(z)$ of AGN is expressed in terms of an integral over the AGN luminosity function

$$\mathcal{L}(z) = \int_{L_{\rm min}}^{L_{\rm max}} L \times \psi(L, z)\,\mathrm{d}\log L. \qquad (13)$$

The X-ray luminosity function $\psi(L, z)\,\mathrm{d}\log L$ is described by the fitting formula of Hopkins, Richards & Hernquist (2007) with $\log L_{\rm min} = 40.4$ and $\log L_{\rm max} = 48.0$. The total contribution to the SXB in the observed 0.5–2.0 keV band is obtained by integrating the X-ray emissivity of AGN over redshift, $F_{\rm AGN} = \int_0^\infty \mathcal{F}(z')\mathrm{d}z' = 5.74 \times 10^{-12}$ ergs s^{-1} cm^{-2} deg^{-2}.

In the following, we conservatively argue that the amount of flux from AGN being scattered far from the original line of sight, i.e. into an extended halo, $F_{\rm halo}$, will effectively be measured as a diffuse background and can thus not be larger than the measured value of the unresolved SXB, $F_{\rm uSXB}$.

When Hickox & Markevitch (2007) measure the unresolved part of the SXB, they exclude regions of radius $\theta < r_{90} = 2.2$ arcsec for *HST* and *Spitzer* sources undetected in X-rays and regions $\theta < 4$–$9r_{90}$ for X-ray detected sources. Dust grains having $a \gtrsim 2\,\mu$m will scatter X-rays into very compact haloes with angular sizes comparable to these excluded regions, thus contributing less flux to the unresolved SXB. While the scattering is dominated by the largest grains, inclusion of smaller grains would cause the halo flux to fall off less rapidly at large angles, and the resulted tail could contain a substantial flux which would effectively be considered as an unresolved background. We verify that a major fraction, $g(\theta > r)$, of the dust scattered halo flux falls outside these apertures (see Fig. 4) for dust models with single grain sizes or MRN grain size distributions, and will henceforth assume that similar exclusion regions apply to the SXB measurements of Moretti et al. (2003).

We calculate the probability of different dust scenarios using

$$\chi^2_{\rm SXB} = \frac{\left(F^{\rm obs}_{\rm uSXB} - F^{\rm mod}_{\rm halo}\right)^2}{\sigma^2_{\rm obs} + \sigma^2_{\rm mod}}, \qquad (14)$$

where $F^{\rm obs}_{\rm uSXB}$ is the unresolved SXB in the 0.5–2 keV band as calibrated by Moretti et al. (2003) and $F^{\rm mod}_{\rm halo} = F_{\rm halo} \cdot g(\theta > r)$ is the modelled halo flux falling outside an aperture of radius r. For values $F^{\rm mod}_{\rm halo} \le F^{\rm obs}_{\rm uSXB}$, we set the corresponding χ^2 value to zero. The model uncertainty will be negligible compared to the uncertainty of the unresolved SXB $\sigma_{\rm obs} = 4.52 \times 10^{-13}$ ergs s^{-1} cm^{-2} deg^{-2}.

5 RESULTS

We present our results from the combined analysis of QSO colours and the unresolved SXB together with the expected dimming in the rest-frame B and V band for a source at redshift $z = 1$, $A_B(z = 1)$ and $A_V(z = 1)$. We also express our constraints as upper limits on the density parameter, $\Omega_{\rm dust} = (n\frac{4\pi}{3}a^3\rho_{\rm grain})/\rho_{\rm crit}$, where $\rho_{\rm crit} = 1.88 \times 10^{-29}\,h^2$ g cm^{-3}.

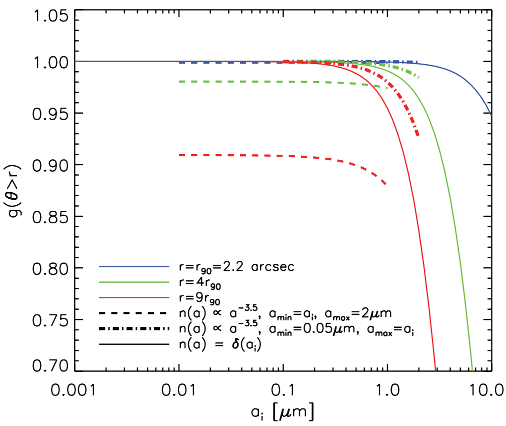

Figure 4. Fraction of halo flux falling outside an aperture of radius $r = r_{90} = 2.2$ arcsec (blue lines), $r = 4r_{90}$ (green lines), $r = 9r_{90}$ (red lines) calculated using equation (6) integrated over angles and an energy range between $E_{\rm min} = 0.5$ keV and $E_{\rm max} = 2.0$ keV assuming a spectral energy distribution, $S(E) \propto E^{-1}$. The solid lines show results for single grain sizes, the dashed lines show models with truncated MRN grain size distributions with $0.01 < a_{\rm min} < 1.0\,\mu$m and $a_{\rm max} = 2.0\,\mu$m and the dotted-dashed lines show models with truncated MRN grain size distributions with $a_{\rm min} = 0.05\,\mu$m and $0.1 < a_{\rm max} < 2.0\,\mu$m.

5.1 Dust models with single grain sizes

In Fig. 5, constraints from the QSO colour analysis for the single-size graphite dust model are shown. Regions (from yellow to red)

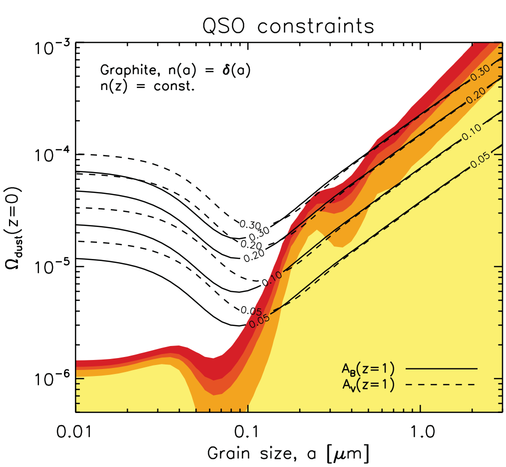

Figure 5. Constraints from the QSO colour analysis on dust models with single size graphite grains and a constant comoving number density. Regions (from yellow to red) indicate allowed-dust models at 68, 90, 95 and 99 per cent confidence levels. The black lines show the rest-frame B- and V-band extinction in magnitudes for a source at $z = 1$, $A_B(z = 1)$ and $A_V(z = 1)$.

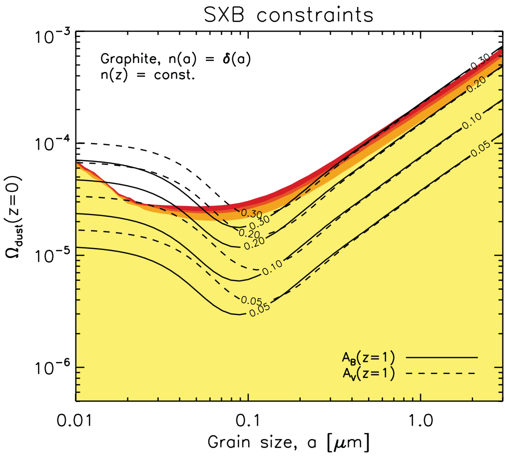

Figure 6. Constraints from the unresolved SXB on dust models with single size graphite grains and a constant comoving number density. Regions (from yellow to red) indicate alloweddust models at 68, 90, 95 and 99 per cent confidence levels. The black lines show the rest-frame B- and V-band extinction in magnitudes for a source at $z = 1$, $A_B(z = 1)$ and $A_V(z = 1)$.

indicate allowed dust models at 68, 90, 95 and 99 per cent confidence levels. The black lines show the rest-frame B and V band extinction in magnitudes for a source at $z = 1$, $A_B(z = 1)$ and $A_V(z = 1)$. Small size dust grains are more effectively constrained and the QSO colour analysis rules out any dimming $A_B(z = 1) \gtrsim 0.05$ mag for grains with $a \lesssim 0.2\,\mu$m. As is evident from Fig. 5, grains with radii $a \gtrsim 0.3\,\mu$m produce very little reddening for cosmological sources and $A_B(z = 1) \approx A_V(z = 1) \gtrsim 0.4$ mag can not be excluded.

Complementary to the QSO colour analysis, the SXB analysis (see Fig. 6) is most effective for grains with sizes $a \gtrsim 0.2\,\mu$m, since for these grain sizes the scattering cross-section for X-rays $\sigma_{\rm sca} \propto a^4$. Here, the unresolved SXB measurements constrain the rest-frame B-band extinction, $A_B(z = 1) \lesssim 0.25$ mag at the 99 per cent confidence level. Combined constraints are shown in Fig. 7. For a dust population of single-size silicate grains, results are both qualitatively and quantitatively similar as can be seen from the QSO and SXB combined constraints shown in Fig. 8.

Assuming that the IGM consists solely of dust grains smaller than $a \sim 0.2\,\mu$m with a constant comoving number density, we can constrain the dust density parameter $\Omega_{\rm dust} \lesssim 10^{-6}–10^{-5}(\rho_{\rm grain}/3\,{\rm g\,cm^{-3}})$, which is close to the astrophysically interesting levels implied by studies of stellar evolution and metallicity as a function of redshift. For grains larger than $a \sim 0.2\,\mu$m, the constraints on $\Omega_{\rm dust}$ are degenerate with a.

5.2 Dust models with continuous grain size distributions

Any realistic dust model will have a distribution of grain sizes. Here, we use an MRN model of separate populations of bare silicate and graphite grains with a power-law distribution of sizes where $dn/da \propto a^{-3.5}$.

First, we study the impact of the smallest grains in the MRN size distributions by varying $a_{\rm min}$ and keeping $a_{\rm max} = 2.0\,\mu$m. Figs 9 and 10 show the combined QSO and SXB constraints on silicate and graphite grains with MRN size distributions and a constant comoving number density. These dust models all have a reddening

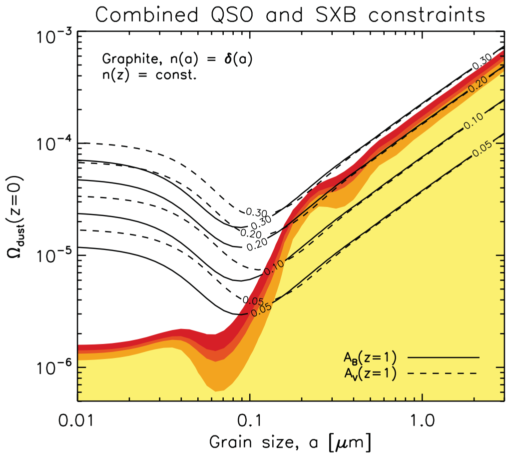

Figure 7. Combined constraints from the QSO colour analysis and the unresolved SXB on dust models with single-size silicate grains and a constant comoving number density. Regions (from yellow to red) indicate allowed dust models at 68, 90, 95 and 99 per cent confidence levels. The black lines show the rest-frame B- and V-band extinction in magnitudes for a source at $z = 1$, $A_B(z = 1)$ and $A_V(z = 1)$.

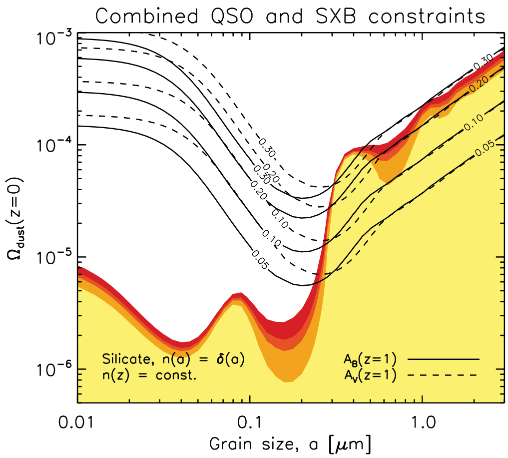

Figure 8. Combined constraints from the QSO colour analysis and the unresolved SXB on dust models with single size silicate grains and a comoving number density proportional to the integrated star formation rate. Regions (from yellow to red) indicate allowed dust models at 68, 90, 95 and 99 per cent confidence levels. The black lines show the rest-frame B- and V-band extinction in magnitudes for a source at $z = 1$, $A_B(z = 1)$ and $A_V(z = 1)$.

parameter $6 \lesssim R_V \lesssim \infty$, representing very grey dust. Allowing dust grains $a \lesssim 0.1\,\mu$m produces enough reddening at optical wavelengths that the QSO colours can limit the extinction in the B band, $A_B(z = 1) \lesssim 0.10$. For models with $a_{\rm min} \gtrsim 0.1–0.3\,\mu$m (completely grey dust) the SXB data help to limit the extinction in the B band to $A_B(z = 1) \lesssim 0.25$.

An interesting aspect of the MRN distribution is that the opacity is dominated by grains with small radii whereas the total dust mass

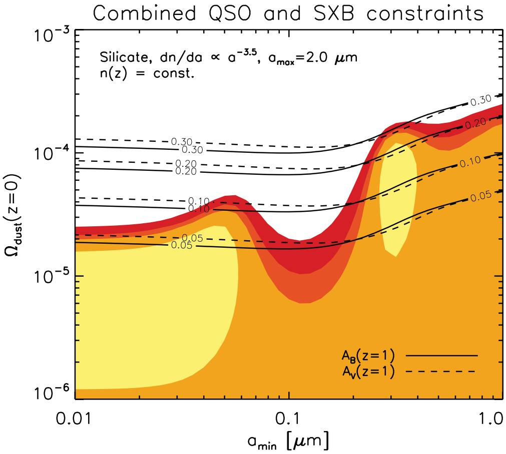

Figure 9. Combined constraints from the QSO colour analysis and the unresolved SXB on dust models with silicate grains with a truncated MRN distribution of $0.01 < a_{\rm min} < 1\,\mu$m and $a_{\rm max} = 2\,\mu$m and a constant comoving number density. Regions (from yellow to red) indicate allowed dust models at 68, 90, 95 and 99 per cent confidence levels. The black lines show the rest-frame *B*- and *V*-band extinction in magnitudes for a source at $z = 1$, $A_B(z = 1)$ and $A_V(z = 1)$.

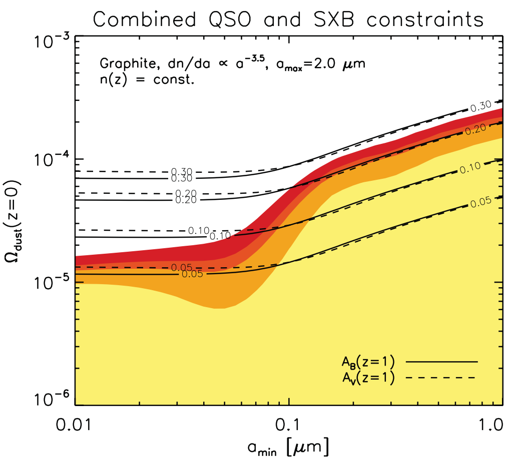

Figure 10. Combined constraints from the QSO colour analysis and the unresolved SXB on dust models with graphite grains with a truncated MRN distribution of $0.01 < a_{\rm min} < 1\,\mu$m and $a_{\rm max} = 2\,\mu$m and a constant comoving number density. Regions (from yellow to red) indicate allowed dust models at 68, 90, 95 and 99 per cent confidence levels. The black lines show the rest-frame *B*- and *V*-band extinction in magnitudes for a source at $z = 1$, $A_B(z = 1)$ and $A_V(z = 1)$.

is dominated by the grains with large radii. Thus, removing the very small grains can affect the opacity dramatically, without radically changing the total mass in dust. Therefore, for MRN distributions with $a_{\rm max} = 2.0\,\mu$m, the combined upper limits on the dust density are quite large, $\Omega_{\rm dust} \lesssim 10^{-5}$–$10^{-4}(\rho_{\rm grain}/3\,{\rm g\,cm^{-3}})$.

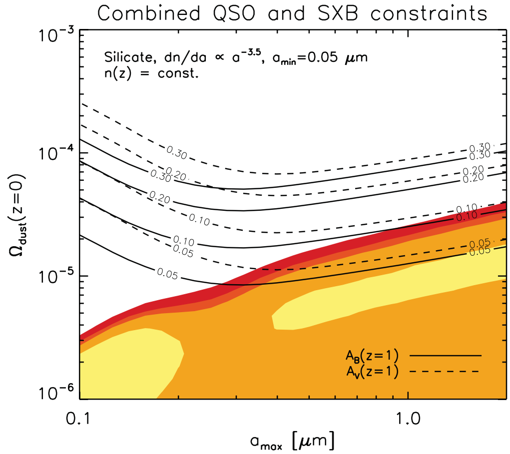

Figure 11. Combined constraints from QSO colour analysis and the unresolved SXB on dust models with silicate grains with a truncated MRN distribution of sizes $a_{\rm min} = 0.05\,\mu$m and $0.1 < a_{\rm max} < 2.0\,\mu$m and a constant comoving number density. Regions (from red to yellow) indicate allowed dust models at 68, 90, 95 and 99 per cent confidence levels. The black lines show the rest-frame *B*- and *V*-band extinction in magnitudes for a source at $z = 1$, $A_B(z = 1)$ and $A_V(z = 1)$.

To relate to the detection of dust reddening of QSOs out to large distances around $z \sim 0.3$ galaxies by Ménard et al. (2010), we focus on dust models with a reddening parameter close to their measured value of the reddening parameter, $R_V = 3.9 \pm 2.6$. Assuming a constant comoving dust density and extrapolating their result to $z = 1$ yields a lower limit on the extinction in the rest-frame *B* band of $A_B(z = 1) \gtrsim 0.02$ mag. If we keep $a_{\rm min}$ fixed at $0.05\,\mu$m (silicate grains, Fig. 11) or at $0.02\,\mu$m (graphite grains, Fig. 12) and vary the largest grain sizes $0.1 < a_{\rm max} < 2\,\mu$m, the dust models span a range of R_V between $\sim$1.3 and 7. For these dust models, the combined QSO colour and SXB analysis puts an upper limit on the extinction in the rest-frame *B* band, $A_B(z = 1) \lesssim 0.05$–0.10 mag, and correspondingly limits the dust density parameter $\Omega_{\rm dust} \lesssim 10^{-6}$–$10^{-5}(\rho_{\rm grain}/3\,{\rm g\,cm^{-3}})$.

6 SUMMARY AND DISCUSSION

In this paper, we studied the optical extinction and X-ray scattering effects of intergalactic dust grains. We find that dust distributions including graphite and silicate grains smaller than $a \lesssim 0.1$–$0.3\,\mu$m produce enough reddening ($1.3 \lesssim R_V \lesssim 10$) to rule out extinction in the rest-frame *B* band, $A_B(z = 1) \gtrsim 0.05$–0.10 mag. By combining the constraints from the QSO colour analysis with constraints from the unresolved SXB, we are able to rule out any systematic dimming in the rest-frame *B* band for a source at redshift $z = 1$ of $A_B(z = 1) \gtrsim 0.25$ mag for a wide range of grain sizes (and consequently a large range of reddening parameters, $1.3 \lesssim R_V \lesssim \infty$). These results have been derived assuming a constant comoving dust density. In the case when the comoving dust density is proportional to the integrated star formation rate density, $n(z) \propto \int_z^\infty {\rm d}z' \frac{\dot{\rho}_\star}{(1+z')\mathcal{E}(z')}$, the dust density decreases with redshift, making the universe increasingly transparent relative to the constant comoving dust density models. Results from these models are qualitatively similar to the models with constant comoving dust densities, except that the constraints

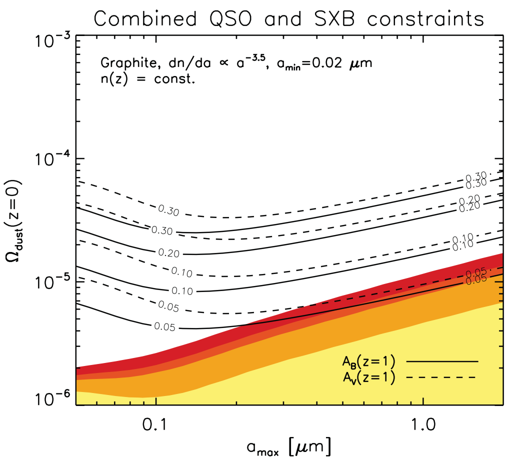

Figure 12. Combined constraints from QSO colour analysis and the unresolved SXB on dust models with graphite grains with a truncated MRN distribution of sizes $a_{\rm min} = 0.02$ µm and $0.1 < a_{\rm max} < 2.0$ µm and a constant comoving number density. Regions (from yellow to red) indicate allowed dust models at 68, 90, 95 and 99 per cent confidence levels. The black lines show the rest-frame *B*- and *V*-band extinction in magnitudes for a source at $z = 1$, $A_B(z = 1)$ and $A_V(z = 1)$.

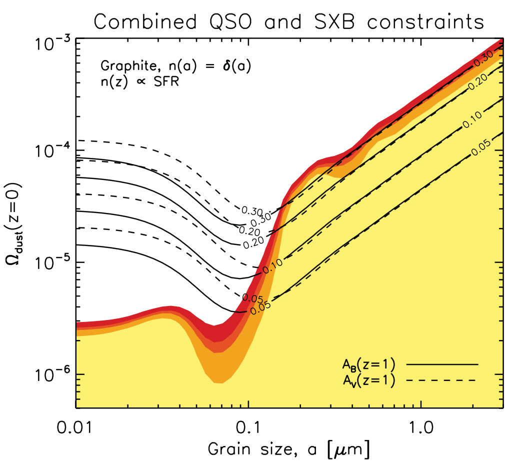

Figure 13. Combined constraints from the QSO colour analysis and the unresolved SXB on dust models with single size graphite grains and a comoving number density proportional to the integrated star formation rate. Regions (from yellow to red) indicate allowed dust models at 68, 90, 95 and 99 per cent confidence levels. The black lines show the rest-frame *B*- and *V*-band extinction in magnitudes for a source at $z = 1$, $A_B(z = 1)$ and $A_V(z = 1)$.

on the induced dimming for sources at redshift $z = 1$ (see Fig. 13) are somewhat weaker, excluding $A_B(z = 1) \gtrsim 0.05$ for small grains with $a \lesssim 0.1$ µm and $A_B(z = 1) \gtrsim 0.35$ mag for large grains with $a \gtrsim 0.2$ µm. However, for the same reasons, the upper limits on the dimming of sources at higher redshift ($z \gtrsim 2$) are stronger compared to the models with constant comoving dust density.

Since the error budget is dominated by systematic template uncertainties, the increase in the number of QSOs does not improve the limits from Mörtsell & Goobar (2003) and Östman & Mörtsell (2005), although the results are not directly comparable since the dust models probed are not equivalent. However, we regard the current error treatment as more realistic and also more effective in handling all possible colour combinations while accurately taking into account all possible colour and redshift correlations. In order to improve the current results from QSO colours (which are most effective in constraining the density of small size dust grains) it would be necessary to be able to decrease the systematic uncertainty of the continuum slope of the template spectrum. For larger dust grains, where the reddening effects are smaller and the dimming and density constraints from the unresolved SXB are weaker, limits could be improved by a better understanding of the different contributions to the unresolved SXB. Furthermore, improved constraints may be obtained by stacking observations of X-ray point sources. The absence of a single X-ray halo around a $z = 4.3$ QSO observed with *Chandra* allowed Petric et al. (2006) to place an upper limit on $\Omega_{\rm dust} \lesssim 2 \times 10^{-6}$ assuming a constant comoving number density of dust grains with a characteristic grain size $a \sim 1$ µm. This result is relaxed in Corrales & Paerels (2012), who find that $\Omega_{\rm dust} \lesssim 10^{-5}$ for a wider range of dust models. However, an increased number of sources will allow us either to measure or to improve the constraints on large dust grain densities, for which the corresponding limits on the dimming of cosmological sources are currently the weakest.

It should be noted that while smaller grains ($a \lesssim 0.05$ µm) may be either destroyed by sputtering or unable to travel far from formation sites as they are inefficiently pushed away by radiation pressure, large grains ($a \gtrsim 0.25$ µm) may be too heavy and remain trapped in the gravitational field of the galaxy where they formed (Aguirre 1999; Aguirre et al. 2001; Bianchi & Ferrara 2005). Combined with stellar evolution models (Fukugita 2011), the lower limits obtained in Ménard et al. (2010) and the upper limits derived in this paper, we conclude that an MRN dust distribution of either silicate or graphite grains – or possibly an admixture thereof – with $a_{\rm min} \sim 0.05$ µm and $a_{\rm max} \sim 0.25$ µm and $\Omega_{\rm dust} \sim$ a few $\times 10^{-6}(\rho_{\rm grain}/3\ {\rm g\,cm^{-3}})$, constitute a viable intergalactic dust model.

ACKNOWLEDGMENTS

We would like to thank Ariel Goobar, Rahman Amanullah, Linda Östman and Hugh Dickinson for useful discussions. We also wish to acknowledge the anonymous referee for helpful comments to the manuscript. EM acknowledge support for this study by the Swedish Research Council.

REFERENCES

Aguirre A., 1999, ApJ, 525, 583
Aguirre A., Haiman Z., 2000, ApJ, 532, 28
Aguirre A., Hernquist L., Schaye J., Katz N., Weinberg D. H., Gardner J., 2001, ApJ, 561, 521
Alcock C., Hatchett S., 1978, ApJ, 222, 456
Bianchi S., Ferrara A., 2005, MNRAS, 358, 379
Cardelli J. A., Clayton G. C., Mathis J. S., 1989, ApJ, 345, 245
Corasaniti P. S., 2007, New Astron. Rev., 51, 332
Corrales L., Paerels F., 2012, ApJ, 751, 93
Dijkstra M., Loeb A., 2009, MNRAS, 397, 1976
Draine B. T., 2003, ApJ, 598, 1026
Draine B. T., Lee H. M., 1984, ApJ, 285, 89
Evans A., Norwell G. A., Bode M. F., 1985, MNRAS, 213, 1P
Fitzpatrick E. L., 1999, PASP, 111, 63

Fukugita M., 2011, preprint (arXiv:1103.4191)
Goobar A., 2008, ApJ, 686, L103
Hauser M. G., Dwek E., 2001, ARA&A, 39, 249
Hayakawa S., 1970, Prog. Theor. Phys., 43, 1224
Henke B. L., Lee P., Tanaka T. J., Shimabukuro R. L., Fujikawa B. K., 1982, At. Data Nucl. Data Tables, 27, 1
Henke B. L., Gullikson E. M., Davis J. C., 1993, At. Data Nucl. Data Tables, 54, 181
Hernquist L., Springel V., 2003, MNRAS, 341, 1253
Hickox R. C., Markevitch M., 2007, ApJ, 661, L117
Hopkins P. F., Richards G. T., Hernquist L., 2007, ApJ, 654, 731
Inoue A. K., Kamaya H., 2004, MNRAS, 350, 729
Laor A., Draine B. T., 1993, ApJ, 402, 441
Loeb A., Haiman Z., 1997, ApJ, 490, 571
Mathis J. S., Lee C.-W., 1991, ApJ, 376, 490
Mathis J. S., Rumpl W., Nordsieck K. H., 1977, ApJ, 217, 425
Mauche C. W., Gorenstein P., 1986, ApJ, 302, 371
Ménard B., Scranton R., Fukugita M., Richards G., 2010, MNRAS, 405, 1025
Ménard B., Kilbinger M., Scranton R., 2010, MNRAS, 406, 1815
Miralda Escudé J., 1999, ApJ, 512, 21
Moretti A., Campana S., Lazzati D., Tagliaferri G., 2003, ApJ, 588, 696
Mörtsell E., Goobar A., 2003, J. Cosmol. Astropart. Phys., 9, 9
Östman L., Mörtsell E., 2005, J. Cosmol. Astropart. Phys., 2, 5
Östman L., Goobar A., Mörtsell E., 2006, A&A, 450, 971
Östman L., Goobar A., Mörtsell E., 2008, A&A, 485, 403
Petric A., Telis G. A., Paerels F., Helfand D. J., 2006, ApJ, 651, 41
Schlegel D. J., Finkbeiner D. P., Davis M., 1998, ApJ, 500, 525
Schneider D. P., Richards G. T., Hall P. B., Strauss M. A., Anderson S. F., Boroson T. A., 2010, AJ, 139, 2360
Smith R. K., Dwek E., 1998, ApJ, 503, 831
Telfer R. C., Zheng W., Kriss G. A., Davidsen A. F., 2002, ApJ, 565, 773
Vanden Berk D. E., Richards G. T., Bauer A., Strauss M. A., Schneider D. P., Heckman T. M., York D. G., 2001, AJ, 122, 549
Vaughan S. et al., 2006, ApJ, 639, 323
Weingartner J. C., Draine B. T., 2001, ApJ, 548, 296

This paper has been typeset from a TEX/LATEX file prepared by the author.

Paper II

J. Johansson, R. Amanullah and A. Goobar
Herschel limits on far-infrared emission from circumstellar dust around three nearby Type Ia supernovae
MNRAS, Vol. 431, L43-L47 (2013).

Monthly Notices of the ROYAL ASTRONOMICAL SOCIETY

MNRASL **431,** L43–L47 (2013)
Advance Access publication 2013 February 11

doi:10.1093/mnrasl/slt005

Herschel limits on far-infrared emission from circumstellar dust around three nearby Type Ia supernovae

J. Johansson,★ R. Amanullah and A. Goobar

Oskar Klein Centre, Stockholm University, SE 106 91 Stockholm, Sweden

Accepted 2013 January 9. Received 2013 January 9; in original form 2012 September 18

ABSTRACT

We report upper limits on dust emission at far-infrared (IR) wavelengths from three nearby Type Ia supernovae: SNe 2011by, 2011fe and 2012cg. Observations were carried out at 70 and 160 μm with the Photodetector Array Camera and Spectrometer onboard the *Herschel Space Observatory*. None of the supernovae were detected in the far-IR, allowing us to place upper limits on the amount of pre-existing dust in the circumstellar environment. Due to its proximity, SN 2011fe provides the tightest constraints, $M_{\rm dust} \lesssim 7 \times 10^{-3}\,{\rm M}_{\odot}$ at a 3σ level for dust temperatures $T_{\rm dust} \sim 500$ K assuming silicate or graphite dust grains of size $a = 0.1$ μm. For SNe 2011by and 2012cg the corresponding upper limits are less stringent, with $M_{\rm dust} \lesssim 10^{-1}\,{\rm M}_{\odot}$ for the same assumptions.

Key words: circumstellar matter – supernovae: general – supernovae: individual: SN 2011by – supernovae: individual: SN 2011fe – supernovae: individual: SN 2012cg – dust, extinction.

1 INTRODUCTION

The use of Type Ia supernovae (SNe Ia) as distance indicators remains essential for the study of the expansion history of the Universe and for explorations of the nature of dark energy (Goobar & Leibundgut 2011). However, a lack of understanding of the progenitor systems and the requirement for empirically derived colour–brightness corrections represent severe limitations for precision cosmology. Information about the progenitor systems of SNe Ia can be obtained by searching for evidence of circumstellar material (CSM) associated with mass-loss prior to the explosion. In the single-degenerate model, a white dwarf (WD) accretes mass from its hydrogen-rich companion star until it reaches a mass close to the Chandrasekhar mass, at which point carbon ignites, triggering a thermonuclear explosion. In the double-degenerate model, a supernova results from the merger of two WDs. Thus, the detection of CSM arising from the transfer of matter to the WD by its non-degenerate binary companion would be a direct confirmation of the single-degenerate scenario. Dust may also be created in the circumstellar (CS) environment before the explosion, which would have important implications for observed colours of SNe Ia. This second scenario is the focus of this Letter. The existence of CSM around nearby SNe Ia has been suggested by studies of sodium absorption lines (e.g. SNe 1999cl, 2006X and 2007le; Patat et al. 2007; Blondin et al. 2009; Simon et al. 2009; Sternberg et al. 2011). High-resolution spectra reveal the presence of time-variable and blueshifted Na I D features, possibly originating from CSM within the progenitor system. Studies of large samples of SNe Ia (Sternberg et al. 2011) find that half of all SNe Ia with detectable Na I D absorption at the host galaxy redshift have Na I D line profiles with significant blueshifted absorption relative to the strongest absorption component, which indicates that a large fraction of SN Ia progenitor systems have strong outflows. Foley et al. (2012) also find that SNe Ia with blueshifted CS/interstellar absorption systematically exhibit higher ejecta velocities and redder colours at maximum brightness relative to the rest of the SN Ia population.

Non-standard reddening has been noted in studies of individual and large samples of SNe Ia. For example, the colour excess indices of SN 2006X were studied in Folatelli et al. (2010), showing that the reddening is incompatible with the average extinction law of the Milky Way. Their findings augmented the large body of evidence indicating that the reddening of many SNe Ia show a steeper wavelength dependence ($R_V < 3.1$) than that which is typically observed for stars in our Galaxy. Previously, Nobili & Goobar (2008) derived $R_V = 1.75 \pm 0.27$ from a statistical study of 80 low-redshift SNe Ia. Similarly, when the colour–brightness relation is fitted jointly with cosmological parameters in the SNe Ia Hubble diagram, using a wide range of SNe Ia redshifts, low values of R_V are obtained (see e.g. Suzuki et al. 2012 for a recent compilation).

Wang (2005) and Goobar (2008) showed that multiple scattering on CS dust could potentially help to explain the low values of $R_V \sim 1.5$–2.5 observed in the sight lines of nearby SNe Ia. Amanullah & Goobar (2011) simulated the impact of thin CS dust shells located at radii $r_{\rm d} \sim 10^{16}$–10^{19} cm ($\sim$0.003–3 pc) from the SN, containing masses $M_{\rm dust} \sim 10^{-4}\,{\rm M}_{\odot}$, and find that this scenario would also perturb the optical light-curve shapes and introduce 'intrinsic' colour variations $\sigma_{E(B-V)} \sim 0.05$–$0.1$.

★E-mail: joeljo@fysik.su.se

Thermal emission at infrared (IR) wavelengths could be the 'smoking gun' for the presence of CS dust. Pre-existing CS dust may be radiatively heated by absorption of UV/optical photons from the SN or collisionally heated by the SN shock. New dust grains could also be formed in SN Ia ejecta. Nozawa et al. (2011) model this process, and find that up to 0.2 $M_{\odot}$ of dust could condense ∼100–300 d after the explosion.

Gerardy et al. (2007) observed two normal SNe Ia (SNe 2003hv and 2005df) at late phases (∼100–400 d after explosion) with the *Spitzer Space Telescope* in the 3.6–22 μm wavelength range. The mid-IR spectral energy distributions (SEDs) and photometry are compatible with strong atomic line emission from the SN, and therefore exhibit no compelling indication of pre-existing or newly formed dust. Nozawa et al. (2011) compare their models with the Gerardy et al. (2007) photometry and derive an upper limit of 0.075 $M_{\odot}$ of newly formed silicate dust. Furthermore, Gomez et al. (2012) studied the Kepler and Tycho supernova remnants (thought to be remnants of SNe Ia that exploded ∼400 yr ago) using observations in the 24–850 μm range and reported the detection of ~ 3–9×10^{-3} $M_{\odot}$ of warm dust (∼90 K). Their findings are consistent with the warm dust originating in the CS (Kepler) and interstellar (Tycho) material swept up by the primary blast wave of the remnant.

In this Letter, we present the earliest far-IR measurements of SNe Ia, within 45 d after explosion, using the *Herschel Space Observatory* (Pilbratt et al. 2010) from 70 to 160 μm. We also derive limits on pre-existing dust in the CS environment of the three observed SNe.

2 TARGETS AND OBSERVATIONS

Thermal emission from heated pre-existing CS dust would be difficult to detect in the near-IR (NIR), except for large masses and high temperatures, but could be detected at mid-IR wavelengths, e.g. with *Spitzer*. However, the degeneracy with the photospheric emission around 5 μm makes it challenging to discriminate between emission by dust and intrinsic light from the SN. Conversely, observations at longer wavelengths (beyond 10 μm) would be dominated by radiating dust, which motivates the use of *Herschel* observations for this study.[1]

To investigate the presence of CS dust shells, the observations were carried out within 45 d from the SN explosion in order to minimize the risk of confusion with any newly formed dust produced in the SN ejecta (as seen in core-collapse SNe; Kotak et al. 2009).

Another factor is the duration of the IR echo, which is expected to scale with the radius of the CS dust shell, $t_{\rm echo} \sim 2r_{\rm d}/c$. For a geometrically thin, spherically symmetric shell, the fraction of emitting dust mass perceived by the observer increases with time, reaching maximum at $t = t_{\rm echo}$.

For shell radii, $r_{\rm d} \sim 10^{16}$ cm, the IR echo would be too short to be captured by our observations. However, in such a scenario, the CS dust would have been heated to high enough temperatures for its NIR emission to dramatically change the early part of the observed light curves. For dust at radii $r_{\rm d} \sim 10^{17}$ cm, the IR echo ($t_{\rm echo}$ = 3–4 months) is partially within our observing window. Thus, although our observational strategy may miss the IR echo maximum, it nonetheless represents a reasonable compromise for exploring possible pre-existing CS dust shells.

[1] At the time our targets were observed, only the *Spitzer* 3.6 and 4.5 μm bands were operational.

In this study, we targeted three SNe Ia: SNe 2011by, 2011fe and 2012cg, selected based on their close proximity. Only one of these three SNe showed significant reddening at optical wavelengths (SN 2012cg), thus making a detection at far-IR wavelengths more challenging for the remaining two.

2.1 Herschel PACS data

The observations of SNe 2011by, 2011fe and 2012cg were obtained using the Photodetector Array Camera and Spectrometer (PACS; Poglitsch et al. 2010) onboard *Herschel*. The mini scan-map observing mode was used with a scan speed of 20 arcsec s^{-1}, resulting in a final map of 3 arcmin × 7 arcmin with a homogeneous coverage in the central region (about 50 arcsec in diameter). The full width at half-maximum (FWHM) of the point spread function (PSF) at 70 and 160 μm are 6 and 12 arcsec, respectively. The flux calibration uncertainty for the PACS 70 and 160 μm bands are currently estimated to be smaller than 5 per cent.[2] The colour corrections to the modelled dust emission spectra for the PACS 70 and 160 μm bands are negligible (maximally ∼5 per cent).

The data reduction was performed up to level2 using the Herschel Interactive Processing Environment (Ott 2010). Each target was observed for 4 h, with simultaneous imaging in the 70 and 160 μm bands resulting in unconfused 5σ point source flux limits of approximately 5 and 10 mJy, respectively.

In addition to our observations, we also include analysis of archival data of the host galaxies of SNe 2011fe (M101 observed as part of the KINGFISH survey; Kennicutt et al. 2011) and 2012cg (NGC 4424 observed as part of the HeVICS survey; Davies et al. 2012). These observations were carried out in the large scan mode, with a medium scan map rate of 20 arcsec s^{-1} resulting in maps with a 3.2 arcsec pixel^{-1} resolution and an unconfused 5σ point source flux limit of approximately 25 mJy in the 70 μm band.

Photometry was performed by using a set of single apertures (with radii defined by the FWHM of the PSF) to estimate the far-IR flux at the SN positions; apertures were also used to determine the average sky background level on the map, and the background fluxes in the vicinity of the SN.

2.2 SN 2011by

SN 2011by was discovered 2011/04/26.823 by Zhangwei Jin and Xing Gao at RA = 11:55:45.56, Dec. = +55:19:33.8 at a location 5.3 arcsec east and 191 arcsec north of the centre of the barred spiral galaxy NGC 3972 ($D = 18.5 \pm 0.8$ Mpc; Tully et al. 2009). The SN reached a peak *B*-band magnitude of ∼13 on around May 9 with a colour excess of $E(B-V) \approx 0.08$ mag (Maguire et al. 2012).

Our PACS 70 μm observations from 2011 May 24 (about two weeks after *B*-band maximum) are shown in Fig. 1. The SN exploded in a region of significant host galaxy background emission. To derive upper limits on possible emission from pre-existing CS dust, we compare the flux at the SN position with the estimated host galaxy background flux in the vicinity (Table 1). The galactic emission was estimated by placing apertures along isoflux contours. We measure no significant excess far-IR emission (3.7 ± 1.5 mJy at 70 μm) with respect to the estimated host galaxy background at the location of SN 2011by.

[2] PACS Observer's Manual, section 3.3.

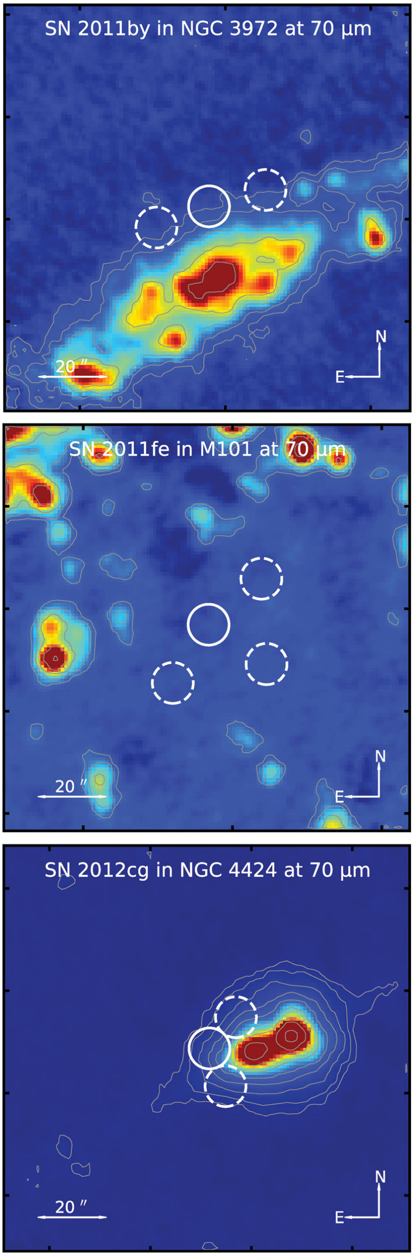

Figure 1. *Herschel* PACS 70 µm observations of SNe 2011by (top panel), 2011fe (middle panel) and 2012cg (bottom panel). The solid circles indicate the position of the supernovae and the FWHM of the PSF (6 arcsec). The dashed circles show the apertures used for background estimation.

Table 1. Photometry of SNe 2011by, 2011fe and 2012cg.

Target	Host galaxy	Days from $B_{\max}$	$F_\nu^{70\,\mu\mathrm{m}}$ (mJy)	$F_\nu^{160\,\mu\mathrm{m}}$ (mJy)
SN 2011by	NGC 3972	+15	3.7 ± 1.5	16 ± 8
	M101[a]	−451	-4.7 ± 6.2	–
SN 2011fe	M101	+23	-1.5 ± 1.6	-16 ± 10
	NGC 4424[b]	−314	-15 ± 5	–
SN 2012cg	NGC 4424	+9	-0.7 ± 1.8	-23 ± 8

Data from [a]Kennicutt et al. (2011) and [b]Davies et al. (2012).

2.3 SN 2011fe

SN 2011fe was discovered 2011/08/24.000 by the Palomar Transient Factory at RA = 14:03:05.81, Dec. = +54:16:25.4 (J2000) at a location 58.6 arcsec west and 270.7 arcsec south of the centre of the nearby spiral galaxy M101 ($D = 6.4 \pm 0.5$ Mpc; Shappee & Stanek 2011). The SN reached a peak *B*-band magnitude of ∼10 on around September 10 (Matheson et al. 2012). The Galactic and host galaxy reddening, deduced from the integrated equivalent widths of the Na I D lines are $E(B-V)_{\mathrm{MW}} = 0.011 \pm 0.002$ and $E(B-V)_{\mathrm{host}} = 0.014 \pm 0.002$ mag, respectively (Patat et al. 2013).

By analysing pre-explosion *Hubble Space Telescope* and *Spitzer* images, Li et al. (2011) and Nugent et al. (2011) are able to rule out red giants and a majority of helium stars as the mass donating companion to the exploding WD. Early phase radio and X-ray observations (Chomiuk et al. 2012; Horesh et al. 2012; Margutti et al. 2012) report non-detections, yielding constraints on the pre-explosion mass-loss rate from the progenitor system $\dot{M} \lesssim 6 \times 10^{-10}$–$10^{-8}(v_{\mathrm{wind}}/100\,\mathrm{km\,s^{-1}})\,\mathrm{M_\odot\,yr^{-1}}$. Although they are model dependent, these limits rule out a large portion of the parameter space of single-degenerate progenitor models for SN 2011fe. The absence of time-variant, blueshifted absorption features also rules out the presence of substantial amounts of CSM (Patat et al. 2013). In summary, previous observations are consistent with the progenitor of SN 2011fe being a binary system with a main-sequence or a degenerate companion star.

Our *Herschel* PACS 70 µm data from 2011 October 02 (about 33 d after *B*-band maximum) are shown in Fig. 1. SN 2011fe is located in a region with low host galaxy background emission. No excess far-IR emission is detected at the position of SN 2011fe (-1.5 ± 1.5 mJy at 70 µm). We also analysed archival data to obtain the far-IR flux before the explosion (described in Section 2.1, Table 1). The measured background subtracted flux at the SN position is -4.7 ± 6.2 mJy. There is no significant far-IR source evident at the location of the SN before or after the explosion.

2.4 SN 2012cg

SN 2012cg was discovered 2012/05/15.790 by the Lick Observatory Supernova Search at RA = 12:27:12.83, Dec. = +09:25:13.2 (J2000) at a location 17.3 arcsec east and 1.5 arcsec south of the peculiar SBa galaxy NGC 4424 ($D = 15.2 \pm 1.9$ Mpc, Cortés, Kenney & Hardy 2008). SN 2012cg reached a peak *B*-band magnitude of 12.1 on 2012 June 2. The SN show signs of host galaxy reddening, with a colour excess of $E(B-V) \approx 0.2$ mag derived from both optical photometry and high-resolution spectroscopy (Marion et al. 2012; Silverman et al. 2012).

Our *Herschel* PACS 70 µm data from 2012 June 11 (about 9 d after *B*-band maximum) are shown in Fig. 1. SN 2012cg is located in a region of significant host galaxy far-IR emission. We derive upper limits on possible emission from pre-existing CS dust (Table 1) in a similar manner to SN 2011by, by comparing the flux at the SN position with the host galaxy background flux in the vicinity. We measure no excess far-IR emission (-0.7 ± 1.8 mJy at 70 µm) with respect to the estimated host galaxy background at the location of SN 2012cg.

In addition, we also analyse pre-explosion archival PACS 70 µm data (described in Section 2.1). The background-subtracted flux at the SN location is -15 ± 5 mJy. There is no significant far-IR source evident at the location of the SN before or after the explosion.

3 UPPER LIMITS FROM DUST MODELS

To model the far-IR emission from pre-existing CS dust, we consider the idealized case (described in Hildebrand 1983; Fox et al. 2010) of an optically thin dust cloud of mass $M_{\rm d}$ with dust particles of radius a, emitting thermally at a single equilibrium temperature $T_{\rm d}$. The expected flux at a distance D is

$$F_\nu = M_{\rm d}\frac{\kappa_\nu(a)B_\nu(T_{\rm d})}{D^2}, \qquad (1)$$

where $B_\nu(T_{\rm d})$ is the Planck blackbody function and the dust mass emissivity coefficient $\kappa_\nu(a)$ is

$$\kappa_\nu(a) = \left(\frac{3}{4\pi\rho a^3}\right)\pi a^2 Q_\nu(a) = \frac{3Q_\nu(a)}{4a\rho}. \qquad (2)$$

$Q_\nu(a)$ is the absorption efficiency and the dust bulk (volume) density, $\rho \approx 2$–$3\,{\rm g\,cm^{-3}}$ depending on grain composition. The expected emission depends on the choice of dust grain composition and size. Interstellar dust is well described by a mixture of silicate and graphitic grains of different sizes, and generally in the far-IR $\kappa \propto \lambda^{-\beta}$ with $\beta \sim 1$–2 and $\kappa \approx 67.0\,{\rm cm^2\,g^{-1}}$ at 70 µm (Draine & Li 2001). However, CS dust around SNe may well be dominated by either silicate or graphitic grains depending on the stellar atmosphere of the involved stars. Since we do not know the nature of the SNe Ia progenitor systems and their potential dust production mechanisms, we will consider separate scenarios of either silicate or graphite grains of radius $a = 0.1$ µm (described in Draine & Lee 1984; Laor & Draine 1993; Weingartner & Draine 2001).

From the non-detections of the SNe in the PACS 70 and 160 µm passbands we calculate upper limits on the CS dust mass surrounding SNe 2011by, 2011fe and 2012cg.

Fig. 2 shows the excluded dust mass range as a function of temperature for the three SNe, irrespective of heating mechanism. The upper limit on the dust temperature, set by the evaporation temperature of the dust grains ($T \lesssim 2000$ K), corresponds to a minimal dust survival radius $r_{\rm evap} \sim 10^{16}$ cm (Amanullah & Goobar 2011). Detections of CSM around SNe Ia have been claimed at somewhat larger distances, $r_{\rm CSM} \sim 10^{17}$ cm (e.g. Patat et al. 2007). To derive an estimate of the expected temperature of CS dust at similar radii, $r_{\rm d} \sim 10^{17}$ cm, we follow the simple IR echo model in Fox et al. (2010) (see their fig. 8b). For a typical peak SN bolometric luminosity of $\sim 10^9\,{\rm L_\odot}$, radiatively heating a pre-existing dust shell of radius $r_{\rm d} \sim 10^{17}$ cm, graphitic dust grains of $a = 0.1$ µm will be heated to $T_{\rm d} \sim 500$ K (silicate grains would be heated to even higher temperatures).

In what follows, we use $T_{\rm d} \sim 500$ K as a point of reference (marked by the dotted line in Fig. 2). The expected dust SED for this specific temperature is shown in Fig. 3, along with the sensitivity of current and future mid- and far-IR facilities.

Due to its proximity, SN 2011fe yields the tightest constraints, $M_{\rm d} \lesssim 7 \times 10^{-3}\,{\rm M_\odot}$ at a 3σ level, assuming graphitic dust grains of size $a = 0.1$ µm heated to temperatures $T_{\rm d} \sim 500$ K (red solid line in Fig. 2). For silicate dust grains, the corresponding upper limit is $M_{\rm d} \lesssim 10^{-2}\,{\rm M_\odot}$ (red dashed line in Fig. 2). The upper limits for SN 2011by are weaker, $M_{\rm d} \lesssim 10^{-1}\,{\rm M_\odot}$ at a 3σ level for similar assumptions (blue solid and dashed lines for graphitic and silicate dust grains in Fig. 2). For SN 2012cg, the upper limits are $M_{\rm d} \lesssim 8 \times 10^{-2}\,{\rm M_\odot}$ at a 3σ level for assuming graphitic dust grains of size $a = 0.1$ µm heated to temperatures $T_{\rm d} \sim 500$ K (green solid line in Fig. 2).

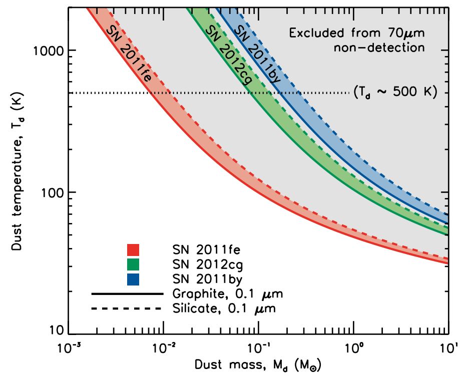

Figure 2. 3σ upper limits on the CS dust mass and temperature, assuming graphitic (solid lines) or silicate (dashed lines) dust grains of size $a = 0.1$ µm, derived from the non-detection in the *Herschel* PACS 70 µm observations of SNe 2011by (blue lines), 2011fe (red lines) and 2012cg (green lines). The horizontal dotted line indicates the expected temperature $T_{\rm d} \sim 500$ K for a pre-existing dust shell of radius $r_{\rm d} \sim 10^{17}$ cm.

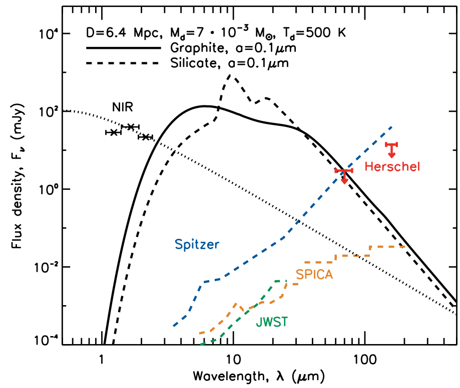

Figure 3. Example of expected IR SEDs of CS dust, assuming a distance of 6.4 Mpc, $M_{\rm d} = 7 \times 10^{-3}\,{\rm M_\odot}$ and $T_{\rm d} = 500$ K with graphitic (solid black line) or silicate (dashed black line) dust grains of size $a = 0.1$ µm. The dotted black line shows a blackbody spectrum at 10^4 K, scaled to match the NIR fluxes of SN 2011fe 33 d after maximum brightness (Matheson et al. 2012). For comparison, the 5σ detection limits of 3 h observations with *Spitzer* (blue dashed line), the *James Webb Space Telescope* (green dashed line) and *SPICA* (orange dashed line) are included. The red symbols indicate the 3σ upper limits on the flux of SN 2011fe in the PACS 70 and 160 µm bands (described in Section 2.3).

4 SUMMARY AND CONCLUSIONS

Searches for evidence of CSM around SNe Ia are an important aspect in the efforts to understand the exact nature of these explosions and their use as accurate distance estimators. For the latter, the presence of pre-explosion CS dust could explain the empirically derived, non-standard reddening corrections that are applied to minimize the scatter in the SNe Ia Hubble diagram (Goobar 2008).

In this work, we searched for far-IR emission from pre-existing CS dust around three nearby SNe Ia *within* a few weeks after maximum brightness. By considering the *Herschel* non-detections, we can exclude dust masses $M_{\rm d} \gtrsim 7 \times 10^{-3}\,{\rm M}_{\odot}$ for dust temperatures $T_{\rm d} \sim 500$ K at a 3σ level for SN 2011fe, and the upper limits are one order of magnitude weaker for SNe 2011by and 2012cg, excluding dust masses $M_{\rm d} \gtrsim 10^{-1}\,{\rm M}_{\odot}$.

Although these are the strictest upper limits on CS dust around newly exploded SNe Ia, our limits cannot completely rule out the presence of CS dust as a contributing source to SN Ia reddening. Our sensitivity for CS dust masses ($M_{\rm d} \sim 10^{-3}$–$10^{-2}\,{\rm M}_{\odot}$) is about one–two order of magnitudes larger than the dust masses that have been suggested in simulations ($M_{\rm d} \sim 10^{-4}\,{\rm M}_{\odot}$ in Amanullah & Goobar 2011).

While current instrumentation allows mainly for exploration of CS dust around SNe within the very local universe ($D \lesssim 5$ Mpc), future missions such as *JWST* and *SPICA*, will have the potential to dramatically improve the sensitivity, as shown in Fig. 3.

ACKNOWLEDGEMENTS

The authors are grateful to the anonymous referee for useful comments that have significantly improved the Letter. We also thank Hugh Dickinson, Ori Fox and Edvard Mörtsell for useful discussions and comments. RA would like to thank the Swedish National Space Board for financial support. AG acknowledges support from the Swedish National Research Council.

REFERENCES

Amanullah R., Goobar A., 2011, ApJ, 735, 20
Blondin S., Prieto J. L., Patat F., Challis P., Hicken M., Kirshner R. P., Matheson T., Modjaz M., 2009, ApJ, 693, 207
Chomiuk L. et al., 2012, ApJ, 750, 164
Cortés J. R., Kenney J. D. P., Hardy E., 2008, ApJ, 683, 78
Davies J. I. et al., 2012, MNRAS, 419, 3505
Draine B. T., Lee H. M., 1984, ApJ, 285, 89
Draine B. T., Li A., 2001, ApJ, 551, 807
Folatelli G. et al., 2010, AJ, 139, 120
Foley R. J. et al., 2012, ApJ, 752, 101
Fox O. D., Chevalier R. A., Dwek E., Skrutskie M. F., Sugerman B. E. K., Leisenring J. M., 2010, ApJ, 725, 1768
Gerardy C. L. et al., 2007, ApJ, 661, 995
Gomez H. L. et al., 2012, MNRAS, 420, 3557
Goobar A., 2008, ApJ, 686, L103
Goobar A., Leibundgut B., 2011, Annu. Rev. Nucl. Part. Sci., 61, 251
Hildebrand R. H., 1983, QJRAS, 24, 267
Horesh A. et al., 2012, ApJ, 746, 21
Kennicutt R. C. et al., 2011, PASP, 123, 1347
Kotak R. et al., 2009, ApJ, 704, 306
Laor A., Draine B. T., 1993, ApJ, 402, 441
Li W. et al., 2011, Nat, 480, 348
Maguire K. et al., 2012, MNRAS, 426, 2359
Margutti R. et al., 2012, ApJ, 751, 134
Marion G. H. et al., 2012, Astron. Telegram, 4159, 1
Matheson T. et al., 2012, ApJ, 754, 19
Nobili S., Goobar A., 2008, A&A, 487, 19
Nozawa T., Maeda K., Kozasa T., Tanaka M., Nomoto K., Umeda H., 2011, ApJ, 736, 45
Nugent P. E. et al., 2011, Nat, 480, 344
Ott S., 2010, in Mizumoto Y., Morita K.-I., Ohishi M., eds, ASP Conf. Ser. Vol. 434, Astronomical Data Analysis Software and Systems XI. Astron. Soc. Pac., San Francisco, p. 139
Patat F. et al., 2007, Sci, 317, 924
Patat F. et al., 2013, A&A, 549, A62
Pilbratt G. L. et al., 2010, A&A, 518, L1
Poglitsch A. et al., 2010, A&A, 518, L2
Shappee B. J., Stanek K. Z., 2011, ApJ, 733, 124
Silverman J. M. et al., 2012, ApJ, 756, L7
Simon J. D. et al., 2009, ApJ, 702, 1157
Sternberg A. et al., 2011, Sci, 333, 856
Suzuki N. et al., 2012, ApJ, 746, 85
Tully R. B., Rizzi L., Shaya E. J., Courtois H. M., Makarov D. I., Jacobs B. A., 2009, AJ, 138, 323
Wang L., 2005, ApJ, 635, L33
Weingartner J. C., Draine B. T., 2001, ApJ, 548, 296

This paper has been typeset from a TEX/LATEX file prepared by the author.

Paper III

A. Goobar, **J. Johansson**, R. Amanullah, Y. Cao, D. A. Perley, M. M. Kasliwal, R. Ferretti, P. E. Nugent, C. Harris, A. Gal-Yam, E. O. Ofek, S. P. Tendulkar, M. Dennefeld, S. Valenti, I. Arcavi, D. P. K. Banerjee, V. Venkataraman, V. Joshi, N. M. Ashok, S. B. Cenko, R. F. Diaz, C. Fremling, A. Horesh, D. A. Howell, S. R. Kulkarni, S. Papadogiannakis, T. Petrushevska, D. Sand, J. Sollerman, V. Stanishev, J. S. Bloom, J. Surace, T. J. Dupuy, M. C. Liu

The Rise of SN 2014J in the Nearby Galaxy M 82

ApJL, Vol. 784, L12 (2014).

The Astrophysical Journal Letters, 784:L12 (6pp), 2014 March 20 doi:10.1088/2041-8205/784/1/L12

THE RISE OF SN 2014J IN THE NEARBY GALAXY M82

A. Goobar[1], J. Johansson[1], R. Amanullah[1], Y. Cao[2], D. A. Perley[2,21], M. M. Kasliwal[3], R. Ferretti[1], P. E. Nugent[4,5], C. Harris[4,5], A. Gal-Yam[6], E. O. Ofek[6], S. P. Tendulkar[2], M. Dennefeld[7], S. Valenti[8,9], I. Arcavi[8,10], D. P. K. Banerjee[11], V. Venkataraman[11], V. Joshi[11], N. M. Ashok[11], S. B. Cenko[12,13], R. F. Diaz[14], C. Fremling[15], A. Horesh[6], D. A. Howell[8,9], S. R. Kulkarni[2], S. Papadogiannakis[1], T. Petrushevska[1], D. Sand[16], J. Sollerman[15], V. Stanishev[17], J. S. Bloom[5], J. Surace[18], T. J. Dupuy[19], and M. C. Liu[20]

[1] The Oskar Klein Centre, Physics Department, Stockholm University, Albanova University Center, SE 106 91 Stockholm, Sweden; ariel@fysik.su.se
[2] Cahill Center for Astrophysics, California Institute of Technology, Pasadena, CA 91125, USA
[3] Observatories of the Carnegie Institution for Science, 813 Santa Barbara Street, Pasadena, CA 91101, USA
[4] Computational Cosmology Center, Computational Research Division, Lawrence Berkeley National Laboratory, 1 Cyclotron Road, MS 50B-4206, Berkeley, CA 94720, USA
[5] Department of Astronomy, University of California Berkeley, B-20 Hearst Field Annex # 3411, Berkeley, CA 94720-3411, USA
[6] Department of Particle Physics and Astrophysics, Weizmann Institute of Science, Rehovot 76100, Israel
[7] CNRS, Institut d'Astrophysique de Paris (IAP) and University P. et M. Curie (Paris 6), 98bis Boulevard Arago, F-75014 Paris, France
[8] Las Cumbres Observatory Global Telescope Network, 6740 Corona Drive, Suite 102, Goleta, CA 93117, USA
[9] Department of Physics, University of California, Santa Barbara, Broida Hall, Mail Code 9530, Santa Barbara, CA 93106-9530, USA
[10] Kavli Institute for Theoretical Physics, University of California, Santa Barbara, CA 93106, USA
[11] Physical Research Laboratory, Ahmedabad 380 009, India
[12] Astrophysics Science Division, NASA Goddard Space Flight Center, Mail Code 661, Greenbelt, MD 20771, USA
[13] Joint Space Science Institute, University of Maryland, College Park, MD 20742, USA
[14] Observatory of Geneva, University of Geneva 51 Chemin des Maillettes, 1290 Sauverny, Switzerland
[15] The Oskar Klein Centre, Astronomy Department, Stockholm University, Albanova University Center, SE 106 91 Stockholm, Sweden
[16] Physics Department, Texas Tech University, Lubbock, TX 79409, USA
[17] CENTRA-Centro Multidisciplinar de Astrofísica, IST, Avenida Rovisco Pais, 1049-001 Lisboa, Portugal
[18] Infrared Processing and Analysis Center, California Institute of Technology, Pasadena, CA 91125, USA
[19] Harvard-Smithsonian Center for Astrophysics, 60 Garden Street, Cambridge, MA 02138, USA
[20] Institute for Astronomy, University of Hawaii, 2680 Woodlawn Drive, Honolulu, HI 96822, USA
Received 2014 February 7; accepted 2014 February 21; published 2014 March 7

ABSTRACT

We report on the discovery of SN 2014J in the nearby galaxy M82. Given its proximity, it offers the best opportunity to date to study a thermonuclear supernova (SN) over a wide range of the electromagnetic spectrum. Optical, near-IR, and mid-IR observations on the rising light curve, orchestrated by the intermediate Palomar Transient Factory, show that SN 2014J is a spectroscopically normal Type Ia supernova (SN Ia), albeit exhibiting high-velocity features in its spectrum and heavily reddened by dust in the host galaxy. Our earliest detections start just hours after the fitted time of explosion. We use high-resolution optical spectroscopy to analyze the dense intervening material and do not detect any evolution in the resolved absorption features during the light curve rise. Similar to other highly reddened SNe Ia, a low value of total-to-selective extinction, $R_V \lesssim 2$, provides the best match to our observations. We also study pre-explosion optical and near-IR images from *Hubble Space Telescope* with special emphasis on the sources nearest to the SN location.

Key words: dust, extinction – galaxies: individual (Messier 82) – supernovae: individual (SN 2014J)

1. INTRODUCTION

Type Ia supernovae (SNe Ia) are among the most luminous transient events at optical wavelengths and extremely valuable tools to measure cosmological distances; see Goobar & Leibundgut (2011) for a recent review. Yet, SNe Ia close enough to allow for detailed scrutiny of their physical properties are very rare, especially in a galaxy like M82, the host of several recent core-collapse SNe (Mattila et al. 2013; Gendre et al. 2013). At an estimated distance to M82 of 3.5 Mpc (Dalcanton et al. 2009), SN 2014J is the closest identified SN Ia in several decades, possibly rivaled by SN 1972E in NGC 5253 (Ardeberg & de Groot 1973) and SN 1986G in NGC 5128 (Phillips et al. 1987). Thus, SN 2014J is exceptionally well-suited for follow-up observations in a wide range of wavelengths, from radio to gamma-rays. These have the potential to yield transformational new clues into the progenitor systems of SNe Ia, as well as the detailed properties of dust along the line of sight, key astrophysical unknowns for the study of the accelerated expansion of the universe.

There is strong evidence that SNe Ia arise from thermonuclear explosions of carbon–oxygen white dwarfs (WDs) in binary systems (Nugent et al. 2011; Bloom et al. 2012). However, the nature of the second star remains unclear. For a long time, the preferred scenario was the single degenerate (SD) model (Whelan & Iben 1973), where a WD accretes mass from a hydrogen or helium rich donor star, thus becoming unstable while approaching the Chandrasekhar mass. The double-degenerate (DD) model involving the merger of two WDs (Tutukov & Yungelson 1981; Iben & Tutukov 1984; Webbink 1984) has gained considerable observational support in recent years; see, e.g., Wang & Han (2012).

In this work, we search for potential signatures of an SD progenitor system, such as variable Na D lines, precursor nova eruptions, features in the early light curve, radio emission, or a coincident source in pre-explosion in *Hubble Space Telescope* (*HST*) images.

[21] Hubble Fellow.

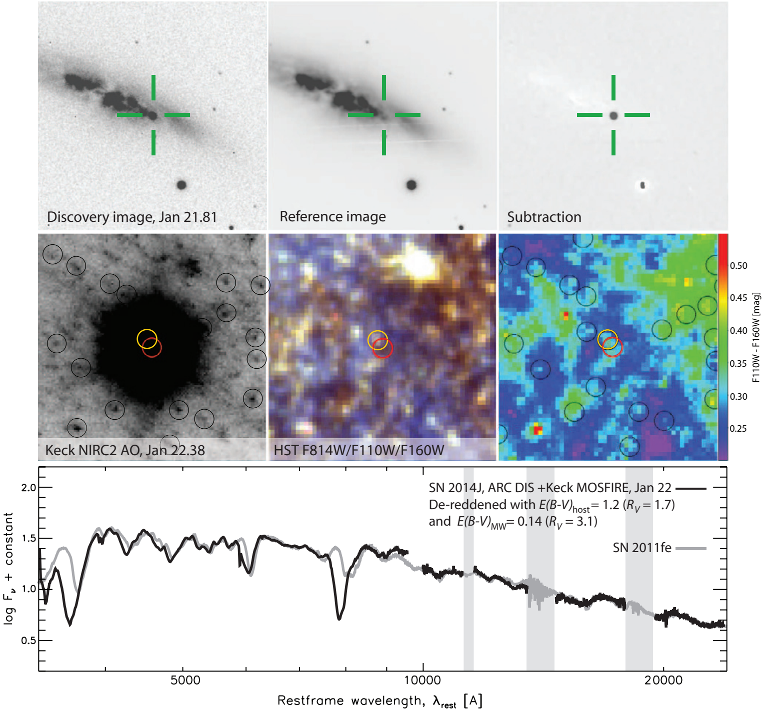

Figure 1. Top panels: $5' \times 5'$ sections of the discovery (Fossey et al. 2014), reference, and the subtraction images. Middle panels (from left to right): $5'' \times 5''$ section of the Keck NIRC2 adaptive optics image used to match the SN coordinates (red circle) to the surrounding sources (black circles). The nearest resolved object (yellow circle) in the pre-explosion *HST* composite images ($F815W/F110W/F160W$) is offset by $0\farcs2$ from the best estimate of the SN position. The middle-right panel shows a color map ($F110W - F160W$) indicating the large scale structures, probably due to patches of dust. The bottom panel shows the first optical and NIR spectrum of SN 2014J and a comparison to a combined spectrum from SN 2011fe by Pereira et al. (2013) and Hsiao et al. (2013), described in the text.

2. DISCOVERY AND CLASSIFICATION

SN 2014J was discovered by Fossey et al. (2014) in *BV R*-band images of M82 obtained on 2014 January 21.81 UT at UCL's University of London Observatory. We have performed image subtractions using pre-explosion data from the Palomar P60 telescope as reference, calibrated with nearby stars listed in the APASS catalog[22] yielding a discovery magnitude of $R = 10.99 \pm 0.03$ mag. The discovery image (S. Fossey 2014, private communication) and the P60 reference image, as well as the difference between the two are shown in Figure 1, along with the pre-explosion *HST* images (GO:11360, PI: R. O'Conell; GO:10776, PI: M. Mountain). The relative position of SN 2014J with respect to neighboring stars (middle panel) was established using multiple short exposures in the *K* band with adaptive optics and the NIRC2 wide camera at Keck (Tendulkar et al. 2014). In Section 5 we present a detailed analysis of the pre-explosion data.

A classification spectrum was obtained by the intermediate Palomar Transient Factory (iPTF) team on January 22.30 with the Dual Imaging Spectrograph on the ARC 3.5 m telescope (Cao et al. 2014), and in the near-IR using the MOSFIRE instrument at Keck. The combined spectra are shown in the bottom panel of Figure 1, while the photometry collected so far is displayed in Figure 2. The object shows characteristic spectral features associated with SNe Ia, e.g., similar to SN 2011fe (Pereira et al. 2013; Hsiao et al. 2013). However, the steep attenuation of the spectrum at short wavelengths is indicative of unusually large extinction by dust in the line of sight. A good match to the overall spectral energy distribution is found invoking a pronounced color excess, $E(B-V)_{\rm host} \approx 1.2$ mag, in addition to Galactic reddening, $E(B-V)_{\rm MW} = 0.14$ mag (Schlafly & Finkbeiner 2011), as shown in Figure 3. For the comparison, the spectra of SN 2011fe were artificially reddened assuming a Milky Way type extinction law (Cardelli et al. 1989), where both the color excess and R_V were allowed to vary freely. The spectrum favors a low value of the total-to-selective extinction, $R_V \lesssim 2$, as also suggested by spectropolarimetry observations by Patat et al. (2014). Low values of R_V are not unusual in SNe Ia, especially in the cases of high extinction; see, e.g., Nobili & Goobar (2008).

3. THE iPTF-LED MULTI-WAVELENGTH MONITORING OF SN 2014J IN M82

As a part of its continuous survey of the sky in the search for transients, iPTF has monitored M82 since 2009 October, with nearly daily cadence over the several months each year when M82 is visible from Palomar. The most recent campaign started on 2013 November 28. For the periods around full moon

[22] http://www.aavso.org/apass

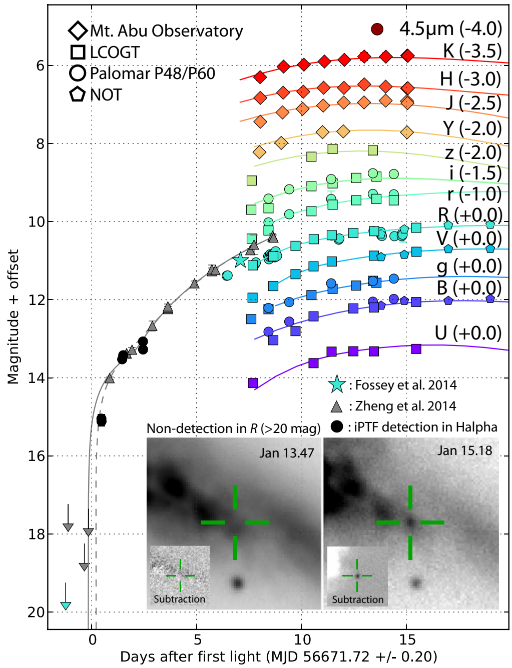

Figure 2. Light curves showing the rise of SN 2014J, along with SNooPy fits described in the text. The first P48 H_α^{656} and H_α^{663} narrowband detections are shown (black circles and inset image), S-corrected (Stritzinger et al. 2002) to the R band. Due to lack of accurate absolute calibration for the H_α filters, a common offset was applied to connect with the data points in the pre-discovery light curve presented in Zheng et al. (2014). We also show their two fits of t_0, suggesting our first detection could be within ∼5 hr from the onset of the supernova.

(e.g., around the time SN 2014J exploded), not well suited for transient searches, $H\alpha$ narrowband imaging was conducted.

The current best fit of the time of explosion, t_0, was reported by KAIT (Zheng et al. 2014) to be January 14.72 UT (±0.2 days). Upon later scrutiny of the pre-discovery P48 data, the SN was found in several observations from the iPTF $H\alpha$ narrowband survey, starting just hours after the fitted t_0. We find a relative flux increase from January 15.18 to January 16.18 of 1.6 mag, consistent with the "method 2 fit" in Zheng et al. (2014). The SN is also prominent on R-band photometry from the P48 prior to January 21 shown in Figure 2, but remained undetected by our automated software due to pixel saturation.

Through an iPTF-led effort, involving also the Las Cumbres Observatory Global Telescope (LCOGT) network (Brown et al. 2013), the Nordic Optical Telescope, and the Mount Abu Observatory (Venkataraman et al. 2014), we have secured optical, near-IR, and mid-IR light curves carefully monitoring the rise of the SN, as shown in Figure 2. The 4.5 μm observations were taken under the Spitzer InfraRed Intensive Transients Survey (SPIRITS; PI: Kasliwal).

The spectra shown in Figure 3 are consistent with those from a normal Type Ia explosion, similar to, e.g., SN 2011fe, but reddened following a CCM law (Cardelli et al. 1989) with $E(B-V) \sim 1.2$ mag and $R_V = 1.3$–2, in addition to Galactic reddening. Figure 2 also shows light curve fits using the SNooPy fitter (Burns et al. 2011) of the photometric data prior to maximum brightness. Best fits are found for $E(B-V)_{\rm host} = 1.22 \pm 0.05$ mag and $R_V = 1.4 \pm 0.15$. We expect the accuracy of the fitted parameters to improve, as the light curve shape estimate will profit from the decreasing part of the SN light curve. However, the available data clearly puts R_V well below the Galactic average value, $R_V = 3.1$.

We also obtained two 1800 s high-resolution ($R = 40{,}000$) spectra with SOPHIE at Observatorie Haute-Provence on January 26.0 and January 28.0. Further, two 1800 s spectra ($R = 67{,}000$) were obtained with the FIbre-fed Echelle Spectrograph (FIES) on January 27.3 and another on February 1.0 with the Nordic Optical Telescope.

All spectra reveal deep multiple component Na I D absorption and diffuse interstellar bands (DIBs), including λλ5780, 5797, 6284, and 6614, also reported by Cox et al. (2014) and Kotak (2014). The SOPHIE spectra further contain well resolved Ca II H & K with features matching those of the Na I D lines, shown in the co-added spectrum in Figure 4. We have not detected any significant time evolution for any of the resolved components of the Na I D doublet over the four epochs (at the ∼10% level for 3σ), thus motivating the combination of the spectra.

Following the procedure outlined by Phillips et al. (2013), we measure the EW of the λ5780 DIB to derive an independent estimate of host galaxy extinction for SN 2014J. We find $\mathrm{EW}(5780) = 0.48 \pm 0.01$ Å corresponding to $A_V^{\rm host} = 2.5 \pm 1.3$ mag.

Given the low recession velocity of M82, it is difficult to separate the contribution from the Milky Way and the SN host galaxy absorption. However, the availability of H I data from the LAB survey[23] in the direction of M82 (see inset panel in Figure 4; Kalberla et al. 2005) clearly indicates which features are Galactic. Hence, all the absorption features redshifted with respect to the Milky Way are due to intervening material in M82.

4. SPECTRAL MODELING

In Figure 3 we present a time-series spectral comparison between SN 2011fe and SN 2014J starting roughly 12 days before peak brightness. The SNe are remarkably similar in their spectral evolution. The main differences seen are that the overall velocities are higher in SN 2014J (see the inset Si II velocity plot) and there is a strong signature of high-velocity Si II and Ca II in this SN.

To further investigate these differences we carried out a set of SYNAPPS (Thomas et al. 2011) fits to these two SNe as well as to SN 2005cf, which was distinct in its pervasive high-velocity features (Wang et al. 2009). We present the results in Figure 5. In our fits to the red-side of the optical spectra we have employed the ions: C II, O I, Mg II, Si II, and Ca II with the latter two having both photospheric and high-velocity components. We see that SN 2014J more closely resembles SN 2005cf with respect to the high-velocity Si II and Ca II features which extend easily over the range of 20,000–30,000 km s^{-1}. Unlike either SN 2005cf or SN 2011fe, C II and O I are absent at this phase in SN 2014J. We searched for the presence of C I λ1.0693 μm line in our NIR spectrum, but the signal-to-noise is too low to do a meaningful fit comparable to that done for SN 2011fe (Hsiao et al. 2013). We do note that due to the stronger than average Mg II features seen in the optical for SN 2014J, this analysis may be more

[23] http://www.astro.uni-bonn.de/en/download/data/lab-survey/

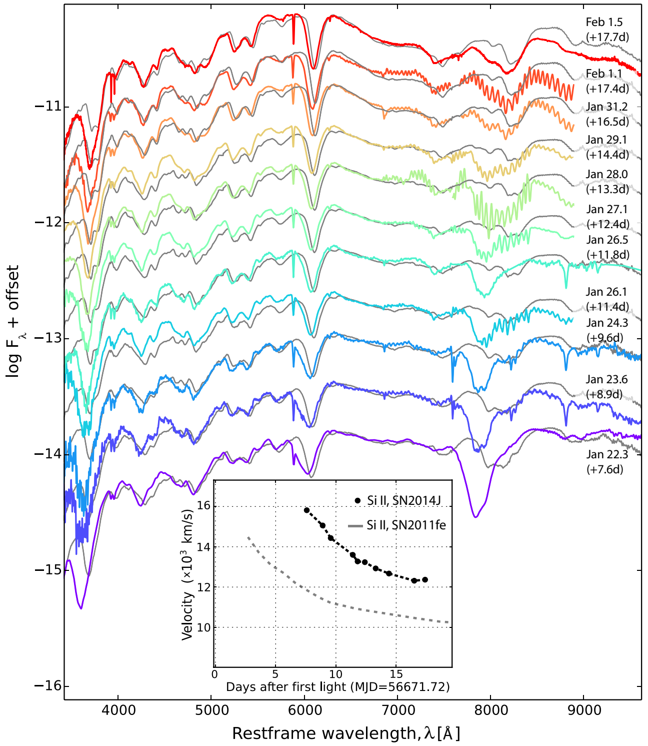

Figure 3. Pre-max spectroscopic follow-up of SN 2014J, starting 7.6 days from estimated supernova onset using the ARC 3.5 m DIS, LCOGT FLOYDS, NOT ALFOSC, and P200 DBSP spectrographs. Spectra of SN 2011fe (Pereira et al. 2013) at similar epochs (gray lines, reddened by $E(B-V)_{\mathrm{host}} = 1.2$ mag with $R_V = 1.7$ and $E(B-V)_{\mathrm{MW}} = 0.14$ mag with $R_V = 3.1$ are shown for comparison). The inset panel shows that SN 2014J has higher Si II velocity than SN 2011fe and a steeper velocity gradient (Benetti et al. 2005).

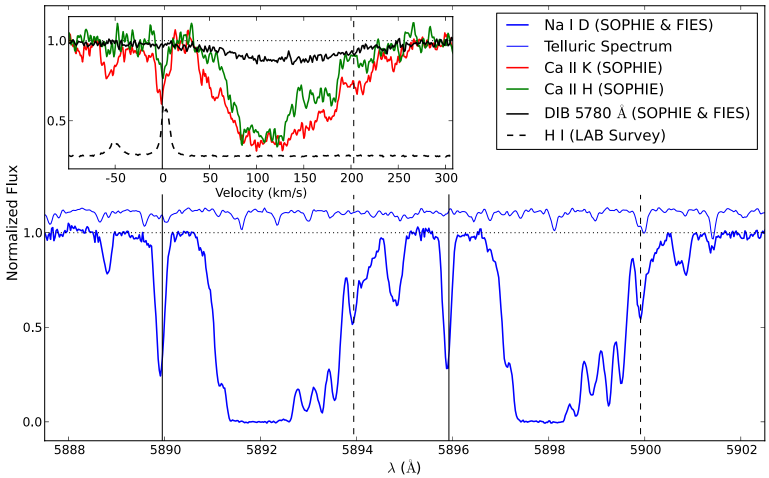

Figure 4. Normalized Na I D doublet, plotted with solid vertical lines indicating the Galactic rest-frame wavelengths and the dashed vertical lines correspond to the mean velocity of M82 (203 km s^{-1}). The inset panel shows the velocity distribution of Ca II H & K (green and red lines) and the λ5780 DIB (black). Additionally, the H I λ21 cm emission spectrum of the line of sight of M82 from the LAB survey (Kalberla et al. 2005) is plotted (dashed gray line). The features of the Na I D and Ca II H & K, at approximately -50 and 0 km s^{-1} with respect to the Galactic rest frame can be attributed to absorption in the Milky Way. The main Na I D absorption features, saturated between 74–135 km s^{-1}, originate in M82.

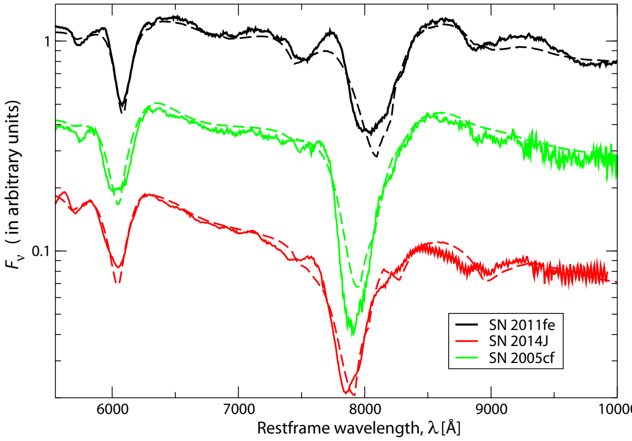

Figure 5. Early spectra of SNe 2011fe, 2005cf, and 2014J, concentrating on the red side of the optical spectra, along with SYNAPSS (Thomas et al. 2011) fits to each (dashed lines). In these fits we have employed the ions: C II, O I, Mg II, Si II, and Ca II with the latter two having both photospheric and high-velocity components. These fits highlight the major difference between these supernovae. SN 2014J shows no sign of either C II or O I in this part of the spectrum and, unlike 2011fe, quite strong high-velocity components of Si II, and Ca II extending well beyond 20,000 km s^{-1}. In addition, the Mg II photospheric feature in SN 2014J is stronger as well at this phase. SN 2005cf shows similar high-velocity Si II and Ca II to SN 2014J, but differs from this supernova as photospheric C II is clearly seen at this phase and our SYNAPPS fits also favor O I at this phase. This suggests that the nuclear burning in the outer layers of SN 2014J was more complete than that of SN 2011fe and the lack of C II compared to SN 2005cf may imply the same or perhaps a viewing angle effect due to an off-center detonation (Parrent et al. 2011).

challenging, even with higher quality spectra, as the presence of Mg II $\lambda 1.0927\ \mu$m should be quite strong as well.

Several explanations for the origin of the high-velocity features have been presented, from density enhancements via swept up circumstellar material (CSM) (Gerardy et al. 2004; Tanaka et al. 2006) to mixing or more complete burning in the outer layers of the SN (Mazzali et al. 2005a, 2005b) to ionization effects in the outer layers (Blondin et al. 2013). What is clear is that the features do offer a unique diagnostic for understanding properties of the progenitor system and/or the explosion mechanism and correlations between the strength of these features and the underlying colors and light curves of the SNe Ia (Childress et al. 2014; Maguire et al. 2013).

SN 2014J is among a class of SNe Ia where high-velocity features are present yet little to no evidence for C II exists even in very early spectra (see the broad-line or high-velocity gradient examples in Parrent et al. 2011). Since extensive UV data from *HST* exists for both SNe 2005cf and 2011fe, it will be interesting to see which of these supernovae SN 2014J most closely matches with respect to both the color and luminosity evolution.

5. THE QUEST FOR THE PROGENITOR SYSTEM

M82 has been extensively imaged by *HST*, thus it is possible to study the environment of the SN prior to the explosion. Because of the large attenuation due to dust in the line of sight, we concentrate on the NIR bands. We perform aperture photometry on the nearest sources to SN 2014J, shown in Figure 1. The closest object (yellow circle in Figure 1) falls $0\farcs2$ from the current best estimate of the SN location (R.A. = $9^{h}55^{m}42\fs217(1)$, decl. = $69°40'26\farcs56(4)$ in J2000 coordinates with respect to the *HST* image; Tendulkar et al. 2014), corresponding to a 4σ spatial offset. For this source, we measure AB magnitudes of $F110W = 21.4 \pm 0.4$, $F128N = 21.9 \pm 0.4$, $F160W = 20.6 \pm 0.4$, $F164N = 21.2 \pm 0.4$. The error is dominated by the uncertain background subtraction as a result of source confusion. The $F110 - F160W$ color is typical of other sources near this position. At a distance of 3.5 Mpc, the corresponding absolute magnitude of the nearest resolved object is $J_{\rm AB} \sim H_{\rm AB} \sim -7$ mag ($A_H < A_J < 0.4$ mag). This source could represent a stellar cluster, a grouping of unrelated objects or a region of relatively low dust attenuation.

Next, we consider the possibility that the source is a donor star in the SD scenario. The derived luminosity would then suggest a very luminous red supergiant. However, in the case where an SN originates from a system with CSM created by a mass-loss from a donor star, the interaction between the SN ejecta and the CSM is expected to give rise to radio emission (Chevalier 1982, 1988). The radio null-detections on January 23 and 24 (Chomiuk et al. 2014; Chandler & Marvil 2014) can therefore be used to derive an upper limit on the mass-loss rate. Adopting an SN shock-wave velocity of 3×10^4 km s^{-1} (about twice the Si II velocity; see Figure 3), and similar parameters as assumed by Horesh et al. (2012) for SN 2011fe, the upper limit on the mass-loss rate is $\dot{M} \leqslant 7 \times 10^{-9} (w/100\,{\rm km\,s^{-1}})\,M_\odot\,{\rm yr}^{-1}$, where w is the mass-loss wind velocity. The upper limit is comparable to the ones obtained for SN 2011fe (Horesh et al. 2012; Chomiuk et al. 2012). Given these tight limits and the spatial displacement, we conclude that the closest resolved source in the pre-explosion *HST* images is unlikely to be a donor star.

Finally, we note that the $F110W - F160W$ color map shown in the middle right panel of Figure 1 suggests that SN 2014J is at the edge of a dust patch, about 4 pc in projected size. Light echoes may thus be expected for this SN.

We have searched for possible nova outbursts in the historic P48 *R*-band data covering a period of about 1500 days prior to the detection of SN 2014J. By binning the data in bins of 15 days, we do not find any excess larger than 4σ (calculated using the bootstrap technique; see Efron 1982). Our limiting magnitude is $R > 19.5$ mag for a total time span of 1000 days, and $R > 20.25$ mag for more than 765 days in this 1500 day time window. Assuming $A_R = 2$ mag, compatible with the extinction we estimate based on the SN colors, this corresponds to absolute magnitudes $M_{\mathrm{R}} = -10.2$ and -9.5 respectively at the distance of M82. However, given the uncertainties on the properties of recurrent novae, see, e.g., Tang et al. (2014), we refrain from drawing firm conclusions against the possibility of recurrent novae preceding SN 2014J based on these non-detections.

6. SUMMARY AND CONCLUSIONS

The discovery of SN 2014J presents us with a unique opportunity to explore the physics of Type Ia SNe and the line-of-sight effects due to intervening matter. Further understanding in these areas is of utmost importance for the use of SNe Ia in cosmology. The early data from P48, starting as early as only hours from the explosion, and the multi-wavelength follow-up by the iPTF team covers an important range of the available windows in the electromagnetic spectrum. Just as the light curve reaches its maximum, we have learned that the SN has suffered non-standard extinction. We have searched for, but not detected, any time variation in our high-resolution spectra of the Na I D doublet. Similarly, we do not detect any pre-explosion activity in the ~1500 days of P48 monitoring. In a study of pre-explosion *HST* images in the near-IR, the nearest resolved source is found $0''.2$ away from the SN location. The source brightness and offset from the SN makes it unlikely to be a donor star in a single-degenerate scenario.

Further, we make a first study of the spectral features of SN 2014J and find that it exhibits high-velocity features from intermediate mass material but lacks C and O often seen in very early spectra. Otherwise, it is a very similar to several well-studied normal SNe Ia.

We thank S. Fossey for making the discovery *R*-band image of SN 2014J available to us. We are grateful to S. Fossey and M. Phillips for helpful comments on the manuscript. We acknowledge A. McKay, A. Bradley, N. Scoville, P. L. Capak, C. M. Carollo, S. Lilly, H. Sheth, V. Bhalerao, P. Donati, S. Geier, F. Saturni, G. Nowak, and A. Finoguenov for cooperating with ToO observations. A.G. and R.A. acknowledge support from the Swedish Research Council and the Swedish Space Board and A.G.-Y. an ERC grant. M.M.K. acknowledges generous support from the Hubble Fellowship and Carnegie-Princeton Fellowship. Based on observations made with the Nordic Optical Telescope, operated by the Nordic Optical Telescope Scientific Association at the Observatorio del Roque de los Muchachos, La Palma, Spain, of the Instituto de Astrofisica de Canarias, Faulkes Telescope North image observed by Gain Lee, the Mount Abu 1.2 m Infrared telescope, India, and the 1.93 m telescope of Haute-Provence Observatory, CNRS, France. This research used resources of the National Energy Research Scientific Computing Center, which is supported by the Office of Science of the U.S. Department of Energy under Contract No. DE-AC02-05CH11231.

REFERENCES

Ardeberg, A., & de Groot, M. 1973, A&A, 28, 295
Benetti, S., Cappellaro, E., Mazzali, P. A., et al. 2005, ApJ, 623, 1011
Blondin, S., Dessart, L., Hillier, D. J., & Khokhlov, A. M. 2013, MNRAS, 429, 2127
Bloom, J. S., Kasen, D., Shen, K. J., et al. 2012, ApJL, 744, L17
Brown, T. M., Baliber, N., Bianco, F. B., et al. 2013, PASP, 125, 1031
Burns, C. R., Stritzinger, M., Phillips, M. M., et al. 2011, AJ, 141, 19
Cao, Y., Kasliwal, M. M., & McKay, A. 2014, ATel, 5786, 1
Cardelli, J. A., Clayton, G. C., & Mathis, J. S. 1989, ApJ, 345, 245
Chandler, C. J., & Marvil, J. 2014, ATel, 5812, 1
Chevalier, R. A. 1982, ApJL, 259, L85
Chevalier, R. A. 1988, Natur, 332, 514
Childress, M. J., Filippenko, A. V., Ganeshalingam, M., & Schmidt, B. P. 2014, MNRAS, 437, 338
Chomiuk, L., Soderberg, A. M., Moe, M., et al. 2012, ApJ, 750, 164
Chomiuk, L., Zauderer, B. A., Margutti, R., & Soderberg, A. 2014, ATel, 5800, 1
Cox, N. L. J., Davis, B. A., Patat, F., & Van Winckel, H. 2014, ATel, 5797, 1
Dalcanton, J. J., Williams, B. F., Seth, A. C., et al. 2009, ApJS, 183, 67
Efron, B. 1982, The Jackknife, the Bootstrap and Other Resampling Plans (Philadelphia, PA: Society for Industrial and Applied Mathematics (SIAM))
Fossey, S., Cooke, B., Pollack, G., Wilde, M., & Wright, T. 2014, CBET, 3792, 1
Gendre, M. A., Fenech, D. M., Beswick, R. J., Muxlow, T. W. B., & Argo, M. K. 2013, MNRAS, 431, 1107
Gerardy, C. L., Höflich, P., Fesen, R. A., et al. 2004, ApJ, 607, 391
Goobar, A., & Leibundgut, B. 2011, ARNPS, 61, 251
Horesh, A., Kulkarni, S. R., Fox, D. B., et al. 2012, ApJ, 746, 21
Hsiao, E. Y., Marion, G. H., Phillips, M. M., et al. 2013, ApJ, 766, 72
Iben, I., Jr., & Tutukov, A. V. 1984, ApJS, 54, 335
Kalberla, P. M. W., Burton, W. B., Hartmann, D., et al. 2005, A&A, 440, 775
Kotak, R. 2014, ATel, 5816, 1
Maguire, K., Sullivan, M., Patat, F., et al. 2013, MNRAS, 436, 222
Mattila, S., Fraser, M., Smartt, S. J., et al. 2013, MNRAS, 431, 2050
Mazzali, P. A., Benetti, S., Altavilla, G., et al. 2005a, ApJL, 623, L37
Mazzali, P. A., Benetti, S., Stehle, M., et al. 2005b, MNRAS, 357, 200
Nobili, S., & Goobar, A. 2008, A&A, 487, 19
Nugent, P. E., Sullivan, M., Cenko, S. B., et al. 2011, Natur, 480, 344
Parrent, J. T., Thomas, R. C., Fesen, R. A., et al. 2011, ApJ, 732, 30
Patat, F., Taubenberger, S., Baade, D., et al. 2014, ATel, 5830, 1
Pereira, R., Thomas, R. C., Aldering, G., et al. 2013, A&A, 554, A27
Phillips, M. M., Phillips, A. C., Heathcote, S. R., et al. 1987, PASP, 99, 592
Phillips, M. M., Simon, J. D., Morrell, N., et al. 2013, ApJ, 779, 38
Schlafly, E. F., & Finkbeiner, D. P. 2011, ApJ, 737, 103
Stritzinger, M., Hamuy, M., Suntzeff, N. B., et al. 2002, AJ, 124, 2100
Tanaka, M., Mazzali, P. A., Maeda, K., & Nomoto, K. 2006, ApJ, 645, 470
Tang, S., Bildsten, L., Wolf, W. M., et al. 2014, arXiv:1401.2426
Tendulkar, S. P., Liu, M. C., Dupuy, T. F., & Cao, Y. 2014, ATel, 5789, 1
Thomas, R. C., Nugent, P. E., & Meza, J. C. 2011, PASP, 123, 237
Tutukov, A. V., & Yungelson, L. R. 1981, NInfo, 49, 3
Venkataraman, V., Banerjee, D. P. K., Joshi, V., Ashok, N., & Bhalerao, V. 2014, ATel, 5793, 1
Wang, B., & Han, Z. 2012, NewAR, 56, 122
Wang, X., Li, W., Filippenko, A. V., et al. 2009, ApJ, 697, 380
Webbink, R. F. 1984, ApJ, 277, 355
Whelan, J., & Iben, I., Jr. 1973, ApJ, 186, 1007
Zheng, W., Shivvers, I., Filippenko, A. V., et al. 2014, arXiv:1401.7968

Paper IV

R. Amanullah, A. Goobar, **J. Johansson**, D. P. K. Banerjee, V. Venkataraman, V. Joshi, N. M. Ashok, Y. Cao, M. M. Kasliwal, S. R. Kulkarni, P. E. Nugent, T. Petrushevska, V. Stanishev
The Peculiar Extinction Law of SN 2014J Measured with the Hubble Space Telescope
ApJL, Vol. 788, L21 (2014).

THE ASTROPHYSICAL JOURNAL LETTERS, 788:L21 (6pp), 2014 June 20 doi:10.1088/2041-8205/788/2/L21

THE PECULIAR EXTINCTION LAW OF SN 2014J MEASURED WITH THE *HUBBLE SPACE TELESCOPE*

R. AMANULLAH[1], A. GOOBAR[1], J. JOHANSSON[1], D. P. K. BANERJEE[2], V. VENKATARAMAN[2], V. JOSHI[2], N. M. ASHOK[2], Y. CAO[3], M. M. KASLIWAL[4], S. R. KULKARNI[3], P. E. NUGENT[5,6], T. PETRUSHEVSKA[1], AND V. STANISHEV[7]
[1] Oskar Klein Centre, Physics Department, Stockholm University, SE-106 91 Stockholm, Sweden; rahman@fysik.su.se
[2] Physical Research Laboratory, Ahmedabad 380009, India
[3] Cahill Center for Astrophysics, California Institute of Technology, Pasadena, CA 91125, USA
[4] Observatories of the Carnegie Institution for Science, 813 Santa Barbara Street, Pasadena, CA 91101, USA
[5] Department of Astronomy, University of California Berkeley, B-20 Hearst Field, Annex # 3411, Berkeley, CA 94720-3411, USA
[6] Computational Cosmology Center, Computational Research Division, Lawrence Berkeley National Laboratory, 1 Cyclotron Road, MS 50B-4206, Berkeley, CA 94720, USA
[7] CENTRA—Centro Multidisciplinar de Astrofísica, Instituto Superior Técnico, Av. Rovisco Pais 1, 1049-001 Lisbon, Portugal
Received 2014 April 9; accepted 2014 May 2; published 2014 May 29

ABSTRACT

The wavelength dependence of the extinction of Type Ia SN 2014J in the nearby galaxy M82 has been measured using UV to near-IR photometry obtained with the *Hubble Space Telescope*, the Nordic Optical Telescope, and the Mount Abu Infrared Telescope. This is the first time that the reddening of an SN Ia is characterized over the full wavelength range of 0.2–2 μm. A total-to-selective extinction, $R_V \geqslant 3.1$, is ruled out with high significance. The best fit at maximum using a Galactic type extinction law yields $R_V = 1.4 \pm 0.1$. The observed reddening of SN 2014J is also compatible with a power-law extinction, $A_\lambda/A_V = (\lambda/\lambda_V)^p$ as expected from multiple scattering of light, with $p = -2.1 \pm 0.1$. After correcting for differences in reddening, SN 2014J appears to be very similar to SN 2011fe over the 14 broadband filter light curves used in our study.

Key words: dust, extinction – galaxies: individual (Messier 82) – supernovae: individual (SN 2014J)

Online-only material: color figures, machine-readable table

1. INTRODUCTION

The study of the cosmological expansion history using Type Ia supernovae (SNe Ia), of which SN 2014J is the closest in several decades (Goobar et al. 2014, hereafter G14), has revolutionized our picture of the universe. The discovery of the accelerating universe (Riess et al. 1998; Perlmutter et al. 1999) has led to one of the biggest scientific challenges of our time: probing the nature of *dark energy* through more accurate measurements of cosmological distances and the growth of structure in the universe. SNe Ia remain among the best tools to measure distances and as the sample grows both in number and redshift range, special attention is required to address systematic effects. One important source of uncertainty is the effect of dimming by dust. Despite considerable effort, it remains unclear why the color–brightness relation for SNe Ia from cosmological fits is significantly different from, e.g., dimming by interstellar dust with an average $R_V = A_V/E(B-V) = 3.1$. In the most recent compilation by Betoule et al. (2014), 740 low- and high-z SNe Ia were used to build a Hubble diagram using the SALT2 lightcurve fitter (Guy et al. 2007). Their analysis yields $\beta = 3.101 \pm 0.075$, which corresponds to $R_V \sim 2$, although the assumed color law in SALT2 differs from the standard Milky-Way-type extinction law (Cardelli et al. 1989).

Several cases of $R_V \lesssim 2$ have been found in studies of color excesses of local, well-measured, SNe Ia (e.g., Krisciunas et al. 2006; Elias-Rosa et al. 2006, 2008; Nobili & Goobar 2008; Folatelli et al. 2010). A low value of R_V corresponds to a steeper wavelength dependence of the extinction, especially for shorter wavelengths. In general terms, this reflects the distribution of dust grain sizes where a low R_V implies that the light encounters mainly small dust grains. Wang (2005) and Goobar (2008) suggest an alternative explanation that non-standard reddening of SNe Ia could originate from multiple scattering of light, e.g., due to a dusty circumstellar medium, a scenario that has been inferred for a few SNe Ia (Patat et al. 2007; Blondin et al. 2009; Dilday et al. 2012).

A tell-tale signature of reddening through multiple scattering is a power-law dependence for reddening (Goobar 2008), possibly also accompanied by a perturbation of the lightcurve shapes (Amanullah & Goobar 2011) and IR emission from heated dust regions (Johansson et al. 2013).

SN 2014J in the nearby galaxy M82 offers a unique opportunity to study the reddening of a spectroscopically normal (G14; Marion et al. 2014) SN Ia, over an unusually wide wavelength range. *Hubble Space Telescope* (*HST*) observations allow us to perform a unique study of color excess in the optical and near-UV, where the difference between the extinction models is the largest. Our data set is complemented by *UBVRi* observations from the Nordic Optical Telescope (NOT) and *JHKs* from the Mount Abu Observatory.

2. OBSERVATIONS AND DATA

2.1. *HST/WFC3*

We obtained observations (Program DD-13621; PI: Goobar) of SN 2014J with *HST* in the four *UV* broadband filters *F218W*, *F225W*, *F275W*, and *F336W* for seven epochs using a total of seven *HST* orbits during Cycle 21. In addition to this we also obtained optical broad-, medium-, and narrowband photometry in filters *F467M*, *F631N,* and *F845M* for visits (1, 3) and optical broadband photometry using *F438W*, *F555W*, and *F814W* for the remaining five visits. All observations were obtained with the Wide-Field Camera-3 (WFC3) using the UVIS aperture `UVIS2-C512C-SUB`.

The data were reduced using the standard reduction pipeline and calibrated through CALWF3 as integrated into the *HST* archive. The flat-fielded images were corrected for charge

Table 1
The Measured Photometry of SN 2014J from *HST*/WFC3, NOT/ALFOSC, and the Mount Abu Infrared Telescope

MJD (1)	Phase (2)	Filter (3)	Mag (4)	A_X (5)	Match (6)	V (7)	A_V (8)	2011fe (9)
56688.8	−0.2	*F218W*	18.03(0.01)	0.20	M	10.68(0.02)	0.15	−3.13
56692.1	2.9	*F218W*	18.03(0.01)	0.20	M	10.67(0.02)	0.15	−3.14
56697.0	7.3	*F218W*	18.35(0.02)	0.20	D	10.81(0.02)	0.15	−3.53
56702.9	12.7	*F218W*	18.88(0.01)	0.19	M	11.02(0.02)	0.15	−4.00
56713.7	22.6	*F218W*	19.85(0.03)	0.17	M	11.55(0.02)	0.15	−4.43
				...				

Notes. All magnitudes are in the natural Vega system. The rest-frame magnitude can be obtained from Columns 4–5, where Columns 5 and 8 are the Galactic extinctions for the two bands, respectively. Column 2 shows the effective, lightcurve-width-corrected phase, while Column 6 specifies whether the V magnitude was measured for the same epoch (D) or if it was calculated using the SNooPy model (M). In the latter case the mean error of the data used for the fit was adopted as the uncertainty of the magnitude. The corresponding synthesized color of SN 2011fe is shown in Column 9.

(This table is available in its entirety in a machine-readable form in the online journal. A portion is shown here for guidance regarding its form and content.)

transfer inefficiencies at the pixel level[8] and photometry was carried out on the individual images following the guideline from the WFC3 Data Handbook. The individual flat-fielded images were corrected by multiplying with the pixel area map[9] following Section 7 of the WFC3 Data Handbook. The SN flux could be measured on all images using an aperture with radius 0″.2. Host contamination is negligible at the SN position and the statistical uncertainties were estimated assuming Poisson noise of the signal together with the readout noise. The resulting photometry is presented in Table 1.

2.2. Optical and Near-IR Data

The *UBVRi* data were obtained with the NOT (Program 48-004; PI: Amanullah). The data were reduced with standard IRAF routines, using the QUBA pipeline (see Valenti et al. 2011, for details). The magnitudes are measured with a point-spread function-fitting technique (using daophot) and calibrated to the Landolt system.

Near-IR (NIR) observations in the Mauna Kea Observatory *JHKs* filters were carried out with the Mount Abu 1.2 m Infrared Telescope. Aperture photometry of the sky-subtracted frames was done using IRAF. The nearby star Two Micron All Sky Survey (2MASS) J09553494+6938552, which registers simultaneously with SN 2014J in the same field, was used for calibration. Results were cross-checked with other 2MASS stars in the field and found to agree within 5%. We adopt this as a systematic uncertainty on the NIR photometry.

All light curves[10] are presented in Table 1 and Figure 1 where we also show a fitted model to the V band using SNooPy (Burns et al. 2011).

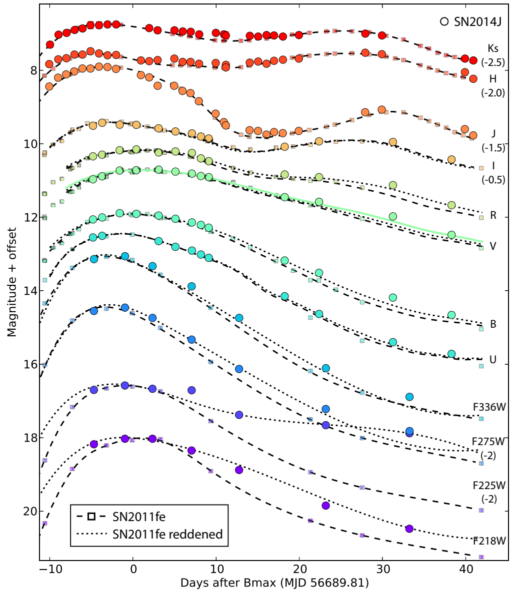

Figure 1. Light curves for all passbands used in this analysis. For the V band we also overplot (solid green line) the fitted model from SNooPy. The black lines are fits to the synthetic photometry of the SN 2011fe spectra (dashed) and the spectra reddened with the best fit FTZ model to SN 2014J.

(A color version of this figure is available in the online journal.)

3. COLOR EXCESS

3.1. Intrinsic SN Ia Colors

In order to study the reddening of SN 2014J, the colors for a pristine, unreddened, SN Ia must be known. Further, we need a color template that includes both the wavelengths and epochs covered by the observations presented in this work.

As described in G14, the early spectral evolution of SN 2014J and SN 2011fe in the nearby spiral galaxy M 101 is remarkably similar. The only difference being that SN 2014J shows overall higher photospheric velocities. SN 2011fe has been observed over a broad wavelength range from the UV (Brown et al. 2012; Mazzali et al. 2014), through the optical (e.g., Pereira et al. 2013), to the NIR (Matheson et al. 2012; Hsiao et al. 2013). The similarity to SN 2014J together with the low Galactic and host galaxy reddening, $E(B-V)_{\mathrm{MW}} = 0.011 \pm 0.002$ and $E(B-V)_{\mathrm{host}} = 0.014 \pm 0.002$ mag (Patat et al. 2013), makes SN 2011fe the best template we can derive of the unreddened spectral energy distribution (SED) of SN 2014J.

We use the spectral series from Mazzali et al. (2014) and Pereira et al. (2013), corrected for Galactic extinction using

[8] J. Anderson 2013, private communication.
[9] http://www.stsci.edu/hst/wfc3/pam/pixel_area_maps
[10] All tables and figures are available at http://www.fysik.su.se/~rahman/SN2014J/.

Fitzpatrick (1999, FTZ hereafter) with $R_V = 3.1$, to compute synthetic colors between in the WFC3 and NOT bands in which SN 2014J was observed. The effective *HST* filters were obtained from SYNPHOT/STSDAS, while we used modified versions of the public effective NOT filters. We further use the SN 2011fe light curves from Matheson et al. (2012) as an unreddened NIR template of SN 2014J. All light curves are shown in Figure 1 (dashed curves) where they have been shifted to overlap with the corresponding SN 2014J photometry at maximum. Smoothed splines are fitted using SNooPy to each individual band to create a pristine lightcurve template.

As seen in Figure 1, the NIR light curves of SN 2011fe provide an excellent description of the corresponding bands of SN 2014J, while this is not the case for the bluer bands. At these wavelengths SN 2011fe appears to both rise and fall faster than SN 2014J, and the difference between the two objects increases with shorter wavelengths. As will be argued in Section 4 this is partially an effect that stems from the fact that broadband observations of SN 2014J are effectively probing longer wavelengths than the corresponding data of SN 2011fe due to the significant extinction. Taking this effect into account leads to the dotted lines for the reddened SED of SN 2011fe in Figure 1.

The spectral series will also be used in the analysis to calculate the expected extinction in each passband for a given extinction law. The Mazzali et al. (2014) data set extend out to $\sim 2\,\mu$m until phase +9. Since this does not cover the entire phase range of our study we extended this spectral series using the template from Hsiao et al. (2007, 2013) for phases past +9.

In order to compare SN 2014J with SN 2011fe, we also need an estimate of the uncertainty within which we would expect the broadband colors of two SNe Ia to agree in the absence of extinction. Folatelli et al. (2010) studied the intrinsic optical and NIR colors of SNe Ia close to lightcurve maximum, and found dispersions in the range 0.06–0.14 mag, after correcting for the lightcurve shape. We conservatively adopt a dispersion of 0.15 mag (the worst case above) for all colors that only include the optical and NIR bands.

Further, Milne et al. (2010) presented an extensive study of the $UV-V$ dispersion based on observations of 12 SNe Ia with the *Swift* satellite. For their low-extinction ($E(B - V) < 0.2$) sample they derive dispersions of 0.1 and 0.25 mag between −12 and +12 days relative to the *B*-band maximum for the $uvw1 - v$ and $uvw2 - v$ colors, respectively. We adopt a dispersion of 0.35 mag for the colors that involve *F218W* and *F225W* and 0.25 mag for *F275W*. For the $V - F336W$ dispersion we adopt the same value as the optical range, i.e., 0.15 mag. Since UV observations of SNe Ia are scarce, it is difficult to fully assess the differences among SNe at the shortest wavelengths considered here. Foley & Kirshner (2013) argued that although SN 2011by was a spectral "twin" to SN 2011fe in the optical, it exhibited a different behavior in the near-UV. We have therefore checked how our estimate of the color excess of SN 2014J would differ under the assumption that it is a better match to SN 2011by instead of SN 2011fe. The offsets at the lightcurve maximum are $\Delta E(V - F225W) = 0.35$ mag and $\Delta E(V - F275W) = 0.03$ mag, i.e., compatible with our estimate of the intrinsic color scatter.

3.2. Color Excesses of SN 2014J

In this work we studied the color excesses, $E(V - X)$, of all photometric bands with respect to the V band. For each photometric observation in Table 1 we also list the corresponding V magnitude. If the SN was observed in both bands within 12 hr we use the observed V for the corresponding epoch, but when this was not the case we use the fitted V-band SNooPy model shown in Figure 1 to calculate the color.

For each epoch we also present the calculated Galactic reddening correction. Unlike G14, we use the Galactic extinction toward M82 from Dalcanton et al. (2009). They argue that the estimates from the dust maps of Schlegel et al. (1998) are contaminated by M82 itself, and derived $E(B - V)_{\rm MW} = 0.06$ from the study of neighboring patches.

We also calculate the corresponding color of SN 2011fe, shown in the last column of Table 1, from the light curves described above. The color excess, $E(V_n - X_n)$, between the V band and some other band X, at an epoch n, can then be obtained under the assumption that the two SNe had nearly identical color evolution. Since the differences in K corrections are negligible for the two very nearby SNe, the color excess is calculated as the difference between the $V_n - X_n$ color, corrected for Galactic extinction, and the corresponding color of SN 2011fe, i.e.,

$$E(V_n - X_n) = [(V_n - A_{V_n}) - (X_n - A_{X_n})] - \left(V_n^{11\rm fe} - X_n^{11\rm fe}\right). \quad (1)$$

The first term on the right-hand side, the extinction-corrected color of SN 2014J, is plotted in Figure 2 together with the best fit colors derived from the reddened SED, as described in the next section. In Figure 3, $E(V_n - X_n)$ is plotted using data around maximum light.

4. FITTING EXTINCTION LAWS

An extinction law, $\xi(\lambda;\, \bar{p})$, where $\bar{p}$ are free parameters, can be fitted by minimizing

$$\chi^2 = \sum_X \sum_n \frac{[(E(V_n - X_n) - (A_{V_n} - A_{X_n})]^2}{\sigma^2_{V_n X_n}}. \quad (2)$$

Here $E(V_n - X_n)$ is the measured color excess as described above and $A_{V_n} - A_{X_n}$, the corresponding model color excess,

$$A_{X_n} = -2.5 \log_{10} \left(\frac{\int \xi(\lambda;\, \bar{p}) T_X(\lambda) S_{11\rm fe}(\lambda;\, n) \lambda \, d\lambda}{\int T_X(\lambda) S_{11\rm fe}(\lambda;\, n) \lambda \, d\lambda} \right), \quad (3)$$

can be calculated from the filter transmission, $T_X(\lambda)$, and the SED of SN 2011fe, $S_{11\rm fe}(\lambda;\, n)$, of the given epoch n.

The uncertainties, $\sigma^2_{V_n X_n}$, include the measurement errors shown in Table 1 but is dominated by the adopted intrinsic SN Ia color uncertainties. If a V-band measurement is included in constructing two different colors for a given epoch, then the contribution from the V uncertainty is treated as fully correlated.

In this work we ignore both calibration uncertainties (except for NIR) and systematic errors due to, e.g., Galactic extinction correction. The reason is that these will be correlated between epochs and are negligible in comparison to the intrinsic color uncertainty, which we also assume to be fully correlated. This will put equal weights to all colors, independent of the number of data points obtained in each band.

We further assume that the different colors are uncorrelated in our final analysis. We have tried inducing different correlations between the colors, but this had a minor impact on the conclusions from the fits.

We fitted three different extinction laws: an MW-like extinction law as parameterized by Fitzpatrick (1999, FTZ), the SALT2 law in the version used in Betoule et al. (2014), and a power-law parameterization, $A_\lambda / A_v = (\lambda/\lambda_V)^p$, shown to be a

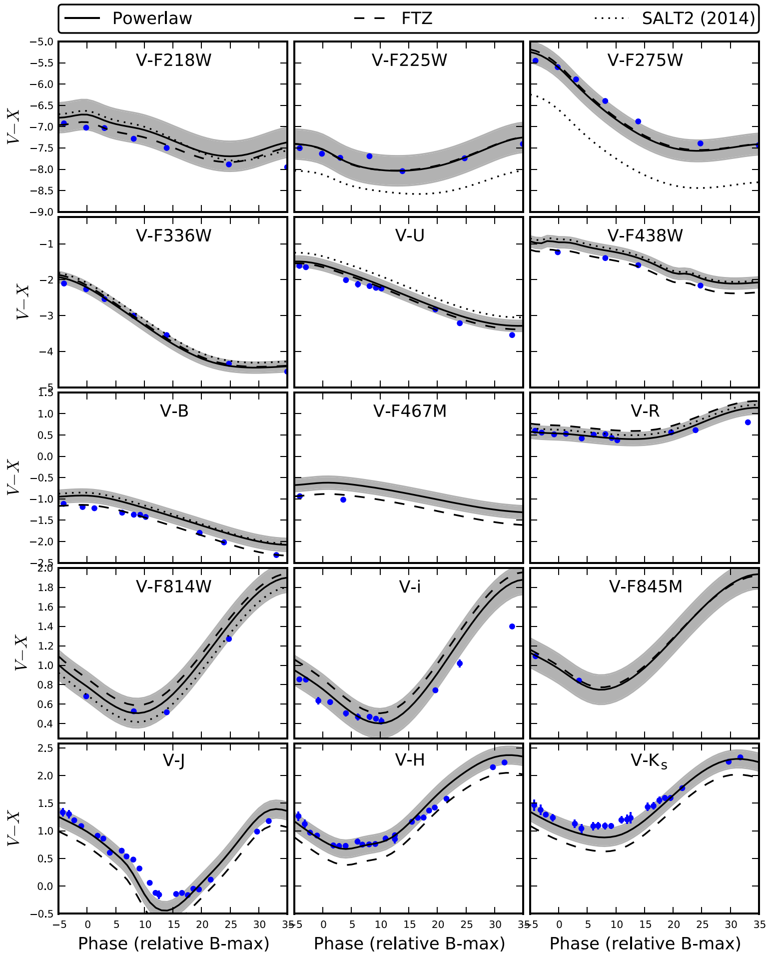

Figure 2. Measured colors (blue points) for the UV, optical, and NIR bands. Also shown are the best fit extinction laws in the [−5, +35] range together with the corresponding predicted colors of SN 2011fe. The gray band shows the adopted intrinsic dispersion of each color plotted with respect to the power-law fit.

(A color version of this figure is available in the online journal.)

good approximation for multiple scattering scenarios (Goobar 2008). Each law was fitted using three different epoch ranges: [−5, +5] days, i.e., around peak brightness, the tail: [+25, +35], and the full epoch range of the *HST* observations, [−5, +35] days since *B*-band maximum. The FTZ and power law were fitted using all filters, while the SALT2 law is only defined in the wavelength range 2000–7990 Å.

The SN colors are compared at the effective phases, computed for both SN 2011fe and SN 2014J by subtracting the date of the *B*-max, 55814.5 and 56689.2, respectively, and dividing by the *i* lightcurve stretches (from SNooPy), 0.96 and 1.14, respectively. For each law we carry out the fit iteratively to all bands except *F555W* and *F631N*. The former completely includes our reference band and the latter is too narrow for our assumption of SN 2014J and SN 2011fe being comparable to hold.

We first calculate the Galactic extinction in each band assuming the pristine SED of SN 2011fe. Then, we carry out the fit by minimizing Equation (2). The fitted extinction law is then applied to the SED of SN 2011fe and the Galactic extinction is recalculated before refitting the law. The procedure is repeated until the value of the fitted parameters changes by less than 1% between iterations. The results of the fits are shown in Table 2, and the best fits to the full range are also shown in Figure 2 while the best fit around maximum is shown in Figure 3. In this figure we also present the best fitted FTZ model with R_V fixed to $R_V = 3.1$, which is clearly excluded by the data. Our best fit FTZ values are $E(B-V) = 1.37 \pm 0.03$, $R_V = 1.4 \pm 0.1$. We find that our data are also compatible with the power-law model with $A_V = 1.85 \pm 0.11$ and $p = -2.1 \pm 0.1$. Finally, we conclude that the SALT2 model provides a somewhat poorer fit description with $c = 1.06 \pm 0.04$. These findings can

Table 2
The Best Fitted Parameters for Each Reddening Law to the Broadband Filters

Phase	FTZ			Power Law: $A_\lambda = A_V\,(\lambda/\lambda_V)^p$			SALT2 (2014)	
	$E(B-V)$	R_V	χ^2/dof	A_V	p	χ^2/dof	c	χ^2/dof
[−5, +5]	1.37(0.03)	1.4(0.1)	1.1	1.85(0.11)	−2.1(0.1)	1.1	1.06(0.04)	5.3
[+25, +35]	1.33(0.04)	1.3(0.1)	1.9	1.52(0.11)	−2.4(0.1)	2.2	1.10(0.05)	6.9
[−5, +35]	1.29(0.02)	1.3(0.1)	3.3	1.77(0.10)	−2.1(0.1)	2.3	1.00(0.01)	5.2

Note. Quoted errors are the uncertainties from the χ^2 fit.

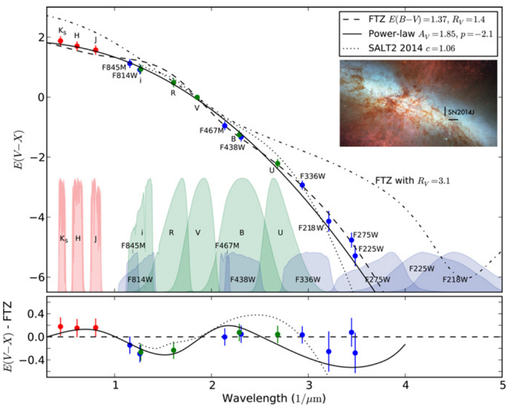

Figure 3. Upper panel shows the average color excesses between −5 and +5 days from the *B* maximum. Blue, green, and red points are measured with *HST*, NOT, and the Mount Abu Infrared Telescope, respectively, while the corresponding effective filter transmissions are plotted, in linear scale, at the bottom of the panel. The same data points are plotted as residuals with respect to the best fit FTZ law in the lower panel. For the *UV* filters the effective wavelengths are significantly redder than the central wavelengths due to the steepness of the reddened SN spectrum.

(A color version of this figure is available in the online journal.)

be compared with the measured global extinction in M82 by Hutton et al. (2014). Unlike our result for the line of sight of SN 2014J, they conclude that FTZ with $R_V = 3.1$ provides a good description of the colors of the galaxy based on stellar modeling. However, for the dust in the superwind, they too conclude that a power-law relation provides the best fit, albeit with $p = -1.53 \pm 0.17$.

As a consistency check, we recalculate the synthetic light curves of SN 2011fe using the best fitted FTZ law to redden the spectra. The result is plotted in Figure 1 as dotted lines for each band. For the redder bands, these reddened light curves are similar to the original, but for the blue bands, and in particular in the UV, the light curves are significantly broader, and show a similar decline as the observed data of SN 2014J. We take this as yet another confirmation that SN 2011fe indeed is very similar to SN 2014J and therefore suitable to use as reference for the extinction study presented here. We further conclude (Nugent et al. 2002, and references therein) that the difference in the lightcurve width between the original light curves in the bluer bands mainly stems from the fact that we are probing redder effective wavelengths for SN 2014J than for SN 2011fe when comparing the same passbands.

This also has implications for Figure 3. Here we calculated the weighted average for each color, taking the full covariance into account. However, the color excess is calculated by comparing the magnitudes of a reddened and an unreddened source. The two magnitudes will correspond to different effective wavelengths, and the broader the filter, and the steeper the spectrum, the larger the difference of the two effective wavelengths will become. For Figure 3 we allowed the wavelength to shift, with respect to the average effective wavelength using the FTZ law, until the residuals of the color excess match the weighted average residual from the fit. For the bluest *F218W* and *F225W*, the shift becomes 330 Å and 240 Å respectively. Both of these filters suffer from minor red leaks, e.g., for *F218W* 0.3% of the light comes from wavelengths redder than 4000 Å. On the other hand, an SN Ia at maximum with the reddening of SN 2014J will typically be ∼6 orders of magnitude brighter at 4000 Å compared to the central wavelength of the *F218W* filter. The significant shift toward redder wavelengths for these filters is in other words not surprising.

5. CONCLUSIONS

We present the results from fitting three extinction laws to observations of SN 2014J in 16 photometric bands spanning the wavelength range 0.2–2 μm between phases −5 and +35 days with respect to the *B* maximum. We find a remarkably consistent picture with the reddening law fits only involving two free parameters. Once reddening is accounted for, the similarity between the multi-color light curves of SN 2014J and SN 2011fe is striking.

We measure an overall steep extinction law with a total-to-selective extinction value R_V at the maximum of $R_V = 1.4 \pm 0.1$ for an MW-like extinction law. We also note that the fitted extinction laws are consistent when fitted separately around maximum and using the full phase range.

Although the fits slightly disfavor the empirically derived SALT2 color law for SN Ia, in comparison to an MW-like extinction law as parameterized by FTZ with a low R_V, conclusions should be drawn cautiously. SALT2 has not been specifically trained for the near-UV region considered here. Also, there is no prediction for the NIR. Intriguingly, the power-law extinction proposed by Goobar (2008) as a model for multiple scattering of light provides a good description of the reddening of SN 2014J.

Increasing this sample is crucial to understand the possible diversity in the reddening of SNe Ia used to measure the expansion history of the universe.

We thank Denise Taylor, Claus Leitherer, and John Mackenty at the Space Telescope Science Institute for advising and assisting us in carrying out this program. R.A. and A.G. acknowledge support from the Swedish Research Council and the Swedish Space Board. M.M.K. acknowledges support from the Hubble Fellowship and Carnegie-Princeton Fellowship.

Observations were made with the *Hubble Space Telescope*; the Nordic Optical Telescope, operated by the Nordic Optical Telescope Scientific Association at the Observatorio del Roque de los Muchachos, La Palma, Spain; and the Mount Abu 1.2 m Infrared Telescope, India. STSDAS is a product of the Space Telescope Science Institute, which is operated by AURA for NASA. V.S. acknowledges support from Fundação para a Ciência e a Tecnologia (Ciência 2008) and grant PTDC/CTE-AST/112582/2009.

REFERENCES

Amanullah, R., & Goobar, A. 2011, ApJ, 735, 20
Betoule, M., Kessler, R., Guy, J., et al. 2014, A&A, in press (arXiv:1401.4064)
Blondin, S., Prieto, J. L., Patat, F., et al. 2009, ApJ, 693, 207
Brown, P. J., Dawson, K. S., de Pasquale, M., et al. 2012, ApJ, 753, 22
Burns, C. R., Stritzinger, M., Phillips, M. M., et al. 2011, AJ, 141, 19
Cardelli, J. A., Clayton, G. C., & Mathis, J. S. 1989, ApJ, 345, 245
Dalcanton, J. J., Williams, B. F., Seth, A. C., et al. 2009, ApJS, 183, 67
Dilday, B., Howell, D. A., Cenko, S. B., et al. 2012, Sci, 337, 942
Elias-Rosa, N., Benetti, S., Cappellaro, E., et al. 2006, MNRAS, 369, 1880
Elias-Rosa, N., Benetti, S., Turatto, M., et al. 2008, MNRAS, 384, 107
Fitzpatrick, E. L. 1999, PASP, 111, 63
Folatelli, G., Phillips, M. M., Burns, C. R., et al. 2010, AJ, 139, 120
Foley, R. J., & Kirshner, R. P. 2013, ApJL, 769, L1
Goobar, A. 2008, ApJL, 686, L103
Goobar, A., Johansson, J., Amanullah, R., et al. 2014, ApJL, 784, L12
Guy, J., Astier, P., Baumont, S., et al. 2007, A&A, 466, 11
Hsiao, E. Y., Conley, A., Howell, D. A., et al. 2007, ApJ, 663, 1187
Hsiao, E. Y., Marion, G. H., Phillips, M. M., et al. 2013, ApJ, 766, 72
Hutton, S., Ferreras, I., Wu, K., et al. 2014, MNRAS, 440, 150
Johansson, J., Amanullah, R., & Goobar, A. 2013, MNRAS, 431, L43
Krisciunas, K., Prieto, J. L., Garnavich, P. M., et al. 2006, AJ, 131, 1639
Marion, G. H., Sand, D. J., Hsiao, E. Y., et al. 2014, ApJ, submitted (arXiv:1405.3970)
Matheson, T., Joyce, R. R., Allen, L. E., et al. 2012, ApJ, 754, 19
Mazzali, P. A., Sullivan, M., Hachinger, S., et al. 2014, MNRAS, 439, 1959
Milne, P. A., Brown, P. J., Roming, P. W. A., et al. 2010, ApJ, 721, 1627
Nobili, S., & Goobar, A. 2008, A&A, 487, 19
Nugent, P., Kim, A., & Perlmutter, S. 2002, PASP, 114, 803
Patat, F., Chandra, P., Chevalier, R., et al. 2007, Sci, 317, 924
Patat, F., Cordiner, M. A., Cox, N. L. J., et al. 2013, A&A, 549, A62
Pereira, R., Thomas, R. C., Aldering, G., et al. 2013, A&A, 554, A27
Perlmutter, S., Aldering, G., Goldhaber, G., et al. 1999, ApJ, 517, 565
Riess, A. G., Filippenko, A. V., Challis, P., et al. 1998, AJ, 116, 1009
Schlegel, D. J., Finkbeiner, D. P., & Davis, M. 1998, ApJ, 500, 525
Valenti, S., Fraser, M., Benetti, S., et al. 2011, MNRAS, 416, 3138
Wang, L. 2005, ApJL, 635, L33

Paper V

J. Johansson, A. Goobar, M. M. Kasliwal, G. Helou, F. Masci,
S. Tinyanont, J. Jencson, Y. Cao, O. D. Fox, M. Kromer, R. Amanullah,
D. P. K. Banerjee, V. Joshi, E. Kankare, T. A. Prince
Spitzer observations of SN 2014J and properties of mid-IR emission in Type Ia Supernovae
arXiv:1411.3332 (Submitted to MNRAS).

Mon. Not. R. Astron. Soc. **000**, 1–?? (2012) Printed 6 December 2014 (MN LaTeX style file v2.2)

Spitzer observations of SN 2014J and properties of mid-IR emission in Type Ia Supernovae

J. Johansson[1⋆], A. Goobar[1], M. M. Kasliwal[2], G. Helou[3], F. Masci[3], S. Tinyanont[4], J. Jencson[2], Y. Cao[2], O. D. Fox[5], M. Kromer[6], R. Amanullah[1], D. P. K. Banerjee[7], V. Joshi[7], A. Jerkstrand[8], E. Kankare[8], T. A. Prince[2]

[1] *The Oskar Klein Centre, Department of Physics, Stockholm University, SE 106 91 Stockholm, Sweden*
[2] *Division of Physics, Mathematics, and Astronomy, California Institute of Technology, Pasadena, CA 91125, U.S.A.*
[3] *Infrared Processing and Analysis Center, California Institute of Technology, M/S 100-22, Pasadena, CA 91125, U.S.A.*
[4] *IHarvey Mudd College, 301 Platt Boulevard, Claremont, CA 91711*
[5] *Department of Astronomy, University of California, Berkeley, CA 94720-3411, U.S.A.*
[6] *The Oskar Klein Centre, Department of Astronomy, Stockholm University, SE 106 91 Stockholm, Sweden*
[7] *Astronomy and Astrophysics Division, Physical Research Laboratory, Navrangpura, Ahmedabad, INDIA 380009*
[8] *Astrophysics Research Center, School of Mathematics and Physics, Queen's University Belfast, BT7 1NN, UK*

Submitted to MNRAS, 12 November 2014

ABSTRACT

SN 2014J in M 82 is the closest Type Ia supernova (SN Ia) in decades. The proximity allows for detailed studies of supernova physics and provides insights into the circumstellar and interstellar environment. In this work we analyze *Spitzer* mid-IR data of SN 2014J in the 3.6 and 4.5 μm wavelength range, together with several other nearby and well-studied SNe Ia. We compile the first composite mid-IR light-curve templates from our sample of SNe Ia, spanning the range from before peak brightness well into the nebular phase. Our observations indicate that SNe Ia form a very homogeneous class of objects at these wavelengths. Using the low-reddening supernovae for comparison, we constrain possible thermal emission from circumstellar dust around the highly reddened SN 2014J. We also study SNe 2006X and 2007le, where the presence of matter in the circumstellar environment has been suggested. No significant mid-IR excess is detected, allowing us to place the most constraining upper limits to date on the amount of pre-existing dust in the circumstellar environment of any SN Ia. For SN 2014J, $M_{\rm dust} \lesssim 10^{-5}\,{\rm M}_{\odot}$ within $r_{\rm dust} \sim 10^{17}$ cm, which is insufficient to account for the observed extinction. Similar limits are obtained for SNe 2006X and 2007le.

Key words: ISM: dust, extinction – supernovae: general - circumstellar matter – supernovae: individual: 2005df, 2006X, 2007af, 2007le, 2007sr, 2009ig, 2012cg, 2011fe, 2014J

1 INTRODUCTION

The use of Type Ia supernovae (SNe Ia) as distance indicators remains essential for the study of the expansion history of the Universe and for exploring the nature of dark energy (see e.g. review by Goobar & Leibundgut 2011). However, a lack of understanding of the progenitor systems and the requirement for empirically derived colour-brightness corrections represent severe challenges for precision cosmology. SN 2014J in the starburst galaxy M 82 is the closest SN Ia in decades and offers a unique opportunity to study progenitor and explosion models, as well as the circumstellar (CS) and interstellar (IS) medium along the line-of-sight across an unprecedented wavelength range, from gamma-rays to radio (Diehl et al. 2014; Pérez-Torres et al. 2014).

Our *Spitzer* observations of SN 2014J, along with observations of other well-studied nearby SNe Ia, allow us to compile the first mid-IR light-curve templates, presenting us with a new wavelength range to confront theoretical models of SNe Ia. For example, the study of the mid-IR light-curve around the near-IR secondary maximum, shown by Kasen (2006) to be a valuable diagnostic of the physical parameters governing SN Ia explosions, could be used to test the validity of the model predictions.

Furthermore, by searching for excess mid-IR emission towards SN 2014J, we set constraints on the amounts of pre-existing CS dust that could account for the non-standard reddening measured by Goobar et al. (2014a); Amanullah

⋆ E-mail: joeljo@fysik.su.se

et al. (2014); Marion et al. (2014); Foley et al. (2014); Brown et al. (2014); Ashall et al. (2014), who otherwise find this SN to be a normal SN Ia, albeit with slightly higher than average expansion velocities, and showing signs of additional sources of luminosity in the first hours after the explosion (Goobar et al. 2014b). We also analyze other SNe Ia with peculiar reddening observed with *Spitzer* , SNe 2006X and 2007le, where CS material has been reported (Patat et al. 2007; Simon et al. 2009).

The outline of this paper is as follows: In Section 2 we present the observations, followed by a description in Section 3 of how the mid-IR light-curve templates are constructed. In Section 4 we add this new wavelength range along with optical and near-IR spectra, to present the spectral energy distribution (SED) in the full range 0.4 – 5.0 μm. The implications for emission from heated CS dust are discussed in Section 5, followed by concluding remarks in Section 6.

2 OBSERVATIONS

2.1 SN 2014J

SN 2014J was observed with *Spitzer* over 6 epochs between January 28 and March 3 and 4 epochs between May 31 and July 8 under the *SPitzer InfraRed Intensive Transients Survey* (SPIRITS) program (PI: M. Kasliwal). SPIRITS is an ongoing infrared survey that systematically searches two hundred nearby galaxies for all types of transients and variables within a volume of 20 Mpc. Data is promptly processed with subtractions relative to archival images in the Spitzer Heritage Archive. The SPIRITS team undertakes a large concomitant ground-based survey in the optical and near-IR to characterize the *Spitzer* findings. For additional details about the survey and first discoveries, see Kasliwal et al. *in prep.*

Aperture photometry was performed at the location of the SN on the aligned *Spitzer* Post-Basic Calibrated Data for the SN and pre-SN images. Throughout the paper we use the zero magnitude fluxes for the IRAC Channels 1 and 2 (CH1 and CH2, with central wavelengths of 3.6 and 4.5 μm, respectively) of $F_{\nu,0}^{\rm CH1} = 280.9$ Jy and $F_{\nu,0}^{\rm CH2} = 179.7$ Jy.

We also present new optical and near-IR spectra (summarized in Table 2) and photometry (to be published in a future paper) of SN 2014J in Figs. 1 and 2.

2.2 Comparison Supernovae

In order to analyze our mid-IR data on SN 2014J we need to compare with other well-studied SNe Ia. For this study, we include SNe that have multi-epoch *Spitzer* data and good optical/near-IR coverage. **SN 2011fe** was observed with *Spitzer* starting 145 days after $B-$band maximum. UV data (Mazzali et al. 2014) and optical to near-IR observations (Pereira et al. 2013; Matheson et al. 2012) together with high-resolution spectroscopy (Patat et al. 2013), show that SN 2011fe suffered little to no extinction, $E(B-V) = 0.026 \pm 0.036$ mag, making it useful as a template of a pristine, normal SN Ia. We adopt a distance modulus to SN 2011fe of $\mu = 28.93 \pm 0.16$ mag ($D = 6.1 \pm 0.45$ Mpc) based on near-IR light curves from Matheson et al. (2012) which is in good agreement with the Cepheid distance in Mager et al. (2013). **SN 2012cg** was observed with *Spitzer* (PI: A. Goobar) starting 58 days after $B-$band maximum. The SN shows signs of modest host galaxy reddening, with a colour excess of $E(B-V) \approx 0.2$ mag, derived from both optical photometry and high-resolution spectroscopy (Silverman et al. 2012; Munari et al. 2013, Amanullah et al. in prep.). Using optical light curves, Munari et al. (2013) put SN 2012cg at a distance $\mu = 30.95$ mag, close to the Tully-Fisher estimate in Cortés et al. (2008). By accounting for the reddening and scaling the NIR photometry in Amanullah et al. (in prep.) to match SN 2011fe, we adopt a distance modulus of $\mu = 30.70 \pm 0.16$ mag ($D = 13.8 \pm 1.0$ Mpc).

To compare our limits on CS dust for SN 2014J we also include archival data of the reddened SNe 2006X and 2007le. **SN 2006X** in M 100 was observed by *Spitzer* (PI's: P. Meikle and R. Kotak) starting 136 days after $B-$band maximum. Similar to SN 2014J, 2006X showed signs of non-standard reddening, $E(B-V) \sim 1.4$ mag with $R_V \sim 1.5$ (Wang et al. 2008b; Folatelli et al. 2010). **SN 2007le** suffered less extinction than SN 2006X, $E(B-V) \sim 0.39$ mag, but also had a low $R_V \sim 1.5$ (Burns et al. 2014). The detection of time varying Na I D absorption for both these SNe has been interpreted as being due to CSM at distances $\sim 10^{17}$ cm from the SN (Patat et al. 2007; Simon et al. 2009). Since the SNe are reddened, it has been speculated that dust in the CS environment could play an important role. We also include data of **SN 2005df** and **SN 2009ig** previously presented in McClelland et al. (2013) and Gerardy et al. (2007), adding two epochs for SN 2009ig at -3 and +36 days from peak brightness, serendipitously observed with *Spitzer* (PI: K. Sheth). **SN 2007af** and **SN 2007sr** were observed with *Spitzer* (PI: R. Kotak) and have well measured optical/near-IR light-curves and precise Cepheid distance estimates (Riess et al. 2011).

3 MID-IR LIGHT CURVES

SN 2014J is the best object to date to build mid-IR light-curve templates, capturing the full range from before peak brightness to the nebular phase. To fill in the gaps, caused by limited visibility windows and scheduling constraints, we make use of archival data of the SNe Ia described in Sect. 2.2. The composite light-curves shown in Fig. 1 are compiled by shifting each SN by their estimated distance modulus and correcting for host galaxy and Milky Way extinction (see Table 1). We do not find evidence for variations in the in the mid-IR light-curve shapes corresponding to the different optical decline rates in our sample, $\Delta m_{15}^B = 0.9$ to 1.3, suggesting that SNe Ia are a very homogeneous class of objects at longer wavelengths. A larger sample of SNe Ia with multi-epoch mid-IR coverage is needed to make a more quantitative study. Three different decline time scales can be recognized in the CH1 and CH2 light-curves. Although our first detections are before the optical and near-IR maximum brightness, we can not fully measure the mid-IR light-curve shapes at these epochs, i.e. fitting the time of maximum in CH1 and CH2 is impossible. However, fitting the early epochs (-5 d to 15 d from B-band maximum) gives linear decline rates of 0.081 and 0.135 mag d^{-1} in CH1 and CH2 respectively, similar to the decline rates in optical bands.

A break in the mid-IR light-curves occurs ~15 days after $B-$band maximum. This roughly coincides with the onset of the secondary maximum in the near-IR bands, although data from +15 to +30 days show no signs of a secondary maximum in the mid-IR. From 15 days after $B-$band maximum and onwards, the decline rate changes to 1.67 and 1.93 mag/100d in CH1 and CH2, respectively. After $\sim$ 150 days past $B-$band maximum the linear decline rates of SN 2011fe are 1.48 mag/100d and 0.78 mag/100d in CH1 and CH2, respectively. The decline rate in CH1 is similar to what is observed at optical wavelengths, while the decline in CH2 is slower, which can also be seen in the CH1$-$CH2 color panel in Fig. 1 as a change towards redder colors. McClelland et al. (2013) analyze the mid-IR late-time (> 200 days) decline rates for four SNe (SN 2011fe, SN 2009ig, SN 2008Q and SN 2005df) and argue that the different decline rates are a result of doubly ionized elements dominating the bluer CH1 band (3.6 μm) while singly ionized iron-peak species are controlling the redder CH2 band (4.5 μm). They also suggest that the interpolated color at +230 days correlates with the light-curve decline rate at maximum brightness, i.e. with Δm_{15}^{B}.

4 SPECTRAL ENERGY DISTRIBUTION

Lacking spectra in the wavelength range probed by our *Spitzer* observations, we examine how the shape of the SED, as measured through optical/near-IR spectroscopy together with the *Spitzer* broad-band observations, matches model spectra from numerical simulations. In Fig. 2 we show observed optical and near-IR spectra (red lines) together with optical, near-IR and mid-IR broad-band photometry (red circles) of SN 2014J at three epochs (5, 31 and 126 days after B-band maximum).

To this end, we have calculated synthetic spectra for the hydrodynamic explosion model W7 (Nomoto et al. 1984). W7 is known to reproduce the observed characteristics of normal SNe Ia at optical (e.g. Branch et al. 1985) and near-IR wavelengths (e.g. Gall et al. 2012). To obtain synthetic spectra at 5 and 31 days past B-band maximum we performed radiative transfer simulations using the ARTIS code (Kromer & Sim 2009) and the atomic data set described in Gall et al. (2012). For the latest epoch (+126 days past B-band maximum) we used a nebular code (described in Jerkstrand et al. 2011, 2014). The flux in the model spectra between $B-$band maximum and +10 days stems from a mixture of Co II, Co III and Fe II features and a tiny contribution from intermediate-mass elements. Starting at 10 days after maximum, the flux in the 2.8 to 3.5 micron region is dominated by singly-ionized iron-group elements. The lines in the W7 model possibly contributing to the flux in CH1 can be attributed to Ni II (at 2.85, 2.95, 3.11, 3.29 and 3.54 μm) and Fe II (3.08 μm).

In the late-time model spectrum (+126 days after maximum), the fluxes in the optical and near-IR agree with the observations while the flux levels in the mid-IR are underpredicted. The dominant lines in CH1 and CH2 are [Fe II], with little contribution from [Co II]. In CH1 there is also [Fe III] (at 2.90 and 3.04 μm) and [Co III] (at 3.48 μm) emission.

Our observations, shown in Figs. 1 and 2, bridge the gap between the late-time near-IR spectra in Friesen et al. (2014) and mid-IR spectra of SN 2014J in the 8–13 μm wavelength range in Telesco et al. (2014). Friesen et al. (2014) present near-IR spectra of SN 2014J at 70 days past maximum and find that [Ni II] fits the emission feature near 1.98 μm, suggesting that a substantial mass of ^{58}Ni exists near the center of the ejecta, arising from nuclear burning at high density. A tentative identification of Mn II at 1.15 μm may support this conclusion as well. Telesco et al. (2014) compare their observed mid-IR spectra to a delayed detonation model with $\sim$ 0.6 M$_\odot$ of ^{56}Ni and claim that the model is consistent with observations. Recent multi-dimensional hydrodynamical simulations of Chandrasekhar-mass explosions, however, struggle in producing a concentration of stable iron-group elements near the center of the ejecta (e.g. Seitenzahl et al. 2013).

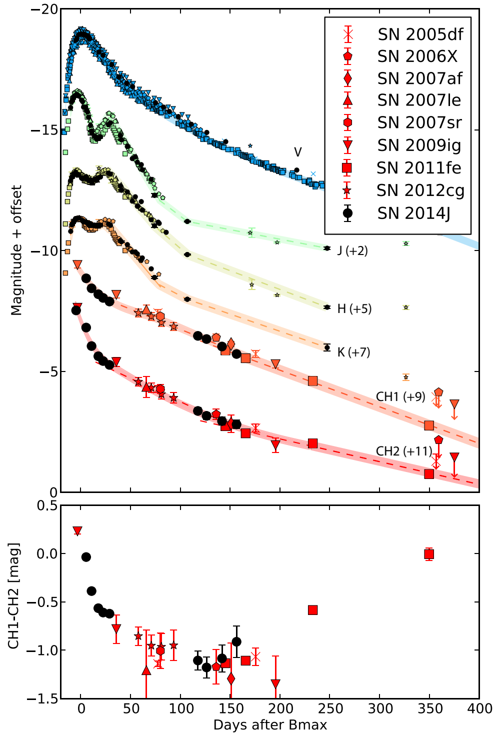

Figure 1. Upper panel: Absolute magnitude V-band, near-IR (J, H and K-band) and mid-IR light-curves of the Type Ia SNe used in this study. The magnitudes have been de-reddened using the best fit extinction values and shifted by the distance moduli (typically known to $\sim$ 0.2 mag accuracy) listed in Tab. 1. The lower panel shows the *Spitzer* CH1$-$CH2 colour evolution.

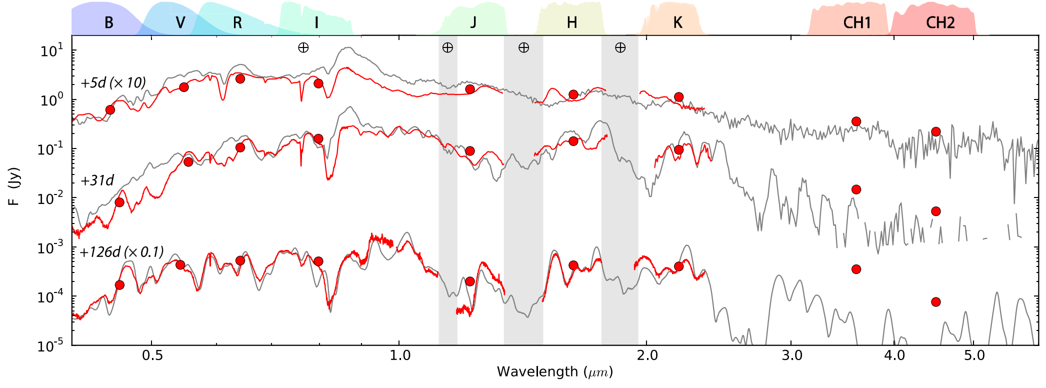

Figure 2. Observed SEDs at +5, +31 and +126 days past *B*-band maximum from optical/NIR spectroscopy (red lines) and broad band *BVRIJHK* and *Spitzer* CH1 and CH2 photometry (red circles). For comparison, synthetic spectra of the W7 model (gray lines) at similar epochs are shown. Vertical, gray bars indicate regions of low atmospheric transmission.

5 CONSTRAINTS ON EMISSION FROM CS DUST

The existence of CS material around individual nearby SNe Ia has been suggested by studies of sodium absorption lines (e.g. SNe 1999cl, 2006X, 2007le, and PTF11kx Patat et al. 2007; Blondin et al. 2009; Simon et al. 2009; Dilday et al. 2012). High-resolution spectra reveal the presence of time-variable and blueshifted Na I D features, possibly originating from CSM within the progenitor system. Studies of large samples of SNe Ia (Sternberg et al. 2011) find that half of all SNe Ia with detectable Na I D absorption at the host-galaxy redshift have Na I D line profiles with significant blueshifted absorption relative to the strongest absorption component. This indicates that the absorption occurs in the vicinity of the progenitor systems rather than in the ISM. For SN 2014J, high-resolution spectra show that the line of sight is very rich in absorbing material, but reveal no signs of time-variable Na I D absorption (Goobar et al. 2014a; Foley et al. 2014; Welty et al. 2014; Ritchey et al. 2014). The wavelength dependent extinction towards SN 2014J has been measured with great accuracy using a very wide wavelength range, 0.2 – 2.2 μm, through a combination of *Hubble Space Telescope* and ground-based observations. Amanullah et al. (2014) found that the reddening can be described with either a MW-type extinction law with a low value of the total-to-selective extinction, $R_V = 1.4 \pm 0.1$, i.e., corresponding to non-standard dust grains in the ISM, or by invoking the effective extinction law from Goobar (2008). The latter arises from multiple scattering of photons on “normal” dust grains, but surrounding the supernova, i.e., in the CS medium, as also discussed by Wang (2005).

Non-standard reddening has been noted in studies of individual and large samples of SNe Ia. For example, the extinction of SN 2006X was studied in Folatelli et al. (2010), showing that the reddening is incompatible with the average extinction law of the Milky Way. Their findings augmented the large body of evidence indicating that the reddening of many SNe Ia show a steeper wavelength dependence ($R_V < 3.1$) than that which is typically observed for stars in our Galaxy. Previously, Nobili & Goobar (2008) derived $R_V = 1.75 \pm 0.27$ from a statistical study of 80 low-redshift SNe Ia. Similarly, when the colour-brightness relation is fitted jointly with cosmological parameters in the SN Ia Hubble diagram, using a wide range of SN Ia redshifts, low values of R_V are obtained (see e.g. Betoule et al. 2014, for a recent compilation).

Amanullah & Goobar (2011) simulated the impact of thin CS dust shells located at radii $r_{\rm d} \sim 10^{16} - 10^{19}$ cm ($\sim 0.003 - 3$ pc) from the SN and found that this scenario would also perturb the optical light-curve shapes and introduce a time dependent color excess, $\Delta E(B-V) \sim 0.05 - 0.1$ mag. Foley et al. (2014) claim to have detected a time variable color excess for SN 2014J, which led them to conclude that dimming by CS dust accounts for about half of the extinction. However, this interpretation has been challenged by Brown et al. (2014). By exploring the mid-IR wavelength range, we have a unique way to test if dust in the CSM plays a significant role in explaining the non-standard reddening towards SN 2014J and other highly reddened normal SNe Ia.

5.1 Dust models

If pre-existing CS dust is the source of non-standard reddening, it will be radiatively heated by absorption of UV/optical photons from the SN or collisionally heated by the SN shock. Thermal emission at IR wavelengths could therefore be the “smoking gun” for detecting or ruling out the presence of CS dust. To model the emission from pre-existing CS dust we consider the idealized case (described in Hildebrand 1983; Dwek 1985; Fox et al. 2010) of an optically thin (at mid-IR wavelengths) dust cloud of mass $M_{\rm d}$ with dust particles of radius a, emitting thermally at a single equilibrium temperature $T_{\rm d}$. The expected flux at a distance D is,

$$F_\nu = M_d \frac{\kappa_\nu(a) B_\nu(T_{\rm d})}{D^2}, \quad (1)$$

where $B_\nu(T_\mathrm{d})$ is the Planck blackbody function and the dust mass emissivity coefficient, $\kappa_\nu(a)$, is

$$\kappa_\nu(a) = \left(\frac{3}{4\pi\rho a^3}\right)\pi a^2 Q_\nu(a) = \frac{3Q_\nu(a)}{4a\rho}. \quad (2)$$

$Q_\nu(a)$ is the absorption efficiency and the dust bulk (volume) density, $\rho \approx 2-3\,\mathrm{g\,cm^{-3}}$ depending on grain composition. Since we do not know the nature of the SN Ia progenitor systems and their potential dust production mechanisms, we will consider separate scenarios of either silicate or graphite grains of radius $a = 0.1\,\mu$m and a mixture of silicate and graphitic grains of different sizes (MW3.1) that reproduce the standard $R_V = 3.1$ Milky Way dust properties (described in Draine & Lee 1984; Laor & Draine 1993; Weingartner & Draine 2001).

In what follows, we treat the low-reddening SNe 2011fe and 2012cg as mid-IR templates of a SN Ia, to put limits on any possible excess emission from CS dust around the highly-reddened SNe 2014J, 2006X and 2007le. Taking both instrumental noise and distance modulus uncertainties into account, the differences between the reddened and un-reddened SNe are not statistically significant. Hence, we compute 3σ upper limits on the dust temperature and mass for SN 2014J (red contours in Fig. 3) as well as for other SNe (red contours in Fig. 4). We complement this with a similar analysis using $K-$band data of SNe 2014J and 2006X (green contours in Fig. 4).

5.2 Expected emission from heated dust in the thin shell approximation

Although the geometric distribution of CS dust could be complex, we adopt the simple thin shell approximation to provide an estimate of the expected mid-IR emission from heated dust, to be compared with the models for reddening proposed in Goobar (2008); Amanullah & Goobar (2011). This allows us to estimate the expected temperature as a function of shell radius, shown as the right-hand side vertical axis of Figs. 3 and 4. We estimate the minimal dust shell radius, $r_\mathrm{d} = ct/2$, that could give rise to a detectable IR echo at each observed epoch, t. Dust at this radius will be heated to

$$T_\mathrm{d,exp} \sim 4.0\left(\frac{L}{a}\right)^{\frac{1}{6}} r_\mathrm{d}^{-\frac{1}{3}}, \quad (3)$$

where we assume that the peak SN bolometric luminosity of $\sim 3\times10^9\,\mathrm{L}_\odot$ is heating a spherical dust shell with grain sizes of $a = 0.1\,\mu$m (Kruegel 2003). The upper bound on the dust temperature is set by the evaporation temperature of the dust grains ($T \lesssim 2000\,$K), corresponding to a minimal dust survival radius $r_\mathrm{evap} \sim 10^{16}$ cm.

Furthermore, in order for a thin dust shell at r_d to have significant opacity in the optical $V-$band, $\tau(V) \sim 1$, the required dust mass can be estimated from the absorption cross-sections, $\sigma_\mathrm{abs}(\lambda = 0.55\mu\mathrm{m})/m_\mathrm{dust} = \kappa_V$, as

$$M_\mathrm{d,exp} \sim 4\pi r_\mathrm{d}^2 \frac{\tau(V)}{\kappa(V)}, \quad (4)$$

where $\kappa(V) \sim 5\cdot10^4\mathrm{cm^2\,g^{-1}}$ for graphitic grains, $\kappa(V) \sim 2\cdot10^3\mathrm{cm^2\,g^{-1}}$ for silicate grains of size $a = 0.1\,\mu$m and $\kappa(V) \sim 2\cdot10^3\mathrm{cm^2\,g^{-1}}$ for the MW3.1 mixture. Thus, for a thin spherical dust shell at r_d the total dust mass, $M_\mathrm{d,exp} \sim 10^{-4} - 10^{-5}\left(r_\mathrm{d}/10^{16}\mathrm{cm}\right)^2\mathrm{M}_\odot$, depending on dust grain composition, is needed to explain the observed reddening if it mainly arises in the CS environment. This corresponds to the blue lines in Figs. 3 and 4. The black horizontal lines in Fig. 3 indicate the expected dust temperature (and corresponding shell radius) at two of the epochs (29 and 157 days from B-band maximum) from where the limits are derived for SN 2014J. Similarly, the symbols in Fig. 4 indicate the limits derived at different epochs for an extended sample of SNe observed with *Spitzer*.

Using K-band data for SNe 2014J and 2006X, to explore possible emission from hot CS dust close to the exploding star ($T_\mathrm{d} \gtrsim 1200$ K for $r_\mathrm{d} < 5\cdot10^{16}$ cm), we are able to rule out $M_d > 10^{-5}\,\mathrm{M}_\odot$. By adding the *Spitzer* data we can significantly reduce the allowed parameter space, excluding $M_\mathrm{d} > 10^{-6}\,\mathrm{M}_\odot$ ($T_\mathrm{d} > 700$ K, for $r_\mathrm{d} < 2\cdot10^{17}$ cm).

Our combined limits for SNe 2014J correspond to a very severe upper limit on the possible amount of pre-existing dust surrounding the SN progenitor, $M_\mathrm{d} \lesssim 10^{-5}\,\mathrm{M}_\odot$ within $r_\mathrm{d} \sim 2\cdot10^{17}$ cm, depending on the assumed grain size and composition. However, regardless of the specific dust grain composition, the derived upper limits on the CS dust mass are significantly lower than what would be required to explain the observed reddening of SN 2014J, in apparent contraction to the claims in Foley et al. (2014). Similar limits are obtained for the reddened SNe 2006X and 2007le (see Fig. 4). For reference, we also show detections of dust around a subset of peculiar SNe Ia interacting strongly with a dense CSM (SNe Ia-CSM) in Fig. 4. *Spitzer* observations of SNe Ia-CSM 2002ic, 2005gj and 2008J (Fox et al. 2011; Fox & Filippenko 2013; Taddia et al. 2012) show evidence for late-time (>500 days after maximum brightness) mid-IR emission from warm ($T_\mathrm{d} \sim 500$–$800\,$K) dust. Assuming a simple dust population of a single size ($a = 0.1\mu$m) graphitic grains yield dust masses of $0.006 - 0.022\,\mathrm{M}_\odot$. The dust parameters are most consistent with a pre-existing dust shell that lies beyond the forward-shock radius, most likely radiatively heated by optical and X-ray emission continuously generated by late-time CSM interaction.

6 SUMMARY AND CONCLUSIONS

We have analyzed the mid-IR light curves of SN 2014J and several other SNe Ia observed with *Spitzer*, spanning the range from before peak brightness well into the nebular phase. We have characterized, for the first time, the SN Ia light-curve evolution at 3.6 and 4.5 μm. Our observations indicate that SNe Ia form a very homogeneous class of objects at these wavelengths, possibly without any light-curve shape variations. In particular, the mid-IR light curves do not show any evidence for a secondary maximum, as opposed to the case in the near-IR. The latter was investigated by Kasen (2006) to explore the physics of the exploding system. Extending these studies to the now probed longer wavelengths should provide critical tests for SN Ia models.

The *Spitzer* observations provide a completely new way to test models for the circumstellar environment of SNe Ia and may help understanding the non-standard reddening measured both for individual SNe Ia and in the large SN Ia samples used to derive cosmological parameters.

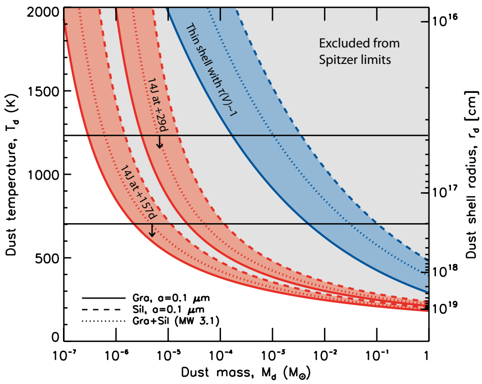

Figure 3. 3σ upper limits on dust emission around SN 2014J at 29 and 157 days after maximum brightness. The solid, dashed and dotted contours indicate limits using the graphitic, silicate and MW3.1 dust models. Assuming the thin shell approximation, we can estimate the expected dust temperatures and shell radii probed at these epochs (black lines) and the expected dust mass from Eq. 4 (blue lines).

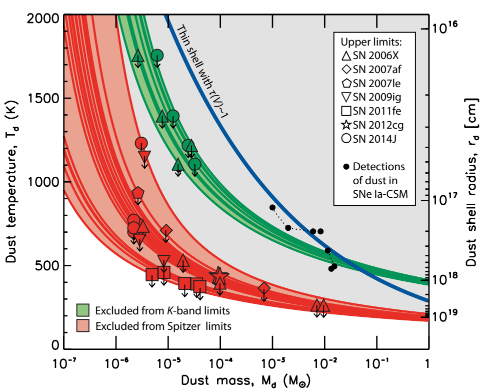

Figure 4. 3σ upper limits on CS dust emission around the reddened SNe 2014J, 2006X and 2007le at different epochs from $K-$band data (green contours and symbols) and *Spitzer* mid-IR data (red contours and symbols), assuming graphitic dust gains of radius 0.1 μm. Also shown are the *Spitzer* limits for SNe 2007af and 2009ig along with the late time non-detections of SNe 2011fe and 2012cg. The blue solid line indicates the expected dust mass from Eq. 4. Black dots are detections of warm dust around Ia-CSM SNe.

By comparing the measured mid-IR fluxes at different epochs for the reddened SNe 2014J, 2006X and 2007le to unreddened SNe, we can place strong constraints on the emission from heated dust within $\sim 10^{18}$ cm from the exploding stars. This allows us to exclude the possibility that the bulk of the observed extinction towards these highly-reddened SNe Ia is due to CS dust. Foley et al. (2014) claim that half of the extinction ($A_V \sim 1$ mag) towards SN 2014J can be attributed to CS dust, while the other half is due to interstellar dust in M 82. However, our limits on dust emission imply that at most $\tau(V) \approx A_V \lesssim 0.1$ mag of extinction can be accounted for by CS dust. We emphasize that the derived limits are relatively insensitive to the assumed dust models (as illustrated in Fig. 3). Thus, our findings reaffirm the conclusions from polarization studies of SNe 2014J and 2006X, which indicate that the dust in the line of sight towards these objects is most likely of interstellar nature (Kawabata 2014; Patat et al. 2014). Furthermore, the lack of heated material in the CS environment of SN 2014J is compatible with the non-detection in X-rays and radio (Margutti et al. 2014; Pérez-Torres et al. 2014). The only comparable previous study of searches for emission from heated circumstellar dust to date was carried out by Johansson et al. (2013), presenting far-IR non-detections of both SNe 2011fe and 2012cg using the *Herschel* PACS 70 μm instrument. These non-detections exclude CS dust masses $M_{\rm d} \gtrsim 7 \times 10^{-3}\,{\rm M}_\odot$ for dust temperatures $T_{\rm d} \sim 500$ K at a 3σ-level for SN 2011fe, while the upper limits are one order of magnitude weaker for SN 2012cg, excluding dust masses $M_{\rm d} \gtrsim 10^{-1}\,{\rm M}_\odot$. Thus, our *Spitzer* study is more than two orders of magnitude more sensitive than previous attempts.

The mid-IR non-detections for SNe 2006X, 2007le, 2011fe and 2012cg at late epochs (>600 days after max) can constrain the possible presence of dust at very large radii ($>10^{18}$ cm). E.g., Soker (2014) proposed that the sodium responsible for the time variable absorption seen in SNe 2006X and 2007le is released from dust grains. In this model, the absorbing shell/ring, $\sim 1-10\,{\rm M}_\odot$, resides at distances $10^{17}-10^{19}$ cm away from the SN, most likely concentrated in an equatorial plane. This range, probed by our observations shown in Fig. 4 , is larger than what a regular AGB wind can supply, but is compatible with a planetary nebula shell or a planetary nebula shell that entrained some interstellar medium (ISM). Light echoes have been detected for reddened SNe 2014J and 2006X (Crotts 2014; Wang et al. 2008a), and reportedly from the low-reddening SNe 2007af and 2009ig (Drozdov et al. 2014; Garnavich et al. 2013). Our observations can provide limits on the allowed distance at which the reflecting dust responsible for these echoes can exist. Furthermore, Nozawa et al. (2011) investigate the possibility of forming new dust grains in SN Ia ejecta. They compare their dust-formation models with *Spitzer* photometry for SN 2005df (Gerardy et al. 2007) and derive an upper limit of $0.1\,{\rm M}_\odot$ of newly formed dust after $\sim 100-300$ days. Our limits are stricter by at least an order of magnitude.

To summarize, this work significantly expands on previous efforts to study the wide wavelength range of the SED of SNe Ia and provides the first statistical sample of SNe Ia in the mid-IR and a detailed study of the highly reddened object SN 2014J and its CS environment. The non-detection of thermal emission from heated dust in the CS environment of SN 2014J, as well as for SNe 2006X and 2007le where the detection of circumstellar matter at 10^{17} cm has been claimed, argues against the proposed explanation for the non-standard reddening of SNe Ia invoking multiple-scattering on CS dust (Wang 2005; Goobar 2008). Thus, the non-standard reddening may be unrelated to the SN site and originate from the host galaxy ISM being different than what has been derived for the Milky Way. This could have a serious impact for our understanding of the properties of dust grains in distant galaxies, with profound implications for essentially all areas of extragalactic astronomy.

ACKNOWLEDGEMENTS

We are greatful to Claes Fransson for stimulating discussions. RA and AG acknowledge support from the Swedish Research Council and the Swedish Space Board. MMK acknowledges support from the Hubble Fellowship and Carnegie-Princeton Fellowship. We acknowledge the John von Neumann Institute for Computing for granting computing time on the supercomputer JUQUEEN at the Jülich Supercomputing Centre. Observations made with the *Spitzer* telescope, the Nordic Optical Telescope, operated by the Nordic Optical Telescope Scientific Association at the Observatorio del Roque de los Muchachos, La Palma, Spain, of the Instituto de Astrofisica de Canarias and the Mount Abu 1.2m Infrared telescope, India.

REFERENCES

Amanullah R., Goobar A., 2011, ApJ, 735, 20
Amanullah R. et al., 2014, ApJL, 788, L21
Ashall C., Mazzali P., Bersier D., Hachinger S., Phillips M., Percival S., James P., Maguire K., 2014, ArXiv e-prints
Betoule M. et al., 2014, A&A, 568, A22
Blondin S., Prieto J. L., Patat F., Challis P., Hicken M., Kirshner R. P., Matheson T., Modjaz M., 2009, ApJ, 693, 207
Branch D., Doggett J. B., Nomoto K., Thielemann F.-K., 1985, ApJ, 294, 619
Brown P. J. et al., 2014, ArXiv e-prints
Burns C. R. et al., 2014, ApJ, 789, 32
Cortés J. R., Kenney J. D. P., Hardy E., 2008, ApJ, 683, 78
Crotts A., 2014, ArXiv e-prints
Diehl R. et al., 2014, Science, 345, 1162
Dilday B. et al., 2012, Science, 337, 942
Draine B. T., Lee H. M., 1984, ApJ, 285, 89
Drozdov D., Leising M. D., Milne P. A., Pearcy J., Riess A. G., Macri L. M., Bryngelson G. L., Garnavich P. M., 2014, ArXiv e-prints
Dwek E., 1985, ApJ, 297, 719
Folatelli G. et al., 2010, AJ, 139, 120
Foley R. J. et al., 2012, ApJ, 744, 38
Foley R. J. et al., 2014, ArXiv e-prints
Fox O. D., Chevalier R. A., Dwek E., Skrutskie M. F., Sugerman B. E. K., Leisenring J. M., 2010, ApJ, 725, 1768
Fox O. D. et al., 2011, ApJ, 741, 7
Fox O. D., Filippenko A. V., 2013, ApJL, 772, L6
Friesen B., Baron E., Wisniewski J. P., Parrent J. T., Thomas R. C., Miller T. R., Marion G. H., 2014, ApJ, 792, 120
Gall E. E. E., Taubenberger S., Kromer M., Sim S. A., Benetti S., Blanc G., Elias-Rosa N., Hillebrandt W., 2012, MNRAS, 427, 994
Garnavich P. M., Milne P., Bryngelson G. L., Leising M. D., 2013, in American Astronomical Society Meeting Abstracts, Vol. 222, American Astronomical Society Meeting Abstracts, p. #209.04
Gerardy C. L. et al., 2007, ApJ, 661, 995
Goobar A., 2008, ApJL, 686, L103
Goobar A. et al., 2014a, ApJL, 784, L12
Goobar A. et al., 2014b, ArXiv e-prints
Goobar A., Leibundgut B., 2011, Annual Review of Nuclear and Particle Science, 61, 251
Hicken M. et al., 2009, ApJ, 700, 331
Hildebrand R. H., 1983, QJRAS, 24, 267
Jerkstrand A., Ergon M., Smartt S. J., Fransson C., Sollerman J., Taubenberger S., Bersten M., Spyromilio J., 2014, ArXiv e-prints
Jerkstrand A., Fransson C., Kozma C., 2011, A&A, 530, A45
Johansson J., Amanullah R., Goobar A., 2013, MNRAS, 431, L43
Kasen D., 2006, ApJ, 649, 939
Kawabata, K. S. e. a., 2014, ArXiv e-prints
Kromer M., Sim S. A., 2009, MNRAS, 398, 1809
Kruegel E., 2003, The physics of interstellar dust. Taylor & Francis
Laor A., Draine B. T., 1993, ApJ, 402, 441
Mager V. A., Madore B. F., Freedman W. L., 2013, ApJ, 777, 79
Margutti R., Parrent J., Kamble A., Soderberg A. M., Foley R. J., Milisavljevic D., Drout M. R., Kirshner R., 2014, ApJ, 790, 52
Marion G. H. et al., 2014, ArXiv e-prints
Marion G. H. et al., 2013, ApJ, 777, 40
Matheson T. et al., 2012, ApJ, 754, 19
Mazzali P. A. et al., 2014, MNRAS, 439, 1959
McClelland C. M., Garnavich P. M., Milne P. A., Shappee B. J., Pogge R. W., 2013, ApJ, 767, 119
Milne P. A. et al., 2010, ApJ, 721, 1627
Munari U., Henden A., Belligoli R., Castellani F., Cherini G., Righetti G. L., Vagnozzi A., 2013, New Astronomy, 20, 30
Nobili S., Goobar A., 2008, A&A, 487, 19
Nomoto K., Thielemann F.-K., Yokoi K., 1984, ApJ, 286, 644
Nozawa T., Maeda K., Kozasa T., Tanaka M., Nomoto K., Umeda H., 2011, ApJ, 736, 45
Patat F. et al., 2007, Science, 317, 924
Patat F. et al., 2013, A&A, 549, A62
Patat F. et al., 2014, ArXiv e-prints
Pereira R. et al., 2013, A&A, 554, A27
Pérez-Torres M. A. et al., 2014, ApJ, 792, 38
Riess A. G. et al., 2011, ApJ, 730, 119
Ritchey A. M., Welty D. E., Dahlstrom J. A., York D. G., 2014, ArXiv e-prints
Schweizer F. et al., 2008, AJ, 136, 1482
Seitenzahl I. R. et al., 2013, MNRAS, 429, 1156
Silverman J. M. et al., 2012, ApJL, 756, L7
Simon J. D. et al., 2009, ApJ, 702, 1157
Simon J. D. et al., 2007, ApJL, 671, L25
Soker N., 2014, MNRAS, 444, L73
Sternberg A. et al., 2011, Science, 333, 856
Taddia F. et al., 2012, A&A, 545, L7
Telesco C. M. et al., 2014, ArXiv e-prints
Wang L., 2005, ApJL, 635, L33
Wang X., Li W., Filippenko A. V., Foley R. J., Smith N., Wang L., 2008a, ApJ, 677, 1060
Wang X. et al., 2008b, ApJ, 675, 626
Weingartner J. C., Draine B. T., 2001, ApJ, 548, 296
Welty D. E., Ritchey A. M., Dahlstrom J. A., York D. G., 2014, ApJ, 792, 106

Table 1. Type Ia supernovae observed in the mid-IR

Target	$t_{B,\mathrm{max}}$ MJD	Host galaxy	Distance modulus (mag)	Distance (Mpc)	$E(B-V)$ (mag)	R_V	Δm_{15}^{B} (mag)	Reference
2005df	53598.4	NGC 1559	31.26 (0.14)	15.7 (2.3)	0.03	3.1	1.20	1, 2, 3
2006X	53785.6	NGC 4321	30.91 (0.14)	15.2 (1.0)	1.24	1.6	1.29	4, 5
2007af	54173.8	NGC 5584	31.72 (0.07)	22.0 (0.7)	0.04	3.0	1.20	6, 7, 8
2007le	54398.9	NGC 7721	32.24 (0.16)	28.1 (2.1)	0.39	1.5	1.10	9
2007sr	54448.3	NGC 4038	31.66 (0.08)	21.5 (0.8)	0.13	1.6	0.97	6, 10
2009ig	55080.9	NGC 1015	32.82 (0.09)	36.6 (1.5)	<0.05	-	0.89	2, 11, 12
2011fe	55815.8	NGC 5457	28.93 (0.16)	6.1 (0.5)	0.03	3.1	1.11	2, 13, 14
2012cg	56082.0	NGC 4424	30.70 (0.16)	13.8 (1.0)	0.18	2.7	0.89	14, 15,16
2014J	56689.2	M 82	27.60 (0.16)	3.3 (0.15)	1.37	1.4	0.95	17, 18, 19

(1): Gerardy et al. (2007), (2): McClelland et al. (2013), (3): Milne et al. (2010), (4): Wang et al. (2008b), (5): Folatelli et al. (2010) (6): Riess et al. (2011), (7): Simon et al. (2007), (8): Hicken et al. (2009), (9): Burns et al. (2014), (10): Schweizer et al. (2008), (11): Foley et al. (2012), (12): Marion et al. (2013), (13): Matheson et al. (2012), (14): Munari et al. (2013), (15): Silverman et al. (2012), (16): Amanullah et al., *in prep.*, (17): Amanullah et al. (2014), (18): Foley et al. (2014), (19): Marion et al. (2014)

Table 2. Log of spectroscopic observations of SN 2014J

UT date	MJD	Days from B_{max}	Observatory / Instrument	Wavelength range (μm)	Exp. time (s)	Airmass
2014-02-06[a]	56694.9	+5.1	NOT/ALFOSC	0.35 – 0.90	180	1.61
2014-02-06[a]	56695.0	+5.2	Mt Abu	0.85 – 2.35	1200	1.59
2014-03-03	56718.9	+29.1	Mt Abu	0.85 – 2.35	1080	1.48
2014-03-05	56721.1	+31.3	NOT/ALFOSC	0.35 – 0.90	180	1.35
2014-06-07	56815.3	+125.5	Keck/MOSFIRE	1.15 – 2.35	480	2.19
2014-06-09	56817.2	+127.4	ARC/DIS	0.35 – 0.95	120	1.73

[a] Published in Marion et al. (2014).

Table 3. Spitzer observations and photometry of Type Ia supernovae in the mid-IR.

SN	MJD	Epoch (days)	$F_\nu^{\rm CH1}$ (μJy)	$F_\nu^{\rm CH2}$ (μJy)	CH1 (mag)	CH2 (mag)	Sub? (y/n)
2005df	53676.0	77.6	327.0 (6.7)	73.2 (5.7)	14.835 (0.022)	15.976 (0.082)	y
2005df	53774.0	175.6	68.3 (5.6)	16.4 (5.3)	16.535 (0.085)	17.602 (0.307)	y
2005df	53955.1	356.7	13.3 (5.2)	4.6 (5.3)	>18.136	>17.642	y
2006X	53922.2	136.1	157.9 (8.0)	35.3 (6.0)	15.626 (0.054)	16.768 (0.171)	y
2006X	54145.4	359.3	19.7 (8.0)	13.3 (6.0)	>17.750	>17.572	y
2006X	54662.7	876.6	-0.7 (7.6)	1.8 (5.9)	>17.731	>17.520	y
2006X	56722.8	2936.7	-6.9 (8.3)	-1.3 (6.5)	>17.633	>17.415	y
2006X	56751.9	2965.8	1.6 (8.6)	0.2 (6.3)	>17.586	>17.447	y
2007af	54324.9	151.1	62.2 (4.6)	12.8 (5.0)	16.594 (0.081)	17.865 (0.357)	y
2007af	55280.4	1106.6	2.4 (5.0)	2.2 (5.0)	>18.181	>17.696	y
2007le	54464.7	66.0	152.0 (5.0)	32.0 (5.0)	15.667 (0.059)	16.873 (0.312)	y
2007sr	54528.1	80.1	220.0 (8.0)	55.7 (10.0)	15.265 (0.146)	16.271 (0.146)	y
2007sr	55616.4	1168.4	3.3 (8.0)	19.2 (8.0)	>17.671	>17.186	y
2009ig	55076.9	-3.1	580.7 (10.0)	459.1 (10.0)	14.211 (0.019)	13.982 (0.023)	n
2009ig	55115.9	35.8	186.1 (8.0)	57.9 (8.0)	15.447 (0.046)	16.229 (0.140)	n
2009ig	55275.7	195.6	13.3 (1.4)	2.4 (0.7)	18.316 (0.110)	19.668 (0.270)	n
2009ig	55455.2	375.2	2.9 (1.1)	1.5 (0.8)	>19.876	>19.672	n
2011fe	55960.7	145.4	670.6 (8.5)	150.9 (6.4)	14.055 (0.014)	15.190 (0.045)	y
2011fe	55981.0	165.6	498.2 (8.1)	114.9 (6.3)	14.378 (0.018)	15.486 (0.058)	y
2011fe	56048.4	233.0	209.2 (7.0)	78.1 (5.7)	15.320 (0.036)	15.905 (0.076)	y
2011fe	56165.0	349.7	38.3 (5.7)	24.4 (5.4)	17.163 (0.151)	17.168 (0.217)	y
2011fe	56337.1	521.8	3.3 (5.6)	14.1 (6.1)	>18.058	17.763 (0.390)	y
2011fe	56348.1	532.8	2.5 (5.8)	15.6 (5.0)	>18.020	17.654 (0.302)	y
2011fe	56393.8	578.5	4.4 (5.1)	7.8 (7.7)	>18.160	>17.227	y
2011fe	56452.6	637.3	3.9 (6.0)	-2.6 (4.6)	>17.983	>17.787	y
2011fe	56742.8	927.5	-	2.4 (5.7)	-	>17.554	y
2011fe	56771.8	956.5	-	1.9 (5.8)	-	>17.534	y
2011fe	56902.0	1086.7	3.1 (7.4)	-8.9 (11.2)	>17.755	>16.820	y
2012cg	56139.9	57.9	549.0 (20.3)	160.0 (13.3)	14.272 (0.039)	15.126 (0.087)	y
2012cg	56152.9	70.9	481.0 (19.0)	128.0 (12.3)	14.416 (0.042)	15.368 (0.100)	y
2012cg	56163.1	81.1	380.0 (20.4)	100.0 (11.9)	14.672 (0.057)	15.636 (0.122)	y
2012cg	56175.4	93.4	326.0 (20.6)	87.0 (12.2)	14.838 (0.067)	15.788 (0.142)	y
2012cg	56723.8	641.8	11.9 (17.2)	6.2 (12.6)	>16.837	>16.694	y
2012cg	56751.9	669.9	4.1 (18.4)	2.2 (12.7)	>16.764	>16.682	y
2014J	56685.4	-4.5	-	42273.0 (200.0)	-	9.071 (0.005)	y
2014J	56695.4	5.6	35895.9 (154.9)	22130.1 (97.1)	9.734 (0.005)	9.774 (0.005)	y
2014J	56700.8	11.0	24508.9 (149.2)	10554.5 (95.9)	10.148 (0.007)	10.578 (0.010)	y
2014J	56707.6	17.8	18295.8 (117.4)	7130.0 (73.1)	10.466 (0.007)	11.004 (0.011)	y
2014J	56712.4	22.6	16491.0 (121.1)	5932.9 (75.2)	10.578 (0.008)	11.203 (0.014)	y
2014J	56718.8	29.0	14325.6 (129.4)	5145.3 (80.5)	10.731 (0.010)	11.358 (0.017)	y
2014J	56807.5	117.7	3812.2 (127.3)	876.4 (80.3)	12.168 (0.036)	13.280 (0.095)	y
2014J	56816.2	126.4	3273.6 (122.5)	766.0 (75.8)	12.334 (0.040)	13.426 (0.102)	y
2014J	56831.7	141.9	2338.2 (121.3)	600.4 (79.9)	12.699 (0.055)	13.690 (0.136)	y
2014J	56846.3	156.5	1922.3 (126.5)	448.6 (79.9)	12.912 (0.069)	14.007 (0.178)	y

Paper VI

R. Amanullah, **J. Johansson**, A. Goobar, R. Ferretti,
S. Papadogiannakis, T. Petrushevska, P. Brown, C. Contreras, H. Dahle,
N. Elias-Rosa, J. Fynbo, J. Gorosabel, L. Guaita, L. Hangard,
A. Howell, E. Y. Hsiao, E. Kankare, G. Leloudas, P. Lundqvist,
S. Mattila, P. E. Nugent, M. M. Phillips, A. Sandberg, V. Stanishev,
M. Sullivan, F. Taddia, G. Östlin

Diversity in extinction laws of SNe Ia measured with The Hubble Space Telescope

(Work in progress).

Mon. Not. R. Astron. Soc. **000**, 1–22 (2013) Printed December 17, 2014 (MN LaTeX style file v2.2)

Diversity in extinction laws of Type Ia supernovae measured with *The Hubble Space Telescope*

R. Amanullah,[1⋆] J. Johansson,[1] A. Goobar,[1] R. Ferretti,[1] S. Papadogiannakis,[1] T. Petrushevska,[1], P. Brown,[2] C. Contreras,[3] H. Dahle,[4] N. Elias-Rosa,[5] J. Fynbo,[6] J. Gorosabel,[7,8] L. Guaita,[9] L. Hangard,[1] A. Howell, E. Y. Hsiao,[9] E. Kankare,[10] G. Leloudas,[11] P. Lundqvist,[9] S. Mattila,[10] P. Nugent,[12,13] M. M. Phillips,[3] A. Sandberg,[9] V. Stanishev,[14] M. Sullivan,[15] F. Taddia,[9] G. Östlin[9]

Affiliations are listed at the end of the paper.

Draft version, 19 December 2014

ABSTRACT

We present near-ultraviolet (NUV) photometry of six Type Ia supernovae (SNe Ia) obtained with the *Hubble Space Telescope* and the *Swift* satellite and ground-based optical and near-infrared data which combined cover the wavelength range 0.2–2 μm. To this we add archival data of SN 2014J and obtain a sample spanning observed colour excesses $E(B-V) = 0.0$–1.4. We study the reddening time-evolution of each individual SN by comparing them to the colours of the normal SN Ia 2011fe and find a diversity of reddening laws when characterised by the total-to-selective extinction R_V. In particular, we note that for the two SNe with $E(B-V) \gtrsim 1$, for which the reddening is dominated by dust extinction, we find $R_V = 1.5 \pm 0.1$ and $R_V = 2.7 \pm 0.1$. Although high-extinction SNe Ia are rarely used for cosmology, adding NUV photometry reduces the uncertainty of fitted R_V with $\sim 50\,\%$ allowing us to also measure R_V individual low-extinction objects which point to a similar diversity.

Key words: ISM: dust, extinction – supernovae: general - circumstellar matter – supernovae: individual 2011fe, 2012bl, 2012bm, 2012cg, 2012cu, 2012cp, 2012et, 2014J– galaxies: individual ESO 234-19, UGC 8189, NGC 4424, UGC 8713, NGC 4772, MCG +04-55-47, M82

1 INTRODUCTION

Studies of the cosmological expansion history by using Type Ia supernovae (SNe Ia) has greatly improved our understanding of the Universe; starting with the initial discovery of the accelerating Universe from a few dozen SNe Ia (Riess et al. 1998; Perlmutter et al. 1999) to present constraints on the dark energy equation of state from several hundreds of SNe Ia out to $z \sim 1.5$ (e.g. Amanullah et al. 2010; Conley et al. 2011; Sullivan et al. 2011; Suzuki et al. 2012; Betoule et al. 2014).

When high-redshift SNe Ia are used to measure distances and derive cosmological parameters, each SN is first observed repeatedly in two or more broadband filters during its lifetime. The maximum brightness, lightcurve-shape and colour of the object is then obtained by fitting a SN Ia template to the data (eg Nugent et al. 2002; Goldhaber et al. 2001; Guy et al. 2005a; Guy et al. 2007; Hsiao et al. 2007; Conley et al. 2008; Burns et al. 2011). The fitted properties are then typically combined using linear and empirical lightcurve shape-brightness (Phillips 1993) and colour-brightness (Tripp 1998) relations to form a distance-dependant quantity.

The latter of these corrections is based on the observation that red SNe are intrinsically fainter than their bluer cousins, which likely originates from a combination of an intrinsic colour-luminosity relation and extinction by dust in the host galaxy. There is no a priori reason why these two effects should follow the same colour-luminosity relation, nor is it expected that host galaxy dust has the same properties in different SN environments. In fact, even in the Milky Way, different wavelength dependences have been observed for a variety of lines-of-sight.

When SNe Ia are used for studying cosmology these un-

⋆ rahman@fysik.su.se

certainties are handled by introducing a systematic error on the colour-luminosity relation which is propagated to the derived cosmological parameters. For the current cosmological constrains, the systematic uncertainties on the parameters, are of the same order as the statistical and the systematic error on the colour-luminosity relation is one of the dominating astrophysical uncertainties that enter the error budget. Addressing this relation, and in particular breaking the degeneracy between the intrinsic component and extinction is important in order for future SN Ia surveys to improve beyond the current cosmological constraints.

The properties and wavelength dependent extinction of dust in the Milky Way has been carefully studied and is commonly characterised by the total, A_V, to selective, $E(B-V) = A_B - A_V$, extinction ratio as $R_V = A_V/(A_B - A_V)$. Lower values of R_V correspond to *steeper* extinction laws, since, for a given total extinction, A_V, these imply a larger reddening, $E(B-V)$. In the Milky Way the value of R_V typically varies between $R_V = 2$–6, for different lines of sight, with an average value for $R_V = 3.1$.

The reddening law of SNe Ia can be studied by comparing observed SN colours to the expected for a similar unreddened source. Several such studies of individual SNe Ia (e.g. Elias-Rosa et al. 2006, 2008; Krisciunas et al. 2007; Folatelli et al. 2010; Amanullah et al. 2014, from hereon A14) in nearby galaxies, point to significantly lower values than what has been seen in the Milky Way. Also, since several of these SNe Ia are highly reddened, the observed reddening is likely dominated by host extinction. For low extinction SNe this is not the case, and it is in general difficult to measure R_V to high precision for individual SNe. Chotard et al. (2011) and Scolnic et al. (2014) point to the importance of properly accounting for intrinsic colour variations. Further, Chotard et al. (2011) find $R_V = 2.8 \pm 0.3$, consistent with the Milky Way average, for their sample of 72 SNe Ia of which 69 had $E(B-V) < 0.3$.

On the other hand, several other statistical studies of SNe Ia samples have found significantly lower R_V values (e.g. Astier et al. 2006; Nobili & Goobar 2008; Burns et al. 2014, from hereon B14). Although, the B14 results, which are based on SNe Ia colours from the near-infrared (NIR) to the optical observed by the Carnegie Supernova Project, indicate that low extinction SNe Ia follow a reddening law with $R_V \approx 3$ while highly extinguished objects appear to prefer lower values ($R_V \approx 1.7$), which is in agreement with previous studies (Folatelli et al. 2010). If this is the case, reddening laws from SNe Ia samples under the assumption that they all follow the same law could depend on the colour distributions of the samples. Measuring the reddening law for low-extinction SNe Ia is in itself difficult and in this work we will address this challenge by using data over a broad wavelength range, from NIR to near-ultraviolet (NUV).

The degeneracy between an intrinsic colour-luminosity relation and dust extinction, can also be approached by studying the relation between SN colours and spectroscopic properties. Wang et al. (2009) found $R_V = 1.6$ for SNe Ia with "high" photospheric velocities (HV) at maximum ($> 11,800\,\mathrm{km/s}$), while they obtained $R_V = 2.6$ for objects with "normal" velocity (NV) ($< 11,800\,\mathrm{km/s}$). The velocities were quantified by measuring the velocity of the Si II 6355 Å absorption feature. Foley & Kasen (2011) confirmed their findings but further obtain $R_V \approx 2.5$ for the separate subsamples when SNe with $E(B-V) > 0.35$ mag were omitted. A possible velocity-R_V relation could suggest that different SN types, with different velocities, explode in different host environments with different dust properties.

An alternative explanation could be that the scenario leading up to a HV SN may give rise to circumstellar (CS) dust layer. If a SN Ia is surrounded by CS dust, multiple scattering of the emitted SN photons would give rise to reddening laws with low R_V values, similar to what has been observed, even if the dust properties are similar to the Milky Way (Wang 2005; Goobar 2008). The explanation for this is that due to the CS dust geometry, scattered photons can still reach the observer which is extremely unlikely for ordinary interstellar dust. The presence of CS dust could also affect other SN observables (Amanullah & Goobar 2011). For example multiply scattered photons will arrive later and would give rise to a plateau shape of the late-time tail of the lightcurve. Indications of such tails has been observed in $B-V$ (Förster et al. 2013), but the effects are expected to be more significant for shorter wavelengths.

If CS dust exists, we can expect the SN explosion to heat it to a temperature that would depend on the dust properties and the distance from the SN. Heated dust could in principle be detected in mid to far-infrared and evidence of such has been detected (Fox et al. 2011; Taddia et al. 2012; Fox & Filippenko 2013) for a subset of peculiar SNe Ia. However, *Herschel* and *Spitzer* observations (Johansson et al. 2013, 2014) of a handful of normal SNe Ia show no signs of CS dust. Two of these SNe, 2006X and 2007le, together with SNe 1999cl and PTF11kx, have shown evolution of the Na I D absorption features in their spectra on time-scales comparable to the SN variations (Patat et al. 2007; Blondin et al. 2009; Simon et al. 2009; Dilday et al. 2012), which have been interpreted as evidence for circumstellar material (although Patat et al. 2010 suggest that patchy inter stellar material along the line of sight could give rise to similar signatures). Narrow Na I D absorption lines are a commonly used proxy for dust and the equivalent width of the lines have been shown to correlate well with extinction in the Milky May (see Munari & Zwitter 1997; Poznanski et al. 2012). Variations of Na I D equivalent width on SN time-scales have been explained by photo-ionisation of neutral sodium (e.g. Borkowski et al. 2009) and subsequent recombination. In the recent study by Soker (2014) this explanation has been questioned and an alternative model of photon-induced desorption of sodium from dust in planetray nebulae remnents was proposed.

A more extensive study with multiple epoch high-resolution spectra of 14 SNe (Sternberg et al. 2014) have failed to reveal further examples of time varying Na I D. Nevertheless, a statistically significant preponderance of Na I D features which are blue shifted with respect to the local velocity have been observed in high- and mid-resolution spectra (Sternberg et al. 2011; Maguire et al. 2013, respectively), suggesting that there is outflowing material from the SN progenitor system. A further peculiarity revealed by Phillips et al. (2013) is that $\sim 25\,\%$ SNe, of which most have blue shifted Na I D features, have unusually high neutral sodium column densities compared to the value expected from the Poznanski relation. It is currently unclear whether the high abundance of sodium is intrinsic to the environment of some SN Ia or whether the Milky Way reference value is anomalous compared to other galaxies. It has thus been suggested that other species asociated with the ISM, such as the diffuse interstellar band (DIB) feature at 5780 Å (Phillips et al. 2013), may be better proxies for reddening.

In this work we present NIR–NUV lightcurves of the six SNe Ia based on data mainly obtained from The Nordic Optical Telescope and *The Hubble Space Telescope* (*HST*). The observations and data reduction is presented in Section 2 while the lightcurves and spectroscopic properties are shown in Sections 3 and 4, respectively. The method for deriving individual reddening laws for each SN is described in Section 5, and after adding SN 2014J from A14 to the sample we present the results and discuss them in Section 6. The conclusions are summarised in Section 7.

All the SNe are shown together with their host galaxies in Figure 1 while the six SNe for which we introduce NUV data here, are listed together with their host galaxies in Table 1, and briefly summarised here. **SN 2012bl** was discovered by the Chilean Automatic Supernova Search (CHASE) 42".9 east and 14".6 north of the center of the galaxy ESO 234-19 on Mar. 26.38 UT from an unfiltered image (Pignata et al. 2012). A spectrum (Prieto 2012) was obtained with the 2.5 m du Pont telescope at the Las Campanas Observatory on Mar. 27.28 and object was classified as a SN Ia using SNID (Blondin & Tonry 2007). **SN 2012bm**, located 10".95 west and 10".4 north of the galaxy UGC 8189, was discovered on Mar. 27th by Puckett et al. (2012). A spectrum was obtained on Mar. 28.05 UT and it was classified (Cappellaro et al. 2012) as a SN Ia using GELATO (Harutyunyan et al. 2008). **SN 2012cg** was discovered (Kandrashoff et al. 2012) by the Lick Observatory Supernova Search (LOSS, Filippenko et al. 2001) on May 17.220 UT. The redder than normal SN was located 17".3 east and 1".5 south (Cenko et al. 2012) of the center of the Virgo Cluster member NGC 4424 in a region with many blue stars and disturbed dust lanes. Graur & Maoz (2012) could use pre-explosion *HST* images of this well-studied galaxy to rule-out most supergiants as possible binary companions for the progenitor scenario. **SN 2012cp** was discovered 6".7 east and 1".2 south of the center of UGC 8713 on May 23.2 UT by the Puckett Observatory Supernova Search (Cox et al. 2012). Milisavljevic (2012) and Zhang et al. (2012) obtained a spectroscopy of the object May 25.3 and May 25.7, respectively, and reported that it was consistent a SNe Ia before maximum. **SN 2012cu** was discovered by Itagaki et al. (2012) in the galaxy NGC 4772 and later classified as a SN Ia by Marion et al. (2012). Pre-explosion *Chandra* observations are available of the host galaxy and were used by Nielsen et al. (2013) to constrain the X-ray emission from the progenitor scenario. **SN 2012et**, located 5".3 east and 0".8 north of the center of MCG +04-55-47, was discovered by Rich et al. (2012) on Sep. 12.057 UT, and later classified on Sept. 13.80 UT as a high-velocity SNe Ia (Dennefeld et al. 2012).

2 OBSERVATIONS AND DATA REDUCTION

2.1 Hubble Space Telescope

All previously unpublished *HST* observations discussed in this work are listed in Table 2. Each SN was observed at two different epochs (four for SN 2012et) with the Wide-Field Camera 3 (WFC3) during the *HST* Cycle 19 under

Civil date	MJD	Aperture	SN
2012-04-09	56026.4	UVIS1-2K2A-SUB	2012bm
2012-04-09	56026.5	STIS 52X0.2 G230LB	2012bm
2012-04-13	56030.6	UVIS1-2K2A-SUB	2012bm
2012-04-13	56030.7	STIS 52X0.2 G230LB	2012bm
2012-04-16	56033.1	STIS 52X0.2 G230LB	2012bl
2012-04-16	56033.8	UVIS1-2K2A-SUB	2012bl
2012-04-20	56037.4	STIS 52X0.2 G230LB	2012bl
2012-04-21	56038.2	UVIS1-2K2A-SUB	2012bl
2012-06-04	56082.4	UVIS2-M1K1C-SUB	2012cg
2012-06-04	56082.4	IRSUB64	2012cg
2012-06-04	56082.6	UVIS1-2K2A-SUB	2012cp
2012-06-04	56082.5	STIS 52X0.2 G230LB	2012cg
2012-06-04	56082.5	STIS 52X0.1 G430L	2012cg
2012-06-04	56082.7	STIS 52X0.2 G230LB	2012cp
2012-06-16	56094.6	UVIS1-2K2A-SUB	2012cp
2012-06-17	56095.6	STIS 52X0.2 G230LB	2012cp
2012-06-18	56096.4	STIS 52X0.2 G230LB	2012cg
2012-06-18	56096.4	STIS 52X0.1 G430L	2012cg
2012-06-19	56097.5	UVIS2-M1K1C-SUB	2012cg
2012-06-19	56097.5	IRSUB64	2012cg
2012-07-02	56110.8	UVIS2-M1K1C-SUB	2012cu
2012-07-02	56110.8	IRSUB512	2012cu
2012-07-07	56115.8	UVIS2-M1K1C-SUB	2012cu
2012-07-07	56115.8	IRSUB512	2012cu
2012-10-01	56201.5	UVIS2-M1K1C-SUB	2012et
2012-10-01	56201.5	IR	2012et
2012-10-01	56201.8	STIS 52X0.2 G230LB	2012cg
2012-10-01	56201.8	STIS 52X0.2 G430L	2012cg
2012-10-05	56205.6	UVIS2-M1K1C-SUB	2012et
2012-10-05	56205.6	IR	2012et
2012-10-09	56209.8	UVIS2-M1K1C-SUB	2012et
2012-10-09	56209.8	IR	2012et
2012-10-13	56213.9	UVIS2-M1K1C-SUB	2012et
2012-10-13	56213.9	IR	2012et

Table 2. Wide-Field Camera-3 observations together with the WFC3 sub-arrays used, where UVIS1 and UVIS2 are the two chips of the WFC3/UVIS channel.

the programme GO-12582 (PI: Goobar). All SNe were imaged with the WFC3/UVIS channel through the passbands F225W, F275W and F336W. In addition to this, NIR imaging in the *HST* passbands F125W and F160W was obtained for the SNe 2012cg, 2012cu and 2012et with the WFC3/IR channel.

WFC3/UVIS consists of two 4096 × 2051 e2V CCD detectors with a plate scale of 0.04"/pixel, while the Teledyne HgCdTe infrared detector used in the WFC3/IR channel has a pixel scale of 0.13"/pixel. For each observation, only the sub-arrays (apertures), listed in Table 2, of the detectors were read-out. All WFC3 data were reduced using the standard STScI reduction pipeline and calibrated using CALWF3.

The WFC3/UVIS CCDs, like all *HST* CCDs, are plagued with charge transfer inefficiencies (CTI), i.e. degradations of the detector performance over time due to damage in the silicon lattice from cosmic rays. The CTI can be reverse corrected at the pixel level using `wfc3uv_ctereverse`[1] for all frames except for images obtained with the UVIS2-M1K1C-SUB sub-array. For this aperture we instead used

[1] `http://www.stsci.edu/hst/wfc3/tools/cte_tools`

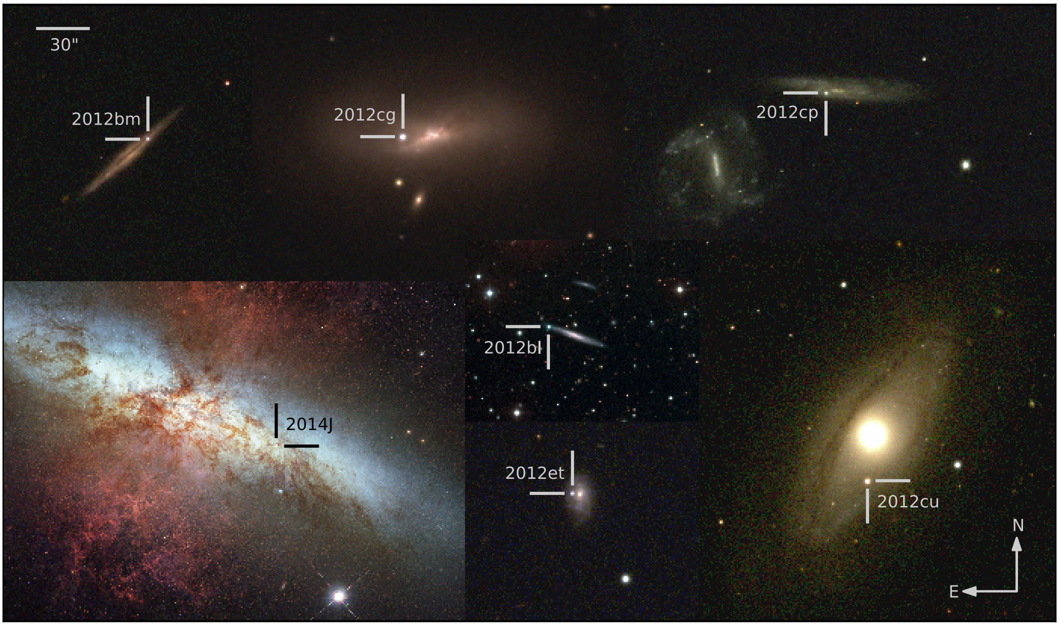

Figure 1. The seven SNe analysed in this work. The patches for SNe 2012bm, 2012cg, 2012cp, 2012cu and 2012et are constructed from *BVR* images from NOT, while the images for SNe 2012bl and 2014J are obtained from Swope and SN 2014J HST/WFC3 (Program DD-13621; PI Goobar) images respectively.

SN	$\alpha_{\rm SN}$ (2000)	$\delta_{\rm SN}$ (2000)	Host galaxy	$\alpha_{\rm h}$ (2000)	$\delta_{\rm h}$ (2000)	$v_{\rm h}$ (km/s)	Distance (Mpc)	MW A_V
2012bl	20:23:55.28	−48:21:17.3	ESO 234-19	20:23:51.0	−48:21:32	5608	72.2(0.1)	0.098
2012bm	13:05:45.66	+46:27:52.9	UGC 8189	13:05:46.6	+46:27:42	7436	102.9(7.9)[a]	0.033
2012cg	12:27:12.83	+09:25:13.2	NGC 4424	12:27:11.6	+09:25:14	437	15.4(0.9)	0.057
2012cp	13:47:01.79	+33:53:35.0	UGC 8713	13:47:01.2	+33:53:37	4956	55.0(3.0)	0.058
2012cu	12:53:29.35	+02:09:39.0	NGC 4772	12:53:29.1	+02:10:06	1040	29.3(9.7)	0.074
2012et	23:42:38.82	+27:05:31.5	MCG +04-55-47	23:42:38.4	+27:05:31	7483	105.0(7.4)[a]	0.221

[a] Galactocentric distance calculated based on the redshift with $H_0 = 73 \pm 5$ km/s/Mpc.

Table 1. SN coordinates are quoted from the discovery telegrams. All host galaxy data were obtained from the Nasa Extragalacic Database (NED), where $v_{\rm host}$ is the measured recession velocity, and the Milky Way extinction originated from the Schlafly & Finkbeiner (2011) calibration of the Schlegel et al. (1998) infrared-based dust map.

the recipe suggested by Bourque & Anderson (2014). The individual flat-fielded images of both WFC3/UVIS and WFC3/IR were then resampled and combined using `astrodrizzle` (Fruchter & et al. 2010).

Aperture photometry was carried out on the combined images using an aperture radius of 0.4", although in some cases a smaller aperture of 4 pixel radius had to be used for the WFC3/UVIS data. This was the case for the low signal-to-noise measurements of SN 2012bm, observations of SN 2012cg that were plagued by nearby coincidence cosmics, and all epochs of SN 2012et, where a nearby object contaminated the larger aperture. The smaller radius measurements had to be aperture corrected to the 0.4" radius for which STScI provides zeropoints[2] for WFC3. Since there were no bright stars present in the fields we used the general enclosed energy tables provided by STScI for this purpose. Since the WFC3/UVIS aperture corrections are in practice both time and wavelength dependent we will adopt an additional uncertainty of 0.05 mag for all measurements using the 4 pixel radius, which was derived by comparing the enclosed energy tables with photometry from different aperture radii of the high signal-to-noise data.

Only the SN 2012et NIR measurements suffered from host galaxy contamination. The host contribution was esti-

[2] We used the zeropoints from March 6th, 2012

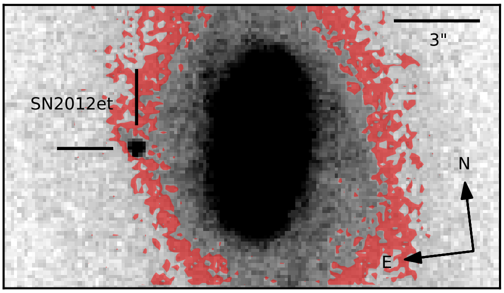

Figure 2. SN 2012et in the F160W filter from Oct. 1. The marked (red) region show the isophot from which the host galaxy background was estimated as explained in the text.

mated by placing apertures of the same radius used for the SN photometry along the isophot of the galaxy that intersects with the position of SN 2012et as illustrated in Figure 2. The background was then estimated as the median of these measurements, and the root-mean-square was added as an additional uncertainty to the photometric uncertainty.

For each HST visit we also obtained long-slit spectroscopy with the Space Telescope Imaging Spectrograph (STIS) where the1024 × 1024 pixel SITe CCD detector was used with the G230LB grating covering the wavelength range 1600-3100 Å, and for two SNe (2012cg, 2012et) G430L, 2900–5700 Å. The data were reduced using `calstis` pipeline which is part of the `STSDAS` package. The pipeline was ran for all spectra up to the point where the calibrated 2D spectra created. The only spectra to contained any significant signal were those of SNe 2012cg and 2012et for which we extracted the spectra using the `calstis x1d` routine using a 4 pixel aperture.

2.2 Swift/UVOT

Swift/UVOT UV photometry was obtained of the SNe 2012bl, 2012cg, 2012cp and 2012cu in the *uvw1*, *uvw2* and *uvm2* filters. However, the *uvw1* and *uvw2* filters are not well suited for extinction studies due to the significant "red-tails" of these filters. Milne et al. (2010) used the UV spectra of SN 1992A (Kirshner et al. 1993) and estimated that 52 % and 44 % of the light in in *uvw1* and *uvw2* respectively, originate from wavelengths redder than 3000 Å.

The *uvm2* filter, on the other hand, is much better constrained (1 % of the light come from > 3000 Å) and will be used for the extinction studies in this work. The *uvm2* fluxes were measured using aperture photometry as described in Brown et al. (2014). Only SNe 2012bl and 2012cg showed a significant SN flux in the *uvm2* band. The flux measured for SN 2012cp was consistent with the host galaxy brightness and no signal was measured for SN 2012cu.

2.3 Ground based observations

The ground based spectroscopic observations are listed in Table 3 while the photometric observations are summarised together with the measured magnitudes in Table 4. All SNe except for SN 2012bl were observed with the 2.56 metre Nordic Optical Telescope (NOT) under programmes 45-009 and 46-018 (PI: Amanullah). Imaging and spectroscopy was obtained with the $6.4' \times 6.4'$ Andalucia Faint Object Spectrograph and Camera (ALFOSC) using the filter set U (#7)[3], B (#74), V (#75), R (#76), i (#12) and the $R = 360$ grism (#4)[4]. The data were reduced using standard IRAF routines and the QUBA pipeline (Valenti et al. 2011). The photometry was measured with point-spread-function-fitting using DAOPHOT (Stetson 1987) and calibrated against Landolt fields (Landolt 1992).

With the NOT we also obtained high-resolution spectroscopy of SN 2012cg using the FIbre-fed Echelle Spectrograph (FIES, Telting et al. 2014) in its high-resolution mode, $R = 67000$. Simultaneous wavelength reference (Thorium-Argon) spectra were observed and the data were reduced using the software `FIEStool` which is provided by the observatory.

NIR observations were carried out of SNe 2012bm, 2012cg and 2012cp with the $4' \times 4'$ NOTCam instrument in the J, H and Ks. We used the wide field imaging option of the 1024 × 1024 pixel HgCdTe NOTCam detector with a plate scale of $0''.234$/pixel. The observations were carried out using either 5 or 9-point dithering patterns. In the case where the galaxy was extended, beam-switching was used to estimate the sky background. We used the QuickLook reduction package based on IRAF scripts[5]. Bad pixels (which includes two dead colums) are masked and we used master differential skyflats which were obtain from bright and faint skyflats. Further, the images were corrected for geometric distortions[6] before the individual images were aligned and coadded.

SN 2012cg was also observed in *JHKs* with the $4, 3' \times 4.3'$ CAIN instrument on the 1.52 metre Carlos Sanchez Telescope at Observatorio del Teide on Tenerife. CAIN III is a 256 × 256 pixel HgCdTe NIR detector, where we used the wide field option with a plate scale of 1.0"/pixel. The data were reduced using a dedicated IRAF package provided by J. Pullido and A. Barrena.

3 LIGHTCURVE PROPERTIES AND SN COLOURS

SN Ia lightcurves are typically quantified by a few parameters as described in the introduction. SNe Ia are very bright in the rest-frame B-band and the maximum brightness and light-curve shape of this filter is historically what has been used to measure SN Ia distances. The lightcurve shape can be quantified using different methods, where perhaps the most straight-forward is to measure how much the lightcurve has declined during a given time past the time of B-maximum, t_B. Phillips (1993) showed that fast declining SNe Ia are typically intrinsically fainter than slow declining objects which lay the foundation for using SNe Ia as distance indicators for precision cosmology. An alternative approach to quantify the lightcurve shape is to introduce

[3] NOT filter ID
[4] NOT grism ID
[5] Amanda Djupvik, private communication.
[6] Magnus Gålfalk, private communication.

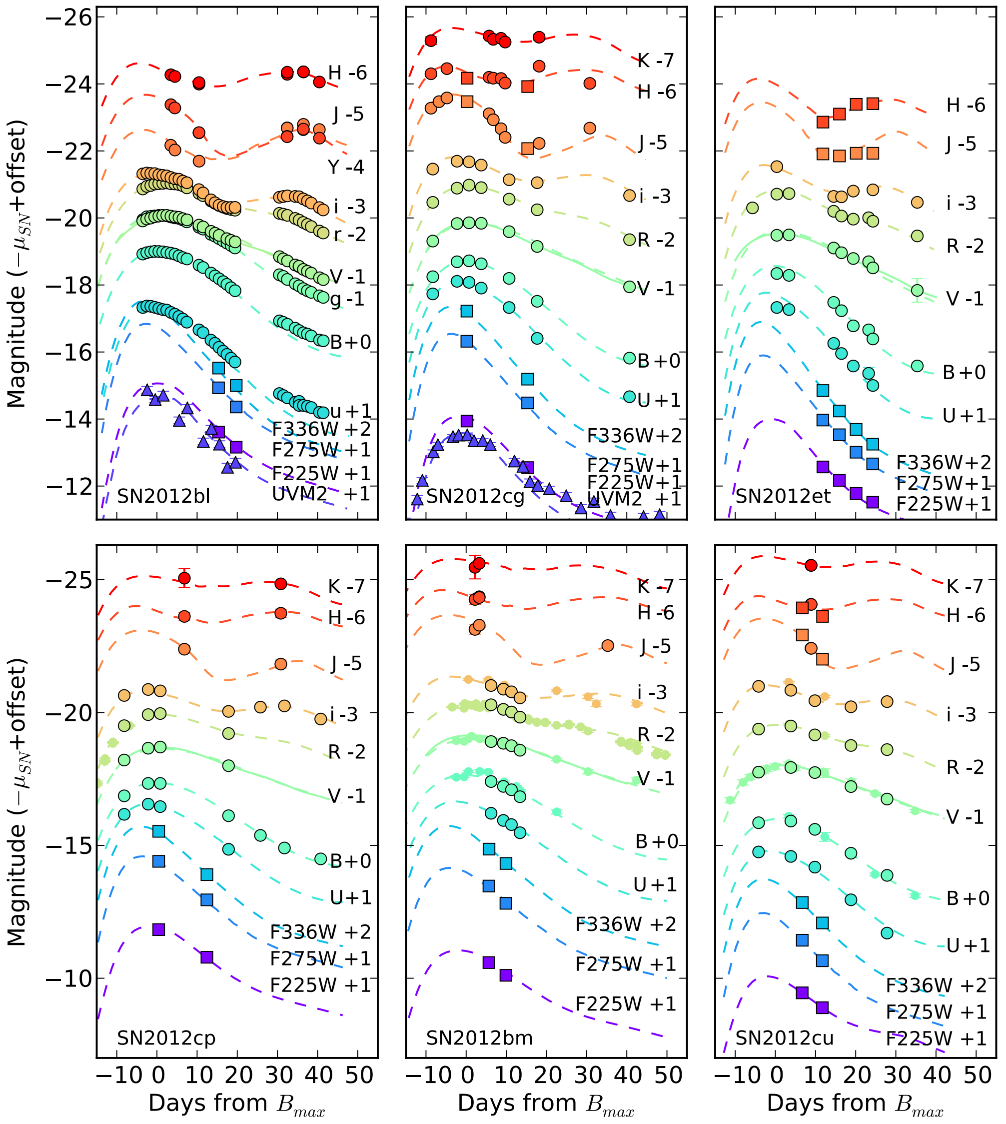

Figure 3. Observed lightcurves for the SN sample. Our analysis is based on optical *UBVRI* and NIR *JHK* photometry from ground based observatories (cirles), NUV (F225W,F275W,F336W) and NIR (F125W,F160W) photometry from the HST (squares). For some of the SNe we also use *SWIFT* photometry (SNe 2012bl, 2012cg, 2012cp and 2012cu). The data have been shifted using the distance moduli in Tab 1 and offset for clarity. The solid lines show the SNooPy *V*-models used to calculate colours as described in the text, while the dashed lines show synthetic spectrophotometry of SN 2011fe, reddened by the best fitted F99 law (Section 6, arbitrarily shifted to match the photometry of each band.

Civil date	MJD	Instrument	λ ($\AA$)	Exp. (s)	SN
2012-03-30	56016.3	DuPont/WFCCD/WF4K-1	3600−9200	700	2012bl
2012-03-31	56017.4	DuPont/WFCCD/WF4K-1	3600−9200	700	2012bl
2012-05-01	56048.3	DuPont/WFCCD/WF4K-1	3600−9200	900	2012bl
2012-04-09	56027.0	NOT/ALFOSC	3200−9000	2400	2012bm
2012-04-16	56034.1	NOT/ALFOSC	3200−9000	2400	2012bm
2012-05-26	56074.0	NOT/ALFOSC	3200−9000	2700	2012cp
2012-06-04	56083.0	NOT/ALFOSC	3200−9000	1800	2012cp
2012-05-24	56071.9	NOT/ALFOSC	3700−7200	5477	2012cg
2012-05-28	56075.9	NOT/ALFOSC	3700−7200	6588	2012cg
2012-06-04	56082.9	NOT/ALFOSC	3200−9000	300	2012cg
2012-07-05	56113.9	NOT/ALFOSC	3200−9000	1200	2012cu
2012-09-13	56183.8	ASIAGO/AFOSC	3500−8200	2700	2012et
2012-09-22	56193.1	NOT/ALFOSC	3200−9000	600	2012et

Table 3. Ground based spectroscopic observations.

MJD (days)	Phase (days)	Filter	X (mag)	$A_X^{\rm MW}$ (mag)	K_X (mag)	Match	V (mag)	$A_V^{\rm MW}$ (mag)	K_V (mag)	$(V-X)_0$ (mag)
					SN2012cg					
56082.4	0.2	WFC3 F336W	11.74(0.06)	0.09	0.01	M	12.04(0.04)	0.06	0.00	0.61
56097.5	14.0	WFC3 F336W	13.75(0.01)	0.09	0.02	M	12.53(0.07)	0.06	0.00	−0.90
56082.4	0.2	WFC3 F125W	12.37(0.01)	0.01	0.05	M	12.04(0.04)	0.06	0.00	−0.55
56097.5	14.1	WFC3 F125W	13.88(0.03)	0.02	−0.07	M	12.53(0.07)	0.06	0.00	−1.91
56082.4	0.2	WFC3 F225W	16.38(0.05)	0.13	0.02	M	12.04(0.04)	0.06	0.00	−2.55
56097.5	14.0	WFC3 F225W	17.60(0.08)	0.13	0.02	M	12.53(0.07)	0.06	0.00	−3.68
56082.4	0.2	WFC3 F160W	12.67(0.02)	0.01	0.01	M	12.04(0.04)	0.06	0.00	−0.88
56097.5	14.1	WFC3 F160W	13.24(0.03)	0.01	0.55	M	12.53(0.07)	0.06	0.00	−0.69
					...					

Table 4. The photometry of all SNe. All magnitudes are in the natural Vega system. The rest-frame magnitude can be obtained from Columns 4–6. Columns 5 and 9 are the Galactic extinctions and Columns 6 and 10 are K_X and K_V corrections for the two bands, respectively. Both of these were calculated based on the fitted F99 law for each SN. The V is only shown for data points used in the colour analysis, i.e. with phases between −5 and +35 days. Column 2 show the effective lightcurve-width-corrected phase, while Column 7 specifies whether the V magnitude was measured for the same epoch (D) or if it was calculated using the `SNooPy` model (M). The corresponding intrinsic colour for the SN 2011fe template is shown when available in Column 11. (This table is available in its entirety in a machine-readable form in the online journal. A portion is shown here for guidance regarding its form and content.)

a *stretch* parameter (Perlmutter et al. 1997), s_B, defined as the value needed to match the time-evolution of an observed B lightcurve to a standard SN Ia template.

In this work we used the `SNooPy` lightcurve fitter (Burns et al. 2011) to obtain the lightcurve parameters for each SN. We used their `max_model` where the maximum flux is fitted for each individual band together with t_B and s_B using the spectral energy distribution (SED) from Hsiao et al. (2007, H07 from hereon) without making any assumptions or attempting to fit the reddening.

We adopted an iterative method where all lightcurves were refitted after the extinction laws have been determined, as will be described below, and the photometry had been corrected for this. This approach addresses the issue that the observed lightcurve shape is extinction dependent (see e.g. Leibundgut 1988; Phillips 1993; Nugent et al. 2002, A14). Any broadband measurement of an object suffering from extinction will effectively probe redder wavelengths than the observation of the same unreddened object would have. Since the SN Ia lightcurve decline rate varies with wavelength this will lead to observations of a slower decline, larger stretch, for a reddened object. The iterative procedure described here will converge towards the lightcurve parameters that we would have been observed for the SNe in the absence of extinction. The fitted results from the last iteration are shown together with the data in Figure 3 and the fitted lightcurve parameters are listed in Table 5.

SN	$t_{\rm max}$ (MJD)	s_B
2012bl	56018.4(0.1)	1.11(0.02)
2012bm	56020.7(0.2)	1.19(0.02)
2012cg	56082.2(0.6)	1.09(0.02)
2012cp	56082.2(0.2)	1.11(0.03)
2012cu	56104.1(0.3)	1.09(0.07)
2012et	56189.7(0.7)	1.11(0.05)

Table 5. Fitted B-band lightcurve parameters.

For each photometric measurement in each filter, X, where $X \in \{uvm2, \mathrm{F218W}, \ldots, Ks\}$, we calculate the colour $X - V$. When X and V-band measurements were available for the same dates, the colour could be calculated directly, but when this was not the case we used a fitted `SNooPy` V-band model to calculate the V magnitude for each X observation.

For these colours we add a 0.05 mag uncertainty to account for the inaccuracy of the model. When applicable, we fitted a smoothed spline rather than the `SNooPy` SN Ia template to avoid introducing any model dependence, but for the SNe 2012bm and 2012cp the V-band data were too sparsely sampled to allow a reliable spline fit. The fitted V-band models used for each SN are shown as thick lines in Figure 3.

All measured colours were corrected for Galactic extinction, A^{MW}, using the parametrisation introduced by (Cardelli et al. 1989, CCM) with $R_V = 3.1$ and the A_V values shown in the last column of Table 1. These values were taken from the Schlafly & Finkbeiner (2011) recalibration of the Schlegel et al. (1998) dust maps, except for SN 2014J where we use the Dalcanton et al. (2009) value obtained from studying neighbouring regions.

The colours were also K (e.g. Nugent et al. 2002) and S (e.g. Suntzeff 2000; Stritzinger et al. 2002; Krisciunas et al. 2003) corrected to a common rest-frame filter system used for the remaining analysis throughout the paper. The analysis were carried out using the WFC3/UVIS and SWIFT/UVOT filters for the UV, the ALFOSC filter set for the optical and the NOTCAM filters for the NIR, since most SNe have been observed using these filters. The combined K and S corrections (K_X from now on) are calculated synthetically using the SED of SN 2011fe as described in Section 5.1 and the filter transmissions provided by the different observatories.

To summarise, all colours are obtained as

$$X - V = (m_X - A_X^{\mathrm{MW}} - K_X) - (\mathcal{M}_V - A_V^{\mathrm{MW}} - K_V)\,,$$

where m_X are the measured instrumental magnitudes in filter X and $\mathcal{M}_V$ is the V magnitude for the same phase either measured or obtained from the spline or template fit. All values used are presented in Table 4.

The time-evolution of the SN Ia $X - V$ colours depend on lightcurve shape. For example, Nobili & Goobar (2008, from hereon N08) present colour-lightcurve shape relations in the optical while B14 argues that the SNe Ia colours can be standardised over a wide range of decline rates by introducing *colour stretch*, $s_{BV} = t_{BV}/30$ days, where t_{BV} is the time between t_B and the maximum of the $B - V$ colour. This does however require $B - V$ coverage up to $t \sim t_B + 40$ in order to accurately determine s_{BV}.

As can be seen in Table 5 the SNe used in this work span a narrow range in stretch and for the analysis presented here it will be sufficient to standardise the measured colours using s_B. All colours will be studied and compared as a function of *phase*, p, defined as $p = (t - t_B)/s_B$, where t are the observing dates and the results from Table 5 will be used for t_B and s_B for each SN. A subset of all the measured colours as a function of phase is shown in Figure 4 where the colours calculated from using the fitted V-band spline or template are shown with open symbols and colours that could be measured directly are shown with filled symbols.

4 SPECTROSCOPIC PROPERTIES

To the set of spectroscopic data already described above we also add the classification spectrum of SN 2012et (Tomasella et al. 2014). Spectra for all SNe around maximum are shown in Figure 5 where for SN 2012cg we have combined the STIS G250LB and G430L spectra with the ALFOSC spectrum obtained the same day. All these spectra were used for retyping and all SNe are classified as "normal" using SNID (Blondin & Tonry 2007) except SN 2012bl where best match was SN 1999aa. For SN 2012bl the spectrum of SN 1999aa is shown at the top of Figure 5 while we show the spectrum of SN 2011fe at max (Mazzali et al. 2014) for comparison for the other SNe.

SN	Phase (days)	pW (5750) (Å)	pW (6100) (Å)	Type
2012bl	-0.9	1	88	CN
2012bm	+5.1	12	77	CN
2012cg	+0.7	9	72	CN
2012cp	+0.7	10	75	CN
2012cu	+9.2	24	93	CN
2012et	+3.5	12	132	BL

Table 6. Calculated pW based on the optical spectra. See the text for details.

Another approach to classify SNe Ia suggested by Branch et al. (2006) is to compare the absorption features near 5750 Å and 6100 Å usually associated with Si II λ5972 and λ6355. These are conveniently quantified by calculating their pseudo-equivalent widths (pW), where pseudo refers to to the fact that the equivalent widths are obtained using a pseudo continuum since proper continua are absent in SN Ia spectra. The pseudo continuum is defined with a straight line between the two flux peaks surrounding an absorption feature and the pW is then calculated as the integral of the spectrum flux relative to the continuum. Using this method, the error of the measurement will be dominated by the systematic uncertainty introduced by determining the pseudo-continuum. Branch et al. (2006) identify four different groups when considering pW (5750) and pW (6100) for their sample where in particular the "core normal" (CN) SNe are tightly clustered and show a high degree of general spectral homogeneity.

After correcting our spectra for host galaxy reddening (although this is not expected to have any major impact on the results Nordin et al. 2011) using the fitted reddening laws from Section 6 the pW are measured and the results are shown in Table 6. Using the classification criteria from (Blondin et al. 2012) we can classify all SNe as CN except for SN 2012et which lands in what Branch et al. (2006) call the "broad-line" group. These SNe Ia have broader and deeper 6100 Å absorption but are in most aspects not very different from CN SNe. In fact, when the observed spectra from the different groups are compared with synthetic spectra generated with SYNOW (Branch et al. 2003) similar photospheric velocities and excitation temperatures can be used to describe both the CN and BL groups (Branch et al. 2006).

For all spectra we also determined the photospheric expansion velocity around maximum of the Si II λ6355. The velocities were determined from the minimum of the λ6355 absorption by fitting a Gaussian profile to the feature and the results are shown in Figure 6. We also present the velocities around maximum in Table 7, which were determined either from the direct measurements except for SN 2012bm where we obtained the value by first fitting a second order polynomial to the measurements. Following Wang et al.

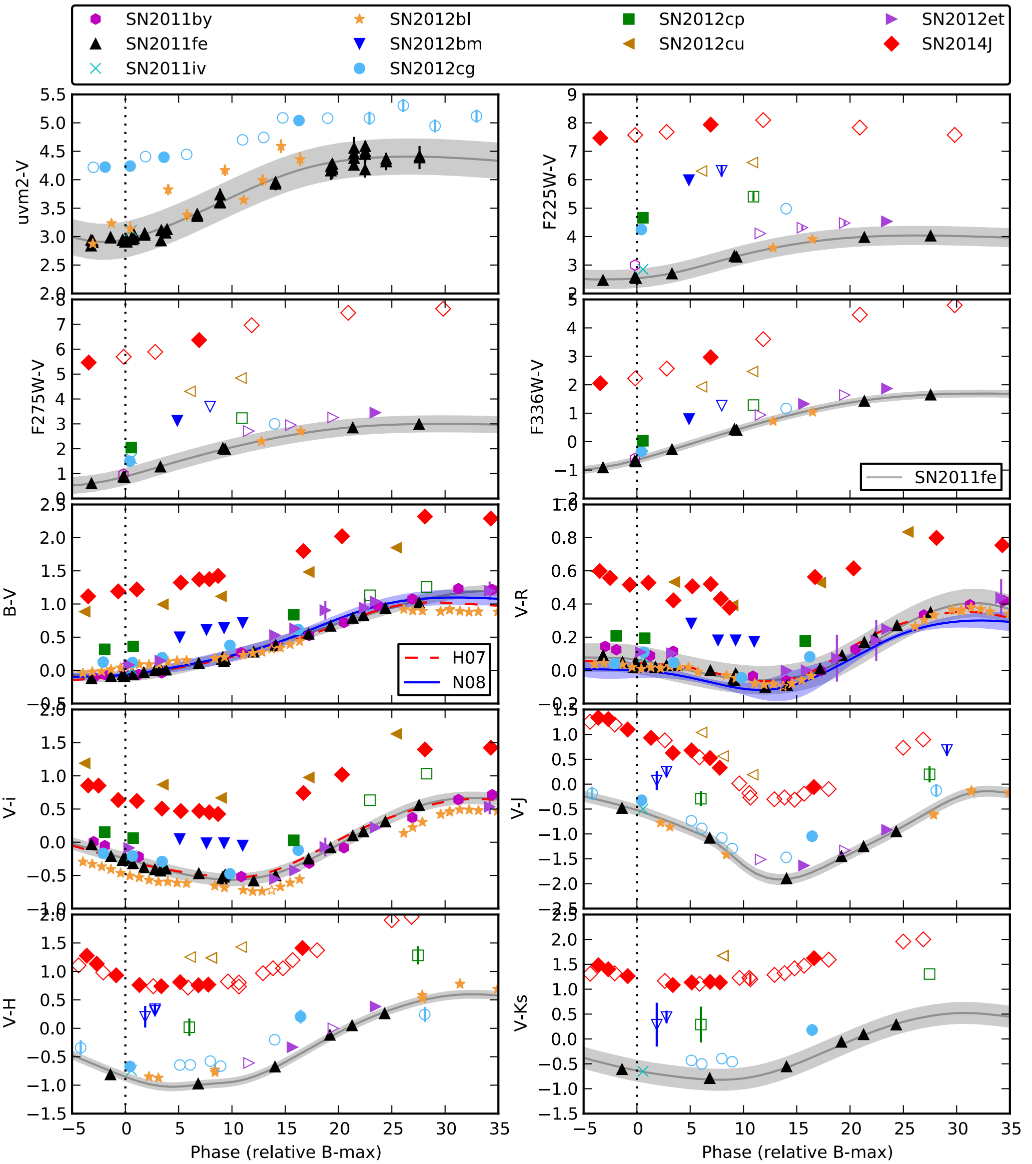

Figure 4. A selection of measured colors from UV to NIR for the SNe used in this work shown together with the comparison SNe 2011by, 2011fe and 2011iv. The colour laws from H07 (dashed red) and Nobili & Goobar (2008) (N08, solid blue with dispersion region) are also shown together with the derived colour model of SN 2011fe (solid black) with the adopted dispersions (grey region). Filled symbols show colours where a *V*-band measurement was obtained for the same date, while a spline *V*-band model was used to obtain the measurements showed with open symbols. Errorbars are only plotted for data points where the uncertainty exceeds 0.1 mag. See text for details.

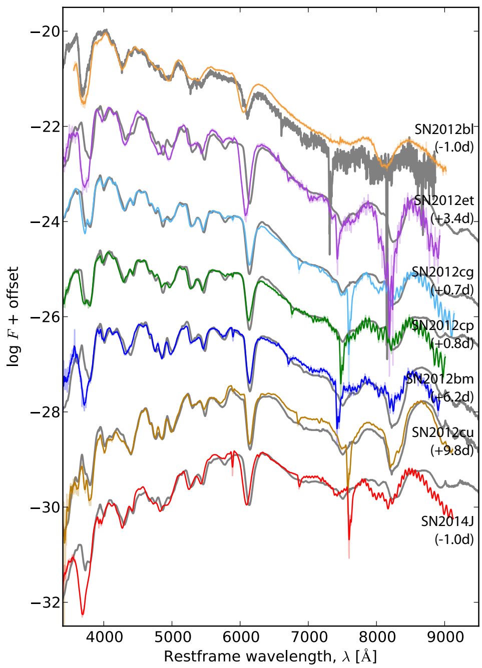

Figure 5. Optical spectra near maximum light for the SNe in our sample. The grey bands show the corresponding 2011fe (except for SN 2012bl, where a comparison with SN 1999aa is shown) at similar epochs, reddened by our best fit F99 extinction.

SN	Phase (days)	v Si II ($10^3\,\mathrm{km\,s^{-1}}$)	Type
2011fe	+0	10.4	NV
2012bl	−1	14.4	HV
2012bm	+5	10.2	NV
2012cg	+0	10.4	NV
2012cp	+0	10.6	NV
2012cu	-	-	NV
2012et	+2	13.0	HV
2014J	+0	12.5	HV

Table 7. Measured and fitted photospheric velocities based on Si II 6355. The phase is specified for SNe with near-max spectroscopy for SN 2012bm the velocity at max was obtained from a parabola fit.

(2009), we also classify the SNe with Si II velocities of $v > 11,800\,\mathrm{km\,s^{-1}}$ as "high velocity" (HV) and the remaining as "normal velocity" (NV). It has been shown (Foley & Kasen 2011; Blondin et al. 2012; Folatelli et al. 2013; Mandel et al. 2014) that there is an optical colour-velocity dependence with HV SNe being on average intrinsically redder.

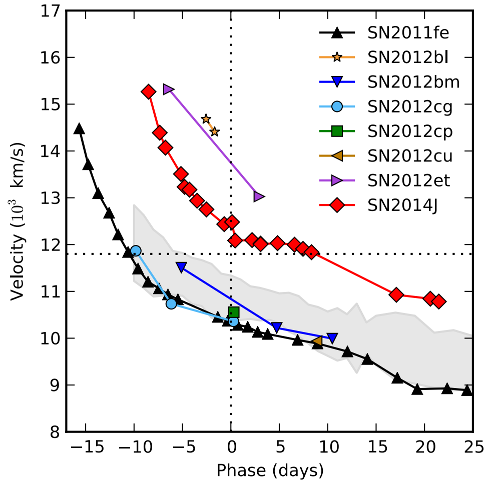

Figure 6. Measured velocities of Si II λ6355 for different phases of the SNe studied in this work together with reference objects. The grey region is the normal velocities from Folatelli. The dashed line marks the difference used to separate high- and low velocity objects by Wang et al. (2009) at maximum.

Civil Date	Phase (days)	S/N
2012-05-26	-8.5	59
2012-06-02	-1.5	15
2012-06-14	10.5	21

Table 8. High resolution spectra of SN 2012cg observed with FIES with R=67000. The signal-to-noise (S/N) were calculated from the continuum bracketing the Na I D feature.

4.1 Interstellar absorption features

The three high-resolution spectra of SN 2012cg with FIES are listed in Table 8 where we also specify the measured signal-to-noise of the continuum in vicinity of the Na I D doublet. All spectra contain well resolved unsaturated Na I D features and narrow Ca II K&H features could be measured from the first epoch. Phillips et al. (2013) further quote the detection of the DIB feature at 5780 Å with an equivalent width of 84 ± 5 mÅ, consistent with the non-detection in our spectra within the S/N. The spectra were normalised by fitting 3rd-order polynomials to the continuum bracketing the features of interest. No telluric corrections were performed on the spectra. spectra.

No significant changes beyond the noise level and changes expected from telluric features can be detected in the subtracted spectra from different epochs. Furthermore, we fitted Gaussian profiles to detect any non-obvious evolution of any of the prominent features, none of which evolve by a significant amount within the time coverage. The deepest absorption features are all redshifted with respect to v_h from Table 1. The apparent stellar velocity of ~ 460 km/s along the line of sight of 2012cg (see Cortés et al. 2006) roughly agrees with the two most prominent features of the Na I D doublet. Additional features of the Na I D and Ca II K&H profiles span a range from $\sim$ 400–550 km/s. Cortés et al. (2006) remark that the stellar velocities appear suprisingly low around the center of NGC 4424, where as the apparent Na I D absorption features backlit from the SN might indicate that the stellar light is dominated by foreground stars which are not obscured by dust.

We further analyse Mg II features (at 2796 and 2803 Å) of 2012cg in the *STIS* spectra. Due to the resolution of the spectra and the low redshift of 2012cg, the Mg II lines of the host galaxy and the Milky Way are blended. We fit four Gaussian profiles to the features, assuming the mean wavelength of the features are given by the atomic transition values and the recession velocity of NGC 4424. Furthermore, the features are assumed to all have the same width, limited by the resolution of the spectra. The equivalent width of the feature corresponding to 2796 Å in the host galaxy rest frame is of particular interest as it is considered a reddening proxy in Ménard et al. (2008). Supposing we trust the fit and that the component has been identified correctly, the feature has an equivalent width of 1.8 ± 0.2 Å, implying an low $E(B-V)$ of ~ 0.01. If however the entire feature is considered, the upper limit to the equivalent width of the host galaxy contribution of Mg II at 2796 Å is 5.5 ± 0.3 Å and an $E(B-V)$ of 0.2 ± 0.1.

Four epochs of high-resolution spectra of SN 2012cu have been described in Sternberg et al. (2014). No variations are detected in the deep Na I D absorption lines which are likely several blended features. The velocity of the Na I D lines of $\sim$1130 km/s is in good agreement with the H I velocity along the line of sight of 2012cu in NGC 4772 (Haynes et al. 2000).

In Table 9 values of $E(B-V)$ are estimated using empirical relations to the equivalent widths of Na I D (Poznanski et al. 2012) and the DIB at 5780 Å (Phillips et al. 2013) for the SNe of which we have obtained spectra or published data exists.

5 FITTING REDDENING LAWS

We will use the method described in A14 to fit different parameterised reddening laws to our measured colour excesses,

$$E(X-V) = (X-V) - (X-V)_0 \ ,$$

where $(X-V)_0$ is the corresponding $X-V$ colour for the unreddened source. Note that the observed $E(X-V)$ is expected to vary with time for broad-band photometry for the same reason that the stretch s_B changes with reddening. As the intrinsic colour of the source varies with time the effective wavelengths of all broad-band filters will change as well, but since the first term on the right-hand side in the equation above is also affected by a reddening law, any change in the effective wavelength of the filters X and V will affect this term more than the second term which will induce a time-variability for $E(X-V)$. For most filters, X, the time-variability will be negligible but in the NUV (where the extinction has a steep wavelength dependence), and in particular for filters with red tails, this effect is significant.

Further, the shape of the NUV-filters and the steep nature of the SED of our reddened sources, also has the implication that the Galactic extinction, $A_X^{\rm MW}$, and K_X corrections will depend on the reddening law. We take this into account by fitting each reddening law, $A(\lambda;\bar{a})$, iteratively by first minimising,

$$\chi^2 = \sum_X \sum_p \frac{\left[E(X_p - V_p) - (A_{X_p} - A_{V_p})\right]^2}{\sigma^2_{X_p V_p}} \ . \qquad (1)$$

Here A_{X_p} and A_{V_p} are the predicted extinctions in X and V for the phase p from the extinction law and can be calculated synthetical for a given set of parameters, $\bar{a}$, as

$$A_{X_p} = -2.5 \log_{10} \left(\frac{\int T_X(\lambda) A(\lambda;\bar{a}) S_0(\lambda;p) \lambda \, d\lambda}{\int T_X(\lambda) S_0(\lambda;p) \lambda \, d\lambda} \right) ,$$

if the effective filter transmission, $T_X(\lambda)$, and the spectral energy distribution (SED), $S_0(\lambda;p)$, of the unreddened source are known. Once the fit has converged, we update $A_X^{\rm MW}$ and K_X and repeat the fit until the change in the fitted parameters is less than 1 % between iterations.

5.1 SN Ia intrinsic colours and SED

In order to fit reddening laws using equation (1), we need to make an assumption of the intrinsic colours, $(X-V)_0$, and SED, $S_0(\lambda;p)$ of the corresponding unreddened sources. The reddening law for SNe Ia can be derived by either comparing them to individual objects that show similarities in lightcurve properties and spectral evolution (e.g. Krisciunas et al. 2006, A14) or to an average model of the spectral energy distribution of SNe Ia (e.g. Guy et al. 2005b, 2007). In Figure 4 the H07 template is plotted for the optical colours (dashed red). Although, the H07 template does extend from the NUV to NIR, the data it is based on is sparsely sampled in the NUV. N08 studied the intrinsic optical colours in between -10 and $+50$ days from B-band maximum. Two of their colour laws are shown (in blue) for a normal, $s_B = 1$, SN Ia in Figure 4 together with the colour dispersions they derive. Although these templates provide excellent coverage at optical wavelengths none of them cover, to high accuracy, the full wavelength range required for the NUV-NIR analysis in this work.

The best studied unreddened SNe Ia to date is SN 2011fe (PTF11kly, Nugent et al. 2011) discovered by the Palomar Transient Factory in the nearby spiral galaxy M101. Its close distance allowed detailed observations over a broad wavelength range from the NUV (Brown et al. 2012; Mazzali et al. 2014), through the optical (e.g. Munari et al. 2013) to the near- (Matheson et al. 2012; Hsiao et al. 2013), and mid- (McClelland et al. 2013), infrared. The SN was also targeted in the far-IR (Johansson, Amanullah & Goobar 2013) and radio (Chomiuk et al. 2012), but could not be detected at any of these wavelengths.

Both the optical and near-IR lightcurves of SN 2011fe appear to be those of normal SNe Ia (Munari et al. 2013; Matheson et al. 2012) and it does not show any spectroscopic peculiarities (Pereira et al. 2013). Further, the low Galactic and host galaxy reddening along the line of sight, $E(B-V)_{\rm MW} = 0.011 \pm 0.002$ and $E(B-V)_{\rm host} = 0.014 \pm 0.002$ mag (deduced from the integrated equivalent widths of the Na I D lines; Patat et al. 2013) makes it an excellent comparison object for studying reddening of SNe Ia.

SN	Na I D1 (mÅ)	Na I D2 (mÅ)	$E(B-V)$	DIB 5780 (mÅ)	A_V
2014J	2558(6)	2831(9)	-	344(4)	1.8(0.9)
2012cg	713(2)	1035(6)	$1.57^{+0.35}_{-0.29}$	85(5)†	0.4(0.2)
2012cu	849(3)‡	925(3)‡	$1.68^{+0.37}_{-0.31}$	-	-
2012et	-	650(40)*	$0.31^{+0.25}_{-0.14}$	-	-

Equivalent width values retrieved from † Phillips et al. (2013), ‡ Sternberg et al. (2014), * Maguire et al. (2013).

Table 9. Equivalent width values of Na I D and the DIB feature at 5780 Å for which $E(B-V)$ can be inferred from Poznanski et al. (2012) and A_V from Phillips et al. (2013), respectively. In the case of SN 2014J, the Na I D equivalent width extrapolates the relation by Poznanski et al. (2012) beyond any reasonable $E(B-V)$.

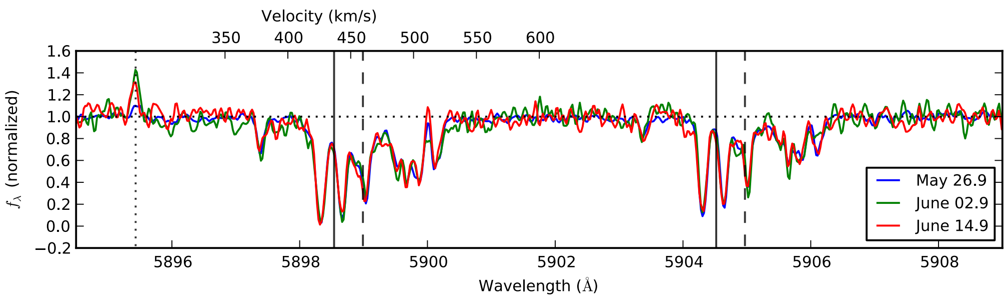

Figure 7. Na I D absorption doublet of SN 2012cg. The the rest frame wavelength of Na I D in NGC 4424 (solid lines) and for the approximate stellar velocity along the line of sight (dashed) are indicated. The dotted vertical line indicates a sky emission line.

The colours of SN 2011fe shown in Figure 4 (solid black lines) has been obtained by combining the available NUV–NIR data as described in Appendix A. We have also combined the spectroscopic data to create the SED template shown in Figure A1.

Although the colour evolution of SN 2011fe appear to be well matched by the H07 and N08 templates, based on many normal SNe Ia, in the optical, it does not automatically mean that this statement extends to the NUV. For example, SN 2011fe and SN 2011by are close to identical at optical colours but the latter is significantly fainter in the NUV (Foley & Kirshner 2013; Graham et al. 2014a).

Milne et al. (2013, from hereon M13), following the work of Brown et al. (2010) and Milne et al. (2010), studied the NUV colours of 23 SNe Ia observed with *Swift* and suggest that SNe Ia can be divided in up to four groups. Here, SNe 2011fe and 2011by are both found to belong to what they call the "NUV-blue" group which they conclude is on average 0.44 mag bluer in $u-v$ than the reddest, "NUV-red", group when all SNe with a total colour excess of $E(B-V) < 0.25$ are considered. A possible explanation for this discrepancy is that redder SNe Ia could be NUV-blue objects that suffer from extinction where the given constraint could impose a reddening of up to 0.9–1.3 mag in $uvm2-v$, depending on extinction law. However, they show that the two groups are still distinguishable even after correcting for reddening. Further, they also conclude that the groups, on average, show different spectroscopic properties. All NUV-blue SNe have "normal" Si II λ6355 velocities (as defined by Wang et al. 2009) and also show evidence of unburned C II in their optical spectra, while the remaining groups are populated with both normal and high Si II velocity SNe and both with and without unburned C II detections. These finding are consistent with the results from studies of optical spectroscopy where SNe Ia with unburned carbon in their spectra show indications of being slightly bluer in the optical (e.g. Thomas et al. 2011; Folatelli et al. 2012) and where objects with high expansion velocities are on average redder in than those with normal velocities SNe (e.g. Foley & Kasen 2011).

These discrepancies between seemingly normal SNe points to the importance of adopting accurate dispersions for the different colours. Not doing this has been shown to bias reddening laws derived from large SNe Ia samples (Chotard et al. 2011; Scolnic et al. 2014). For a complete analysis it would be desirable to both know the intrinsic dispersion for all colours, how they vary in time, and how they are correlated both in time and with different colours. Since we do not know this for all colours involved in this analysis, we treat them equally and adopt a phase-independent dispersion for each colour. We further follow A14 and assume that the colour uncertainties between SN epochs are fully correlated.

M13 report a dispersion of ~ 0.3 mag in $uvw1-v$ for the full $E(B-V) < 0.2$ sample after correcting the SNe for extinction and the result does not seem to be affected significantly by their choice of R_V. We will adopt this dispersion for the $uvm2 - V$, F218W $- V$, F225W $- V$, and F275W$-V$ colours which is shown as grey bands around the SN 2011fe colour template in Figure 4. For the F336W $- V$ and $U - V$ we adopt a dispersion of 0.2 mag based on the $u - v$ dispersion.

B14 derive a dispersion for the pseudo-colour $B_{\max} - V_{\max}$ of 0.06 mag using a Cauchy Prior for the colour distribution of their SNe Ia observed with the Carnegie Supernova Project. This is consistent with the phase-dependent results of N08 who derive a $B-V$ dispersion of $\lesssim 0.1$ mag within the phase range -5 to $+40$ days, which we will conservatively adopt for this work. Note that the colour-velocity relation for $B - V$ is within this dispersion for the velocity range of the reddened SNe in Figure 6 (Mandel et al. 2014). Mandel et al. (2014) further find no evidence for such a relation for the $V - R$ and $V - i$ colours and for these we adopt a dispersion of 0.08 mag respectively based on N08.

For the NIR-optical $V - J$ and $V - H$ colours we estimate the dispersion in our phase range by using all SNe with $E(B - V) < 0.2$ from the "Gold Sample" in Stanishev & et al. (2015) and find 0.12 mag and 0.13 mag respectively. For $V - Ks$ we conservatively adopt 0.2 mag based on the studies carried out at maximum (B14) and the dispersion of the *Ks*-band Friedman (2012).

The observed colour excesses, $E(X - V)$, for each reddened SN with respect to SN 2011fe, together with adopted colour dispersions, shown as background regions, are plotted in Figure 8. SN 2012bl has not been plotted in the figure since it does not show any signs of extinction in its colours in Figure 4. From Figure 6 we note that this SN show high velocities around maximum but despite this appear to be consistent with SN 2011fe in all colours, including the NUV, except for $V - i$. Note however, that this SN is spectroscopically more similar to SN 1999aa as shown in Figure 5.

5.2 Reddening laws

We will test three different extinction law parametrisations. In addition to the widely used Cardelli et al. (1989) law modified by O'Donnell (1994, hereafter CCM+O), which has been derived from studying different lines of sight in the Milky Way, we will also fit the parametrisation from Fitzpatrick (1999, hereafter F99). For each of these we fit both the colour excess $E(B - V)$, which relates to the optical depth, and the ratio of the total-to-selective extinction, R_V.

Further, we will also test a simple power law model

$$A(\lambda; A_V, a, p) = A_V \left[1 - a + a\left(\frac{\lambda}{\lambda_V}\right)^p\right],$$

where the reference wavelength, λ_V, will be chosen as $\lambda_V = 0.55\,\mu$m and a and p are free parameters (although A_V and a are degenerate when fitting to colour excesses). G08 showed that the observed reddening law of an object embedded in circumstellar dust can be approximated by this expression with $a = 0.8$ ($a = 0.9$) and $p = -2.5$ ($p = -1.5$) for Milky Way (LMC) like dust. The reason why the original extinction laws are not preserved in in the CS scenario is due to the geometry where multiply scattered photons in the CS dust will reach the observer while this is extremely unlikely for an ordinary interstellar dust geometry.

6 RESULTS AND DISCUSSION

The fitted results for the three extinction laws described above are presented in Table 10 for each SN. We present the results for two cases, where the laws have been fitted with and without using the colours from the *HST* and *Swift* NUV filters. The fitted laws using all data are also shown in Figure 8 together with the measured $E(X - V)$, where each law only is plotted for the data phase range used for the fit.

The overall goodness of fit in terms of the reduced χ^2 is acceptable for the number of degrees of freedom (~ 10), in particular for the low-reddening SNe[7], which suggests that the observed colours can indeed be described by the colours of SN 2011fe with the adopted intrinsic dispersions, together with an extinction law with only two (three for the power-law) free parameters. The six SNe span a broad range both in reddening, $E(B - V) = 0.2$–1.3, and in $R_V = 1.3$–2.7 which confirms previous optical and NIR studies (B14), pointing to a diversity of observed reddening laws. We also note that the three laws in general fit the data well and that the difference between the laws for one SN is often within the adopted uncertainties as shown in Figure 8. The difference in reddening law properties between the different SNe is much more significant than the difference between the individual laws for one SN. Based on this, we will simplify the analysis and mainly compare the F99 fits for the rest of the paper.

While Figure 8 is a comprehensive way to present the results, it can be simplified by projecting the colour excesses over phase. In Figure 9 we show the extinction, $A_X/A_V = 1 - E(X - V)/A_V$, for the four SNe with $E(B - V) > 0.2$. Here, A_X/A_V was obtained by calculating the weighted mean $E(X - V)$ for all phases for each filter together with the fitted F99 parameters $A_V = R_V \cdot E(B - V)$. The effective wavelength was then calculated for each filter X for both the unreddened SED of SN 2011fe and after this has been reddened by the fitted F99 law. The difference between these two calculated wavelengths is small for the NIR and optical filters, but becomes larger for the bluer filters as expected. We then follow the procedure from A14 and allow the wavelengths to shift within the range until the residuals $(A_X - A_\lambda)/A_V$ match the weighted average residuals, for all epochs, with respect the fitted F99 law from Figure 8. The figure illustrates the significant difference in the derived extinction law between the SNe and the others and the diversity is particularly striking bluewards of the U, demonstrating the power of using NUV data to study extinction.

6.1 Time-dependent reddening

For low-extinction SNe the fitted reddening laws are more sensitive to the assumptions of the intrinsic colours and how these evolve with SN phase. For SN 2012cg this is particularly striking where there is a clear systematic colour evolution in NIR and NUV. Although the variations are within the adopted uncertainties and the χ^2 goodness of fit is acceptable, the systematic colour evolution indicate that

[7] The reduced χ^2 for SN 2014J is higher compared to A14 which originates from the lower colour dispersions adopted in this work.

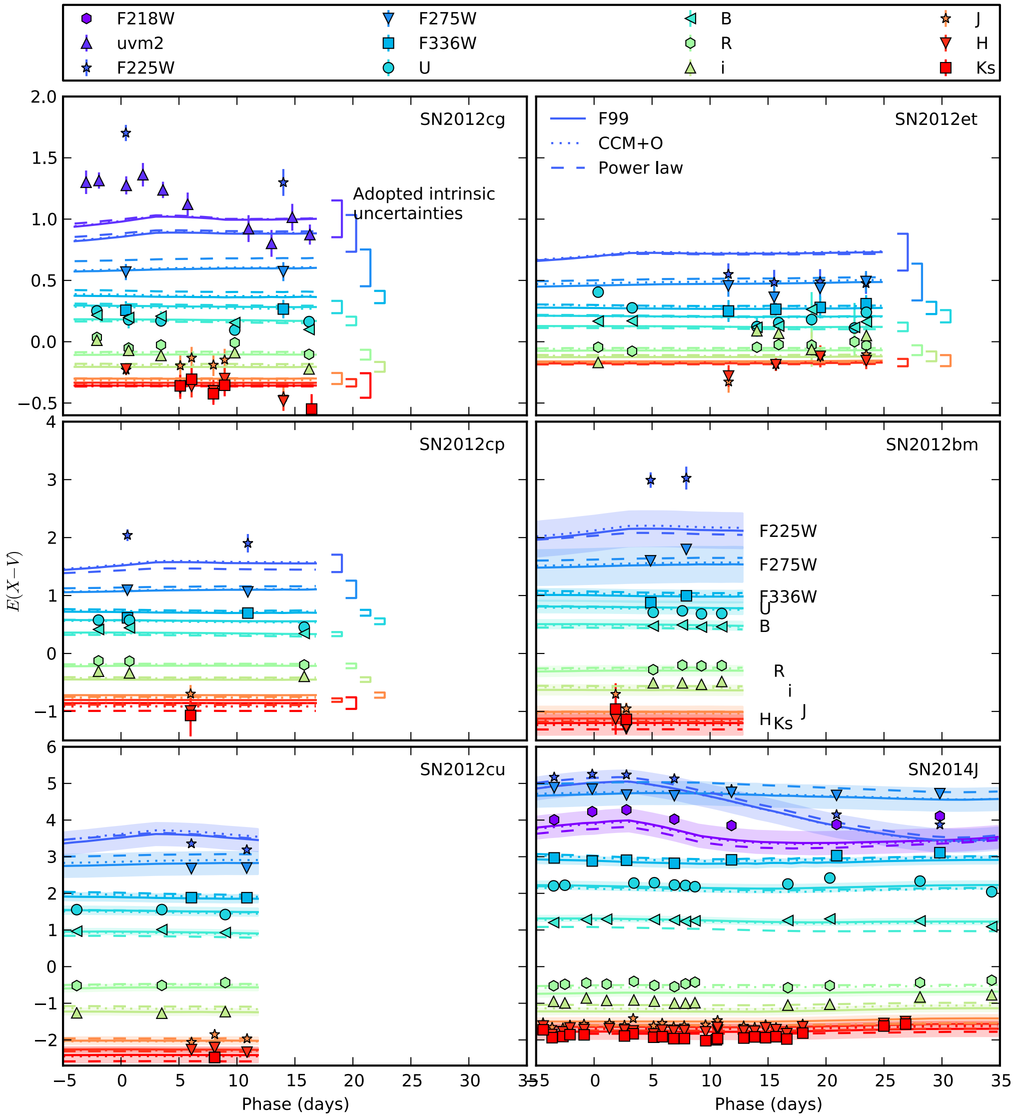

Figure 8. The difference between the measured colour, $X - V$, and the corresponding colour for SN 2011fe colour model against phase for all supernovae and filters. The fitted extinction laws presented in Table 10 are shown as lines and the adopted intrinsic colour uncertainty is marked as shaded regions with respect to the best fit F99 law. All fitted extinction laws are only plotted over the fitted phase ranges. The apparent time-dependece of $E(X - V)$ for the F218W and F225W originates from the red-tails of these filters which causes the observed color excess to vary with the intrinsic colour of the source.

these colours evolve slower than the corresponding SN 2011fe colours, resulting in an apparent decrease with time of the colour excesses.

However, evolving SN colours, or a reddening law that changes with time is also predicted if there is circumstellar dust around the SN as discussed above. Photons that scatter on the CS dust but still reach the observer will arrive later than photons that do not interact. In other words, an observation 1–2 weeks past maximum will be a superposition of the SN SED at the given epoch and the SED from earlier

	F99			CCM+O			Power law			
SN	$E(B-V)$	R_V	χ^2/ν	$E(B-V)$	R_V	χ^2/ν	A_V	a	p	χ^2/ν
2012cg	0.11(0.04)	$3.6^{+2.4}_{-1.1}$	0.51	0.12(0.05)	$3.7^{+3.0}_{-1.4}$	0.52	1.23(2.32)	0.6(1.2)	−0.6(0.6)	0.24
2012cg†	0.19(0.02)	$2.1^{+0.4}_{-0.4}$	1.23	0.19(0.02)	$2.0^{+0.5}_{-0.4}$	1.29	0.89(1.16)	0.4(0.6)	−1.5(0.3)	1.25
2012et	0.17(0.04)	$0.9^{+0.6}_{-0.6}$	1.13	0.18(0.05)	$0.6^{+0.7}_{-0.5}$	0.90	0.12(0.32)	1.0(2.7)	−3.6(1.3)	1.43
2012et†	0.13(0.02)	$1.6^{+0.5}_{-0.4}$	0.77	0.14(0.03)	$1.2^{+0.7}_{-0.6}$	0.64	0.20(0.44)	1.0(2.2)	−1.9(0.5)	0.62
2012cp	0.36(0.04)	$2.7^{+0.6}_{-0.5}$	1.13	0.39(0.05)	$2.5^{+0.6}_{-0.5}$	0.91	1.32(1.49)	1.0(1.1)	−1.0(0.3)	0.78
2012cp†	0.37(0.03)	$2.6^{+0.4}_{-0.4}$	1.08	0.37(0.03)	$2.6^{+0.4}_{-0.4}$	0.91	1.29(1.15)	1.0(0.9)	−1.0(0.2)	1.21
2012bm	0.46(0.05)	$3.0^{+0.4}_{-0.3}$	1.23	0.48(0.05)	$2.9^{+0.5}_{-0.4}$	0.94	1.91(1.26)	1.0(0.7)	−0.9(0.2)	0.84
2012bm†	0.52(0.03)	$2.6^{+0.2}_{-0.2}$	2.11	0.52(0.03)	$2.5^{+0.2}_{-0.2}$	1.66	1.66(0.92)	1.0(0.6)	−1.1(0.1)	2.34
2012cu	0.99(0.05)	$2.7^{+0.2}_{-0.1}$	0.67	1.05(0.05)	$2.5^{+0.2}_{-0.2}$	0.54	2.94(0.87)	1.1(0.3)	−1.1(0.1)	1.50
2012cu†	0.99(0.03)	$2.7^{+0.1}_{-0.1}$	0.42	1.00(0.03)	$2.7^{+0.1}_{-0.1}$	0.73	3.17(0.80)	1.1(0.3)	−1.0(0.1)	1.67
2014J	1.28(0.04)	$1.6^{+0.1}_{-0.1}$	2.63	1.37(0.04)	$1.2^{+0.1}_{-0.1}$	1.67	1.84(0.51)	1.0(0.3)	−2.1(0.1)	1.62
2014J†	1.37(0.02)	$1.5^{+0.0}_{-0.0}$	2.24	1.40(0.02)	$1.2^{+0.1}_{-0.1}$	1.27	1.87(0.34)	1.0(0.2)	−2.1(0.1)	1.69

† Including colours based on *HST* and *Swift* NUV photometry.

Table 10. The best fitted parameters for the reddening laws investigated in this work, where the data and phase ranges used for the different SNe are shown in Figure 8 together with the fitted laws. In the table the fits are presented without and with including the *HST* and *Swift* NUV colours based on the broadband filters *uvm2*, F218W, F225W, F275W and F336W. All quoted uncertainties are at the 68 % level, considering each parameter individually.

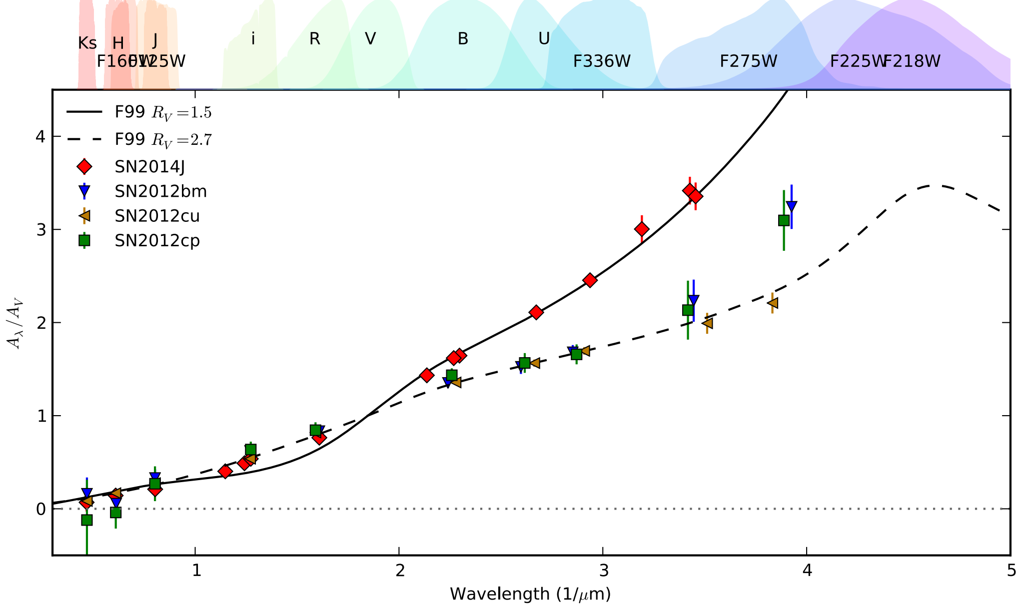

Figure 9. The normalised extinction, A_X/A_V, for the four SNe with $E(B-V) > 0.2$, calculated as the weighted mean for all epochs. Each data point has been shifted within the wavelength range spanned by the effective wavelengths of its filter for the reddened and unreddened case until it matched the weighted mean residual with respect to the fitted F99 law for the corresponding SN in Figure 8. The filter passbands for the filters used are shown at the top.

epochs, when the SN was bluer, which would lead to a slower colour evolution similar to what is observed for SN 2012cg. However, since the scattering cross section drops with wavelength the observed effect is expected affect the NUV to a much higher degree than the NIR which argues against this interpretation for SN 2012cg where also the $V - i$ and NIR colours seem to evolve to the same degree.

Further, the early discovery of SN 2012cg (Silverman et al. 2012) and the close distance allowed extensive follow-up of the SN and no evidence of CS material has been seen. As discussed above we do not detect any significant evolution of the Na I D absorption features. Chomiuk et al. (2012) reported deep limits of the 5.9 GHz radio flux density of four epochs and concluded that if CS material would be present around the SN, it must be located either at a radius $> 10^{16}$ cm or distributed in thin shells of widths $\lesssim 10^{15}$ cm. Observations with Herschel also disfavours CS dust and puts a limit on the dust mass of $M_{\rm dust} \lesssim 10^{-1}\,{\rm M}_{\odot}$ for temperatures and grain sizes of Tdust ~ 500 K $0.1\,\mu$m respectively based on non-detections at $70\,\mu$m and $160\,\mu$m (Johansson et al. 2013).

Note that while SN 2012cg show a clear time-evolution in its colours this is less apparent for the other low-reddening SN 2012et. However, this SN lack the same temporal coverage, and we only have full NUV-NIR coverage at $> +10$ days which does not allow a fair comparison between the two.

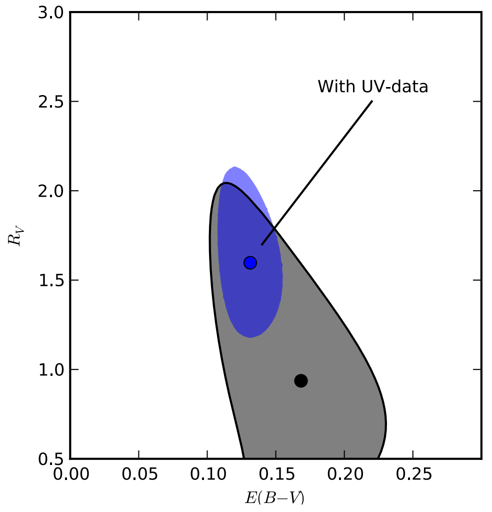

Figure 10. Contours showing the joint 68 % uncertainty region for the fitted parameters R_V and $E(B-V)$ for a F99 extinction laws for SN 2012et. The two contours show the fit results when the full data set is used (blue contour region) and when the colours based on *HST* and *Swift* UV observations are omitted (grey contour region).

6.2 The impact of the NUV-data

In order to study both the impact of the NUV data on the fits but also to test the consistency of the fitted reddening laws across the full wavelength range, the extinction laws were fitted both with and without including the NUV data. We have already seen in Figures 8 and 9 that all colours of SNe 2012cu and 2014J are consistent with their fitted reddening laws. It is therefore not surprising that the NUV-colours only has a minor impact on the best fitted central values as seen in Table 10. The change in R_V is marginal also for SN 2012cp while it drops by $\sim 1\sigma$ for SN 2012bm when the NUV-colours are added. For both of these SNe there is a tentative tension between the bluest colour and the fitted reddening law but this does not appear to significantly affect the fitted parameters.

The major impact of adding the NUV-colours is on the uncertainties of the fitted values. This is illustrated in Figure 10 where the grey contour shows the 68 % confidence region for $E(B-V)$ and R_V when the F99 law is fitted to the NIR–optical data of SN 2012et, while the blue contour shows the uncertainties from the full NIR–NUV fit. The fitted uncertainties for R_V are asymmetric for low extinction SNe. For these, the fitted extinction law is in general less constrained against high R_V values since these predict flatter extinction laws with a weak wavelength dependence of $E(X-V)$. Low R_V values on the the other hand result in a steeper extinction law, i.e. a steeper wavelength dependence of $E(X-V)$, which can be constrained even for moderately reddened SNe. However, using data over a wide wavelength range can significantly improve the constraints of R_V. This is illustrated both by the contours in Figure 10 as well as the results in Table 10 where the uncertainties drop by up to ~ 50 % when the NUV data is added, despite the high intrinsic dispersion adopted for the *Swift* and *HST* colours (see Section 5.1).

6.3 The origin of the SN extinction

As already discussed we can expect observed SN Ia colours to be a mixture of an intrinsic SN Ia colour relation and extinction. We can also assume that with increased observed reddening, the latter of these two effects is expected to dominate, and for the most reddened objects in our sample, SNe 2012cu and 2014J, the fits will be less sensitive to intrinsic SN Ia variations. It is therefore particularly interesting to note that these two SNe point to quite different extinction laws with $R_V = 1.5 \pm 0.1$ and $R_V = 2.7 \pm 0.1$ for SNe 2014J and 2012cu respectively as clearly illustrated in Figure 9.

In the light of the velocity-colour relation for the $B - V$ and the findings of M13 that all "NUV-blue" SNe belong to the photospheric NV class while the "NUV-red" consists of both NV and HV SNe it is worth to also compare the derived extinction parameters with the Si II λ6355 Å velocities, where both SNe that prefer a low R_V are HV SNe while the remaining are NV. This is consistent with the statistical study of samples of SNe Ia by Wang et al. (2009) that found $R_V = 1.6$ and $R_V = 2.4$ for HV and NV samples respectively. Foley & Kasen (2011) however obtained $R_V \approx 2.5$ when both subsamples were fitted separately after the SNe with $E(B-V) > 0.35$ mag were omitted. A possible velocity-R_V relation would suggest that either the reddening is related to SN properties or the immediate environment or point to different explosion channels in different host galaxies. Since circumstellar dust would give rise to low R_V values the former is a possible explanation and

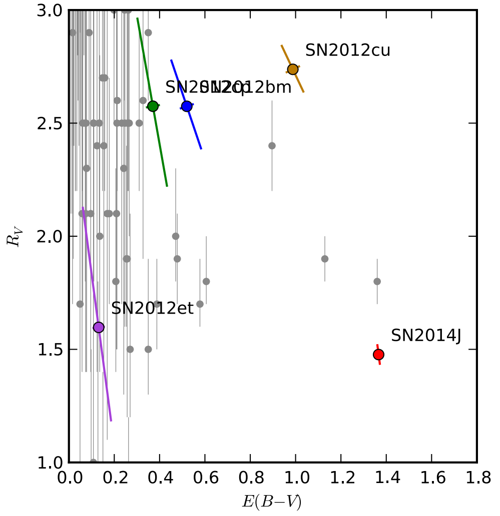

Figure 11. Best fitted R_V and $E(B-V)$ values using the F99 law for the SNe of this sample together with the results from Burns et al. (2014) (in grey).

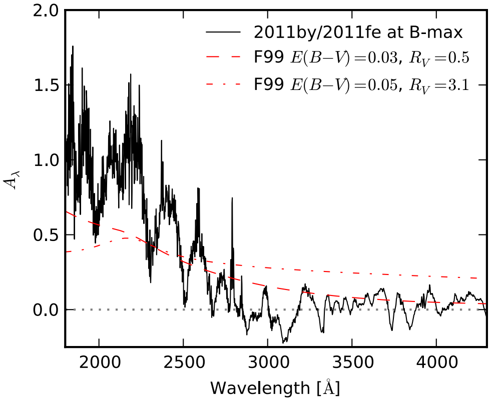

Figure 12. The flux ratio between SN 2011by and SN 2011fe after that they have been corrected for Galactic extinction, shifted to rest frame, and normalized to have the same flux for wavelengths $\lambda > 3000$ Å. Overplotted are also the best fit F99 laws for $R_V = 0.5$ and $R_V = 3.1$.

supported by individual SNe such as SN 2006X that both favours a low R_V (Folatelli et al. 2010, $R_V = 1.6 \pm 0.1$) and showed evidence of circumstellar material from studying time-variation of the Na I D absorption features over the time-scale of the SN (Patat et al. 2007). On the other hand, the polarisation angle of the light is well aligned with the spiral structure of the host galaxy (Patat et al. 2014) suggesting that the majority of the dust reddening is of interstellar nature. The same is also true for SN 2014J and for this SN no Na I D variation was found (Goobar et al. 2014; Foley et al. 2014b; Graham et al. 2014b) while both K I variation (Graham et al. 2014b) and light echoes (Crotts 2014) has been detected and is consistent with material at $r \gtrsim 10^{19}$ cm.

In other words, although it is clear that both of these SNe exploded in dusty environment there are no conclusive evidence showing that the neither the immediate environment nor the intrinsic SN properties are responsible for the observed peculiar reddening law.

6.4 Using SN 2011by as the unreddened template

Two SNe, 2012bm, 2012cg and 2012cp, both show a tension for the F225W $-V$ color where the measured excess is redder than the best fit model predict. This is particular striking for SN 2012cg at maximum where the F225W $-V$ color is $\sim 2\sigma$ redder than any of the fitted extinction laws in Figure 8, which suggests that the reddening laws we have tested may provide an even better fit if the colour excesses are derived using a SN that is intrinsically fainter in the NUV than SN 2011fe.

SN 2011by was discovered by Jin & Gao (2011) in NGC 3972 and found to be a spectroscopically normal SN Ia (Silverman et al. 2013) with minimal reddening (Maguire et al. 2012). It is very similar to SN 2011fe in the optical but fainter in the NUV (Foley & Kirshner 2013; Graham et al. 2015). This is shown in Figure 13, where the ratio between the two SN spectra are plotted at B-maximum. To emphasise that the difference between the two SNe cannot be explained, nor mimicked, by extinction we also show the F99 law for $R_V = 0.5$ and $R_V = 3.1$.

HST/STIS spectroscopy in the NUV of SN 2011by was obtained at -10 and -1 days with respect to B-maximum, where the latter phase is overlapping with NUV observations of both SN 2012cg and SN 2012cp. In addition to this, SN 2014J also have NUV data at maximum, which allows us to study the reddening of the three SNe with respect to SN 2011by under the assumption that the intrinsic colour evolution is modest within -1 to $+1$ days from B-max. We further assume for SNe 2012cg and 2014J, which also have NIR measurements at maximum, that SN 2011by is identical to SN 2011fe in the NIR, and we use the latter to extend the *STIS* spectrum. Synthetic colours are derived for all bands for SN 2011by, and we then proceed to fit the F99 law as already described in Section 5.

The best fitted laws to the measured colour excesses at maximum are shown in Figure 13, with the parameters in Table 11. The fit results are presented for both template SNe, and the results are similar. From this we can conclude that the imposed systematic uncertainty from the intrinsic NUV diversity, at least when it comes to comparing these SNe, are of the same order, or smaller than the statistical uncertainties.

7 CONCLUSIONS

In this work we have presented and analysed broadband photometry of seven Type Ia supernovae covering the wavelength range 0.2–2 μm. The SNe have colour excesses in the range $E(B-V) = 0.0$–1.4 and we have studied the reddening properties by comparing them to the normal SN Ia

	SN2012cg			SN2012cp			SN2014J		
Templ.	$E(B-V)$	R_V	χ^2/dof	$E(B-V)$	R_V	χ^2/dof	$E(B-V)$	R_V	χ^2/dof
2011fe	0.17(0.03)	$1.0^{+0.4}_{-0.3}$	1.06	0.35(0.03)	$1.6^{+0.5}_{-0.4}$	1.17	1.31(0.03)	$1.5^{+0.1}_{-0.1}$	3.25
2011by	0.15(0.02)	$1.0^{+0.5}_{-0.4}$	0.70	0.33(0.03)	$1.5^{+0.5}_{-0.4}$	0.52	1.30(0.03)	$1.6^{+0.1}_{-0.1}$	3.23

Table 11. Best fitted parameters of the F99 law where only data within 1 day of B-band maximum is considered for the four SNe in the sample with observations that fulfil this condition. The results are shown for two different cases where SNe 2011fe and 2011by, respectively, are assumed to describe the unreddened objects.

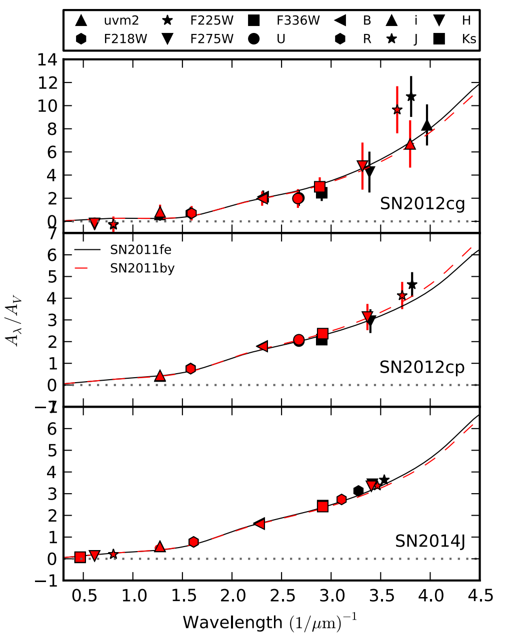

Figure 13. Best fitted F99 laws with the parameters presented in Table 11 where only data within 1 day of B-band maximum is considered for the four SNe in the sample with observations that fulfil this condition. The results are shown for two different cases where SNe 2011fe (solid black lines) and 2011by (dashed red lines), respectively, are assumed to describe the unreddened objects.

2011fe and testing three different extinction laws to the data: O'Donnell (1994), Fitzpatrick (1999), and a power-law as parametrised by Goobar (2008). We summarise the main findings as follows:

(i) The difference between the fitted reddening laws for different SNe is significantly greater than discrepancy between the laws for a single SN.

(ii) For the Goobar (2008) law, we obtain a range of values for the total-to-selective extinction, $R_V = 1.5^{+0.1}_{-0.1}$–$2.7^{+-0.6}_{-0.3}$ when fitted together with $E(B-V)$.

(iii) For our two reddest SNe with $E(B-V) > 1$ we observe significantly different values of R_V of $R_V = 2.7 \pm 0.1$ (SN 2012cu) and $R_V = 1.5 \pm 0.1$ respectively, and four our small sample we do not see any indications of a relation between $E(B-V)$, and R_V as suggested by e.g. Burns et al. (2014).

ACKNOWLEDGEMENT

We would like to thank Denise Taylor at Space Telescope Science Institute for advising and assisting us in carrying out this program. R.A. and A.G. acknowledge support from the Swedish Research Council and the Swedish Space Board. Observations were made with the *Hubble Space Telescope*; the Nordic Optical Telescope, operated by the Nordic Optical Telescope Scientific Association at the Observatorio del Roque de los Muchachos, La Palma, Spain STSDAS and PyRAF is a product of the Space Telescope Science Institute, which is operated by AURA for NASA. V.S. acknowledges support from Fundação para a Ciência e a Tecnologia (Ciência 2008) and grant PTDC/CTE-AST/112582/2009.

APPENDIX A: A SPECTRAL AND COLOUR MODEL FROM SN 2011fe

SN 2011fe is a normal SN Ia with excellent temporal and wavelength coverage with negligible extinction along the line of sight and is therefore a suitable object for reddening studies. In A14 we used the available NUV-NIR spectroscopic time-series (Pereira et al. 2013; Mazzali et al. 2014) and the NIR lightcurves (Matheson et al. 2012) to derive the extinction law of SN 2014J. In this work we extend this model with NUV photometry (Brown et al. 2012) and optical photometry at 25 to 40 days past B-band maximum.

The lightcurves in the NUV F218W, F225W, F275W, F336W and the optical $BVRi$ bands are first constructed by synthesizing the spectra from Mazzali et al. (2014) and Pereira et al. (2013). A lightcurve model for each filter is then obtained by fitting smoothed splines using `SNooPy` (Burns et al. 2011). For the redder optical R and i bands, the sparse temporal coverage after 20 days past B-maximum does not allow an accurate spline fit of the second bump. We therefore also use the data from Munari et al. (2013) to constrain the spline fit at > 25 days past B-max. For the Swift/UVOT *uvm2* filter and the NIR *JHKs* we fit spline models to the measured lightcurves from Brown et al. (2012) and Matheson et al. (2012) respectively. The lightcurve models are then used to calculate the $(X-V)_0$ colour models shown in Figure 4.

As explained in 5 we also need a model of the spectral energy density of the *unreddened* object in order to be able to calculate the expected extinction for each passband for a given extinction model. In A14 the extinction for a given set reddening law parameters was first calculated for all available spectra of SN 2011fe and the extinction for any given epoch was then obtained using spline interpolation. Similar to the lightcurve spline model, this approach is adequate for the NUV, but due to the sparse spectral coverage will cause the model to deviate from the lightcurve for the redder optical bands and NIR at > 25 days past maximum. In A14 this did not affect the final results due to the high extinction of SN 2014J and the conservative intrinsic color dispersions adopted in the analysis.

In this work we have developed a more accurate SED model by first resampling the spectral time series used in A14 to a resolution of 10 Å, which are shown as the red spectra in Figure A1. These were then used to calculate the missing wavelength and temporal elements through linear interpolation (shown in grey in Figure A1), and finally the full matrix is mangled to match the lightcurve models described above after the synthetic lightcurves have been calculated. The agreement between the synthetic colors calculated from the SED and the spline color model is < 0.05 mag for all epochs.

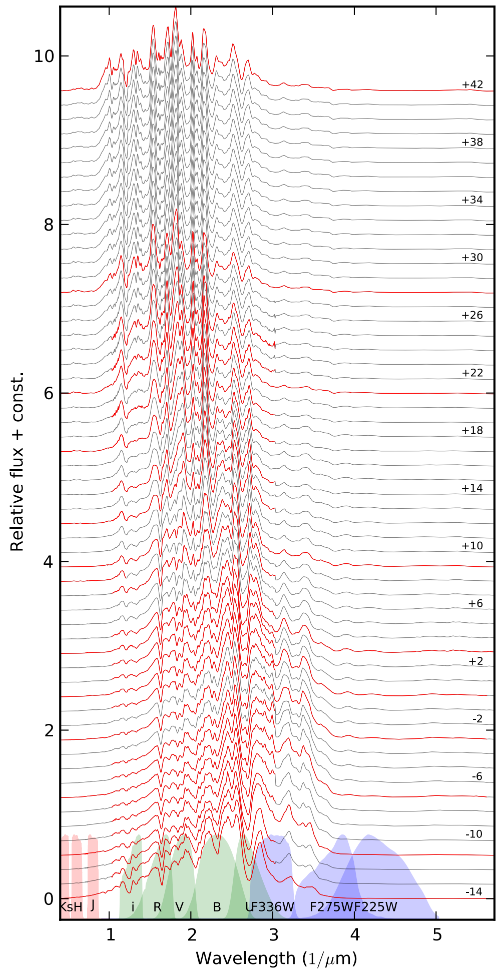

Figure A1. The spectral model constructed from measured spectra of SN 2011fe. Sections based on measured data are shown in red, while the interpolated sections and warped to the lightcurve template are shown as grey. The filters used for the warping are shown at the bottom of the figure.

APPENDIX B: RED TAILS OF THE HST FILTERS

The HST-filters used in this work, shown in the upper panel of Figure B1, all suffer from red tails. As mentioned in A14, these are relatively small, e.g. the transmission of F225W is roughly one part in 100 000 at 5000 Å compared to the peak transmission at $\sim$ 2250 Å, but they still have implications for studying reddened SNe Ia. For example, from spectrophotometry of SN 2011fe at maximum (thin black line in the middle panel), we can conclude that $\sim$ 0.5 % of the flux (thick black line) in the F225W filter will originate from wavelengths > 4000 Å. However, extinction will suppress the UV-flux significantly and after applying a F99 reddening law with $E(B-V) = 1.4$, $R_V = 1.4$, $\sim$ 60 % of the F225W flux (think gray line) comes from photons with $\lambda > 4000$ Å.

Another way to illustrate the effect of the red tails is shown in the lower panel of Figure B1 where the effective wavelength of the filters for the 2011fe spectrum is shown with various amounts of reddening applied. As seen in the figure, F275W and F336W are less plagued by red tails than F218W and F225W which, in fact, both will be probing redder effective wavelengths of the SN spectrum than the two former filters for $E(B-V) \gtrsim 1$.

The fact that we are comparing different effective wavelengths when calculating the color excess between a reddened and unreddened source is true for all broad band observations. However, fitting extinction properties based on filters with red tails that span a wavelength range where the SED drops rapidly, also puts demands on knowing the passband throughput accurately even when the transmission drops several orders of magnitude as for the filters in Figure B1.

The expected WFC3/UVIS passband red tails were tested (Brown 2011) in the final round of thermal vacuum tests of WFC3 prior to launch. They studied the filter throughputs in four wavelength bins centered on 450, 600, 750 and 900 nm and found deviations of up to $\sim$ 40 % between the measured and expected transmission. If the deviations are taken as an estimate of the throughput uncertainty at these wavelengths, we can evaluate its impact on the extinction analysis.

We carried out this test by first applying a F99 reddening law with $E(B-V) = 1.4$, $R_V = 1.4$ to the SED of SN 2011fe described in Section 5.1. The impact on the calculated extinction for the three bands, F218W, F225W and F275W (the test of F336W was not carried out due to limitations in the setup as described in Brown 2011) can be then be obtained by comparing synthetic magnitudes from the original SYNPHOT throughputs to when these have been multiplied by a spline function derived from the deviations measured for the four wavelength bins above. The impact on the calculated extinction was found to always be < 0.05 mag. Further, the worst case scenario can be estimated by letting all the measured deviations from Brown (2011) maximise the amount of red light entering the filter. The result on the extinction from this was < 0.10 mag for $t < 20$ days with respect to B max and 0.15–0.20 mag for $t = 20$–40, which is still within the dispersion that we have adopted for the intrinsic UV colours.

It is also possible to investigate the accuracy of the full HST/WFC3/UVIS SYNPHOT throughput by comparing spectrophotometry of objects, with known spectra, to WFC3/UVIS photometry. This is in fact the most direct test we can carry out of our method for fitting extinction laws since this is using the very same procedure. In figure B2 we have plotted stars from CALSPEC[8] with the corresponding UVIS-photometry using the same analysis path as in Section 2.1 with a 0.4" radius. The agreement is in general more than sufficient for the purpose of this analysis, but it is unfortunate that data are not available for redder stars for which the impact of the red tail can be expected to be more significant. The star P330E should be discarded from the comparison since this star has been used for calibrating the WFC3/UVIS system.

If despite these tests the adopted WFC3/UVIS passband throughputs do not accurately describe the real throughput we would expect to fit different extinctions as the intrinsic colour of the SNe evolve with time. In our analysis, as described by equation (1) in Section 5, we are comparing the *measured* extinction between two bands to the *synthetically calculated*, using the assumptions that we know the underlying intrinsic SED and the relevant passband throughputs. An inaccurate description of the throughputs would also give rise to an inaccurate synthetically calculated extinction, and since the SED evolves with time, different time evolutions of the first (measured) and second (synthetic) terms of equation (1) are to be expected. Note, that similar time-variations can of course also be expected if the assumed intrinsic SED in the analysis does not describe the intrinsic colours of the reddened objects within the adopted uncertainties. It is therefore reassuring that the extinction of the reddest SN Ia in our sample, 2014J, does not appear to change with time in our analysis (although Foley et al. (2014a) come to a different conclusion from analysing spectroscopic data).

References

Amanullah R., Goobar A., 2011, ApJ, 735, 20
Amanullah R. et al., 2014, ApJL, 788, L21
Amanullah R. et al., 2010, ApJ, 716, 712
Astier P. et al., 2006, A&A, 447, 31
Betoule M. et al., 2014, A&A, 568, A22
Blondin S. et al., 2012, AJ, 143, 126
Blondin S., Prieto J. L., Patat F., Challis P., Hicken M., Kirshner R. P., Matheson T., Modjaz M., 2009, ApJ, 693, 207
Blondin S., Tonry J. L., 2007, ApJ, 666, 1024
Borkowski K. J., Blondin J. M., Reynolds S. P., 2009, ApJL, 699, L64
Bourque M., Anderson J., 2014, Technical report, CTE Correction for UVIS Subarrays Without Pre-Scan Bias Pixels. STScI
Branch D. et al., 2006, PASP, 118, 560
Branch D. et al., 2003, AJ, 126, 1489
Brown P. J., Breeveld A. A., Holland S., Kuin P., Pritchard T., 2014, Ap&SS, 354, 89
Brown P. J. et al., 2012, ApJ, 753, 22
Brown P. J. et al., 2010, ApJ, 721, 1608
Brown T., 2011, Instrument Science Report WFC3, 2008-49
Burns C. R. et al., 2014, ApJ, 789, 32
Burns C. R. et al., 2011, AJ, 141, 19
Cappellaro E., Pastorello A., Tomasella L., Benetti S., Fiaschi M., Ochner P., Turatto M., Valenti S., 2012, Central Bureau Electronic Telegrams, 3077, 2
Cardelli J. A., Clayton G. C., Mathis J. S., 1989, ApJ, 345, 245
Cenko S. B., Filippenko A. V., Silverman J. M., Gal-Yam A., Pei L., Nguyen M., Carson D., Barth A. J., 2012, Central Bureau Electronic Telegrams, 3111, 2
Chomiuk L., Soderberg A., Simon J., Foley R., 2012, The Astronomer's Telegram, 4453, 1
Chomiuk L. et al., 2012, ApJ, 750, 164
Chotard N. et al., 2011, A&A, 529, L4
Conley A. et al., 2011, ApJS, 192, 1
Conley A. et al., 2008, ApJ, 681, 482
Cortés J. R., Kenney J. D. P., Hardy E., 2006, AJ, 131, 747
Cox L. et al., 2012, Central Bureau Electronic Telegrams, 3130, 1
Crotts A., 2014, ArXiv e-prints
Dalcanton J. J. et al., 2009, ApJS, 183, 67
Dennefeld M., Pizzella A., Valentini M., Tomasella L., Benetti S., Cortes M., Ozel N., Rajpurohit A., 2012, Central Bureau Electronic Telegrams, 3226, 2
Dilday B. et al., 2012, Science, 337, 942
Elias-Rosa N. et al., 2006, MNRAS, 369, 1880
Elias-Rosa N. et al., 2008, MNRAS, 384, 107
Filippenko A. V., Li W. D., Treffers R. R., Modjaz M., 2001, in Paczynski B., Chen W.-P., Lemme C., eds, Astronomical Society of the Pacific Conference Series Vol. 246, IAU Colloq. 183: Small Telescope Astronomy on Global Scales. p. 121
Fitzpatrick E. L., 1999, PASP, 111, 63
Folatelli G. et al., 2013, ApJ, 773, 53
Folatelli G. et al., 2010, AJ, 139, 120
Folatelli G. et al., 2012, ApJ, 745, 74
Foley R. J. et al., 2014a, ArXiv e-prints
Foley R. J. et al., 2014b, MNRAS, 443, 2887
Foley R. J., Kasen D., 2011, ApJ, 729, 55
Foley R. J., Kirshner R. P., 2013, ApJL, 769, L1
Förster F., González-Gaitán S., Folatelli G., Morrell N., 2013, ApJ, 772, 19
Fox O. D. et al., 2011, ApJ, 741, 7
Fox O. D., Filippenko A. V., 2013, ApJL, 772, L6

[8] `http://www.stsci.edu/hst/observatory/crds/calspec.html`

Friedman A. S., 2012, PhD thesis, Harvard University
Fruchter A. S., et al. 2010, in 2010 Space Telescope Science Institute Calibration Workshop, p. 382-387. pp 382–387
Goldhaber G. et al., 2001, ApJ, 558, 359
Goobar A., 2008, ApJL, 686, L103
Goobar A. et al., 2014, ApJL, 784, L12
Graham M. L. et al., 2014a, ArXiv e-prints
Graham M. L. et al., 2015, MNRAS, 446, 2073
Graham M. L. et al., 2014b, ArXiv e-prints
Graur O., Maoz D., 2012, The Astronomer's Telegram, 4226, 1
Guy J. et al., 2007, A&A, 466, 11
Guy J. et al., 2007, A&A, 466, 11
Guy J., Astier P., Nobili S., Regnault N., Pain R., 2005a, A&A, 443, 781
Guy J., Astier P., Nobili S., Regnault N., Pain R., 2005b, A&A, 443, 781
Harutyunyan A. H. et al., 2008, A&A, 488, 383
Haynes M. P., Jore K. P., Barrett E. A., Broeils A. H., Murray B. M., 2000, AJ, 120, 703
Hsiao E. Y., Conley A., Howell D. A., Sullivan M., Pritchet C. J., Carlberg R. G., Nugent P. E., Phillips M. M., 2007, ApJ, 663, 1187
Hsiao E. Y. et al., 2013, ApJ, 766, 72
Itagaki K. et al., 2012, Central Bureau Electronic Telegrams, 3146, 1
Jin Z., Gao X., 2011, Central Bureau Electronic Telegrams, 2708, 1
Johansson J., Amanullah R., Goobar A., 2013, MNRAS, 431, L43
Johansson J. et al., 2014, ArXiv e-prints
Kandrashoff M. et al., 2012, Central Bureau Electronic Telegrams, 3111, 1
Kirshner R. P. et al., 1993, ApJ, 415, 589
Krisciunas K. et al., 2007, AJ, 133, 58
Krisciunas K., Prieto J. L., Garnavich P. M., Riley J.-L. G., Rest A., Stubbs C., McMillan R., 2006, AJ, 131, 1639
Krisciunas K. et al., 2003, AJ, 125, 166
Landolt A. U., 1992, AJ, 104, 340
Leibundgut B., 1988, PhD thesis, PhD thesis. Univ. Basel.137 pp. , (1988)
Maguire K. et al., 2012, MNRAS, 426, 2359
Maguire K. et al., 2013, MNRAS, 436, 222
Mandel K. S., Foley R. J., Kirshner R. P., 2014, ApJ, 797, 75
Marion G. H., Milisavljevic D., Rines K., Wilhelmy S., 2012, Central Bureau Electronic Telegrams, 3146, 2
Matheson T. et al., 2012, ApJ, 754, 19
Mazzali P. A. et al., 2014, MNRAS, 439, 1959
McClelland C. M., Garnavich P. M., Milne P. A., Shappee B. J., Pogge R. W., 2013, ApJ, 767, 119
Ménard B., Nestor D., Turnshek D., Quider A., Richards G., Chelouche D., Rao S., 2008, MNRAS, 385, 1053
Milisavljevic D., 2012, Central Bureau Electronic Telegrams, 3130, 3
Milne P. A., Brown P. J., Roming P. W. A., Bufano F., Gehrels N., 2013, ApJ, 779, 23
Milne P. A. et al., 2010, ApJ, 721, 1627
Munari U., Henden A., Belligoli R., Castellani F., Cherini G., Righetti G. L., Vagnozzi A., 2013, New Astronomy, 20, 30
Munari U., Zwitter T., 1997, A&A, 318, 269
Nielsen M. T. B., Voss R., Nelemans G., 2013, MNRAS, 435, 187
Nobili S., Goobar A., 2008, A&A, 487, 19
Nordin J. et al., 2011, A&A, 526, A119
Nugent P., Kim A., Perlmutter S., 2002, PASP, 114, 803
Nugent P. E. et al., 2011, *Nature*, 480, 344
O'Donnell J. E., 1994, ApJ, 422, 158
Patat F. et al., 2007, Science, 317, 924
Patat F. et al., 2013, A&A, 549, A62
Patat F., Cox N. L. J., Parrent J., Branch D., 2010, A&A, 514, A78
Patat F. et al., 2014, ArXiv e-prints
Pereira R. et al., 2013, A&A, 554, A27
Perlmutter S. et al., 1999, ApJ, 517, 565
Perlmutter S. et al., 1997, ApJ, 483, 565
Phillips M. M., 1993, ApJL, 413, L105
Phillips M. M. et al., 2013, ApJ, 779, 38
Pignata G. et al., 2012, Central Bureau Electronic Telegrams, 3076, 1
Poznanski D., Prochaska J. X., Bloom J. S., 2012, MNRAS, 426, 1465
Prieto J. L., 2012, Central Bureau Electronic Telegrams, 3076, 2
Puckett T. et al., 2012, Central Bureau Electronic Telegrams, 3077, 1
Rich D. et al., 2012, Central Bureau Electronic Telegrams, 3226, 1
Riess A. G. et al., 1998, AJ, 116, 1009
Schlafly E. F., Finkbeiner D. P., 2011, ApJ, 737, 103
Schlegel D. J., Finkbeiner D. P., Davis M., 1998, ApJ, 500, 525
Scolnic D. M., Riess A. G., Foley R. J., Rest A., Rodney S. A., Brout D. J., Jones D. O., 2014, ApJ, 780, 37
Silverman J. M. et al., 2012, ApJL, 756, L7
Silverman J. M., Ganeshalingam M., Filippenko A. V., 2013, MNRAS, 430, 1030
Simon J. D. et al., 2009, ApJ, 702, 1157
Soker N., 2014, MNRAS, 444, L73
Stanishev V., et al. 2015
Sternberg A. et al., 2011, Science, 333, 856
Sternberg A. et al., 2014, MNRAS, 443, 1849
Stetson P. B., 1987, PASP, 99, 191
Stritzinger M. et al., 2002, AJ, 124, 2100
Sullivan M. et al., 2011, ApJ, 737, 102
Suntzeff N. B., 2000, in Holt S. S., Zhang W. W., eds, American Institute of Physics Conference Series Vol. 522, American Institute of Physics Conference Series. pp 65–74
Suzuki N. et al., 2012, ApJ, 746, 85
Taddia F. et al., 2012, A&A, 545, L7
Telting J. H. et al., 2014, Astronomische Nachrichten, 335, 41
Thomas R. C. et al., 2011, ApJ, 743, 27
Tomasella L. et al., 2014, Astronomische Nachrichten, 335, 841
Tripp R., 1998, A&A, 331, 815
Valenti S. et al., 2011, MNRAS, 416, 3138
Wang L., 2005, ApJL, 635, L33
Wang X. et al., 2009, ApJL, 699, L139
Zhang T.-M., Wu C.-J., Wang X.-F., 2012, Central Bureau Electronic Telegrams, 3130, 2

SUPPORTING INFORMATION

Additional Supporting Information may be found in the on-line ver- sion of this article.

[1] *Oskar Klein Centre, Physics Department, Stockholm University, SE 106 91 Stockholm, Sweden*
[2] *George P. and Cynthia Woods Mitchell Institute for Fundamental Physics & Astronomy, Texas A. & M. University Department of Physics and Astronomy, 4242 TAMU, College Station, TX 77843, USA*
[3] *Carnegie Observatories, Las Campanas Observatory, Casilla 601, La Serena, Chile*
[4] *Institute of Theoretical Astrophysics, University of Oslo, P.O. Box 1029, Blindern, NO-0315 Oslo, Norway*
[5] *Institut de Ciéncies de l'Espai (IEEC-CSIC), Facultat de Ciéncies, Campus UAB, 08193 Bellaterra, Spain*
[6] *Dark Cosmology Centre, Niels Bohr Institute, Copenhagen University, Juliane Maries Vej 30, 2100 Copenhagen O, Denmark*
[7] *Instituto de Astrofísica de Andalucía (IAA-CSIC), Glorieta de la Astronomía s/n, E-18008, Granada, Spain*
[8] *Unidad Asociada Grupo Ciencias Planetarias UPV/EHU-IAA/CSIC, Departamento de Física Aplicada I, E.T.S., Ingeniería,*
Universidad del País Vasco UPV/EHU, Bilbao, Spain
[9] *Oskar Klein Centre, Astronomy Department, Stockholm University, SE 106 91 Stockholm, Sweden*
[10] *Finnish Centre for Astronomy with ESO (FINCA), University of Turku, Väisäläntie 20, FI-21500 Piikkiö, Finland*
[11] *Benoziyo Center for Astrophysics, Faculty of Physics, Weizmann Institute of Science, 76100 Rehovot, Israel*
[12] *Department of Astronomy, University of California, Berkeley, CA 94720-3411, USA*
[13] *Computational Cosmology Center, Lawrence Berkeley National Laboratory, 1 Cyclotron Road, Berkeley, CA 94720, USA*
[14] *CENTRA - Centro Multidisciplinar de Astrofísica, Instituto Superior Técnico, Av. Rovisco Pais 1, 1049-001 Lisbon, Portugal*
[15] *School of Physics and Astronomy, University of Southampton, Southampton, SO17 1BJ, UK*

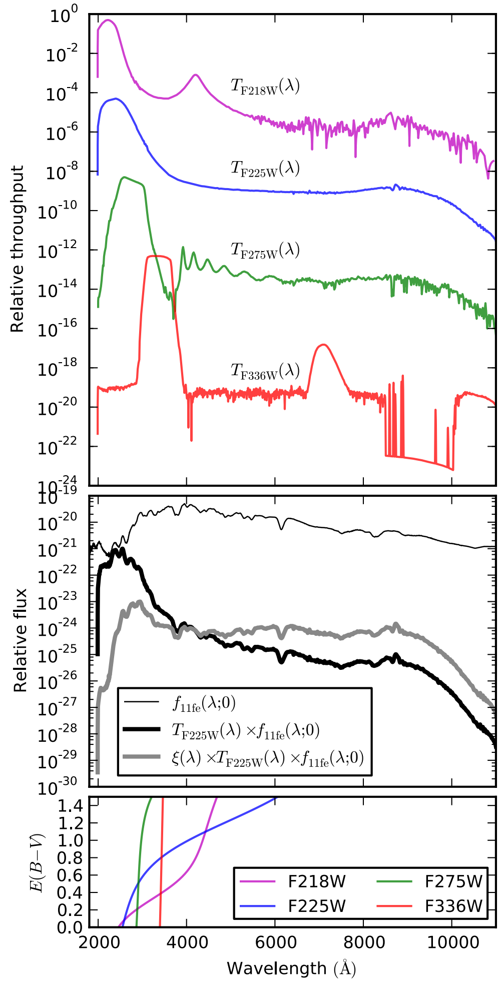

Figure B1. The *upper* panel show the filter transmissions, $T_X(\lambda)$, of the WFC3/UVIS passbands with arbitrary normalisation. The thin black line in the *middle* panel shows the spectra of 2011fe at B band maximum, while the thick black line show the same spectra after it has been multiplied by the F225W throughput. The thick, gray, line show the same spectra after it has been reddened with a F99 extinction law with E(B - V)=1.4 and $R_V = 1.4$. All three spectra are arbitrarily normalised. The *lower* panel shows the effective wavelength for the three passbands for 2011fe at B maximum, reddened with a F99 extinction law ($R_V = 1.4$) with increasing extinction.

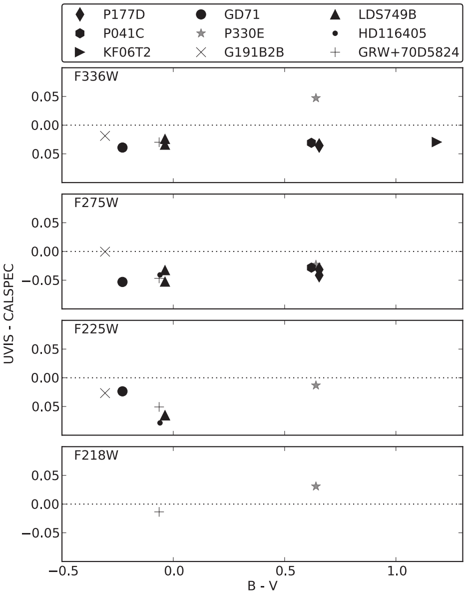

Figure B2. Comparison between spectrophotometry of CALSPEC stars using the WFC3/UVIS filter throughputs, with the corresponding WFC3/UVIS photometry against the synthetically calculated $B - V$ colour. The star P330E was used for calibrating WFC3/UVIS.